SCUOLA DI DOTTORATO
UNIVERSITÀ DEGLI STUDI DI MILANO-BICOCCA

Dipartimento di / Department of

Physics ‘G. Occhialini’

Dottorato di Ricerca in / PhD program Physics and Astronomy Ciclo / Cycle XXX

Curriculum in (se presente / if it is) Condensed Matter Physics, Plasma Physics and Biophysics

TITOLO TESI / THESIS TITLE

Experimental investigation and gyro-kinetic modelling of turbulent transport in thermonuclear plasmas

Cognome / Surname Bonanomi Nome / Name Nicola

Matricola / Registration number 705403

Tutore / Tutor: Dr. Paola Mantica, CNR-IFP

Coordinatore / Coordinator: Prof. Marta Calvi

ANNO ACCADEMICO / ACADEMIC YEAR 2016/2017

"Experimental investigation and gyrokinetic modelling of turbulent transport in thermonuclear plasmas"

Nicola Bonanomi
University of Milano-Bicocca, Milano, Italy
Department of Physics 'G. Occhialini'

PhD in Physics and Astronomy

Supervisor: Dr. Paola Mantica
CNR-Plasma Physics Institute 'P. Caldirola', Milano, Italy

Milano, Italy, 07/02/2017

Contents

Summary 4

I Introduction 9

1 Nuclear Fusion 10
- 1.1 Controlled thermonuclear fusion reactions . . . 10
- 1.2 Tokamak . . . 12

2 The JET tokamak 20
- 2.1 Main features . . . 20
- 2.2 Main plasma heating systems . . . 21
- 2.3 Diagnostics . . . 24
- 2.4 JET operational scenarios . . . 28

3 Transport 30
- 3.1 Transport in tokamak plasma core . . . 30
- 3.2 Drift waves, ITG, ETG, TEM . . . 31
- 3.3 Gyrokinetic equations . . . 36
- 3.4 Numerical codes . . . 37
- 3.5 Experimental methods for transport study . . . 41
- 3.6 Thesis work . . . 43

References 45

II Effects of light impurities and fast particles on thermal transport in the plasma core 48

Introduction . . . 49

4 Light impurity transport in JET ILW L-mode plasmas 51
- 4.1 Introduction . . . 51
- 4.2 Experimental set-up . . . 52
- 4.3 Numerical simulation set-up . . . 54
- 4.4 Light impurity transport . . . 57
- 4.5 Discussion and conclusions . . . 58
- Figures . . . 61
- References . . . 64

5 Effects of nitrogen seeding on core ion thermal transport in JET ILW L-mode plasmas 66
5.1 Introduction . . . 67
5.2 Experimental set-up . . . 67
5.3 Numerical simulation set-up . . . 69
5.4 Light impurity effects on thermal transport . . . 70
5.5 Discussion and conclusions . . . 73
Figures . . . 76
References . . . 85

6 Turbulent transport stabilization by ICRH minority fast ions in low rotating JET ILW L-mode plasmas 87
6.1 Introduction . . . 88
6.2 Experimental set-up and methods . . . 89
6.3 Gyrokinetic simulation set-up . . . 90
6.4 Experimental observations . . . 91
6.5 Gyrokinetic simulations . . . 92
6.6 Conclusions . . . 94
Figures . . . 96
References . . . 100

III Electron heat transport 102
Introduction . . . 103

7 Trapped electron mode driven electron heat transport in JET: experimental investigation and gyrokinetic theory validation. 105
7.1 Introduction . . . 106
7.2 Experimental set up and methods . . . 107
7.3 TEM studies in dominant ICRH heating plasmas . . . 109
7.4 Modelling and comparison with experiments . . . 113
7.5 TEM studies in plasmas with dominant NBI heating . . . 116
7.6 Conclusions . . . 117
Figures . . . 119
References . . . 134

8 Impact of electron scale modes on electron heat transport in the JET tokamak 136
Figures . . . 139
References . . . 141

9 Impact of electron scale turbulence and multi-scale interactions in the JET tokamak 142
9.1 *Introduction* . . . 142
9.2 *Experimental observations* . . . 143
9.3 *Gyro-kinetic simulation results* . . . 145
9.4 *Quasi-linear simulations* . . . 146
9.5 *Discussion* . . . 146
Figures . . . 148

References 152

IV Effects of the isotope mass 154

10 Effects of the isotope mass of the main ion species on thermal transport in JET L-mode plasmas 155
10.1 Introduction 155
10.2 Experimental set-up and methods 156
10.3 Experimental results 157
10.4 Gyrokinetic simulations 159
10.5 Conclusions 160
Figures 161
References 168

V Conclusions and future work 169

11 Conclusions and future work 170

List of publications 176

Summary

The realization of controlled thermonuclear fusion represents an opportunity to solve permanently the world energetic problem without the high environmental impact of fossil fuels and the risk associated with nuclear fission power plants. During the last fifty years, great efforts have been made in this direction and, with the realization of the ITER (International Thermonuclear Experimental Reactor) tokamak, a breakthrough is expected in physics and technology of controlled thermonuclear fusion, reaching the goal of producing fusion power with a gain of a factor ~ 10 with respect to input power. Among the physical and technological problems still open, the understanding and the ability to control the heat and particle transport in the plasma is crucial for the optimization of ITER operations, which require the achievement of high levels of temperature, density and plasma confinement. Given the extreme complexity of the transport processes in a plasma, we have not yet reached a comprehensive understanding of these phenomena. Nevertheless, the research has made considerable progress thanks to a strong interaction between theory and experiment: on one hand with the design of diagnostics and experiments increasingly sophisticated, on the other hand with the development of numerical codes increasingly complex. This thesis mainly focuses on the thermal turbulent transport in the tokamak plasma core and lies within this effort of experimental analysis, numerical modelling and comparison between the two. On the experimental side, it covers the execution and analysis of specific transport experiments in JET L-mode plasmas, in which heat flux scans and temperature modulation were used to determine in detail the transport properties of the ion and electron heat channels. On the modelling side, it makes use mainly of gyrokinetic codes, which are the most complete simulation tools available though highly demanding in terms of computational time and complexity of use, although we have limited our study to the local flux-tube approximation. Using gyrokinetic codes has proven essential for physics understanding of the experimental observations, which requires a full theoretical description of the mechanisms at play. Many of the experimental observations described in this thesis have found a qualitative and in most cases also quantitative explanation in the gyrokinetic simulations, therefore also providing a validation of such codes. On the other hand, since for practical purposes of scenario simulations, and extrapolation to ITER and future reactors, simpler and faster models are required. For a couple of topics also the performance of these simplifies quasi-linear models has been evaluated both against experiments and against the more complete gyrokinetic results. This exercise has yielded some positive results but also has shown some limitations of the presently available quasi-linear models, providing useful indications on their regimes of validity and for further improvements.

The thermal transport experimentally observed in tokamak plasmas is much higher than that predicted by the theory of collisional transport. The dominant mechanism that causes this 'anomalous' transport has been identified in the turbulent phenomena that occur on different spatial and temporal scales, causing a flow of heat and particles from the

center to the periphery of the plasma. Three main micro-instabilities are responsible for a high fraction of energy and particle loss from the plasma core: the Ion Temperature Gradient modes (ITG), the Electron Temperature Gradient modes (ETG) and the Trapped Electron Modes (TEM). ITGs and TEMs are characterized by typical scale-lengths of the order of the ion gyro-radius ρ_i (˜mm) while ETGs act on scales that lie between the ion and the electron gyro-radius ρ_e ($\sim \rho_i/60$ for D plasmas). All these instabilities are driven by the temperature gradients in the plasma and develop over a critical threshold in the normalized temperature gradient length $R_0/L_T = R_0 \left|\nabla T\right|/T$ (where R_0 is the tokamak major radius used for normalization), with ITGs driven by ion temperature (T_i) gradients (R/L_{Ti}) and TEM and ETGs driven by electron temperature (T_e) gradients (R/L_{Te}). Above threshold, the turbulent heat flux increases with a rate that determines how stiff the temperature profiles are against an increase of heating power. One of the objectives of turbulent transport studies is therefore to understand which plasma parameters regulate threshold and stiffness and control them in order to achieve high values of the critical threshold and low value of stiffness to maximize performance. This is why all the experiments presented in this thesis focus on the determination of threshold and stiffness level, with direct comparison to gyrokinetic predictions, which is a more powerful way of validating models with respect to the more usual approach of comparing the heat flux/gradient values of a stationary temperature profile.

In this thesis we focus on four aspects regarding thermal transport in the plasma core: the effects of light impurities, the effects of fast particles, the role of ETGs and of the interactions between ion-scale instabilities and electron-scale instabilities (multi-scale interactions) and the effects of the plasma main ion mass (isotope effect). All these four topics are highly ITER relevant. Indeed ITER will be electron heating dominated (both via the external heating systems and via collisions between fast fusion born He atoms and electrons) and T_e and T_i will be strongly coupled. Any instability that will increase the electron heat transport in the plasma core will have a strong impact on both temperature profiles and performances. For these reasons it is important to take into account all the instabilities that will be important for the electron heat flux (q_e) in ITER conditions, including ETGs. While not often considered in the past, recent works showed that ETG modes can be determinant for the thermal transport, especially when ion-scale instabilities (TEM/ITG) are stable or close to marginal stability, as will be the case in ITER. So far, just two comparisons have been made between multi-scale simulations and experiment, one for a C-MOD L-mode plasma and one for a DIII-D H-mode plasma. Both studies showed that ETGs can be determinant in some plasma conditions, but more studies, both experimental and numerical, are needed to clarify the role of ETGs and how the instabilities on different scales interact with each other. Another problem for ITER will be the need of puffing light impurities at the plasma edge to reduce via radiation the heat loss deposition on the divertor. Furthermore, intrinsic light impurities, like Be from the first wall or He from the fusion reactions, will be present in ITER plasmas. On one hand, a stabilizing effect of light impurities on turbulence is predicted by theory, on the other hand, impurities dilute the fuel ions thus reducing fusion power. Therefore, it is important to understand how they propagate into the plasma and what their impact is on the turbulent transport in the core, validating the existing models in order to evaluate the trade-off between positive and negative effects and achieve optimal conditions for fusion in future machines. Also fast particles can affect the turbulent phenomena in the plasma. Fast He atoms will be produced by the $D-T$ fusion reactions, fast D or fast T can be injected in the plasma with the NBI heating system and fast ions can be also created using the ICRH heating with a minority species, such as ^3He, in the plasma. In JET and ASDEX-Upgrade a strong stabilization of ITG modes has been associated to a nonlinear electromagnetic mechanism related to the presence of fast ions (D and ^3He) or high plasma β. Recent results indicate that also an electrostatic mechanism, related to a wave–fast particle resonant interaction, can play an important role in the stabilization of ITGs in some conditions. So far, in all the experimental cases, a high plasma rotation was present and a complete separation of the stabilization due to fast ions and due to rotation was impossible to obtain. The last aspect studied in this thesis regards the effect of the plasma main ion mass on the turbulent transport. In dedicated experiments in different machines it has been observed that the plasma thermal energy confinement time varies significantly with the mass of the plasma hydrogen isotope of the main ion species, in particular it increases with increasing isotope mass, while theoretically the opposite would be expected on the basis of a gyro-Bohm scaling. This is of particular interest as many studies in nowadays tokamaks have been carried out using H or D isotopes, while in a future thermonuclear reactor a $D-T$ mixture will be used. It is therefore important to understand why and how the plasma confinement time varies with the isotope mass and how the isotope mass affects the plasma turbulence.

All experimental results presented in this thesis have been obtained in the JET tokamak (UK), focusing on an L-mode scenario friendly to transport studies, with high edge safety factor to avoid MHD instabilities, low density to avoid collisional coupling between ions and electrons, high toroidal field to couple Ion Cyclotron Resonance Heating (ICRH) with 3He as minority species, which allows narrow deposition both to ions and electrons, depending on its concentration. The Neutral Beam Injection (NBI) power has been varied in order to study plasmas at low and high rotation. Dedicated experimental sessions in JET with C-Wall (CW) and with ITER-Like Wall (ILW) have been studied. By depositing the ICRH power on-axis ($R \approx 3.0\,m$) and off-axis ($R \approx 3.6\,m$) varying the ICRH frequency, it is possible to obtain scans of the gyro-Bohm normalized heat flux as a function of R/L_T. The ICRH power was also square wave modulated in time to allow the use of perturbative techniques. In total, data from 5 dedicated experimental sessions have beed analyzed in this thesis, three of them have been planned and performed during the thesis work. A wider database including past JET CW L-mode plasmas has been also used for the analysis.

Numerical modelling has been performed with local flux-tube gyrokinetic simulations using the code GENE and, to smaller extent, GKW. Both linear and non-linear single scale simulations have been run for each of the four topics, and one non-linear multi-scale simulation for the study of electron heat transport. In the simulations, Miller geometry, collisions, external flow shear and finite-β. effects were included. Suitable converge tests have been made to optimize the numerical resolution. Main ions, electrons and, depending on the topic, light impurity ions or fast ions were retained as kinetic species. Scanning R/L_T in non-linear simulations, it is possible to compare the theoretical and the experimental relation between heat flux and R/L_T and study the effect of changes in the different plasma parameters, to reach understanding of the experimental observations and theory validation. For two topics also the quasi-linear models QuaLiKiz and TGLF have been evaluated, both in stand-alone runs and in profile simulations using the code ASTRA.

The experimental electron threshold was found to depend strongly on the magnetic shear $s$and on the parameter $\tau = Z_{eff}T_e/T_i$. Whilst the former dependence is common to TEMs and ETGs, the latter is a fingerprint of a significant role of ETGs in the JET plasmas under study. Such role is further confirmed by the finding that the measured electron stiffness is significantly higher than predicted by simulations based on low-k modes (ITG/TEM), calling for a contribution from the high-k ETGs in the order of 50% of the total electron flux. Consistently, an increase of electron stiffness is observed when increasing NBI power, leading to a more pronounced role of ETGs with respect to ICRH dominated plasmas. Multi-scale simulations (the first ever made for JET) have been run to quantitatively compute q_e in such conditions. The contribution of the ETGs was found significant although still below what needed to match the experiment. From the simulations it appears that the ion-scale turbulent structures lead to a strong saturation of the ETG flux but also that the electron-scale structures can act on the ion-scale structures though inverse energy cascades. This indicates that the level of ETG flux is very sensitive to the level of low-k modes, opening the way to a better match of the electron flux when more physical effects influencing the low-k range will be included. In fact the effects of impurities and fast ions and e.m. effects, presently not included for the sake of computational time, will stabilize the ITG modes and boost the ETG component further. An important point that has been understood is that unfortunately a stabilization of ion-scale turbulence will lead to a deterioration of the electron transport. This is in fact observed in high power JET scenarios, where T_i can achieve high peaking but Te_i is stuck to the same peaking irrespective of power. This does not penalize the JET performance since ion heating is dominant, but of course will be penalizing in electron heated ITER plasmas, calling for a work of optimization of the level of stabilization in the two instability scales. The TGLF quasi-linear model, built taking into account also multi-scale interactions, has been tested against our multi-scale simulation and the experiment. When the ion heat flux q_i is matched, TGLF and GENE are in good agreement, with TGLF predicting a strong increase of q_e due to ETG over a certain value of R/L_{Te}. Therefore this tool is suitable for at least a qualitative exploration of these effects in future scenarios. The nonlinear gyrokinetic simulations performed for this study have been also used to improve the QuaLiKiz quasi-linear model for ETG modes.

For the study of the light impurity transport in the plasma core, the profiles of 5 light impurities, $^3He, Be, C, N$ and Ne, measured with charge-exchange spectroscopy in JET ILW L-mode plasmas, have been modelled with quasilinear and nonlinear gyrokinetic simulations. Different density profile peaking has been observed for the different impurities in our conditions, with C and N becoming flat/hollow in the mid plasma region ($3.4 \lesssim R \lesssim 3.7\,m$), whilst theory predicts always the same level of peaking. These discharges have low rotation so that roto-diffusion is not an important player. The missing physical effect to explain the flat profiles has still to be found. On the other hand, the effects of light impurities on thermal transport seem well understood. Discharges with N injection have shown higher peaking of T_i, which was ascribed both to the direct effect of the impurity and to indirect effects via changes in Ti/Te and q profile. The direct effect can be on ion threshold in presence of highly peaked impurity density profiles or on ion stiffness in presence of flattish impurity profiles. Very good match with experiment has been obtained by gyrokinetic simulations. TGLF tends to generally underestimate the ion stiffness, but concerning the impurity effects it is able to reproduce quantitatively the gyrokinetic runs. QuaLiKiz reproduces much better the ion stiffness, but it indicates always a shift of the critical R/L_{Ti} threshold with impurities, also in cases where an effect on stiffness is seen with GENE and TGLF. The effect of geometry has also been found important. These results call for an improvement of both QL models.

In this work we show the first experimental evidence of a strong thermal transport stabilization due to the presence of fast ions in plasmas with low rotation in JET ILW. This has been obtained by applying 7 MW of ICRH ion heating in (3He-D) scheme with minimal NBI power for Charge Exchange measurements. A strong peaking of T_i inside $\rho_{tor} \approx 0.35$ is observed, demonstrating that ion de-stiffening takes place irrespective of rotation. The only difference with respect to low ICRH plasmas with stiff ions is an enhancement of the fast ^3He ion energy density. Linear and nonlinear gyrokinetic simulations reproduce the experiment, predicting two strong stabilization mechanisms, related to the presence of the fast ^3He. One mechanism is electrostatic and has been related a resonant wave-fast particle interaction, while the other mechanism is nonlinear electromagnetic and sensitive to the total pressure gradient. It was also found that the fast ion distribution function influences the quantitative prediction of the stabilization, with better match to experiment when a numerically calculated distribution is used in place of the approximated Maxwellian. Another effect of fast ions is the destabilization of high-k instabilities such as ETG modes, associated to a reduction of the value of τ.

Regarding the effects of the isotope mass on the core turbulent transport, a dataset of JET CW and ILW L-mode deuterium (D) plasmas has been compared to discharges obtained in JET ILW L-mode hydrogen (H) plasmas. When the same operational settings (heating power, I_p, B, q, n_e) are used, both T_e and T_i are lower in H plasmas, the difference starting at the plasma edge. In low power plasmas, q_i in the plasma core does not deviate from the gyro-Bohm scaling outside error bars, but, as the strong influence of T_i dominates over the mass in the gyro-Bohm normalization, it is difficult to make a certain conclusion from our data. A difference in q_i in H and D plasmas has instead been observed at higher power, in the situation where a strong stabilization of ITG modes by fast ions was expected. In this case, the stabilization of the ion heat transport is less strong in H plasmas with respect to D plasmas. A simple explanation has been found in the differences between the fast ion populations, with H plasmas featuring $\sim 1/2$ of the fast ion pressure in D. This was mainly due to the differences in the beam injection energies, in the beam slowing down time and in the ^3He concentration needed for the ICRH minority scheme heating. No deviations from the gyro-Bohm scaling have been observed in the nonlinear gyrokinetic simulations even when considering fast ions and electromagnetic effects. The electron heat transport shows in general higher values of R/L_{Te} in H plasmas. Also, the strong correlation between R/L_{Te} and τ observed in D plasmas has not been observed in H plasmas, suggesting a reduced importance of ETGs.

In conclusion, different fundamental aspects of thermal turbulent transport have been studied in JET L-mode plasmas. An interpretation of the experimental results has been reached with the help of gyrokinetic simulations, and some physical effects have been evidenced in JET plasmas that are relevant for future ITER scenarios. Some important indications on the validity of the available numerical models of turbulent transport have been obtained, as well as suggestions for possible improvements.

Part I

Introduction

Chapter 1

Nuclear Fusion

1.1 Controlled thermonuclear fusion reactions

In a nuclear fusion reaction, two or more atom nuclei fuse together generating new atom nuclei and subatomic particles. For atoms with $A \lesssim 56$ (Iron) the binding energy per nucleon grows with A (see figure 1.1). So, if two atoms fuse together and create an atom with $A \lesssim 56$, the total energy of the bound atom is lower and the difference between the mass of the reagents and the mass of the products is positive and energy is released from the reaction following the mass-energy relation $E = (m_{reagents} - m_{product})c^2 = (\Delta m)c^2$.

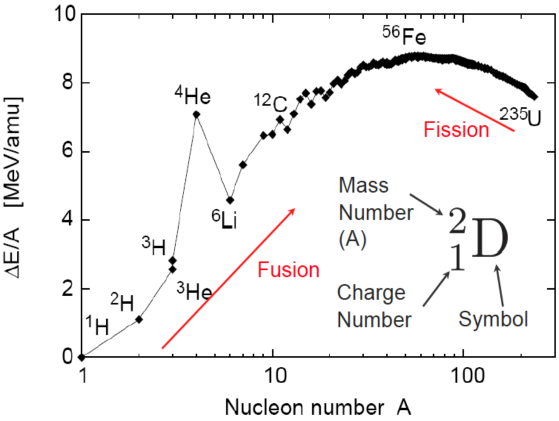

Figure 1.1: *Binding energy per nucleon ($\Delta E/A$) of some of the elements as a function of the atomic mass number A[1].*

In order to fuse together, two atom nuclei must be at distances of the order of $10^{-15}\,m$. At these distances, the strong interaction takes over the Coulomb interaction. To have a good probability to fuse together (through the quantum-mechanical tunnel effect), the atoms must have high energy ($\sim 10\,keV$). In order to provide such energy to the atoms, extremely high temperatures must be reached in controlled thermonuclear fusion reactors on earth. At such temperatures the gas is completely ionized and is in the state of a plasma.

The fusion reaction rate of two atom nuclei in the plasma depends on the temperature, on the density and on the ion species used for the reaction. Considering just two ion species in the plasma, the fusion reaction rate can be written as [2]

$$\Re = n_1 n_2 \langle \sigma v' \rangle \tag{1.1}$$

where n_1, n_2 are the densities of the two ion species, σ is the reaction cross-rate and $v' = v_1 - v_2$ is the difference between the velocities of the two ion species $v_i = \sqrt{T_i/m_i}$, $m_{i,} T_i$ being the ion mass and temperature. Three reactions have been considered for a thermonuclear fusion reactor; $D-D$, $D-^3He$ and $D-T$ reaction. The cross-sections, as a function of T_i, of these reactions are shown in figure 1.2. The $D-T$ reaction, due to the higher cross-section at lower temperatures, is the easiest to obtain and is the one chosen for the realization of the controlled thermonuclear fusion.

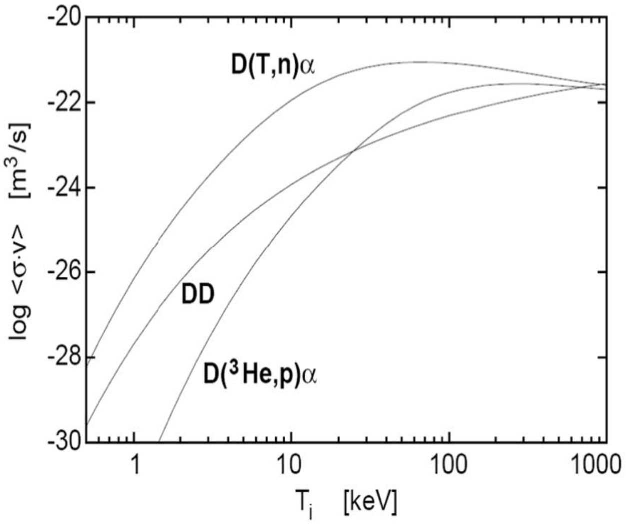

Figure 1.2: *log(*$\langle \sigma v \rangle$ *as a function of* T_i *for the reactions* $D-T$, $D-D$ *and* $D-He^3$.

The $D-T$ reaction is

$$D + T \longrightarrow \alpha + n + 17.6\,MeV \tag{1.2}$$

where the α particle (^4He) brings $3.5MeV$ while the neutron n brings $14.1MeV$ of energy for a total of $17.6\ MeV$. The optimal temperature for this reaction is $\sim 30\,keV$, that corresponds to $\sim 300{\cdot}10^6$ °C. Two main problems arise from bringing the $D-T$ plasma to such temperatures. The first one is how to confine the plasma, to minimize interaction of the hot particles with plasma wall materials, the second problem is how to maximize the triple product of ion temperature, density and confinement time to obtain an energy gain

$$Q = \frac{P_{out}}{P_{in}} \gg 1, \tag{1.3}$$

P_{out} being the power obtained from the fusion processes and P_{in} being the power used to maintain the plasma at the required temperatures. The ideal situation would be $Q \to \infty$, that corresponds to the situation in which no external power would be necessary, the plasma being maintained at high temperatures by the fusion processes themselves though the α particle energy. This condition is called ignition.

Regarding the plasma confinement, different configurations have been considered. One possibility is the magnetic confinement: since the plasma particles are charged it is possible to use magnetic fields to confine them, maintaining the plasma suspended in a vacuum chamber. In this way, the damages to the materials that surround the plasma would be highly reduced. The most studied and advanced configuration for the magnetic confinement is the toroidal configuration. One machine that confines the plasma using this configuration is the tokamak (from the Russian 'toroidalnaya kamera' and 'magnitnaya katushka', literally 'toroidal chamber' and 'magnetic coils').

1.2 Tokamak

The tokamak has been invented in the 50's of last century by the Russian scientists Andrei Sakharov and Igor Tamm. A schematic representation of a tokamak is shown in figure 1.3. In this section some characteristics of a tokamak and of a tokamak plasma, at least the ones used for the studies reported in this thesis, are given. The information reported in this section is mainly based on ref. [2].

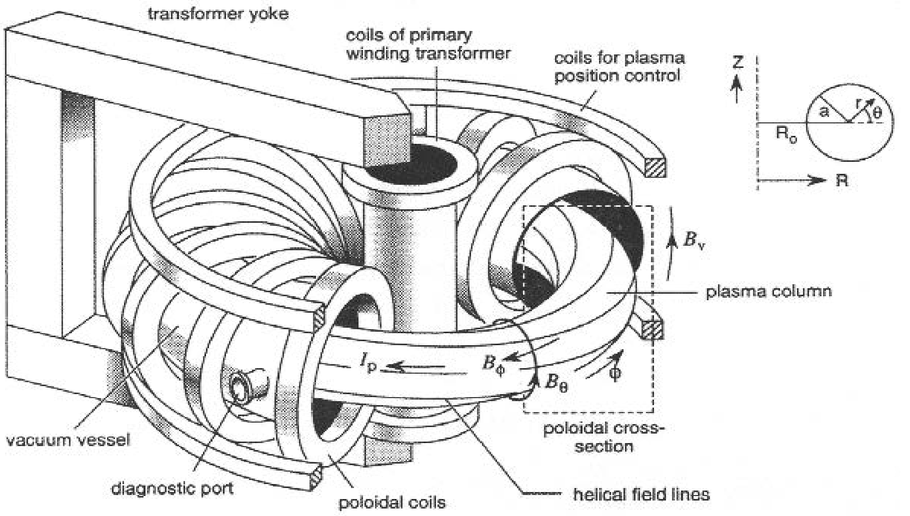

Figure 1.3: *Schematic representation of a tokamak [2].* ϕ *indicates the toroidal direction,* θ *the poloidal direction and* z *the vertical one. The toroidal magnetic field* B_ϕ *is created by the external poloidal coils while the poloidal magnetic field* B_θ *is created by the plasma current* I_p*. This is induced by a variating magnetic field across the tokamak center created by the currents in the primary coils. Other external coils determine the vertical position and the shape of the plasma confined inside the vacuum vessel. The tokamak is also characterized by a major radius* R_0 *and by a minor radius* a*.*

1.2.1 Tokamak magnetic field

The plasma in a tokamak is confined inside a vacuum chamber using a magnetic field **B** (see figure 1.3). The main component of **B** is the toroidal one, B_ϕ, created by the external coils placed around the torus. It varies along the radius R as

$$\mathbf{B} \approx B_\phi \mathbf{e}_\phi \approx \frac{\mu_0 I_c}{2\pi R}\mathbf{e}_\phi \tag{1.4}$$

where I_c is current flowing in the coils. Because the magnetic field varies with R and is curved, it originates plasma particle drift velocities perpendicular to **B** given by

$$\mathbf{v}_{\nabla\mathbf{B}} = \frac{\mu}{q}\frac{\mathbf{B}\times\nabla\mathbf{B}}{B^2} = -\frac{mv_\perp^2}{2qB_\phi R}\mathbf{e}_z;\ \mathbf{v}_{curv} = \frac{mv_\parallel^2}{qB^2}\frac{\mathbf{R}_{curv}\times\mathbf{B}}{R_{curv}^2} = -\frac{mv_\parallel^2}{qB_\phi}\frac{1}{R_{curv}}\mathbf{e}_z \tag{1.5}$$

where m is the mass of a particle with charge q that moves along the magnetic field lines with a velocity $v_\parallel$ and across the field lines with a velocity $v_\perp$, $\mu = mv_\perp^2/2B$ is the magnetic moment of the particle and R_{curv} is the curvature radius of the field lines. These drift velocities, depending on the particles charge, create a density separation between electrons and ions that leads to an electric field $\mathbf{E_z} = E\mathbf{e_z}$. This electric field generates a $\mathbf{E}\times\mathbf{B}$ drift velocity in the radial direction and independent from q that leads to a loss of particles from the plasma. In order to prevent this loss, a poloidal magnetic field $B_\theta\mathbf{e}_\theta$ is added to the toroidal field, obtaining an helical shaped magnetic field

$$\mathbf{B} = B_\phi \cdot \mathbf{e}_\phi + B_\theta \cdot \mathbf{e}_\theta. \tag{1.6}$$

In this way, the $\mathbf{E}\times\mathbf{B}$ drift, related to the magnetic geometry drift, is in opposite directions in opposite plasma hemispheres and the two opposite drifts compensate every poloidal turn. The poloidal magnetic field is induced by the plasma current I_p, that is induced in the plasma using the external primary coils of the tokamak. This introduces a technical limit on the tokamak operations, that must be impulsive if the plasma current is inductively provided by the external coils.

1.2.2 Safety factor and magnetic shear

The safety factor $q$is related to the magnetic geometry and indicates the number of toroidal turns that a magnetic field line has to do before completing a poloidal turn. Considering an infinitesimal annulus of radius R and infinitesimal width dr in the radial direction, the poloidal flux through this ring is given by

$$d\Psi = 2\pi R B_\theta dr,$$

while the toroidal flux is given by

$$d\Phi = \oint (B_\phi d\phi) ds,$$

where ds is the distance moved in the poloidal direction while moving through a toroidal angle $d\phi$. The safety factor can the be written as

$$q = \frac{d\Phi}{d\Psi}. \tag{1.7}$$

$q$is related to the plasma current density profile $\mathbf{j}(r)$ and varies with the radius, usually having its minimum value close to the magnetic axis $R \approx R_0$ and increasing outwards. The safety factor has a great importance for the plasma stability and has an important role in the plasma transport phenomena. Another important parameter, related to q, is the magnetic shear

$$s = \frac{r}{q}\frac{dq}{dr}. \tag{1.8}$$

The safety factor q is important for MHD (magneto-hydro-dynamic) instabilities. High q values ensure a more stable MHD configuration, while, for example, q$\leq$1 close to the magnetic axes can trigger the Sawtooth instability [2]. The magnetic shear is important for the turbulent transport stability. The main operational scenarios of a tokamak are characterized also by the safety factor and the magnetic shear values (see section 2.4).

1.2.3 Plasma equilibrium

In axisymmetric conditions, the magnetic field lines of a tokamak plasma lye on nested surfaces, called magnetic surfaces. From MHD considerations, imposing a null force on the plasma, an equilibrium equation is derived, that states that the forces due to the plasma pressure must be equal to the $\mathbf{j} \times \mathbf{B}$ force

$$\mathbf{j} \times \mathbf{B} = \nabla p \tag{1.9}$$

$\mathbf{j}$ being the plasma current density and p the plasma pressure. From this equation it can be derived that

$$\begin{gathered} \mathbf{B} \cdot \nabla p = 0 \\ \mathbf{j} \cdot \nabla p = 0. \end{gathered} \tag{1.10}$$

These expressions indicate that along the magnetic field lines the pressure is constant and that the current lines, being at constant pressure, are placed on the magnetic surfaces.

Considering the poloidal magnetic flux Ψ, with the property

$$\mathbf{B} \cdot \nabla \psi = 0 \tag{1.11}$$

, i.e. that it is constant on every flux surface, an equation in Ψ for the flux surfaces at the equilibrium can be derived, the Grad-Shafranov equation [2]. Typical solutions of this equation are shown in figure 1.4.

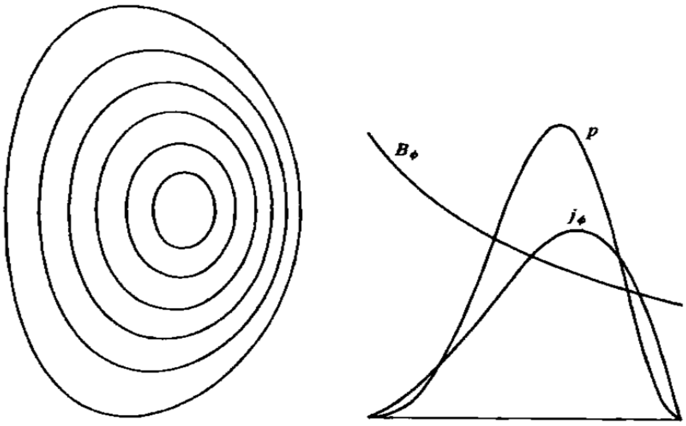

Figure 1.4: *Equilibrium magnetic flux surfaces, derived from the Grad-Shafranov equation, and radial profiles of the toroidal plasma current* j_ϕ, *of the plasma pressure* p *and of the toroidal magnetic field* B_ϕ *[2].*

1.2.4 Plasma β

Starting from

$$\nabla \times \mathbf{B} = \mu_{\mathbf{o}} \mathbf{j}$$

$$\nabla \cdot \mathbf{B} = 0$$

$$\nabla p = \mathbf{J} \times \mathbf{B}$$

can be derived the equation

$$\nabla(p+\frac{B^2}{2\mu_0})=(\mathbf{B}\cdot\nabla)\frac{\mathbf{B}}{\mu_\mathbf{0}} \tag{1.12}$$

known as pressure balance equation. The term $B^2/2\mu_o$ is the magnetic pressure, associated to the magnetic field, while $p = nT$ is the plasma thermal pressure. The plasma β factor is defined as the ratio between the plasma thermal and magnetic pressure

$$\beta=\frac{p}{B^2/2\mu_0}, \tag{1.13}$$

and indicates how good the magnetic confinement is. High values of plasma β are desired for optimal tokamak operations, but upper limits are set by stability considerations.

1.2.5 Tokamak plasmas characteristics

The plasma is a quasi-neutral gas of charged particles that exhibit collective behaviors. Continuous charge separation and flow take place into the plasma, creating magnetic and electric fields. These fields apply forces on the plasma particles and rule the collective behavior of the plasma. As soon as an electrostatic potential is created into the plasma, the charged particles move to shield the potential within a certain length called the Debye length

$$\lambda_D=(\frac{\epsilon_0 T_e}{ne^2}). \tag{1.14}$$

Therefore a plasma, that must respect the quasi-neutrality condition, i.e. $n_{e^-}\approx n_{i^+}$, must have an extension $L\gg\lambda_D$ and a particle density high enough to shield an electrostatic potential created by a charge separation in the plasma within the Debye length, so that

$$N_D=n\cdot\frac{4}{3}\pi\lambda_D^3\gg 1 \tag{1.15}$$

where N_D is called plasma parameter.

A plasma particle in a tokamak, being subject to a strong external magnetic field $\mathbf{B}$, moves along a magnetic field line with a velocity $v_\parallel$ and around it with a cyclotron frequency and a cyclotron radius given by

$$\begin{aligned}\omega_c &= \tfrac{qB}{m}\\ \rho_L &= \tfrac{mv_\perp}{\omega_c}\end{aligned} \tag{1.16}$$

q, m being the charge and the mass of the particle and $v_\perp$ its velocity perpendicular to $\mathbf{B}$. The particles in the plasma are also subject to drift velocities due to any force perpendicular to the magnetic field. These drifts are very important for the transport phenomena inside the plasma. The main drift velocities are the $\mathbf{E}\times\mathbf{B}$ drift velocity, caused by the presence of an electric field perpendicular to $\mathbf{B}$

$$\mathbf{v_E}=\frac{\mathbf{E}\times\mathbf{B}}{B^2}, \tag{1.17}$$

the drift velocities caused by the gradient and the curvature of the magnetic field (equation 1.5), the drift due to a spatial non-uniformity of an electric field ($\mathbf{E}(\mathbf{r})=\mathbf{E_0}+(\mathbf{r}\cdot\nabla)\mathbf{E}+\frac{1}{2!}(\mathbf{r}\cdot\nabla)^2\mathbf{E}+...$)

$$\mathbf{v}_{\nabla E} = (1 + \frac{r_L^2}{r}\nabla^2)\frac{\mathbf{E_0} \times \mathbf{B}}{B^2} \tag{1.18}$$

and the drift due to temporal variations of an electric field (or polarization drift)

$$\mathbf{v}_p = -\frac{m}{qB^2}\frac{d\mathbf{E}}{dt}. \tag{1.19}$$

There is another kind of drift in the plasma that does not involve the single particles, but the particles as a fluid. This drift, called diamagnetic drift, is related to a pressure gradient in the plasma and is defined as

$$\mathbf{v}_* = \frac{\mathbf{B} \times \nabla \mathbf{P}}{nqB^2}.$$

To the diamagnetic drift a plasma current is associated

$$\mathbf{j}_* = \sum_s n_s q_s \mathbf{v}_{*\mathbf{s}} \tag{1.20}$$

where the sum is over all the species of the plasma.

1.2.6 Particle orbits and trapped particles

In a uniform magnetic field B, a charged particle with nonzero parallel (to B) velocity is free to move along the magnet field line without restrictions. The magnetic field in a tokamak is proportional to $1/R$. It is weaker in the external region of the torus (Low Field Side, LFS) and stronger in the internal region (High Field Side, HFS). Due to this characteristic of a tokamak magnetic field, magnetic mirrors can be created and the particles with a parallel velocity not high enough to escape from the magnetic mirrors are reflected [2, 3]. The particles that are not reflected by the magnetic mirrors are called passing particles, the other ones are called trapped particles. A schematic representation of the passing and of the trapped particle orbits is shown in figure 1.5.

The condition for the particle to be trapped by B can be written as

$$\frac{B_b}{B_{min}} = 1 + (\frac{v_{\parallel 0}}{v_{\perp 0}})^2, \tag{1.21}$$

where B_b, B_{min} indicate the value of the magnetic field at which the particle is reflected and the minimum value of the magnetic field and v_0 is the velocity of the particle at $B = B_{min}$. Considering a uniform distribution for the particle velocities, an approximate equation for the fraction of trapped particles in the plasma, as a function of the plasma radius r, can be written as

$$f = (\frac{2r}{R_0 + r})^{1/2}. \tag{1.22}$$

The bounce frequency with which a trapped particle moves around its orbit can be written as

$$\omega_b = \frac{v_\perp}{qR_0}(\frac{r}{2R_0})^{1/2}. \tag{1.23}$$

An important factor for the trapped particles is the collisionality. Collisions can change the velocity of the particles so that the conditions for the particle to be trapped are not

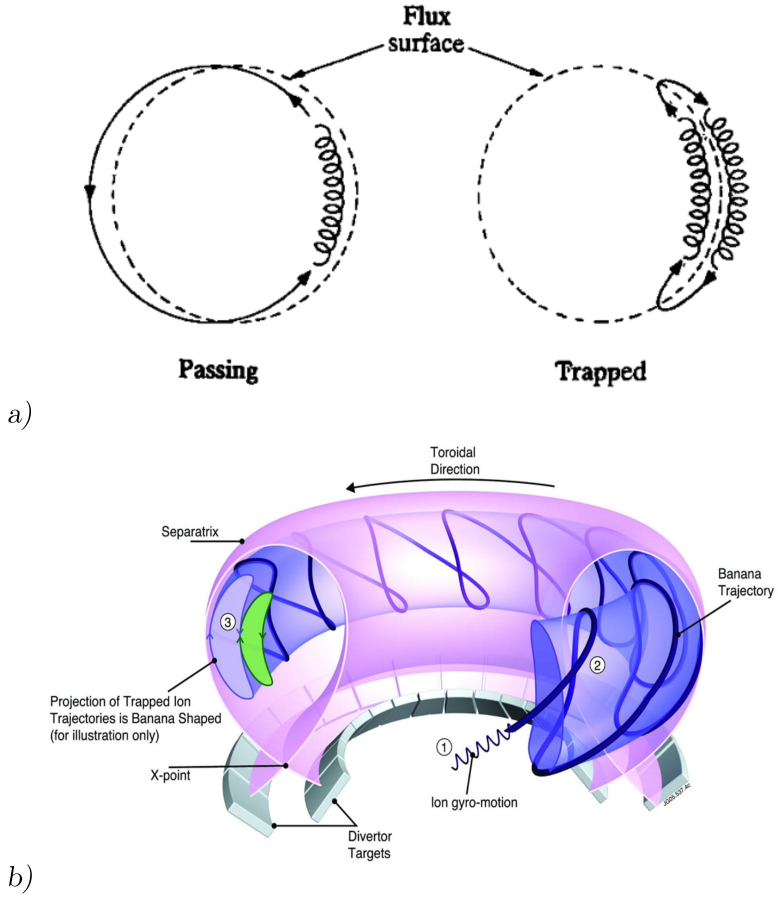

Figure 1.5: *a)Representation of the orbits of passing and trapped particles on a flux surface in a tokamak plasma [2]. b)Representation of the banana trajectory of trapped particles along a magnetic field line in the tokamak.*

satisfied anymore. In this way collisions can cause de-trapping of the particles. The time for collisions to free the trapped-particles can be approximated as

$$\tau_{detrap} \simeq \frac{2r}{R_0}\tau_{coll} \tag{1.24}$$

where τ_{coll} is the collisional time at big angles. If $\tau_{detrap} < \omega_b^{-1}$ the collisions prevent the trapping of the particles.

1.2.7 Limiter and divertor

The plasmas in a tokamak have densities typically in the range $n \sim 10^{18} - 10^{20}\, m^{-3}$. In order to obtain such densities (a million time lower than the atmospheric one), powerful pumping systems are used to create the vacuum in the plasma chamber and to minimize impurities in the plasma. The plasma has also to be kept away from the chamber walls. In order to do this, two ways have been adopted: the first consists in using a limiter that touches the plasma in presence of closed field lines; the second, more advanced and used as the standard today and for future reactors, is the divertor. The divertor is able to modify the magnetic field lines in order to obtain a X configuration (see figure 1.6) and move the particles that escape from the plasma in the divertor region, where special targets absorb the heat fluxes from the plasma and special pumps eliminate the particles ejected from the plasma.

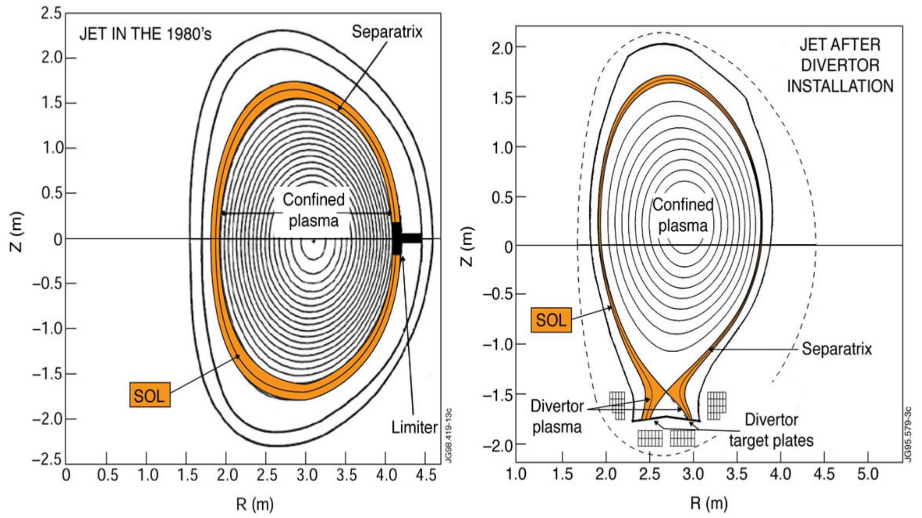

Figure 1.6: *Limiter and divertor configurations of the JET tokamak (from www.efda.org). The SOL (Scrape-Off Layer) region is where the plasma particles and energy are ejected from the confined region (i.e. from the region where the magnetic field lines are closed). The 'Separatrix' is the last magnetic field line that is closed, and so the last magnetic field line of the confined region.*

1.2.8 Ignition

The energy in the tokamak plasma, considering ions and electrons at the same temperature and considering $n_{ions} \approx n_{electrons}$, can be derived as

$$W = \int_V 3nTdV = 3\overline{nT}V \tag{1.25}$$

V being the plasma volume. Introducing the energy confinement time τ_E, the rate of energy loss from the plasma can be written as

$$P_{Loss} = \frac{W}{\tau_E} = \frac{3\overline{nT}V}{\tau_E}. \tag{1.26}$$

This loss of energy must be compensated using external heating systems. If nuclear fusion reactions, in a $D - T$ plasma, are occurring, the α particles can heat the plasma through collisions, providing a power P_α to the plasma, and the heating power needed to compensate the energy loss can be calculated as

$$P_{Heating} = P_{Loss} - P_\alpha. \tag{1.27}$$

The ideal situation where P_α is high enough to completely compensate P_{Loss} and so no external heating power is necessary, that is ignition, can be achieved if

$$n_i T_i \tau_E > 3 \times 10^{21}\, m^{-3} keV s. \tag{1.28}$$

When this condition is reached, the power gain from the fusion reactions $Q \longrightarrow \infty$. All the three parameters in formula 1.28 strongly depend on the transport phenomena in the plasma.

1.2.9 Tokamak research and development: ITER

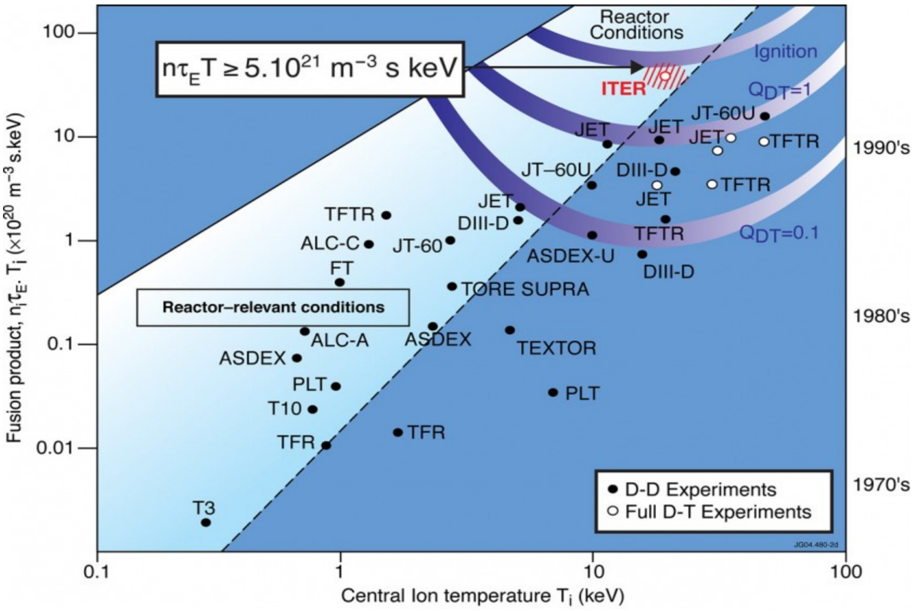

Figure 1.7: *Progresses obtained on the three product $nT\tau_E$ since the 70ies.*

Since its invention during the 50ies of last century, numerous effort have been done to obtain tokamak with always more advanced technology and with better performances. As can be seen in figure 1.7, this continuos evolution of tokamaks leaded to reach conditions always closer to ignition. The data collected from this enormous worldwide effort, have been used to develop the next generation of tokamaks and in particular to develop ITER (International Thermonuclear Experimental Reactor). ITER, actually being build in Cadarache (France), is an international (China, European Union, India, Japan, Korea, Russia and United States) research project that will have to demonstrate the possibility for a tokamak to produce net energy ($Q \gtrsim 10$) and to maintain the fusion reactions for long periods of time and that will have to test for the first time the integrated system (technology and physics) necessary for a future commercial production of electricity from fusion [4]. It is therefore essential to prepare the ITER scenarios in the best way possible. Some numbers of the ITER tokamak are reported in table 1.1.

Plasma major radius	$6.3\,m$	Weight	$23000\,t$
Plasma minor radius	$2\,m$	NBI power (1 MeV beams)	$\leq 33\,MW$
Plasma volume	$840\,m^3$	ICRH power	$\leq 10\,MW$
Magnetic field	$\leq 11.8\,T$	ECRH power	$\leq 24\,MW$
Fusion pulse time	$\geq 300\,s$	Q	≥ 10

Table 1.1: *'Numbers' of the ITER tokamak [4].*

Chapter 2

The JET tokamak

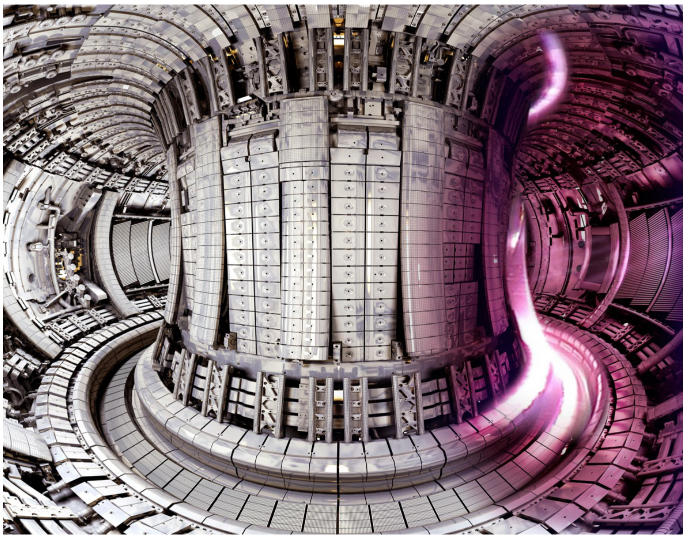

Figure 2.1: *Picture of JET plasma chamber with a typical view of a plasma on the right.*

The informations reported in this chapter are mainly based, when not indicated otherwise, on ref. [2] and on www.euro-fusion.org/jet/.

2.1 Main features

The JET (Joint European Torus) tokamak, located in Culham (UK), is the largest tokamak in the world and the only one that can handle a D-T gas mixture. It is in operation since 1983. After a first phase with limiter configuration, the divertor configuration has been introduced in 1992. In 1996, the world record ($\sim 16\ MW$) amount of power produced by fusion reactions has been obtained in a $D-T$ plasma at JET. Before 2009, JET plasma facing materials (or first wall) were made in carbon (C-Wall), later substituted, between 2009 and 2011, by beryllium and by tungsten for the divertor. This new configuration is called ITER-like wall (ILW) since it is the one chosen for the ITER (International Thermonuclear Experimental Reactor) tokamak, which makes JET operations even more relevant for ITER.

JET has 32 D-shaped, equidistant poloidal magnetic coils that provide a toroidal magnetic field up to $\approx 4\,T$. The iron central solenoid induces a plasma current up to $I_p \approx 4.5\,MA$, which generates the poloidal magnetic field necessary for the plasma confinement. Other 11 coils are used to control and stabilize the position and the shape of the plasma. A complex vacuum system ensures the ultra-high vacuum $(10^{-7}Pa)$ required to achieve the necessary conditions for the tokamak operations. As mentioned above, JET is the only tokamak able to handle tritium, which requires precautions for active isotope handling. All the gases that are pumped from the vessel go to the Active Gas Handling System, that allows to separate and safely storage the different atoms from gas (T, D, He). The main heating systems available at JET are a Radio Frequency (RF) system based on the Ion Cyclotron Resonance (ICRH), and a Neutral Beam Injection (NBI) system. Numerous diagnostics provide all the information useful to study the plasma $(n, T, B, q, ...)$. Typical JET discharges can be maintained up to $\sim 10\,s$. In table 2.1 the main parameters of the JET tokamak are reported.

Major radius (R_0)	$\sim 2.96\,m$
Minor radius (a)	$\sim 1\,m$
Plasma volume	$\sim 90\,m^3$
Plasma triangularity	$0 \leq \delta \leq 1$
Plasma elongation	$1 \leq \kappa \leq 2$
Magnetic field	$B \lesssim 4\,T$
Plasma current	$I_p \lesssim 4.5\,MA$
ICRH power	$\leq 7\,MW$
NBI power	$\leq 30\,MW$

Table 2.1: *Main parameters of the JET tokamak.*

2.2 Main plasma heating systems

In order to achieve the necessary conditions for $D-T$ nuclear fusion reaction, the plasma (at low densities) must be heated up to $\approx 10^8\ K$. A powerful heating system is then necessary to bring the plasma to these temperatures. The JET heating system has been studied to maintain the plasma in these conditions for many seconds (up to 10-20 seconds). The main heating power is supplied, in addition to the ohmic heating due to the plasma current, by an injection of highly energetic neutron beams (Neutral Beam Injections, NBI) and by electromagnetic waves in the ion cyclotron range of frequencies (Ion Cyclotron Resonant Heating, ICRH). In the following these three plasma heating system are briefly described.

2.2.1 Ohmic heating

In order to confine the plasma, a toroidal plasma current (I_p) is induced in the plasma through the central transformer. This current, flowing though the plasma with nonzero resistivity, generates heating through the Joule effect (collisions). Experimental evidences indicate that the plasma resistivity is mainly due to the collisions between ions and electrons described by the neoclassical theory [2, 5] and strongly depends on the electron temperature T_e. The ohmic heating power can be written as

$$P_{Ohm} = \eta j^2, \tag{2.1}$$

η being the plasma resistivity and j being the plasma density current. $\eta(r) = Z_{eff} \cdot \eta_s / (1 - (r/R_0)^{0.5})^2$ where $Z_{eff} = \sum_{ions} (n_i/n_e) Z_i^2$, n_i, n_e and Z_i being respectively the ion and electron density and the ion charge, r and R are respectively the minus radius where η is measured and the major radius of JET and where

$$\eta_s = 1.65 \cdot 10^{-9} \frac{ln(\Lambda)}{T_e^{1.5}} \ \Omega \cdot m \tag{2.2}$$

is the Spitzer resistivity. $ln(\Lambda) = ln(\lambda_D / r_o)$ is the Coulomb logarithm, $r_o = e^2/(4\pi\epsilon_0 m_e v_e^2)$ being the 90° collisions impact parameter and $\lambda_D = (\epsilon_0 T_e / n_e e^2)^2$ the Debye length. As can be seen from equation 2.2, the ohmic heating power is strongly limited by its $T_e^{-1.5}$ dependence. It is also limited by the central transformer operational limits, the transformer having limits in inducing the plasma current and not being able to operate in a steady state condition but just impulsively. The ohmic heating power supplied at JET is up to ~1 MW.

2.2.2 Neutral beam injection (NBI)

The NBI heating system consists in the injection in the plasma of highly energetic neutral atoms. Once launched in the plasma, the beam atoms collide with the plasma particles and are ionized. The ions and the electrons from the highly energetic beams are then captured by the magnetic field of the tokamak and the energy of the ionized particles, brought mainly by the more massive ions, is transferred to the plasma through Coulomb collisions with the thermal ions and electrons. The NBI not only represent a plasm heating system but also a source of plasma particles and momentum.

The deposition of the NBI power depends on how much the neutral beam can penetrate in the plasma before being completely ionized and slowed down by the collisions with the plasma particles. The three main processes that determine how the neutral beam is absorbed in the plasma are:

- charge exchange: $I_{beam} + I^+_{plasma} \rightarrow I^+_{beam} + I_{plasma}$
- ionization due to ions: $I_{beam} + I^+_{plasma} \rightarrow I^+_{beam} + I^+_{plasma} + e^-$
- ionization due to electrons: $I_{beam} + e^- \rightarrow I^+_{beam} + 2e^-$

with certain cross sections indicated by, respectively, $\sigma_{cx}, \sigma_I, \sigma_E$. If the beam intensity, as a function of the position x, is

$$I_b(x) = N_b(x) v_b(x) \tag{2.3}$$

where N_b is the number of neutral particles of the beam and v_b is the velocity of the beam particles, its decay is described by

$$\frac{dI_b}{dx} = -n \left(\sigma_{cx} + \sigma_I + \frac{\langle \sigma_E v_e \rangle}{v_b} \right) I_b. \tag{2.4}$$

σ_{cx}, σ_I and σ_E strongly depend on the beam energy and also the plasma density and temperature play an important role. At JET the injected neutral beam is able to reach

the center of the plasma, but in future reactors, as ITER, the penetration of the beam will be limited. A possible solution is to use negative charged ions, that are ionized at higher energies and can penetrate more into the plasma.
An indicative formula for the amount of power absorbed by thermal electrons and ions is

$$P = P_e + P_i = m_b A_D \left(\frac{2 m_e^{1/2} \varepsilon_b}{3 (2\pi)^{1/2} T_e^{3/2}} + \frac{m_b^{3/2}}{2^{3/2} m_i \varepsilon_b^{1/2}} \right) \tag{2.5}$$

where m_b and $\varepsilon_b = m_b v_b^2/2$ are the mass and the kinetic energy of the beam ions and $A_D = (ne^4 ln(\Lambda))/(2\pi\varepsilon_0^2 m_b^2)$. As can bee seen from equation 2.5, at high beam energy the electron heating is dominant. When the beam is slowed down, the ion heating takes over. At JET up to 35 MW of NBI heating power for ~10s is available using H, D, T and He atoms.

2.2.3 Ion cyclotron resonance heating (ICRH)

A charged particle in a magnetic field B_0, with a non-zero velocity in the direction perpendicular to B_0, moves in a circular motion around the magnetic field lines (cyclotron motion) with an angular frequency

$$\omega_j = \frac{q_j B_0}{m_j} \tag{2.6}$$

where q_j and m_j are the particle's charge and mass. If an electromagnetic wave is launched into the plasma with an angular frequency ω_{rf}, the particles with $\omega_j = \omega_{rf}$ can absorb energy from the wave by resonant effects. Three main radio frequency heating schemes are used in tokamaks to heat the plasma. The one used and discussed within this thesis is the ion cyclotron resonance heating (ICRH).

Using a cold plasma approximation in a slab limit and solving the dispersion relation (see ref. [2]) to obtain a perpendicular resonance (i.e. to obtain a value of the perpendicular refractive index $n_\perp \to \infty$) when $\omega_{rf} \sim \omega_i$, where ω_i is the ion cyclotron angular frequency, one finds that the resonant condition can be obtained only when two or more ion species are present in the plasma (ion-ion hybrid resonance, IIH). Using two ion species, the ion-ion hybrid resonant frequency is approximately

$$\omega_{i-i}^2 = \frac{\omega_{i,1}\omega_{i,2}(1 + n_{i,2}m_{i,2}/n_{i,1}m_{i,1})}{(m_{i,2}Z_{i,1}/m_{i,1}Z_{i,2} + n_{i,2}Z_{i,2}/n_{i,1}Z_{i,1})}$$

where n_i, m_i and Z_i are the ion density, mass and charge. This equation gives a frequency in the range $\sim 30 - 120\, MHz$. Controlling the densities of the two ion species in the plasma and knowing that the ion cyclotron frequencies depend on the radius because B_0 depends on the radius, it is possible to control the radial position where the resonance occurs and to which species the heating power is mainly deposited. In a common ICRH scheme used in JET, called minority scheme, the power is absorbed by a minority ion species with density small compared to the main ion one. Then, the minority ions give energy to the electrons and the main ions though collisions. In all the cases studied in this thesis, ^3He has been used as minority ion species in D or H plasmas (H minority species has been used in D plasmas in few cases included in the database used for the study of ETG modes presented in chapter 9). Using $^3He \approx 6\%$ in D plasmas and $^3He \approx 3\%$ in H plasmas, the majority of the RF power is deposited on ions ([6], see figure 2.3). The power deposition radial location depends on the toroidal magnetic field and on the RF frequency. In the plasma studied in this thesis a magnetic field $B_T \approx 3.3\,T$ has been used, directing the RF ion heating on-axis ($R \approx 0\,m$) or off-axis ($R \approx 3.6\,m$) using RF frequencies $\nu_{on} = 33\,MHz$ and $\nu_{off} = 29\,MHz$. In order to perform perturbative studied on the ion heat transport (see section 3.5), the RF power has been modulated using a modulation frequency of $6\,Hz$.

ICRH in Mode Conversion scheme

A second absorption scheme, based on mode conversion (MC), is possible to direct the power to electrons. This is particularly useful at JET for electron heat transport studies as there is no direct electron radio-frequency (RF) heating such as ECRH. For this scheme the minority ion species used in all the cases studied in this thesis is ^3He. If the ^3He density is high enough ($[^3He] \gg 10\%$ in D plasma and $[^3He] > 4\%$ in H plasmas), the way the RF power is absorbed by the plasma changes [6]. A mode conversion phenomenon occurs, that allows to create a highly localized electron heat source by the absorption of the energy by the electrons from an electrostatic wave called Bernstein wave. This wave is generated from the injected fast wave at the ion-ion hybrid resonance position and its energy is absorbed directly by electrons with a very narrow deposition profile (see figure 2.2). A small fraction of the injected fast wave is also damped into electrons by Electron Landau Damping phenomena (FW-ELD), with a broad central deposition profile. The position of the ion-ion hybrid resonance depends on the minority species concentration and on the magnetic field and RF frequency. It is then essential to control these parameters, particularly the ^3He concentration, as much as possible to obtain the desired results. In the typical situation studied in this thesis, with a toroidal magnetic field $B_T \approx 3.45\,T$ and with $^3He \approx 18\%$, it is possible to direct the power deposition both on-axis ($R \approx 0\,m$) and off-axis ($R \approx 3.6\,m$) using the RF frequencies $\nu_{on} = 33\,MHz$ and $\nu_{off} = 37\,MHz$.

In order to study where the power is deposited, it is possible to modulate the RF power and use a Fourier analysis of the perturbations induced on the $T_e(R)$ profiles. In this way the phases and amplitudes of the heat wave harmonics are obtained. Studying the profiles of these quantities, it is possible to understand if the RF power is well coupled to the electrons and were the power is deposited. Also, as no reliable models to calculate the electron heating in MC is available yet, the perturbative studies allow, using transport simulations in order to reproduce the experimental profiles of temperatures and phases and amplitudes from the Fourier analysis, to calculate the total amount of power absorbed by electrons. Using the right concentration of ^3He, up to the 80% of the RF power can be coupled to the electrons [6, 7]. In order to perform perturbative studies on the electron heat transport (see section 3.5), the RF power has been modulated using a modulation frequency of $20\,Hz$.

2.3 Diagnostics

A high number of diagnostics are available at JET. In the following, a brief description of the main diagnostics used in this thesis work to measure the densities and the temperatures of the plasma are given.

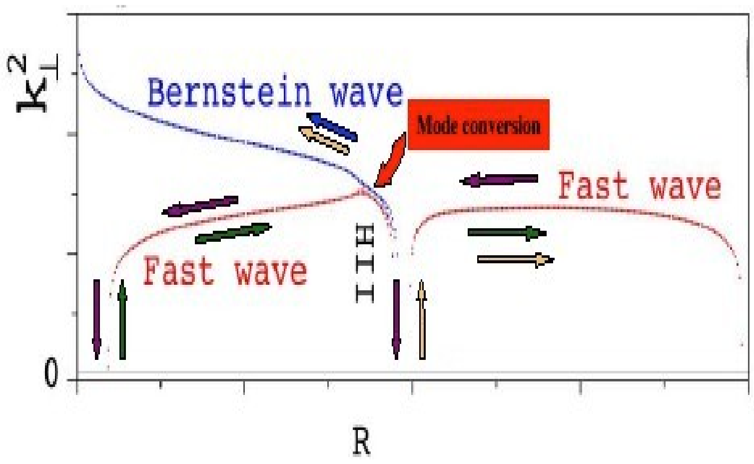

Figure 2.2: *Schematic representation of the ICRH Mode Conversion principle. The fast wave propagates to the Ion-Ion Hybrid resonance position, where it gives its energy to an electrostatic wave, called Bernstein wave, that gives its energy directly to the electrons.*

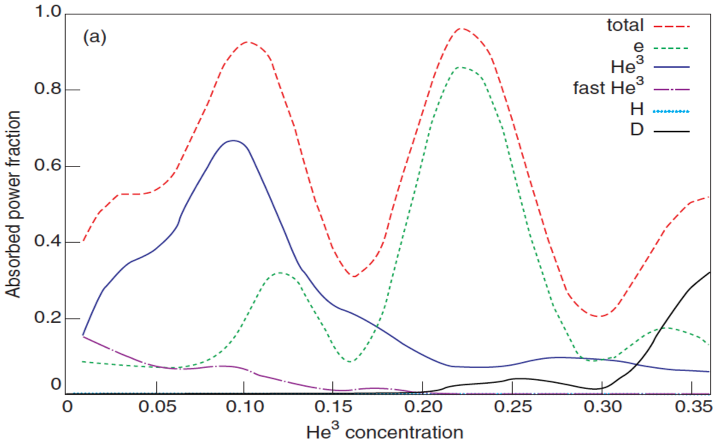

Figure 2.3: *Fraction of absorbed power from the various species in a* $(^3He) - D$ *plasma as a function of the* ^3He *concentration. These results have been obtained from a simulation using the TOMCAT code [?].*

2.3.1 High Resolution Thomson Scattering (HRTS)

The high resolution Thomson scattering at JET [8] is a conventional 90° geometry system, which measures electron temperature (T_e) and electron density (n_e) profiles with up to 63 points along the outer (low field side) radius of the plasma ($R = 2.9 - 3.9\,m$) at a frequency of ~20 Hz and with a resolution of $\sim 15\,mm$. It uses a Nd:YAG laser situated in the roof-laboratory above the JET Torus Hall. The light launched into the plasma has a wavelength of $1064\,nm$ and each pulse last $20\,ns$ with an energy of $\sim 3\,J$.

The light interacts with the plasma electrons through Thomson scattering causing the emission of photons of the same wavelength as the incident light and the scattered light is collected through an upper main vertical port. The Doppler effect due to the plasma temperature broadens the emission spectrum of the photons. Measuring the emitted light from each laser pulse the radial profiles of T_e and n_e can be measured with an uncertainty of $\sim 15\%$ considering that:

- The intensity of the scattered light is proportional to the number of the emitted photons and so to the number of the electrons $\Longrightarrow n_e$;

- The broadening of the spectrum depends on the electron temperature $\Longrightarrow T_e$.

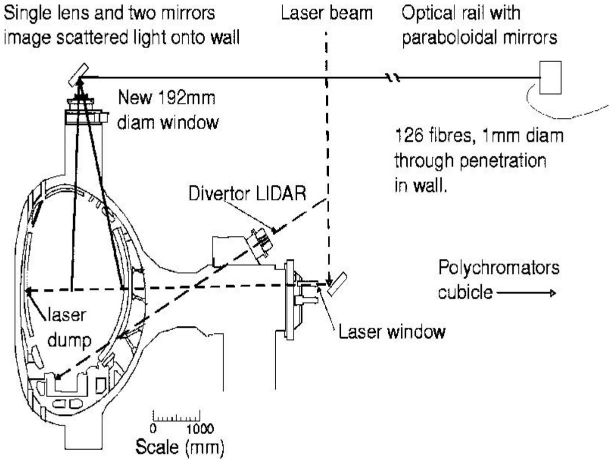

Figure 2.4: *General layout of the HRTS system components in Torus Hall [8].*

2.3.2 Electron Cyclotron Emission (ECE)

The ECE diagnostic at JET is used to measure the electron temperature in the plasma core. It measures T_e at frequencies of $5\,kHz$ and at 96 radial positions (spatial resolution of $\sim 2\,cm$) with uncertainties of $\sim 5\%$. There are a series of effects that can influence the ECE resolution and usually the loss of resolution is higher on the high field side of the tokamak and in the outer part of the plasma. The ECE diagnostic is essential in the experiments that require a high temporal resolution of T_e, like the perturbative studies shown in this thesis.

The electrons in the plasma, being charged particles moving in presence of a magnetic field (B_0), move around the field lines with an angular frequency $\omega_e = eB_0/m_e$ emitting electromagnetic radiation. This radiation is emitted at angular frequencies $\omega_n = n{\cdot}\omega_e$, where n is an integer. In some circumstances, the intensity of this emission is directly related to T_e. In a tokamak, due to the intensity of the magnetic fields used, the ECE emission has a wavelength $\lambda \sim mm$. At these wavelengths, the Rayleigh-Jeans law can be applied and the intensity of the emission of the $n-th$ harmonic, as a function of the angular frequency ω_n and of the radius R, can be written as

$$I_n(\omega_n, R) = \frac{\omega_n^2 T_e(R)}{8\pi^3 c^2}. \tag{2.7}$$

From 3.1, knowing $B(R)$ and measuring the emission at different frequencies, $T_e(R)$ can be derived. Some effects must be considered to avoid errors in the measurements, such as the temporal variation of B_0, the corrections to the vacuum $B(R)$ due to plasma diamagnetism and paramagnetism, the density of the plasma (important for the propagation of the radiation in the plasma due to refraction effects).

2.3.3 Charge Exchange Spectroscopy (CX)

When neutral atoms are injected into the plasma using NBI, the fast neutrals react with the plasma ions through charge exchange reactions and emit radiation. A typical charge exchange reaction is

$$I_{NBI} + I^{+s}_{plasma} \rightarrow I^{+}_{NBI} + I^{+(s-1)}_{plasma}.$$

After the reaction, the electron received by the plasma ion can be in an excited state and decade emitting visible radiation. If this radiation is observed at an angle to the beam, localized measurements of plasma parameters can be made by fitting the Doppler broadened line of the CX emission (it depends on the species used). From the shift of the peaks of the spectra, also the plasma rotation can be measured.

The JET CX [9] has a typical spatial resolution of $\sim 7\,cm$ and a measurement frequency of $20\,Hz$. The species usually used for charge exchange T_i measurements are D, He, N, Ne, C, Be. A simplified scheme of the JET CX is shown in figure 2.5.

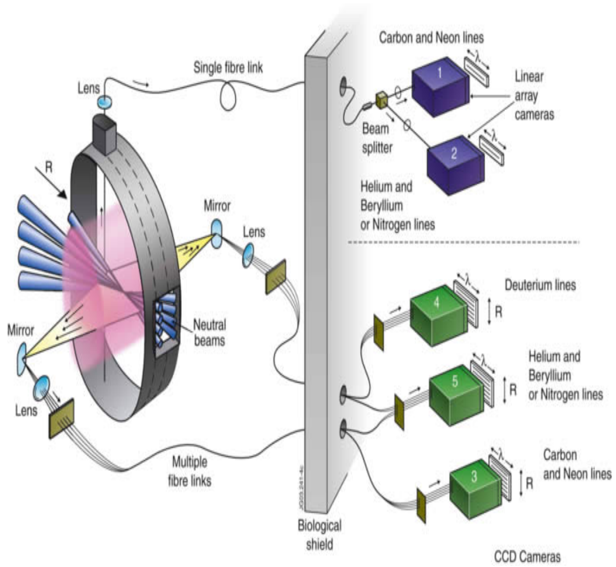

Figure 2.5: *Simplified schematic representation of the JET CX (www.euro-fusion.org).*

2.3.4 Equilibrium reconstruction (EFIT)

At JET, the equilibrium code EFIT [10, 11], is used to solve the Grad-Shafranov equation and calculate important quantities like plasma current density, safety factor $q$and flux surface geometry. EFIT is based only on magnetic probe measurements. To improve the accuracy of the calculations, internal diagnostic information like the pitch angle as measured with the motional stark effect (MSE), the Faraday rotation angles or pressure profile information can be used. In order to use MSE measurements, the use of a specific NBI launcher is required. These measurements have a spatial resolution of $5 - 8\,cm$ and a temporal resolution $\Delta t \sim 20 - 40\,ms$. Regarding the Faraday rotation constraint, the JET setup for the interferometer-polarimeter allows a measurement of the line integrated density and Faraday rotation along the same lines of sight. A successful analysis of the line integrated Faraday rotation requires an accurately known density profile [12].

Error bars on the safety factor measurements depend on the diagnostic used to constrain the equilibrium reconstruction. For magnetic measurements only, the errors on the central q value can be quite large (up to 50% in the worst cases), but in L-mode discharges the uncertainties are lower. Using the Faraday rotation constraint, typical errors are ~20%, while using the MSE constraint the error bars are reduced to ~10%. The error bars on the magnetic shear are in general larger with respect to the ones on the safety factor. An error of 10% on q would correspond to an error of ~20% on s. Good measurements of the safety factor q (and of the magnetic shear s) are very important for turbulent transport studies and MSE or Faraday rotation constraints are essential in order to have reliable measurements of these quantities, especially in particular conditions (like for reversed safety factor profiles) or in the inner part of the plasma core. For these reasons MSE or Faraday rotation constraints have always been requested for the discharges analyzed in this thesis.

2.4 JET operational scenarios

The JET tokamak is capable of operating in different scenarios and, at the present day, is the only tokamak capable of operating with a $D-T$ gas mixture. One of the main characteristics of the different scenarios is the energy confinement time. This parameter, as already pointed out, is of great importance for future reactors such ITER, as the ability of maintain high plasma pressure for a long time is fundamental to achieve a high Q factor. Scaling laws for the confinement time have been developed, collecting a worldwide database of tokamak discharges. One of the most used, developed for the baseline H-mode scenario, is the ITERH-98P(y,2) scaling law, which depends on different plasma parameters: major radius R_0, absorbed power P, toroidal magnetic field B_T, plasma elongation κ, plasma current I_p, plasma central line averaged density $\langle n \rangle$ and main hydrogen isotope mass

$$\tau_{ITERH-98P(y,2)} = 5.62{\cdot}10^{-2} R_0^{1.97} P^{-0.69} B_T^{0.15} \kappa^{0.78} I_p^{0.93} \langle n \rangle^{0.41} M^{0.19}. \tag{2.8}$$

It is common to compare a plasma confinement time in a different scenario to the H98P(y,2) value, defining a H_{98} factor

$$H_{98} = \frac{\tau_E}{\tau_{ITER-98P(y,2)}}. \tag{2.9}$$

Below, the main scenarios in which JET can operate, and that are considered also as ITER scenarios, are listed.

L-mode The L-mode is a low power scenario with low confinement time ($H_{98} \sim 0.5$), due to the absence of an edge transport barrier. Despite the low confinement time, plasmas in L-mode are very useful to study the properties of the plasma core transport as possible effects related to the plasma edge are minimized. Transport studies using heat flux scans and perturbative techniques can be achieved in L-mode plasmas, while this kind of studies are very difficult in more advanced scenarios like H-modes. These studies, used and described in this thesis, allow to study properties of the turbulent transport such as the temperature stiffness or the turbulent critical threshold in $L_T^{-1} = -\nabla T/T$ (see section 3.2), that help to characterize the turbulent state of the plasma core in the various conditions. All the plasmas studied in this thesis, that focuses on core turbulent transport, are L-mode plasmas.

H-mode The H-mode plasmas feature a high power and the presence of an edge transport barrier that highly enhances the plasma density and temperature. These discharges provide a high confinement time, $H_{98} \sim 1$ and are the main scenario envisaged for ITER high fusion power production. This scenario features the presence of strong MHD activity at the plasma edge, the Edge Localized Modes (ELMs), that periodically eject high quantities of energy and particles outside the plasma. Due to its high current ($q_{95} \sim 3$) , the scenario has also $q < 1$ values in the inner core region. This leads to another kind of MHD activity, the sawtooth instability, that causes the ejection of particles and energy from the inner core of the plasma reducing the inner core plasma pressure. If the plasma β is high enough, these modes can also cause neoclassical tearing modes (NTMs), which lead to the formation of magnetic islands, further reducing the plasma confinement.

Advanced Tokamak scenarios If an internal transport barrier (ITB) is created in the plasma core, the high pressure gradients inside the barrier strongly enhance the bootstrap current fraction of the plasma current, leading to a scenario that can operate steady state (H-mode steady-state scenario), without the need of an externally induced plasma current. The ITB is typically formed by creating a region of negative magnetic shear. In this steady H-mode scenario, the confinement time can be highly enhanced, $H_{98} \sim 2$, but it needs a high control of the plasma current and pressure profiles, difficult to achieve, and has also a low β limit, to avoid strong MHD instabilities (kink modes, Resistive Wall Modes (RWM), Infernal modes). These are mitigated by lowering the plasma current ($q_{95} \sim 5$) and density with respect to the baseline H-mode.

Hybrid scenario The Hybrid scenario ($H_{98} \sim 1-1.5$) stays in the middle between the H-mode scenario and the H-mode steady state scenario. It does not require an internal transport barrier and negative magnetic shear values, but operates with a flat q profile in the inner plasma core. This leads to $q \gtrsim 1$, that helps to avoid the MHD activity in the plasma core and is easier to achieve with respect to a reversed $q$profile. This, due to the suppression of NTMs, also allows higher β limit. The discharge pulse length is also increased with respect to the standard H-mode but do not reach steady state operations. This scenario has also higher values of q ($q_{95} \sim 4$) and s at the plasma edge, with respect to baseline, that help to stabilize the turbulent transport in this region.

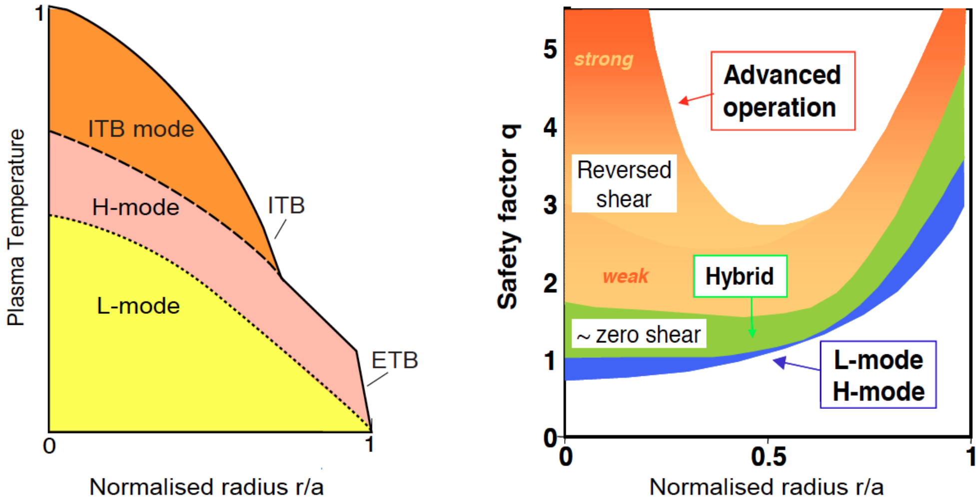

Figure 2.6: *Representation of the radial profile of the plasma ion temperature (a) and of the safety factor (b) in the main tokamak operational scenarios.*

Chapter 3

Transport

3.1 Transport in tokamak plasma core

Since the first experiments in tokamaks, it was clear that the confinement time of the plasma expected from neoclassical theory (i.e. from collisional processes in toroidal geometry [5]) was one-two orders of magnitude above the one measured experimentally. This has been related to the 'anomalous' transport caused by turbulent phenomena [13, 14]. The gradients of the plasma pressure, the tokamak magnetic geometry and the quasi-neutrality of the plasma drive collective plasma oscillations, described as drift waves [13], that arise on ion and electron Larmor radius scales. These plasma oscillations have frequencies of the order of the diamagnetic frequencies

$$\omega \sim \omega_{s*} = \mathbf{k} \cdot \frac{\mathbf{B} \times \nabla n_s T_s}{n_s q_s B^2}, \tag{3.1}$$

where the subscript s indicates the species considered, with a typical range

$$\Delta\omega \sim \omega_{s,*}. \tag{3.2}$$

They are characterized by spatial scales Δr of the order of Larmor radius ρ_L

$$\Delta r \sim k_\perp^{-1} \sim \rho_L \tag{3.3}$$

and by relative oscillations $(\delta n, \delta T, ...)$ small compared to the 'background' plasma quantities $(n, T, ...)$

$$\frac{\delta n}{n} \sim 10^{-3} - 10^{-1}, \tag{3.4}$$

where the values $\sim 10^{-1}$ are usually reached at the plasma edge. They cause fluctuations of the electrostatic potential, ϕ, that cause $\mathbf{E} \times \mathbf{B}$ drift velocities and an associated turbulent flux across the flux surfaces, for example a turbulent heat flux

$$q = \left\langle \frac{3}{2} \delta p v_{E,r} \right\rangle \tag{3.5}$$

where $v_{E,r}$ is the radial component of the $\mathbf{E} \times \mathbf{B}$ drift velocity, δp is the pressure oscillation and $\langle\rangle$ denotes a time averaging. The radial component of v_E is considered because the parallel (to B) transport is assumed high enough to ensure constant densities and temperatures on a flux surface. The changes of density and temperature and the turbulent fluxes are then considered along the radial direction.

Assuming a random walk diffusivity, and so local processes, we can relate the turbulent fluxes to the plasma pressure gradients, for example for the heat flux q:

$$q = -nD_{turb}\nabla T, \tag{3.6}$$

where D_{turb} is the turbulent heat diffusivity. Considering $\Delta r \sim \rho_L$ and $\Delta t \sim \Delta\omega^{-1}$ as the typical random walk step size and time scale, an estimate of D_{turb} can be given by

$$D_{turb} \sim \frac{(\Delta r)^2}{\Delta t} \sim \frac{\rho_s}{a}\frac{T_s}{q_s B} = \rho_s^* \frac{T_s}{Bq_s}, \tag{3.7}$$

where a is the tokamak minor radius. This scaling law is known as the gyro-Bohm scaling and is assumed to be valid for sufficiently small values of ρ_i^* [15]. In the JET plasma core, in the conditions studied in this thesis, typical values are $\rho^* \lesssim 1/400$ and the gyro-Bohm scaling law and the local limit approximation are considered to be valid.

3.2 Drift waves, ITG, ETG, TEM

As introduced in the previous section, the turbulent transport in a tokamak plasma is caused by micro-instabilities described as drift waves. Drift waves are modes of collective plasma oscillations driven by density and temperature gradients and by the different ion and electron motions in the plasma [13, 16]. While electrons and ions are free to move independently in the plasma, any large scale (i.e. spatial scales larger than the Debye length and time scales larger then the plasma oscillations $\omega_p = \sqrt{n_e e^2/(m_e\varepsilon_0)}$) charge separation is prevented by the strong electrostatic potential formed by the charge separation itself. The mechanisms that ensure the plasma quasi-neutrality are then the same mechanisms that drive the drift waves. Let's assume for example a plasma in a magnetic field $\mathbf{B} = B\mathbf{e}_z$, with a density gradient ∇n along the negative x direction. The system of coordinates is a simple 3D cartesian system (x, y, z), where z indicates the direction parallel to the magnetic field, x can be seen as the radial direction. $n = n_e = n_i$ is constant in time and on each flux surface, labelled in this case by x. Due to the presence of a density gradient, a diamagnetic drift velocity develops

$$\mathbf{v}_{*e} = \frac{T_e}{eBL_n}\mathbf{e_y}, \tag{3.8}$$

where $L_n^{-1} = -\nabla n/n$. Using an electrostatic approximation and neglecting collisions, the parallel (to $\mathbf{B}$) dynamic of the electrons is given by

$$\frac{\partial v_{\parallel e}}{\partial t} + (\mathbf{v}_e \cdot \nabla)v_{\parallel e} = \frac{e}{m}\frac{\partial \phi}{\partial z} - \frac{1}{mn_e}\frac{\partial p_e}{\partial z}. \tag{3.9}$$

Considering low frequency processes, we can assume isothermal electrons in equilibrium and neglect the right side of equation 3.9 obtaining

$$e\frac{\partial \phi}{\partial z} - \frac{T_e}{n_e}\frac{\partial n_e}{\partial z} = 0. \tag{3.10}$$

Integrating we then obtain

$$\frac{n_e}{n_0} = e^{e\phi/T_e}. \tag{3.11}$$

Decomposing the electron density in a background part and in a perturbed quantity, $n_e = n_0 + \delta n_e$, and expanding to the first order in δn_e we obtain

$$\frac{\delta n_e}{n_0} = \frac{e\phi}{T}. \tag{3.12}$$

The electric field generated by $\nabla\phi$ causes a $v_{E,x}$ drift. This drift, due to the presence of the density gradient, causes a change in the density in a way that the perturbation moves along y. The ion density continuity equation can be written, neglecting the parallel dynamic of the ions, as

$$\frac{\partial n_i}{\partial t} + v_{Ex}\nabla n = 0. \tag{3.13}$$

Using $v_{Ex} = -1/B_0(\partial\phi/\partial y)$, $n_i = n + \delta n_i$, writing the perturbed quantities as $\delta f = \delta f{\cdot}exp(-i(\omega t - \mathbf{k}{\cdot}r)$ and linearizing in δn_i, the equation becomes

$$i\omega\delta n_i + \frac{ik_y\phi}{B}\frac{n}{L_n} = 0. \tag{3.14}$$

Using the quasi-neutrality relation, we can derive

$$\frac{\omega}{k_y} = v_{*e} \Longrightarrow \omega = \omega_{*,e}. \tag{3.15}$$

The velocity of propagation of the density perturbation, in the y direction, is the electron diamagnetic drift velocity.

If the electrons are free to move along the magnetic field lines, they immediately delete the charge separation and there will not be any instability. But, if for any reason the electron response is not immediate, a delay between the electrostatic potential oscillations and the density oscillations can appear

$$\frac{\delta n_e}{n_0} = \frac{e\phi}{T_e}(1 - i\delta). \tag{3.16}$$

Assuming $\delta \ll 1$, equation 3.15 becomes

$$\omega = \frac{\omega_{*e}}{1 - i\delta} \approx \omega_{*e}(1 + i\delta). \tag{3.17}$$

If $\delta > 0$, an exponentially growing instability can occur. This can be caused, for example, by a friction of electrons due to collisions. Considering for example the radial heat flux generated by the perturbation

$$q = \left\langle \frac{3}{2}\delta p v_{E,r} \right\rangle, \tag{3.18}$$

it can be seen that there is turbulent heat flux only if δp and $v_{E,r}$ (and so ϕ) are out of phase, the time average of this quantity being zero otherwise.

In the low-field-side region of a tokamak plasma, where the temperature gradients and the magnetic field gradient are aligned and where there is the presence of trapped particles, the drift waves can become unstable due to the temperature gradients themselves and originate the high level of transport observed experimentally in the plasma. The exponential linear growth of these instabilities is regulated by nonlinear phenomena. One of the most important nonlinear regulation mechanism for turbulence is related to zonal flows (ZF) [17, 18]. Zonal flows are excited by the plasma micro-instabilities themselves and regulate the transport by shearing the drift waves structures and by extracting energy from them. The main micro-instabilities in a tokamak plasma core are the Ion Temperature Gradient (ITG) modes, the Trapped Electron Modes (TEM) and the Electron Temperature Gradient (ETG) modes.

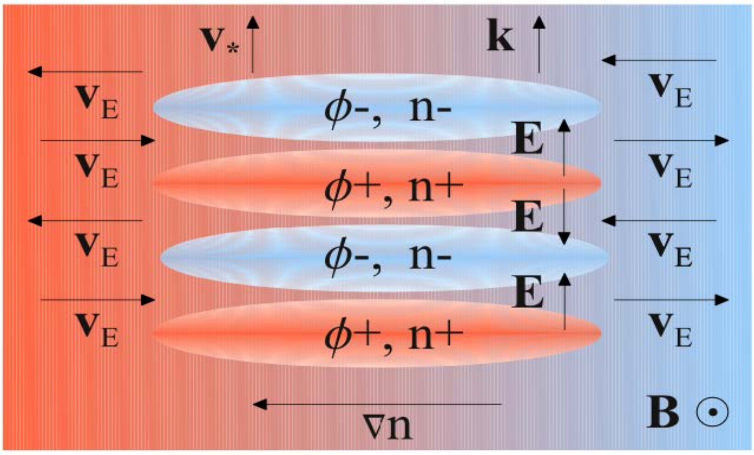

Figure 3.1: *Schematic representation of the electronic drift wave. An initial density perturbation* (n^+/n^-) *leads to a drift wave propagating in the* $\mathbf{k} \parallel y$ *direction. The electrons react more quickly than the ions, causing a charge separation and the formation of an electrostatic potential perturbation* (ϕ^+/ϕ^-)*. The electrostatic perturbation is, in this case, in phase with the density perturbation. The electric field* $\mathbf{E}$*, caused by* (ϕ^+/ϕ^-)*, leads to a* $\mathbf{E} \times \mathbf{B}$ *drift velocity in the direction of the density gradient, causing the movement of the more dense plasma in the less dense region* (n^-) *and vice versa. This causes a propagation of the perturbation in the* $y(\parallel \mathbf{k})$ *direction with a frequency* $\mathbf{k} \cdot \mathbf{v}_*$, v_* *being the diamagnetic velocity.*

3.2.1 ITG

The micro-instabilities caused by the ion temperature gradient are called Ion Temperature Gradient (ITG) modes. These modes are driven unstable due to curvature effects on the low-field-side of the tokamak, where the magnetic field gradient and the ion temperature gradient are in the same direction. It is worth noting that even in the slab limit, with straight magnetic field lines and no magnetic field gradients, the ITG modes are unstable and are caused by parallel compression due to ion acoustic waves [19]. A simplified scheme of the physical mechanisms of the ITG drive is shown in figure 3.2. The ion temperature has been split, for simplicity, into a hot and a cold region. An initial T_i perturbation is present in the low-field-side of the tokamak plasma. The drift velocity due to magnetic field inhomogeneities depends on the particle energy, $v_d \sim (v_\parallel^2 + v_\perp^2/2) \sim (T_\parallel^2 + T_\perp^2)$, causing differences in the drift motion between the hot and the cold region of the plasma. This causes a compression and a rarefaction of the ion density and an electrostatic potential perturbation, which is out of phase with respect to the T_i perturbation. The associated electric field causes an $\mathbf{E} \times \mathbf{B}$ drift that brings hot plasma into the hotter region and cold plasma into the colder region, amplifying the original perturbation of T_i (on the high field side, this process leads to a suppression of the original instability). The presence of an ion temperature gradient is then essential to close this loop and drive the instability.

ITG modes are driven unstable over a certain critical value of $L_{Ti}^{-1} = -\nabla T_i/T_i$ [20, 21]. A useful formula for the ITG critical threshold as a function of some plasma parameters, given in ref. [22], is

$$\left(\frac{R}{L_{Ti}}\right)_{crit}^{ITG} = \frac{4}{3}\left(1 + \frac{T_i}{T_e}\right) \cdot \left(1 + 2\frac{s}{q}\right) \tag{3.19}$$

if $R/L_n < 2(1 + \frac{T_i}{T_e})$.

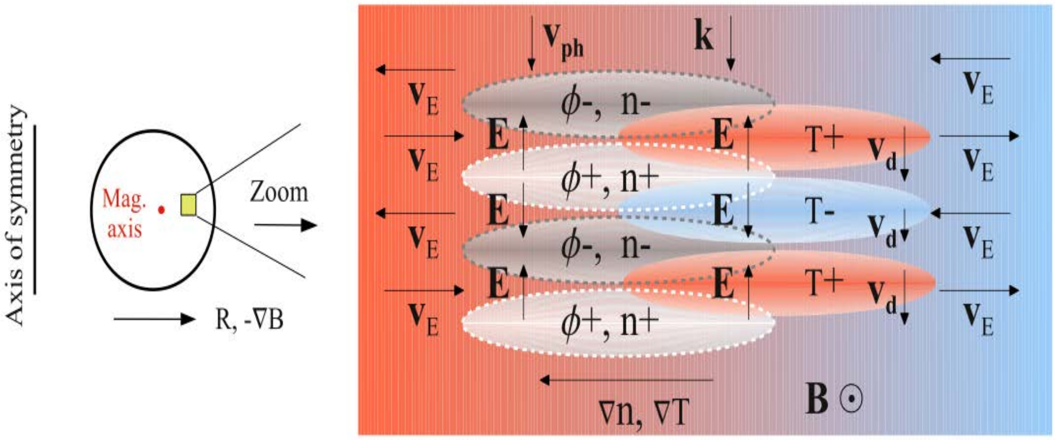

Figure 3.2: *Schematic representation of the physical mechanism of ITG instability in tokamaks.*

3.2.2 ETG

Electron Temperature Gradient modes are driven by the gradient of the electron temperature and act on smaller ($\rho_e \ll \lambda \ll \rho_i$) scales with respect to ITG modes. Their linear physics is very similar to the ITG one, with the roles of the electrons and of the ions interchanged. Due to their short wavelengths, it has been believed for many years that the flux driven by ETGs would be much smaller than the one driven by modes on ion-scale (like TEM or ITGs). This was expected from the gyro-Bohm diffusion coefficient

$$D_{ETG} \sim \rho_e^* \approx \sqrt{\frac{m_e}{m_i}}\rho_i^* \sim \sqrt{\frac{m_e}{m_i}} D_{ITG} \tag{3.20}$$

This mixing-length argument, supported by gyrokinetic theory when only linear and electrostatic terms and adiabatic ions are considered, fails when the nonlinear dynamic of ETGs is considered. Nonlinearly, the isomorphism between ITG modes and ETG modes is broken. For ITGs, the relation between the electrostatic potential and the ion density has a dependence on the flux-surface average of the electrostatic potential, while for ETGs this dependence disappears [23]. Due to this difference, in the ETG case there is a strong suppression of Kelvin-Helmotz like instabilities at long-wavelength (that generate the zonal flows) which in the ITG case strongly suppress the instability. ETG modes can then form radially elongated structures, called ETG streamers (see figure 3.3), that are able to carry an amount of electron heat flux comparable to the one carried from ion-scale instabilities [23, 26]. Recently, in JET [7] in C-MOD [24] and, in some experimental conditions, in DIII-D [25] it was found that neither the q_e values nor their slope vs R/L_{Te}

(which is a measure of the stiffness of the T_e profiles and regulates the propagation speed of heat waves through the plasma) were matched by low-k non-linear gyrokinetic simulations. Other recent works [24, 26, 27] have shown that there are also strong interactions between electron-scale instabilities and ion-scale instabilities. While the ion-scale structures, like ITG zonal flows, can suppress the formation of the ETG streamers, the ETG modes can enhance the flux carried by ion-scale instabilities. Experimentally, in plasmas with internal or edge transport barriers, where inside the barrier the ion-scale instabilities are strongly suppressed by external $\mathbf{E} \times \mathbf{B}$ flow shear and the level of the ion heat flux can be reduced to neoclassical levels, an anomalous electron heat transport, that could be ascribed to smaller-scale instabilities, is still observed inside the barrier. Furthermore, experimental measurements of high-k instabilities have been reported in different machines [30, 31, 32], with a dependence on radius and heating scheme. A correlation between the increase of q_e and the increase of high-k density fluctuations has also been reported [30, 32]. These observations call for a more quantitative evaluation of the amount of q_e carried by high-k instabilities.

A useful formula for the ETG critical threshold is given in [33]

$$\frac{R}{L_{Te}}^{crit} = max\{(1+\tau)(1.33+1.91\cdot\frac{s}{q})(1-1.5\cdot\epsilon)[1+0.3\cdot\epsilon(\frac{d\kappa}{d\epsilon})]; 0.8\cdot\frac{R}{L_n}\},$$

where $\tau = Z_{eff}T_e/T_i$, $\epsilon = r/R$ is the inverse aspect ratio and κ is the plasma elongation.

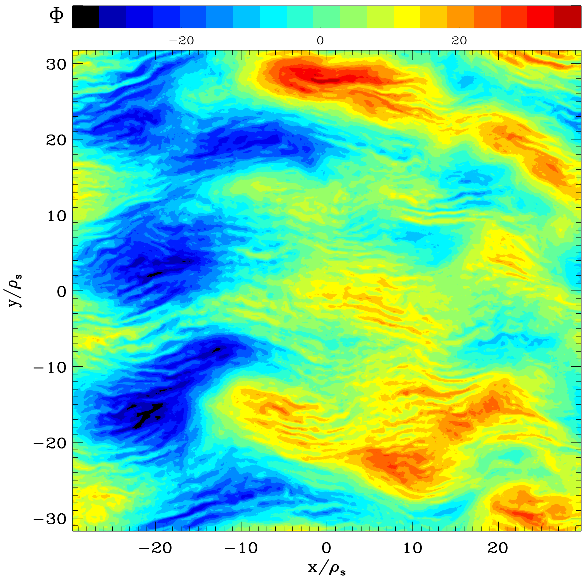

Figure 3.3: *Electrostatic potential snapshot from a gyro-kinetic multi-scale simulation. Big structures are visible as well as thinner and more elongated structures, the ETG 'streamers' (see chapter 9).*

3.2.3 TEM

The magnetic configuration of a tokamak leads to the magnetic trapping of some of the plasma particles. The response to a perturbation of the electrostatic potential (ϕ) fluctuations of trapped electrons is different from the response of passing electrons. This can cause a phase shift between ϕ and $\tilde{n_e}$ and so to an instability. The development of this trapped electrons instability is related to the presence of electron temperature and density gradients [3]. For TEM there is a critical value of R/L_{Te} over which the instability can be produced [34, 35]. This critical value can be written as a function of some plasma parameters [35] as

$$\frac{R}{L_{Te}}^{crit} = \frac{0.357\sqrt{\epsilon} + 0.271}{\sqrt{\epsilon}}[4.90 - 1.31\frac{R}{L_n} + 2.68s + ln(1 + 20\nu_{eff})], \tag{3.21}$$

where $\nu_{eff} = \nu_{ei}/\omega_{*e}$, ν_{ei} and ω_{*e} being the electron-ion collision frequency and the electron diamagnetic frequency, and $\epsilon = r/R$.

3.3 Gyrokinetic equations

In order to properly study the plasma micro-instability, a kinetic approach is necessary. The kinetic equations are a set of 6D equations that calculate the evolution of the particle distribution function and of the electromagnetic potentials. The collisional Vlasov equation

$$\frac{\partial f_s}{\partial t} + \mathbf{v}\cdot\nabla_{\mathbf{x}} f_s + \frac{\mathbf{E} + \mathbf{v} \times \mathbf{B}}{m_s}\nabla_{\mathbf{v}} f_s = C(f_s), \tag{3.22}$$

which describes the evolution of the 6D distribution function of the particles of the s species under the influence of the Lorentz force and collisions, is coupled with the Maxwell equations, in which charges and currents are calculated from the distribution function f_s

$$\rho = \sum_s q_s \int f_s d\mathbf{v}$$

$$\mathbf{j} = \sum_s q_s \int v f_s d\mathbf{v}.$$

The turbulent fluctuations in the plasma are characterized by the following features (observed experimentally) [13, 36]:

- The relative fluctuation levels $(\delta n, e\delta\phi, \delta\mathbf{B}, ...)$ are small compared to the background, not fluctuating, quantities $(n, T, \mathbf{B}, ...)$. Considering, for example, a background part of the density, $n_{0,s}$, and a fluctuating part of the density, δn_s, such as $n_s = n_{0,s} + \delta n_s$, they satisfy

  $$\frac{\delta n_s}{n_{0,s}} \sim \epsilon_\delta \ll 1; \tag{3.23}$$

  This is true in the plasma core for typical plasma parameters. At the plasma edge, the oscillating quantities might reach ~ 10% of the background quantities.

- The fluctuation frequencies ω are of the order of the diamagnetic drift frequencies $\omega_{*,s} = \mathbf{k}\cdot\frac{cT}{eB^2}\mathbf{B} \times \nabla ln(p_s)$ and the frequency spectra are typically broadband with $\Delta\omega \sim \omega$. These frequencies are much smaller than the gyro-frequencies Ω

  $$\frac{\omega}{\Omega} \sim \epsilon_\omega \ll 1. \tag{3.24}$$

  On these time scales, the background quantities, typically evolving on the confinement time scale, can be assumed to be constant.

- The fluctuations are highly anisotropic in the parallel and in the perpendicular (to the magnetic field) directions. Typical perpendicular wavelengths are of the order of $\sim 10 - 100\rho_s$, i.e. few centimeters, while typical parallel wavelength are of the order of several meters. This means

  $$k_\perp \rho_i \sim \epsilon_\perp \sim 1 \tag{3.25}$$

  $$\frac{k_\parallel}{k_\perp} \sim \frac{\epsilon_\omega}{\epsilon_\perp} \ll 1. \tag{3.26}$$

  The last condition is required in order to have an ordering in which a strong wave-particle interaction (e.g., Landau damping) is captured at the lowest order. The background quantities hardly vary on scales comparable with ρ_i. Typically, considering for example the magnetic field,

  $$\rho_i \left|\nabla ln(B)\right| = \rho_i / L_B \sim \epsilon_B \ll 1. \tag{3.27}$$

Thank to these properties, splitting the distribution function in a background, stationary part and in a perturbed, oscillating part $f_s = F_{0,s} + \delta f_s$ and averaging over the particle gyro-motion, it is possible to derive the set of the 5D gyrokinetic equations for the evolution of the fluctuating particle distribution function and electromagnetic potentials. The derivation of these equations requires sophisticated mathematical techniques, such as Lie transformations, and are not described here. A description of their derivation can be found in ref. [36].

3.4 Numerical codes

3.4.1 The gyro-kinetic code GENE

The GENE (Gyrokinetic Electromagnetic Numerical Experiment) code [23, 37] solves the gyrokinetic Vlasov equations coupled with the Maxwell equations within a δf approximation and using a set of field aligned coordinates $\{x, y, z\}$, where z is the coordinate along the magnetic field line, x is the radial coordinate and y is the binormal coordinate. In GENE, a discretization of the phase space fixes a grid of points on which the evolution of the distribution function is calculated. Taking advantage of the gyrokinetic ordering described above, all the simulations carried out for this thesis have been performed in the local limit (or flux-tube approximation). This means that the simulation box covers only a fraction of the flux surface in the y direction rather than the whole flux surface and has a limited extension also in the x direction (this choice is well justified with our values of $\rho*$ $(1/\rho* \lesssim 400)$). Following the flux-tube along just one poloidal turn, due to the axis-symmetry of a tokamak flux surface, it is possible to obtain the information on the turbulent state along the whole flux surface. The periodic boundary conditions in x and $y$in the flux-tube approximation make possible to treat these two coordinates spectrally, allowing a simpler gyro-averaging operator and making the code numerically more stable. The code needs a set of input parameters such as the plasma geometry, densities and temperatures and their gradients for each species considered in the simulation (there is no limit in the number of kinetic species that can be simulated) and gives as output quantities such as the particle and the heat fluxes and information on the turbulent state.

The magnetic equilibrium model used in all our simulations is the Miller geometry [39]. This equilibrium model is local to a flux surface and completely describes its geometry in terms of nine parameters: aspect ratio r/R, elongation κ and its radial derivative $s_\kappa = \frac{r\partial_r\kappa}{\kappa}$, triangularity δ and its radial derivative $s_\delta = \frac{r\partial_r\delta}{\sqrt{1-\delta^2}}$, safety factor q, magnetic shear $s = \frac{r}{q}\frac{dq}{dr}$, Shafranov shift α and $\partial_r R_0$.

A summary of the equations solved by GENE, as reported in ref. [38], is given in the following. The equations are formulated in Fourier space in x and y directions. The gyro-averaged Vlasov equation calculates the evolution of the oscillating part of the distribution function $f = F_0+\delta f$, F_0 being taken as a Maxwellian distribution function. For numerical reasons it is easier to use the modified distribution function g (see equation 3.30)

$$\frac{\partial g}{\partial t} = \mathcal{Z} + \mathcal{L}(g) + \mathcal{N}(g). \tag{3.28}$$

$\mathcal{Z}$ is a constant term that arises due to the fact that, in the presence of curvature and density or temperature gradients, $F_0(i.e., \delta f = 0)$ is not a solution of equation 3.28 of the first order on δf. It only affects the $k_\perp = 0$ mode and decouples linearly and nonlinearly from the rest of the system. It is given by

$$\mathcal{Z} = \frac{T_0(2v_\parallel^2 + \mu B_o)}{qB_0} K_x \left(\omega_n + \left(v_\parallel^2 + \mu B_0 - \frac{3}{2}\right)\omega_{Ts}\right)\delta_{k_x,0}\delta_{k_y,0}F_{0s}. \tag{3.29}$$

The linear operator is given by

$$\begin{aligned}\mathcal{L}(g) = &-\left(\omega_n + \left(v_\parallel^2 + \mu B_0 - \frac{3}{2}\right)\omega_T\right) F_0 i k_y \chi + \frac{\beta T_0}{qB_0^2} v_\parallel^2 \omega_p \Gamma_y - \frac{v_T}{JB_0} v_\parallel \Gamma_z \\ &- \frac{T_o(2v_\parallel^2 + \mu B_0)}{qB_0}\left(K_y\Gamma_y + K_x\Gamma_x\right) + \frac{v_T}{2JB_0}\mu\partial_z B_0 \frac{\partial\delta f}{\partial v_\parallel} + \langle C(\delta f)\rangle ,\end{aligned}$$

consisting (in the order) of the drive term, the pressure term, a term describing the parallel dynamics, the curvature terms, the trapping term and the collisions term and where

$$\begin{aligned}&F_0 = \pi^{-3/2}e^{-(v_\parallel^2+\mu B_0)} && \delta f = g - \tfrac{2q}{mv_T} v_\parallel \bar{\delta A}_\parallel F_0 \\ &\chi = \bar{\phi} - v_T v_\parallel \bar{\delta A}_\parallel && \Gamma_{x,y} = i k_{x,y} g \tfrac{q}{T_0} F_0 i k_{x,y}\chi \\ &\Gamma_z = \partial_z g + \tfrac{q}{T_0} F_0 \partial_z \chi + \tfrac{v_T q}{T_o} v_\parallel \mu F_0 A_\parallel \partial_z B_0 &&\end{aligned} \tag{3.30}$$

and

$$\phi = \frac{\sum_s n_{0s}\pi q_s B_0 \int J_0(\lambda_s) g_s dv_\parallel d\mu}{k_\perp^2\lambda_D^2 + \sum_s \frac{q_{2s}}{T_{os}} n_{0s}(1-\Gamma_0(b_s)} \tag{3.31}$$

$$\delta A_\parallel = \frac{\sum_s \frac{\beta}{2} q_s n_{0s} v_{Ts}\pi B_0 \int v_\parallel J_0(\lambda_s) g_s(\mathbf{k}) dv_\parallel d\mu}{k_\perp^2 + \sum_s \frac{\beta q_{2s}}{m_s} n_{0s}\pi B_0 \int v_\parallel^2 J_0^2(\lambda_s) F_{0s} dv_\parallel d\mu} \tag{3.32}$$

where J is the Jacobian for the field aligned coordinates, ϕ is the electrostatic potential and $\delta A_\parallel$ is the oscillating part of the magnetic potential. J_0 and Γ_0 are the 0-order Bessel and modified Bessel functions and $\lambda_s = ik_\perp\rho_s$. In the simulations it is possible to retain also the $\delta B_\parallel$ perturbation not reported here.

The $\mathbf{E}\times\mathbf{B}$ nonlinearity, that is the only nonlinear term in the equations, in this representation can be written as

$$\mathcal{N}(g) = \sum_{\mathbf{k'}_\perp}(k_x^{'}k_y - k_xk_y^{'})\chi(\mathbf{k}_\perp^{'})g(\mathbf{k}_\perp - \mathbf{k}_\perp^{'}). \tag{3.33}$$

Besides the parallel B0 variation, the most important equilibrium quantities entering the gyrokinetic equations are the gradients and curvature terms,

$$\begin{aligned} \omega_n &= -\tfrac{L_{ref}}{n_0}\partial_x n_0 & \omega_T &= -\tfrac{L_{ref}}{T_0}\partial_x T_0 \\ K_x &= -\tfrac{L_{ref}}{B_{ref}}\left(\partial_y B_0 + \tfrac{\gamma_2}{\gamma_1}\partial_z B_0\right) & K_y &= \tfrac{L_{ref}}{B_{ref}}\left(\partial_x B_0 - \tfrac{\gamma_3}{\gamma_1}\partial_z B_0\right) \\ \omega_p &= -\tfrac{L_{ref}}{n_{ref}T_{ref}}\partial_x p \Rightarrow & \omega_p &= \textstyle\sum_s n_s T_s(\omega_{ns} + \omega_{Ts}) \end{aligned} \tag{3.34}$$

(with parameters $\gamma_{1,2,3}$ related to the metric tensor terms for the field aligned coordinates). In these normalized equations, the physical values of the equilibrium quantities do not enter. However, in the normalization process, three dimensionless parameters relating different normalization scales have been introduced,

$$\beta = \tfrac{8\pi n_{ref}T_{ref}}{B_{ref}^2} \quad \nu_c = \tfrac{\pi ln(\lambda_C)e^4 n_{ref}L_{ref}}{2^{1.5}T_{ref}^2} \quad \lambda_D = \sqrt{\tfrac{B_{ref}^2}{4\pi c^2 n_{ref}m_{ref}}} \tag{3.35}$$

effectively reducing the number of freely scalable parameters. The linearized gyrokinetic equation

$$\frac{\partial g}{\partial t} = \mathcal{L}(g) \tag{3.36}$$

is used for investigations concerning linear stability and e.g. attempts to find quasilinear models of the turbulent behavior in certain regimes.

More details on the GENE code can be found in the thesis and in the papers listed in the GENE code website (www.genecode.org). More details regarding the setting of the simulations presented in this thesis can be found in the respective chapters.

3.4.2 Quasi-linear codes

Quasi-linear transport models are based on linear characteristics of a turbulent state and on certain assumptions to take into account the non-linear physics. The first step consists then in using linearized equations (for example linearized gyrokinetic equations) to obtain the linear expressions of fluctuating quantities such as the densities or the electrostatic potential, while the second step consists in determining how to simulate the non-linear processes that saturate the level of the fluctuations of these quantities. For example, assuming harmonic fluctuations ($\delta n, \delta T, \delta\phi \propto e^{-i(\omega t - \mathbf{k}\cdot\mathbf{x})}$), the ion heat flux can be written as

$$q_i = \left\langle \frac{3}{2}\delta p_i v_{E,r} \right\rangle = \sum_{\mathbf{k},\omega} \frac{3}{2}\delta p_{i,\mathbf{k}\omega}\frac{ik_y\delta\phi_{\mathbf{k}\omega}^*}{B} \tag{3.37}$$

where v_E is the $\mathbf{E}\times\mathbf{B}$ velocity and $y$is the binormal direction to the magnetic field and to the radial direction. Replacing now δp_i with its linear expressions (calculated with linearized equations), the ion heat flux assumes the expression

$$q_i = \sum_{\mathbf{k},\omega} (q_i\ linear\ expression)_{\mathbf{k}\omega} \otimes \left|\delta\phi^2\right|_{\mathbf{k}\omega}. \tag{3.38}$$

It is not possible to calculate $|\delta\phi^2|$ from the linear physics, but it must be derived making some assumptions. Assuming for example random walk diffusivities, a mixing-length rule [40, 41] for the diffusion coefficients is given by

$$D\left(\sim \sum_{\mathbf{k}\omega} \left|\delta\phi^2\right|_{\mathbf{k}\omega}\right) = \sum_k \frac{\gamma_k}{k^2} \tag{3.39}$$

where γ_k is the linear growth rate for the mode with wavenumber k. This is just a simple example, the details of the mixing length rule, that can take into account factors which approximate non-linear phenomena such as zonal flows, depend on the precise model. The development of these models can be helped by the results of non-linear simulations.

In this work two quasi-linear models have been used and tested against nonlinear gyrokinetic simulations and experiment: TGLF (Trapped Gyro-Landau Fluid) [42, 43, 44] and QuaLiKiz [45, 46]. The TGLF model solves a set of gyro-Landau fluid (GLF) equations that take into account kinetic effects like the gyro-averaging and the Landau damping. TGLF treats both trapped and passing electrons, ion and electron-scale instabilities and retains some multi-scale interactions. The linear modes are found numerically while the model for the saturated turbulence is built to fit nonlinear gyrokinetic simulations from the GYRO code, including a few multi-scale simulations. In QuaLiKiz, the eigenvalues are solutions of a linear gyrokinetic equation and the eigenfunctions are solutions of the fluid limit of this equation. A mixing-length rule is then used to calculate the saturated electrostatic potential and fluxes.

The scope of quasi-linear codes is to be able to predict and simulate a tokamak plasma with low computational costs. If a gyrokinetic simulation needs $\sim 10^4 - 10^7$ CPU hours to calculate the level of the flux for one time and at one radial position, quasi-linear codes aim at simulating the whole plasma in few CPU minutes or seconds. Recent developments have shown that using numerical tools such as neural networks is would be possible to simulate the whole plasma evolution in real time [47]. It is then important to understand the plasma phenomenology and to be able to reproduce it with simplified models. More work is needed to reach this goal.

3.4.3 The transport code Astra

The ASTRA (Automatic System for TRansport Analysis) code [48] solves 1D fluid transport equations taking into account the 2D geometry of the flux surfaces through parameters such as triangularity and elongation. The code is extremely flexible, allowing to set a specific transport model in the simulations, including quasi-linear models such as TGLF or user defined empirical models, and to adjust the model variables interactively during the simulation. These aspects make ASTRA a very useful code for perturbative studies, in which a modulated power is used as well as Fourier transforms of the temperature profile time evolution to calculate phases and amplitudes of the heat wave propagating in the plasma. The possibility of interactively changing the model parameters and other quantities, such as the absorbed power, makes easier to achieve simulations with good reproduction of the heat wave propagation. For the description of the tokamak geometry the code uses the coordinate system $\{a, \theta, \zeta\}$, where $a$is a radial parameter, θ is the poloidal angle and ζ is the toroidal angle. The toroidal and poloidal magnetic fluxes are indicated with $\Phi(a,t)$ and $\Psi(a,t)$. $\Psi(a,t)$ is used in the Grad-Shafranov equation, while $\Phi(a,t)$ is used to define the toroidal radius

$$\rho_{tor} \equiv \sqrt{\frac{\Phi}{\pi B_0}}, \tag{3.40}$$

where B_0 is the magnetic field in the vacuum at the geometrical center of the tokamak vacuum chamber. This radial coordinate is used to parametrize the flux surfaces in the code.

Astra solves 1D transport equations, including equations for the plasma density n, the electron and ion temperature and the poloidal magnetic flux, coupled with the Grad-Shafranov equation. It is not necessary to simulate all the plasma profiles, for example it is possible to study just the evolution of T_e, fixing the plasma density and the ion temperature constant in time. Other conditions to be set in the simulations are initial conditions and boundary conditions.

3.5 Experimental methods for transport study

3.5.1 Heat flux scan

In order to obtain a heat flux scan as a function of the normalized temperature gradient, the ICRH power is deposited at two different radial positions at different times (or in different discharges with the same experimental settings and parameters). Usually it is deposited on-axis ($R \approx 3.0\,m$) and off-axis ($R \approx 3.6\,m$). In this way, there is enough difference in the heat flux and in the peaking of the temperature to obtain a clear scan in $q_{gB}(R/L_T)$ at a radial point between the two deposition radii (see figure 3.4). In order to calculate the heat flux, all the heat sources must be considered. The radial profile of the ICRH power density to electrons and ions are usually evaluated using the SELFO code [49, 50] or the PION code [51]. This is possible when the ICRH heating is in the minority scheme, directing the power mainly to ions. When the mode-conversion scheme is used, in order to heat mainly the electrons, no reliable code for the evaluation of the ICRH power density deposition is available yet. In this case, the perturbative studies are essential. Using a transport simulation to fit the temperatures profiles and the profiles of the phase and amplitude of the heat wave harmonics, adjusting also the heat power directed to ions and electrons, it is possible to work out the total amount of heat power absorbed by ions and electrons. The NBI heating power on electrons and on ions is calculated with the PENCIL code [52]. The ohmic power density is calculated analytically using $P_{Ohm} = \eta \cdot j^2$, where η is the resistivity of the plasma and j is the plasma current density. Also the exchanged power density between ions and electrons, p_{ei}, is calculated analytically. The measured radiated power density p_{rad} is taken into account. The powers $P_{OHM}, P_{ICRH}, P_{NBI}, P_{ei}$ and P_{rad} are obtained integrating the power densities on the plasma volume and the ion and electron heat fluxes are expressed in gyro-Bohm units as

$$q_{i,gB_i} = [(P_{ICRH,i} + P_{NBI,i} + P_{ei})/\Sigma] \cdot R_0^2/(n_e T_i \rho_i^2 v_{th,i}) \tag{3.41}$$

$$q_{e,gB_s} = [(P_{ICRH,e} + P_{NBI,e} + P_{OHM} - P_{ei} - P_{rad})/\Sigma] \cdot R_0^2/(n_e T_e \rho_s^2 c_s) \tag{3.42}$$

where Σ is the considered flux surface, $c_s = \sqrt{T_e/M_i}$, $v_{th,i} = \sqrt{T_i/M_i}$, $\rho_i = v_{th,i} M_i/eB_T$ and $\rho_s = c_s M_i/eB_T$. Typical errors on the heat fluxes are $\sim 20\%$. For the measurement of the electron temperature T_e the ECE (Electron Cyclotron Emission) and the High Resolution Thompson Scattering (HRTS) diagnostics are used, while the ion temperature T_i is measured by the Charge Exchange (CX) diagnostic. Local values of $R/L_{Ti} = -R_0 \nabla T_i / T_i$ and $R/L_{Te} = -R_0 \nabla T_e / T_e$ are obtained by local linear fits of $ln(T_i)$ and $ln(T_e)$ radial profiles averaged over a certain time interval (usually $\Delta t \approx 0.5 - 1\, s$). The fits are done using the radius $r = (R - R_{in})/2$, R and R_{in} being the outer and inner radii of the flux surface on the magnetic axis plane, and averaging other multiple fits using a variable number of data points around the chosen radius (usually 3-9 points). Errors on these quantities are typically $\sim 10 - 15\%$.

Once the heat flux scan has been obtained, the turbulent flux threshold and stiffness at a chosen radial location are then determined experimentally by quadratic fits on the diagram of the normalized heat flux as a function of R/L_T using a semi-empirical model called Critical Gradient Model (CGM) [53, 54]

$$q_{gB} = q_s^{res} + \chi_s \frac{R}{L_T} \left(\frac{R}{L_T} - \frac{R}{L_T}^{crit} \right) \cdot \theta \left(\frac{R}{L_T} - \frac{R}{L_T}^{crit} \right) \tag{3.43}$$

where q^{res} is the residual flux not carried by the R/L_T driven instability, $(R/L_T)^{crit}$ is the critical value of $R/L_{Te,i}$ above which the turbulent flux is driven by R/L_T, χ_s is the stiffness coefficient and $\theta(\bullet)$ is the Heaviside function. Considering the residual flux negligible, $(R/L_T)^{crit}$ is found as the intercept to zero flux, whilst χ_s can be inferred from the slope of the curve. An example can be seen in figure 3.4.

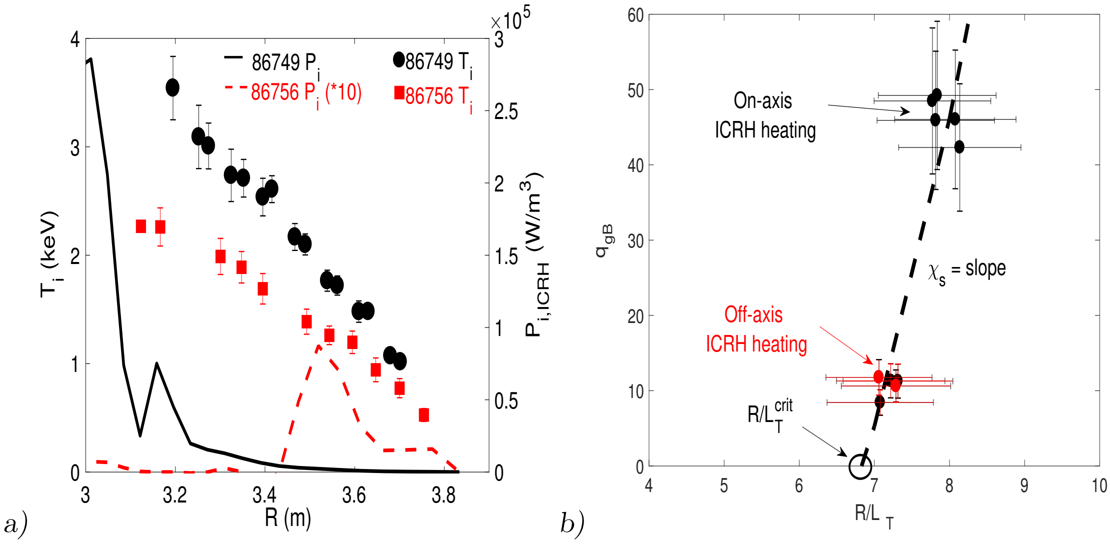

Figure 3.4: *a)Example of the ICRH power density deposition and of the ion temperature profiles obtained in a JET L-mode plasma using on or off-axis ICRH heating. b)Example of the heat flux scan obtained using on and off-axis ICRH heating.*

3.5.2 Perturbative techniques

Perturbative techniques for plasma transport analysis [55, 56] are based on the study of the temporal evolution of a small perturbation introduced in the plasma temperature using, for example, a modulated heat source. In all the cases studied in this thesis, a square-wave modulated ICRH heating has been used, with ad-hoc frequency, modulation amplitude and duty-cycle. In this way, at least the first three harmonics of the perturbation can be obtained by Fourier analysis of the temperature. The radial profiles of the

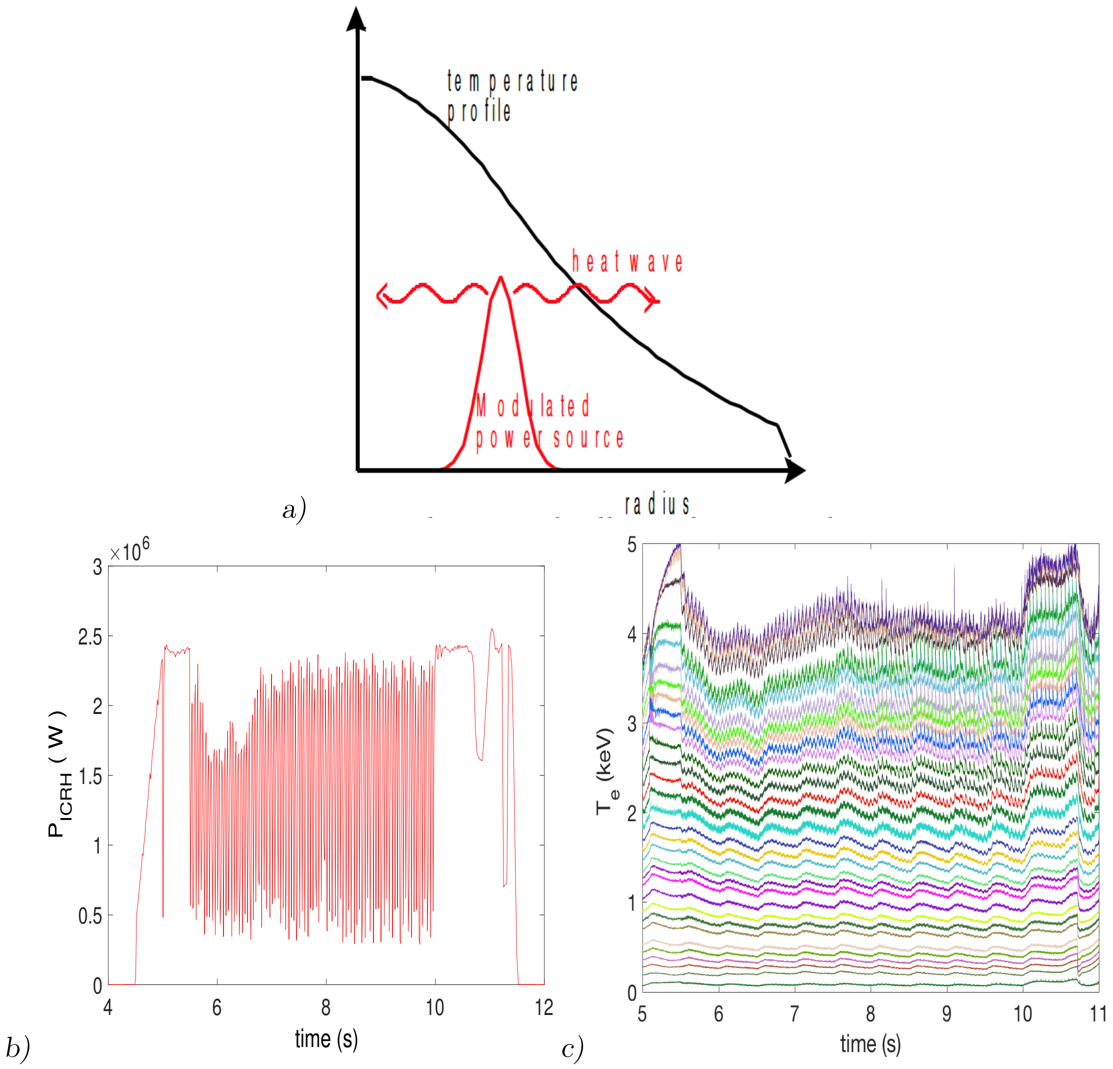

Figure 3.5: *a)Representation of the heat wave propagation principle for the perturbative studies. b)Example of an ICRH modulation used at JET for perturbative studies. c)Example of the perturbation induced in T_e using an ICRH modulation at JET.*

amplitudes and phases at different harmonics yield information both about the transport processes (diffusion and convection) and the modulated power source deposition. Using a transport code, ASTRA in our case, and assuming a space-time dependent model for the diffusivity coefficient, such as the CGM in equation 3.43, the experimental radial profiles of temperature and of amplitudes and phases at various harmonics can be best-fitted by adjusting the model parameters (such as the turbulent transport critical threshold and the stiffness). This provides an independent experimental evaluation of threshold and stiffness in addition to the heat flux scan procedure.

3.6 Thesis work

The work presented in this thesis mainly focuses on the thermal turbulent transport in the tokamak plasma core. The techniques and the numerical codes introduced in the previous sections are used to study the thermal transport using both experimental investigation and numerical modelling. The comparison between these two approaches is most fruitful to understand which physical mechanisms, related to the turbulent phenomena, are at work in relevant conditions for future tokamak scenarios. It also provides validation of the numerical codes against the experiments. On the experimental side, this thesis work covers the execution and the analysis of specific transport experiments in JET C-wall and ITER-like wall L-mode plasmas, in which heat flux scans and temperature modulation were used to determine threshold and stiffness level of the ion and electron heat channels. On the modelling side, it makes use mainly of gyrokinetic codes, but also of quasi-linear models, to explore the dependencies of such quantities on plasma parameters. The availability of such detailed experimental information made the comparison with theory a much more stringent validation exercise than the more common approach based on flux matching of a single steady-state temperature profile. In addition, the comparison of quasi-linear models with gyrokinetic models provides useful indications on their limitations, regimes of validity and needs for further improvements.

Four aspects regarding the turbulent thermal transport in the plasma core have been studied: the effects of light impurities, the effects of fast particles, the role of ETG modes and of the interactions between ion-scale instabilities and electron-scale instabilities (multi-scale interactions) and the effects of the plasma main ion mass (isotope effect). All these four topics are highly ITER relevant. In the next chapters, the results obtained from the experiments and the modelling will be shown and the physical interpretation of the results provided, with a discussion of their implications. In section II (chapters 4, 5 and 6) the ion thermal transport will be mainly studied, considering the effects of light impurities and fast particles. Section III (chapters 7, 8 and 9) is focused on the electron heat transport and on the role of high-k instabilities and multi-scale interactions. In section IV (chapter 10), the study of the effect of the main ion mass is studied. Finally in section V, the main conclusions and possible further work are presented.

References

[1] B. F. McMillan, Lecture Notes, 2014.

[2] J. Wesson and D. J. Campbell, “Tokamaks”, Oxford University Press, 4^{th} edition (2011).

[3] B. B. Kadomstev and O.P. Pogutse, Nucl. Fusion 11, (1971).

[4] ITER webpage: https://www.iter.org.

[5] F. L. Hinton and R. D. Hazeltine, Reviews of Modern Physics 48, 239 (1976).

[6] D .Van Eester, et al., Plasma Phys. Control. Fusion 51, 044007 (2009).

[7] N. Bonanomi et al., Nucl. Fusion 55, 113016 (2015).

[8] R. Pasqualotto et al., Rev. Sci. Instrum. 75, 3891 (2004).

[9] H. Weisen et al., Nucl. Fusion 29, 2187 (1989).

[10] L. L. Lao et al., Nucl. Fusion 25, 1421 (1985).

[11] D. P. O’Brien et al., Nucl. Fusion 32, 1351 (1992).

[12] M. Brixc et al., Review of Scientific Instruments 79, 10F325 (2008).

[13] W. Horton, Reviews of Modern Physics 71, (1999).

[14] X. Garbet et al., Plasma Phys. Control. Fusion 46, (2004).

[15] X. Garbet, Plasma Phys. Control. Fusion 43, (2001).

[16] J. Weiland, “Collective Modes in Inhomogeneous Plasma”, IOP Publishing Ltd, 2000.

[17] P. H. Diamond et al., Plasma Phys. Control. Fusion 47, R35 (2005).

[18] K. Itoh et al., Phys. Plasmas 13, 055502 (2006).

[19] B. Coppi and F. Pegoraro, Nucl. Fusion 17, 969 (1977).

[20] F. Romanelli, Phys. Fluids B 1, 1018 (1989).

[21] P. Mantica et al., Phys. Rev. Lett. 102, 175002 (2009).

[22] S. C. Guo and F. Romanelli, Phys. Fluids B 5 (2), 520 (1993).

[23] F. Jenko, et al., Phys. Plasmas 7, 1904 (2000).

[24] N. T. Howard et al., Physics of Plasmas 21, 112510 (2014).

[25] S. P. Smith et al., Nucl. Fusion 55, 083011(2015).

[26] T. Görler and F. Jenko, Phys. Rev. Lett. 100, 185002 (2008).

[27] S. Maeyama and Y. Idomura, Phys. Rev. Lett. 114, 255002 (2015).

[28] N. T. Howard et al., Nucl. Fusion 56, 014004 (2016).

[29] T. L. Rhodes et al., Physics of Plasmas 14, 056117 (2007).

[30] W. Horton et al., Nucl. Fusion 45, 976 (2005).

[31] A. D. Gurchenko et al., Nucl. Fusion 47, 245 (2007).

[32] A. D. Gurchenko and E. Z. Gusakov, Plasma Phys. Control. Fusion 52, 124035 (2010).

[33] F. Jenko et al., Phys. Plasmas 8, 4096 (2001).

[34] F. Ryter et al., Phys. Rev. Lett. 95, 085001 (2005).

[35] A. G. Peeters et al., Phys. Plasmas 12, 022505 (2005).

[36] A. J. Brizard and T. S. Hahm, Rev. Mod. Phys. 79, (2007).

[37] T. Görler et al., J. Comput. Phys. 230, 7053 (2011).

[38] F. Merz, “Gyrokinetic simulation of multimode plasma turbulence”, PhD thesis, 2008.

[39] R. L. Miller et al., Phys. Plasmas 5, 973 (1998).

[40] F. Jenko, T. Dannert and C. Angioni, Plasma Phys. Control. Fusion 47B, 195 (2005).

[41] A. Casati, et al., Nucl. Fusion 49, 085012 (2009).

[42] G. M. Staebler, J. E. Kinsey and R. E. Waltz, Phys. Plasmas 12, 102508 (2005).

[43] G. M. Staebler, J. E. Kinsey and R. E. Waltz, Phys. Plasmas 14, 055909 (2007).

[44] G. M. Staebler et al., Phys. Plasmas 23, (2016).

[45] C. Bourdelle et al, Phys. Plasmas 14, 112501 (2007).

[46] C. Bourdelle et al., Plasma Phys. Control. Fusion 58, 014036 (2016).

[47] J. Citrin et al., Nucl. Fusion 55, 092001 (2015).

[48] G. V. Pereverzev and P. N. Yushmanov, ASTRA: Automated System for TRansport Analysis, Max-Planck-Institute fur Plasmaphysik, 2002.

[49] J. Hedin et al., Nuclear Fusion 42, 527 (2002).

[50] T. Hellsten et al., Nuclear Fusion 44, 892 (2004).

[51] L. G. Eriksson, T. Hellsten and U. Willén, Nucl. Fusion 33, 1037 (1993).

[52] C. Challis et al., Nucl. Fusion 29, 563 (1989).

[53] G. Cenacchi and A. Taroni, Rapporto ENEA RT/TIB/88/5 (1998).

[54] F. Imbeaux, F. Ryter. and X. Garbet., Plasma Phys. Control. Fusion 43, 1503 (2001).

[55] N. J. Lopes, Plasma Phys. Control. Fusion 37, 799 (1995)

[56] P. Mantica and F. Ryter, Computes Rendus Physique 7, 634 (2006).

Part II

Effects of light impurities and fast particles on thermal transport in the plasma core

Introduction

In all the possible operational scenarios of a tokamak the presence of impurities in the plasma is unavoidable. First of all, the plasma in a tokamak is an open system. This characteristic is essential in order to maintain alive the nuclear fusion reactions as the gas that forms the plasma must be continuously recycled. The plasma strongly interacts with the first wall of the reactor vessel and the plasma-facing materials are always present as plasma impurities. The heating systems, such as the NBI (Neutral Beam Injection) and the RF (Radio Frequency) systems, are also responsible for the presence of impurities in the plasma through the antennas and the beam launcher components. The $D-T$ nuclear reactions are themselves a source of impurity in the plasma, creating highly energetic He ions. Furthermore, one of the ways to reduce the heat loss deposition on the divertor is to puff light impurities at the plasma edge. Also some heating techniques, such as the ICRH (Ion Cyclotron Resonant Heating) in minority scheme, require the presence of an impurity species in the plasma (^3He in the cases analyzed in this chapter). If it is important to avoid an accumulation of these impurities, especially of the heavier ones, in the plasma core, it is also impossible to completely avoid their presence. It is then essential to understand how these impurities propagate into the plasma, how to control this propagation and how the impurities affect the performance of a reactor.

The transport of light impurity particles has been studied, both experimentally and theoretically, in various machines and in different operational conditions (see for examples ref. [2-5,7,10,11,24] of chapter 4). In many conditions turbulent transport has been found to dominate the transport of light impurities in the plasma core and the main mechanisms that drive the transport have been identified (see ref. [8-13] of chapter 4). Despite all the efforts, some differences are still present between the predicted peaking of light impurities and the experimental values. Also the effects of thermal light impurities on the plasma thermal transport and energy confinement have been studied in different machines and regimes (see ref. [6-13] of chapter 5). In all these studies, an increase of plasma confinement in the presence of light impurities has been observed. Especially in H mode, the stabilizing effect has been suggested to be more important at the plasma edge and on the plasma pedestal, with negligible effect of light impurities on the stabilization of the plasma core micro-instabilities, while in some studies, a direct role of light impurity seeding in the stabilization of micro-instabilities in the plasma core has been observed and studied.

Another important contribution to the dynamics of turbulent transport has been found to be related to non-thermal (fast) particles. The presence of fast ions in the plasma is related to radio-frequency heating, NBI injection or, in fusion conditions, to the fusion reactions. A strong stabilization of the turbulent heat transport has been observed in JET (see ref. [2-3] of chapter 6) and ASDEX-Upgrade (see ref. [15] of chapter 6) in the inner core region of the plasma ($R \lesssim 3.4m$) when fast ion pressure is high enough. Recent works are trying to understand the physics mechanisms behind this stabilization and how to take them into account in simplified models (e.g. in quasi-linear models). Experimentally, all the plasmas, where the strong turbulent ion heat transport stabilization by fast ions has been observed, featured high NBI power. High NBI leads to high toroidal plasma rotation, that can also induce a strong stabilizing of ITGs. It is therefore difficult, when using high NBI power, to separate the effects of plasma rotation and the effects related to fast ions.

The work presented in this chapter regards three aspects related to the presence of light impurities and fast ions in the plasma core:

- The comparison between the light impurity transport predicted by numerical simulations and the experimental one
- The effect of puffed light impurities on the core thermal transport
- The effect of non-thermal ions on the core thermal transport

In chapter 4 the density profiles of 5 light impurities ($^3He, C, Be, N, Ne$) measured with active charge-exchange in JET ILW plasmas are shown and their experimental density peaking is compared to the one predicted by gyrokinetic simulations. In chapter 5, the effect of puffing N on the thermal transport in JET ILW L-mode plasmas is studied. This is the first detailed study of the effects of light impurities on the turbulent transport in the JET plasma core. Also in this case, experiment and numerical simulations are compared. Finally, in chapter 6, the effect of fast ^3He ions on the thermal transport in JET ILW L-mode plasmas is investigated. These plasmas feature low NBI power and low rotation and the results obtained give a first experimental evidence of the role of fast ions in the turbulent transport stabilization in absence of high plasma rotation.

Chapter 4

Light impurity transport in JET ILW L-mode plasmas

Paper published in Nuclear Fusion: N. Bonanomi et al., Nucl. Fusion 58, 036009 (2018).[†]

N. Bonanomi[1,2], P. Mantica[2], C. Giroud[3], C. Angioni[4], P. Manas[4], S. Menmuir[3] and
JET contributors*

EUROfusion Consortium, JET, Culham Science Centre, Abingdon, OX14 3DB, UK
1) University of Milano-Bicocca, Milano, Italy
2) CNR - Institute of Plasma Physics "P. Caldirola", Milano, Italy
3) Culham Centre for Fusion Energy, Abingdon, OX14 3DB, UK
4) Max Planck Institute for Plasma Physics, Boltzmannstr. 2, 85748 Garching, Germany
* See the author list of See the author list of "X. Litaudon et al., 2017 Nucl. Fusion 57, 102001"

Abstract

A series of experimental observations of light impurity profiles was carried out in JET (Joint European Torus) ITER-like wall (ILW) L-mode plasmas in order to investigate their transport mechanisms. These discharges feature the presence of $^3He, Be, C, N, Ne$, whose profiles measured by active Charge Exchange diagnostics are compared with quasi-linear and non-linear gyrokinetic simulations. The peaking of ^3He density follows the electron density peaking, Be and Ne are also peaked, while the density profiles of C and N are flat in the mid plasma region. Gyrokinetic simulations predict peaked density profiles for all the light impurities studied at all the studied radii and never predict flat or hollow profiles in our cases.

4.1 Introduction

Puffing light impurities at the plasma edge is one of the ways to reduce the heat loss deposition on the divertor of ITER (International Thermonuclear Experimental Reactor) and perhaps of a future reactor [1, 2]. ^4He will be produced in the plasma central core

---

[†] https://doi.org/10.1088/1741-4326/aaa4d3

region by the $D-T$ fusion reactions. Furthermore, ITER will have a first wall made of beryllium. While decreasing the power at the edge by increasing the radiative power could help to reduce the damages on the machine walls and on the divertor, an accumulation of impurities in the core could lead to a dilution of the main ion species that will participate to the reactions. Understanding how these light impurities are transported in the plasma is then fundamental in order to predict the best scenarios for future machines and achieve optimal conditions for fusion.

In the last years, both experimental and theoretical investigations on light impurity transport have been made in various machines [3-10]. In many conditions, turbulent transport dominates the transport of light impurities in a tokamak plasma core. The main mechanisms that drive the turbulent particle transport have been identified [11-16] and their relative importance for different impurities and plasma conditions has been investigated. Despite all the efforts, some differences are still present between the predicted peaking of light impurities and the experimental values. In JET [3, 5, 8] and ASDEX Upgrade [3] H-mode plasmas, differences between the experimental density peaking of $^3He, C$, B and Ni and the predicted peaking by gyro-kinetic and neoclassical theory have been found, while in DIII-D [17] H-mode plasmas, differences between density peaking of F and quasi-linear and neoclassical predictions have been observed, indicating that something may be missing for a complete understanding of the particle transport of light impurities. With respect to previous JET studies made in C-wall H-modes, this study was performed in JET ILW L-modes, increasing the number of light impurities studied, by measuring in the same discharges the profiles of $^3He, Be, C, N$ and Ne with different heating schemes. Whilst C and Be as intrinsic impurities and ^3He as ICRH minority species were present in all discharges, N and Ne were puffed in some of them. Furthermore, mainly plasmas with low rotation have been studied, in order to minimize the impurity transport terms linked to rotation and test the model performance in this limit. The experimental results are shown and studied through neoclassical and gyro-kinetic simulations, which indicate that, in the studied plasmas, turbulent transport is the dominant transport mechanism, while neoclassical transport plays a minor role.

The paper is organized as follows. In sections 4.2 and 4.3 the experimental and numerical set-up and methods are reviewed. Section 4.4 discusses the study of the light impurity density profiles. A discussion on the results and the conclusions are presented in section 4.5.

4.2 Experimental set-up

The discharges studied in this paper were made in two different experimental sessions (n. 86739-86759 from one session and n. 90666-90672 from the other) in the JET tokamak (major radius $R_0 = 2.96\,m$, minor radius $a = 1\,m$) with ILW. The two sessions have very similar experimental settings and plasma parameters. All plasmas are D plasmas with vacuum toroidal magnetic field $B_T \approx 3.3\,T$, plasma current $I_p \approx 2\,MA$ and safety factor at the flux surface that encloses the 95% of the poloidal flux $q_{95} \approx 5$. The heating power consists of 2.5-7 MW of ICRH (Ion Cyclotron Resonance Heating) using a ^3He minority concentration $n_{^3He}/n_e \approx 6-9\%$, which ensures a dominant ion heating [18], and of 1.7-3 MW of NBI (Neutral Beam Injection) , mainly to provide charge exchange measurements of T_i, plasma rotation Ω_t and impurity density profiles. In all the studied discharges the RF power was deposited on-axis ($R \approx 3.0\,m$). The discharges analyzed were all L-modes, apart from two discharges (n. 86758 and n. 86759) where the NBI heating was increased to 13 MW, in order to study the effect of the presence of higher rotation and plasma beta , changing the plasma condition from L-mode to H-mode.

The measurement of the electron temperature T_e is provided by the ECE (Electron Cyclotron Emission) diagnostic with an error on the measurements of about 5%, while the ion temperature T_i and plasma rotation ω_T are measured by the CX (Charge-Exchange) diagnostic with an error of about 5-10%, depending on the radial position, for the ion temperature and of about 10% for the plasma rotation. The error on T_e/T_i is about 9–12%. The electron density n_e is measured by high-resolution Thomson scattering (HRTS) with an uncertainty of about 15%. Local values of $R/L_{Ti} = -R_0 \nabla T_i/T_i, R/L_{Te} = -R_0 \nabla T_e/T_e$ and $R/L_n = -R_0 \nabla n_e/n_e$ were obtained by local linear fits of $ln(T_i), ln(T_e)$ and $ln(n_e)$ radial profiles averaged over a time interval $\Delta t \approx 1\ s$. The fits are done using $r = (R - R_{in})/2$, R and R_{in} being the outer and inner boundaries of the flux surface on the magnetic axis plane, and averaging other multiple fits using a variable number of data points around the chosen radius (3-9 points). We drop the suffix 0 when indicating these quantities for convenience. The uncertainties on these parameters are then estimated by repeating the same procedure with different space intervals and evaluating the deviation in the set of values so obtained. Errors are typically 10-15% for $R/L_{Te/i}$ and 15-20% for R/L_n. The radial profile of the safety factor q as well as the equilibrium plasma geometry are reconstructed by the EFIT equilibrium code with the MSE (Motional Stark Effect) or the Faraday rotation constraints. Typical errors on the safety factor are about 20%. Radial profiles of T_e, T_i, n_e, q and Ω_t of discharges n. 86740 (L-mode with 3 MW of ICRH + 3 MW of NBI, $n_{^3He}/n_e \sim 6\%, n_{Be}/n_e \sim 1\%, n_C/n_e \sim 0.1\%$), n. 86749 (L-mode with 4 MW of ICRH + 3 MW of NBI, $n_{^3He}/n_e \sim 6\%, n_{Be}/n_e \sim 1\%, n_C/n_e \sim 0.1\%, n_N/n_e \sim 1.2\%$), n. 86758 (H-mode with 2.5 MW of ICRH + 13 MW of NBI, $n_{^3He}/n_e \sim 8\%, n_{Be}/n_e \sim 1\%, n_C/n_e \sim 0.1\%, n_N/n_e \sim 1\%$) and n. 90670 (L-mode with 6 MW of ICRH + 1.7 MW of NBI, $n_{^3He}/n_e \sim 9\%, n_{Be}/n_e \sim 1\%, n_C/n_e \sim 0.1\%, n_{Ne}/n_e \sim 0.1\%$) are shown in *figure 4.1.* The parameters of these shots have been used as input in the simulations for the study of the impurity transport. The ICRH power deposition of discharge n. 90670, obtained with the SELFO code [19, 20], is shown figure 4.1.

The data analysis is carried out at $\rho_{tor} = 0.33, 0.5, 0.7 \rho_{tor} = \sqrt{(\Phi/\pi B_T)/(\Phi/\pi B_T)_{max}}$, where Φ is the toroidal magnetic flux.

4.2.1 Charge exchange impurity measurements

All the density profiles of the light impurities studied in this work have been measured using the charge-exchange diagnostic. C ($n_C/n_e \sim 0.1\%$) and Be ($n_{Be}/n_e \sim 1\%$) were present in all the discharges as intrinsic impurities and ^3He ($n_{He}/n_e \sim 6-10\%$) was puffed into all discharges as ICRH minority species. N ($n_N/n_e \sim 1\%$) was puffed in discharges n. 86749-86759 to study its effect on thermal transport while Ne ($n_{Ne}/n_e \sim 0.1\%$) was puffed in shots n. 90666 - 90672 to optimize the charge-exchange measurements.

The JET Core CXRS diagnostic consists of two periscopes that define toroidal views aligned on the heating neutral beams of octant 8. A neutral beam injector consists of two sets of four positive ion neutral injectors (PINIs) divided into the so-called tangential and normal bank. Due to the arrangement of the heating beams, the toroidal views aligned on PINI 6 (normal) and 7 (tangential) also intersect PINI 1 (tangential). As a result, for each viewing direction, a set of three volumes defines the average spatial position of the measured quantities as well as the radial resolution.

Two rows of sightlines per periscope provide a profile measurement for the low field side edge to the plasma core. The spectral analysis of the plasma light collected by the two periscopes can be performed with five spectrometers and profiles are obtained with 12-15 spatial points with 10ms time resolution. In this paper He/Be-CX spectra, C/Ne-CX spectra ad N-CX spectra was obtained each by one of these rows. The knowledge of the alignment of periscope sightlines with the PINIs is important for the determination for T_i, V_ϕ and, in particular for this paper, the impurity density n_{imp}. Geometrical factors enter the determination of n_{imp}. The exact distance of the probe volumes from the axis of the PINI has a direct impact on the impurity density determined in the line of sight and thereby on the inferred impurity density profile. Any inaccuracy in the periscope alignment corresponds to a systematic error in the value of the impurity density but also to a systematic error in the impurity density profile. An alignment technique has been developed consisting of three steps: the alignment in laboratory , the in-vessel alignment and the use of the so-called He doping and PINI switching calibration shots, described in more detail in [21], which reduce the uncertainty due to alignment to a few %.

As for the analysis for the CX spectra, during the JET C-wall years, the CXRS analysis mostly relied on multi-gaussian fit without the use of the beam modulation technique [22]. Since JET ILW, due to the reduction of the intrinsic C concentration and also to the increase in the intensity of nuisance lines, the CXRS analysis is now relying on the use of beam modulation. This consists in subtracting passive frames, where only the passive emission is collected, from active frames, where both charge-exchange emission and passive emission are collected. Provided that the active and passive frames where collected in equivalent plasmas, we should obtain a single Gaussian shape to fit the active signal of the PINI considered. The difficulty in this technique is the identification of active and passive frames that can be considered equivalent. Experimentally, it was found that the selection of passive frames with the lowest edge nuisance lines (Be-II line in the CVI-CX or He/Be-CX spectra and N-II line in N-CX spectra) and corresponding active frames with the intensity of the nuisance line within 20% of the reference passive frame results in a nice Gaussian. This technique has been used for the data presented in this paper.

The CX Helium measurements are known to be affected by the plume effect [23, 24]. Since a precise quantitative treatment of the helium plume effect is not yet available for the JET charge exchange diagnostics, this effect is not taken into account in this work and only the uncorrected values of $R/L_{n,^3He}$ are reported. Such correction is expected not to vary much with radius, therefore possibly affecting the absolute values of the ^3He density but not much its profile peaking, which is what is addressed by our study.

4.3 Numerical simulation set-up

The density n of each species in the plasma satisfies the continuity equation

$$\frac{\partial n}{\partial t} = -\nabla \cdot \Gamma_n + S_n \tag{4.1}$$

where Γ_n is the particle flux and S_n is the source of the particles. The particle flux of an arbitrary species in the plasma can be written as

$$\Gamma_n = n\left(-D_n \frac{\partial ln(n)}{\partial r} + V_n\right) \tag{4.2}$$

where D_n is the diffusion coefficient of the diagonal diffusive term and V_n is the convection velocity of the off-diagonal convective term. The particle flux can be written as a sum of the neoclassical particle flux [25] and the turbulent particle flux [26] $\Gamma_n = \Gamma_n^{neo} + \Gamma_n^{turb}$.

A further decomposition of the turbulent particle transport is [26, 27]

$$\frac{R\Gamma_n^{turb}}{n} = D_n\frac{R}{L_n} + RV_n = D_n\frac{R}{L_n} + D_T\frac{R}{L_T} + D_u\frac{R^2}{v_{th}}\frac{\partial\Omega_t}{\partial r} + RV_{pn} \tag{4.3}$$

where the terms on the right hand side represent, in order, the diffusion term, the thermo-diffusion term, due to the presence of a temperature gradient [11, 12], the roto-diffusion term [13, 14], due to the presence of a toroidal angular velocity gradient, and a pure convection term [15, 16] related to the curvature of the toroidal magnetic field. The coefficients D_T, D_u and term V_{pn} depend on the plasma micro-turbulence and so on the plasma gradients, therefore the equation (4.3) in general cannot be considered a linear relationship between the particle transport and the plasma gradients. In the case of trace impurities and in the radially local limit though, relation (3.3) becomes linear.

The experimental density peaking of the light impurities are compared to numerical simulations that calculate the neoclassical and the turbulent particle fluxes. For the calculation of the neoclassical contribution to the particle transport the code NEO [28, 29, 30] was used. For the turbulent fluxes, quasi-linear and non-linear gyro-kinetic simulations with the code GENE (Gyrokinetic Electromagnetic Numerical Experiment) [31, 32] have been done. GENE solves the gyro-kinetic Vlasov equations coupled with the Maxwell equations within a δf approximation [33] and using field aligned coordinates $\{x, y, z\}$, where z is the coordinate along the magnetic field line, x is the radial coordinate and y is the binormal coordinate. For a part of the quasi-linear study, also the code GKW (GyroKinetics at Warwick) [34, 35] in the local limit has been used. In particular, the GKW code was used in order to study the contribution of the roto-diffusion term as it allows to use different values of $\partial\Omega_t/\partial r$ for the different kinetic species considered in the simulation.

In stationary conditions, with no sources in the plasma core, equation (4.1) requires that $\Gamma_n = 0$. The density peaking is then calculated, using equation (4.2), as

$$\frac{R}{L_n}(\Gamma_n = 0) = -\frac{RV_n}{D_n}. \tag{4.4}$$

In the gyro-kinetic simulations, in order to evaluate the different terms in equation (4.3), N kinetic species of the light impurity under study (with charge Z, density n_Z, density gradient $R/L_{n,Z}$, temperature gradient $R/L_{T,z}$ and rotation $\Omega_{t,Z}$) are used, that satisfy the conditions

$$\begin{aligned} n_Z^{exp} &= \textstyle\sum_{j=1}^N (n_Z)_j \\ \left(\tfrac{R}{L_{n,Z}}\right)_{exp} &= \tfrac{1}{N}\textstyle\sum_{j=1}^N \left(\tfrac{R}{L_{n,Z}}\right)_j \\ \left(\tfrac{R}{L_{T,Z}}\right)_{exp} &= \tfrac{1}{N}\textstyle\sum_{j=1}^N \left(\tfrac{R}{L_{T,Z}}\right)_j \\ \left(\tfrac{R^2}{v_{th}}\tfrac{\partial\Omega_{t,Z}}{\partial r}\right)_{exp} &= \tfrac{1}{N}\textstyle\sum_{j=1}^N \left(\tfrac{R^2}{v_{th}}\tfrac{\partial\Omega_{t,Z}}{\partial r}\right)_j . \end{aligned} \tag{4.5}$$

Simulations with N kinetic species of the same impurity that satisfy the conditions (4.5) are equivalent to simulations with one kinetic species of that impurity with the total density and gradients due to the linearity of the Vlasov equations with respect to the species.

Linear simulations confirmed that, in our case, the light impurities cannot be considered as traces, as they have a non-negligible influence on the micro-instability growth rate, and that the conditions (4.5) must be satisfied. In order to study the role of the different terms in (4.3), 4 species of the same impurity have been considered in some quasi-linear simulations. By imposing to be non-zero only one of the three gradients in (4.3) ($R/L_{n,Z}, R/L_{T,Z}, \partial\Omega_{t,Z}/\partial r$) in each of the three species equations and using all zero gradients for the fourth species equation (to calculate the convective part), it is possible to calculate the contribution to the impurity particle flux from each of the terms in equation (4.3). This calculation has been carried out for Nitrogen.

In the quasi-linear simulations, a mixing length rule was employed [36, 37]. The mixing length rule used is based on the assumption that the turbulent diffusivity scales as

$$D \propto \frac{(\Delta x)^2}{\Delta t} = \frac{\gamma}{\langle k_\perp^2 \rangle} \tag{4.6}$$

where γ is the linear growth rate of the main micro-instability and $\langle k_\perp^2 \rangle$ can be written, taking into account the extended structure of the electrostatic potential ϕ along the field line, as

$$\langle k_\perp^2 \rangle = \frac{\int |\phi|^2 k_\perp^2 dxdz}{\int |\phi|^2 dxdz}.$$

$k_\perp$ is defined as $k_\perp^2 = k_y^2 g^{yy} + 2k_y k_x g^{xy} + k_x^2 g^{xx}$, where g^{ij} is the (i, j) component of the metric tensor g. The quasi-linear particle flux is then calculated as

$$\Gamma^{QL} = G \cdot \sum_{k_y} \Gamma_{k_y}^{norm} \frac{\gamma_{k_y}}{\langle k_\perp^2 \rangle} \tag{4.7}$$

where the linear particle transport for each value of k_y is normalized as $\Gamma_{k_y}^{norm} = \Gamma_{k_y}/\langle |\phi|^2 \rangle$ and where G is a normalization factor. G, needed to reproduced the saturated non-linear fluxes, is left equal one in this case as it disappears in the calculation of $R/L_{n,Z}$ (equation 4.8). In all the quasi-linear simulations the range $0.1 \leq k_y\rho_s \leq 0.9$ is used, as higher k_y modes do not contribute to particle transport. In order to have reliable results, the condition $q_e^{QL}/q_i^{QL} \approx q_e^{exp}/q_i^{exp}$ was required (q^{QL} is calculated in a similar way as Γ^{QL}). The expected density peaking of the impurity under study is then calculated, using (4.7) with two species of the same impurity to calculate RV_n^{QL} (imposing $R/L_{n,Z} = 0$ for one of the two species) and D_n^{QL} and neglecting the neoclassical contribution (found negligible compared to the turbulent one), as

$$\frac{R}{L_{n,Z}} = -\frac{RV_n^{QL}}{D_n^{QL}}. \tag{4.8}$$

Tests were made in the quasi-linear simulations, changing $s, q, R/L_n, R/L_{Ti}, \Omega_t$ within the experimental error range. The obtained variation of $R/L_{n,Z}$ is indicated by the error bars of the simulated values in table 4.2 and figure 4.3.

In the quasilinear gyro-kinetic simulations Miller geometry [39] was used as well as collisions, external flow shear and finite-β effects and the range $0.1 \leq k_y\rho_s \leq 1.2$ was used in the simulations. In the non-linear simulations the same settings were used and typical grid parameters were as follows: perpendicular box sizes $[L_x, L_y] \approx [190, 125]\rho_s$, phase-space grid discretization $[n_x, n_y, n_z, n_{v\parallel}, n_\mu] = [128-256, 24-64, 32, 32-64, 12-16]$, with $0.25 - 0.5 \leq k_y\rho_s \leq 1.6$, depending on the plasma radius, parameters and on the number of kinetic species considered. In all the simulations main ions and electrons are retained as kinetic species as well as the light impurity species under study. All the quasi-linear and non-linear gyro-kinetic simulations results shown in this work are from simulations carried out with the GENE code, except for the study of the role played by the roto-diffusion term in equation (4.3), that has been studied using the GKW code for the reasons explained above. Using the same input parameters, GENE and GKW quasi-linear simulations gave similar predictions for the light impurity density peaking in the studied cases. In this study we always consider fully ionized impurities.

4.4 Light impurity transport

The radial density profiles, measured with charge exchange, of the light impurities studied in this work are shown in *figure 4.2.* ^3He, Be and Ne profiles are peaked in the whole plasma core region while the profiles of N and C present a flat region inside $0.3 \lesssim \rho_{tor} \lesssim 0.7$. No substantial differences in the peaking of profiles of $^3He, Be$ and N have been observed between L-modes and in H-modes, indicating that the higher rotation, the higher fast D content or the higher plasma β in the H-modes are not modifying substantially the light impurity particle transport in the considered range of parameters (see *table 4.1*). Furthermore, similar $^3He, Be$ and Ne density profiles have been observed in discharges n. 90666, 90668, 90671 and 90672. In these shots 1.7 MW of NBI has been used, but the (on-axis, in ^3He minority scheme) ICRH power has been changed from 2.5 to 7 MW between the shots. This indicates that the amount of the on-axis ICRH ion heating is not affecting the light impurity transport in these discharges.

The input parameters in the numerical simulations (see *table 4.1*) have been taken from discharges:

- n. 86740, averaging on $9.5\,s < t < 10.5\,s$, for the study of C transport;
- n. 86749, averaging on $8\,s < t < 10\,s$, for the study of ^3He and N transport;
- n. 86758, averaging on $7.5\,s < t < 8.5\,s$, for the study of ^3He and N transport in H-modes;
- n. 90670, averaging on $5.8\,s < t < 6.4\,s$, for the study of $^3He, Be$ and Ne.

Using the parameters of discharges n. 86740, 86749 and 86758 at $\rho_{tor} = 0.2, 0.33, 0.4, 0.5, 0.6, 0.7$, the contribution of the neoclassical transport to the particle transport of C and N was investigated with the NEO code. The neoclassical transport has been found to be negligible in the studied region, being $RV^{neo}/RV^{turb}, D^{neo}/D^{turb} \sim 10^{-2}$. To study the turbulent particle transport, gyro-kinetic quasi-linear and some non-linear simulations have been made, as discussed in section 4.3, at $\rho_{tor} = 0.33, 0.5, 0.7$. In the quasi-linear simulations the parameters were adjusted within error bars in order to match the experimental q_e/q_i while in the nonlinear simulations the experimental values of q_e and q_i have been reproduced within error bars. In the quasi-linear simulations, multiple light impurity species have been considered in some cases in order to study the possible impact of the presence of other light impurities on the peaking of the impurity under study. The impact of including multiple species has been found minimal. In the non-linear simulations, just one light impurity kinetic species per time has been considered. The results obtained from gyro-kinetic simulations are shown in *figure 4.3* and reported in *table 4.2.* The gyro-kinetic simulations always predict peaked density profiles for all the light impurities studied and no substantial differences in the peaking of the different impurities. In particular, the simulations never predict flat or hollow density profiles for C, N, in contrast to the experimental observations. The GKW simulations, made using 4 species for N at $\rho_{tor} = 0.5$ in order to study the role of the various terms in equation (4.3), predict a weak role of the roto-diffusion term. They predict that the thermo-diffusion term is $\sim 1/2$ of the geometrical convective term and the roto-diffusion term is $\sim 1/20$ of the geometrical convective term. They also predict the geometrical pinch term to be directed inward while the thermo-diffusion and the roto-diffusion terms to be directed outward. The negligible role of roto-diffusion, supported by comparisons between GENE simulations with and without the effects of the plasma toroidal rotation, is in agreement with the experimental observation that no differences in the light impurity radial profiles have been observed when introducing higher toroidal rotation using high NBI power. As for the other two terms, we cannot discriminate whether it is an overestimate of curvature pinch or an underestimate of the thermo-diffusion pinch (or possibly another mechanism) that leads to peaked simulated profiles instead of the flat experimental ones, because we do not have an independent experimental determination of the two terms, nor of the total convective and diffusive terms separately, which would require the employment of transient techniques of pulse propagation. With regard to the peaked impurity cases, some under-prediction of the impurity density peaking of the more peaked profiles has been observed.

In the above analysis we considered source free light impurity transport; this has been verified for all the impurities except for Ne at $\rho_{tor} \approx 0.7$, where a possible source has been found depending on the plasma parameters. Taking into account the source could modify the obtained results for Ne at this radial position but does not change the overall picture. Also, the effects of the background neoclassical distribution function on turbulent particle transport have not been considered. These effects can affect in particular the roto-diffusion term [40], especially in presence of high plasma rotation. Nevertheless, in our case, due to the low plasma rotation in our discharges, they are not expected to change significantly the picture described above.

4.5 Discussion and conclusions

Radial density profiles of five light impurities, with $2 \leq Z \leq 10$, have been measured by active charge-exchange diagnostics in L-mode shots at JET with ITER-like wall, in conditions where turbulent transport is the dominant transport mechanism in the region of interest. Within the same discharge or very similar discharges, the profiles show different shapes, depending on the impurity Z. The ^3He, Be and Ne density profiles are peaked over the whole plasma core region, while C and N show a flat/hollow profile in the region $0.3 \lesssim \rho_{tor} \lesssim 0.7$. These observations add new experimental information to what observed in the past in JET L-mode and H-mode C-Wall plasmas [3, 5, 8]. Considering the various results on turbulent transport of light impurities published from JET and other devices together with the results in this paper, it seems there is a trend to observe peaked profiles for $Z = 2, 4$ impurities ($^3He, Be$), peaked or flat/hollow profiles, depending on the radial position and on the plasma parameters, for $Z = 5, 6, 7, 9$ impurities (B, C, N, F), and again peaked profiles for $Z = 10, 18$ impurities (Ne, Ar).

Neoclassical, quasi-linear and non-linear gyro-kinetic simulations have been carried out to explain the observed impurity density peaking. Our simulations predict similar peaking of the density profiles for all the light impurities studied and peaked profiles at all the studied radii. They tend to slightly underestimate the peaking of the more peaked profiles and never predict flat/hollow profiles. Quasi-linear gyro-kinetic simulations predict no big role of roto-diffusion, with respect to the geometrical pinch and to the thermo-diffusion, in the off-diagonal convective terms in equation (4.3). Whilst in previous modeling of high NBI power, highly rotating, JET H-modes [3, 5] roto-diffusion helped to reproduce the C hollow profiles, in our low NBI power cases the effects linked to rotation are small. Although recent studies indicate that when considering the effects of the background neoclassical distribution function, the roto-diffusion term can become more important [40], this is not expected to help in our case due to the low plasma rotation in our discharges (see figure 4.1). Therefore the origin of the mismatch between theoretical predictions and experimental results for these low rotation cases is still not understood and hopefully the work described in this paper will trigger further ideas in order to reproduce the experimental observations.

Acknowledgements

The authors would like to thank Yann Camenen, Athina Kappatou and Marco Valisa for precious suggestions and discussions. The authors are grateful to D. R. Mikkelsen for assistance. This research used resources of the National Energy Research Scientific Computing Center, a DOE Office of Science User Facility supported by the Office of Science of the U.S. Department of Energy under Contract No.DE--AC02--05CH11231. A part of this work was carried out using the HELIOS supercomputer system at Computational Simulation Centre of International Fusion Energy Research Centre (IFERC-CSC), Aomori, Japan, under the Broader Approach collaboration between Euratom and Japan, implemented by Fusion for Energy and JAEA. We acknowledge the CINECA award under the ISCRA initiative, for the availability of high performance computing resources and support. This work has been carried out within the framework of the EUROfusion Consortium and has received funding from the Euratom research and training programme 2014–2018 under grant agreement No 633053. The views and opinions expressed herein do not necessarily reflect those of the European Commission.

#	ρ_{tor}	s	q	R/L_{ne}	R/L_{Te}	R/L_{Ti}	β_e	ν_{eff}	T_i/T_e
86740	0.33	0.4	1.2	2.8	7.9	4.5	0.2%	0.08	1.1
	0.5	0.8	1.9	2.8	7.8	5	0.1%	0.16	1.13
	0.7	1.4	2.6	3.5	13	8.5	0.06%	0.46	1.6
86749	0.33	0.4	1.2	2.8	8	4.7	0.25%	0.1	1.2
	0.5	1.1	1.6	2.9	7.9	6	0.14%	0.2	0.9
	0.7	1.5	2.5	3.9	16.5	10	0.06%	0.74	1.6
86758	0.33	0.4	1.2	2.2	6	8.5	0.5%	0.1	1.4
	0.5	1	1.5	2	7	5	0.3%	0.2	1.3
	0.7	1.6	2.5	3.8	10	7	0.1%	0.46	1.7
90670	0.33	0.4	1.6	3.3	8	5	0.33%	0.08	0.74
	0.5	0.8	1.9	2.4	8.2	4.5	0.17%	0.16	0.9
	0.7	1.3	2.8	3.3	13	9	0.08%	0.48	1.2

Table 4.1: Main plasma parameters of the studied discharges at the studied radii. $\nu_{eff} = 0.1 \cdot Z_{eff} n_e / T_e^2$ and $\beta_e = 4.03 \cdot 10^{-03} \cdot n_e T_e / B_0^2$ (n_e in 10^{19} units and T_e in keV).

	Shot #	$\rho_{\mathbf{tor}}$	**Experimental**	**GENE QL**	**GENE NL**
^3He	90670	$\rho_{tor} = 0.33$	3.5 ± 1.2	2.1 ± 0.3	-
		$\rho_{tor} = 0.5$	2.5 ± 1	1.0 ± 0.2	-
		$\rho_{tor} = 0.7$	4 ± 1.5	1.7 ± 0.2	-
Be	90670	$\rho_{tor} = 0.33$	2.5 ± 1.5	1.6 ± 0.1	-
		$\rho_{tor} = 0.5$	1.8 ± 1	1.4 ± 0.1	-
		$\rho_{tor} = 0.7$	4 ± 1.5	1.5 ± 0.1	-
C	86740	$\rho_{tor} = 0.33$	1 ± 1	1.5 ± 0.1	1.2 ± 0.2
		$\rho_{tor} = 0.5$	0 ± 1	1.5 ± 0.2	1 ± 0.2
		$\rho_{tor} = 0.7$	0 ± 1	1.6 ± 0.2	-
N	86749	$\rho_{tor} = 0.33$	1.8 ± 1.2	1.4 ± 0.2	2 ± 0.4
		$\rho_{tor} = 0.5$	0 ± 0.5	1.5 ± 0.3	1 ± 0.2
		$\rho_{tor} = 0.7$	4 ± 2	1.5 ± 0.2	-
Ne	90670	$\rho_{tor} = 0.33$	4 ± 2	1.7 ± 0.1	-
		$\rho_{tor} = 0.5$	1.8 ± 0.5	1.9 ± 0.1	-
		$\rho_{tor} = 0.7$	3 ± 1	1.7 ± 0.1	-

Table 4.2: *Experimental and predicted values (from quasi-linear and, for some cases, non-linear gyrokinetic simulations) of the density peaking of the different light impurities in the plasma.*

Figures

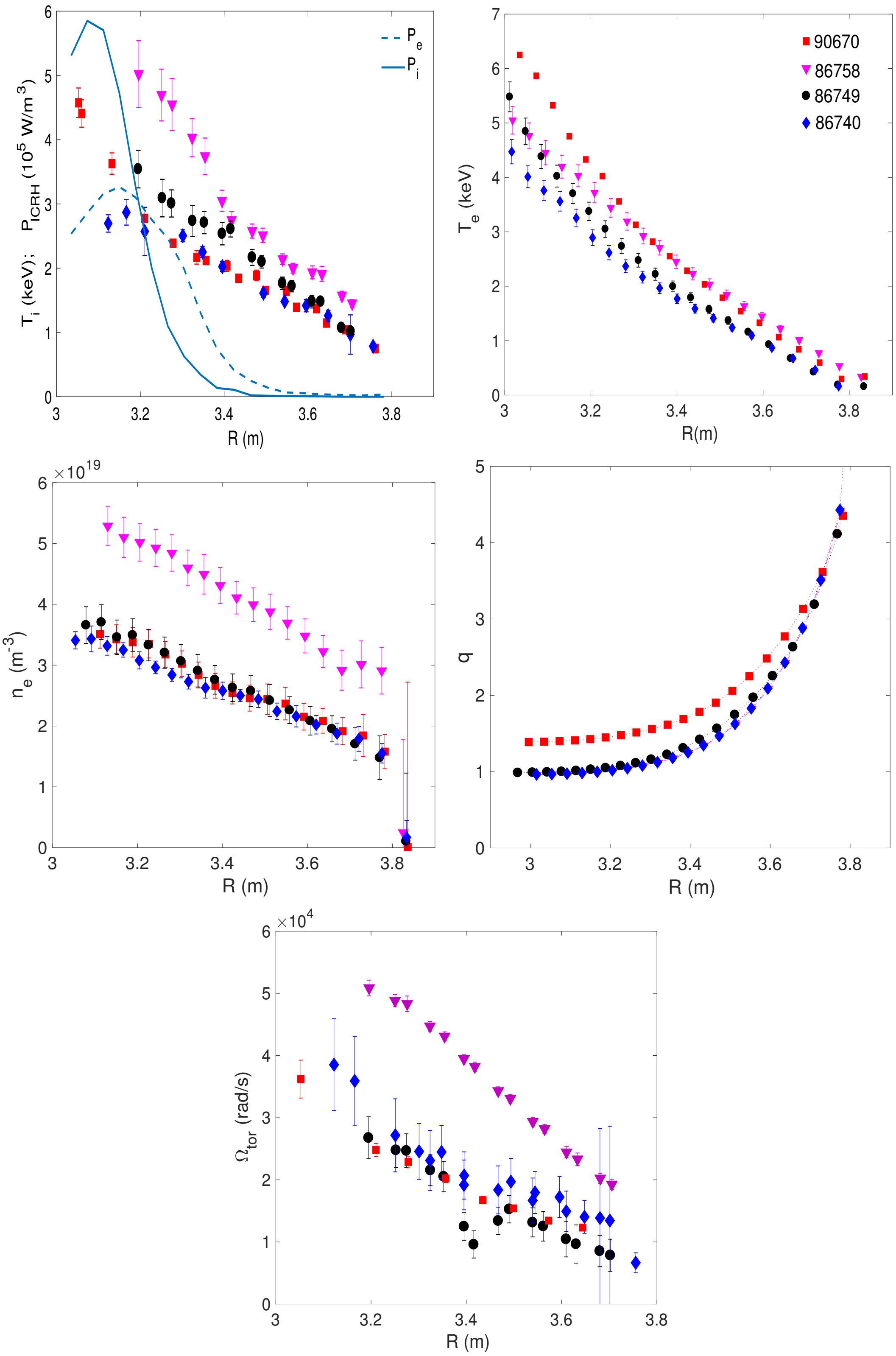

Figure 4.1: *Radial profiles of T_i, T_e, n_e, q and Ω_t of JET discharges n. 86740 at t = 10 s (blue pentagons), n. 86749 at t = 9 s (black circles), n. 86758 at t = 8 s (magenta triangles) and n. 90670 at t = 6 s (red squares). The ICRH power deposition, obtained with the SELFO code, is also shown for discharge n. 90670.*

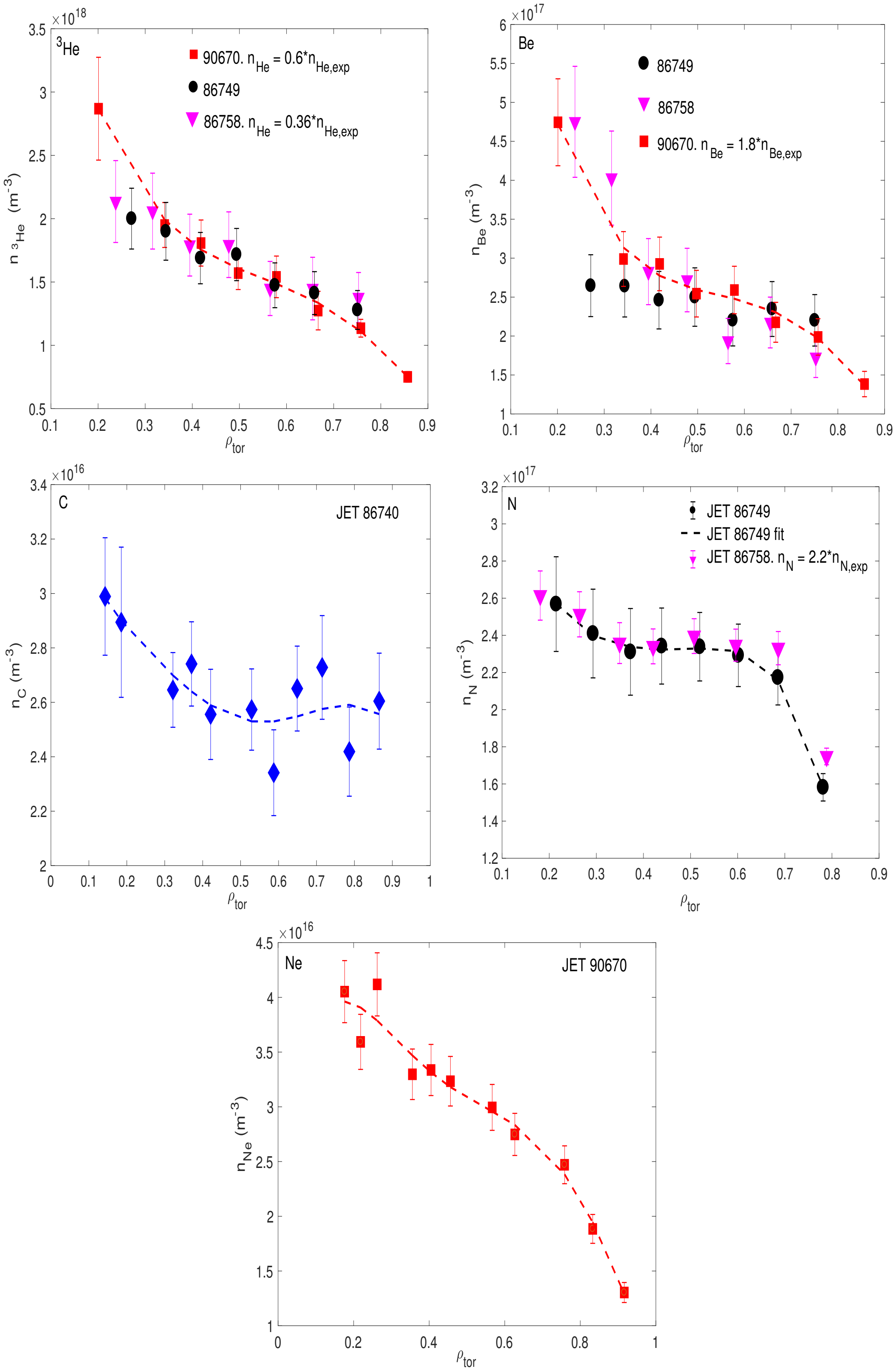

Figure 4.2: *Radial density profiles of* ^3He*, Be, C, N, and Ne. The profiles are taken from JET discharges n. 86740 (3 MW of ICRH + 4 MW of NBI) at t = 10s (blue diamonds), n. 86749 (4 MW of ICRH + 4 MW of NBI) at t = 9s (black circles), n. 86758 (4 MW of ICRH + 13 MW of NBI) at t = 8 s (magenta triangles) and n. 90670 (6 MW of ICRH + 1.7 MW of NBI) at t = 6.2s (red squares). Some of the profiles are rescaled, as indicated, for a better comparison between different discharges.*

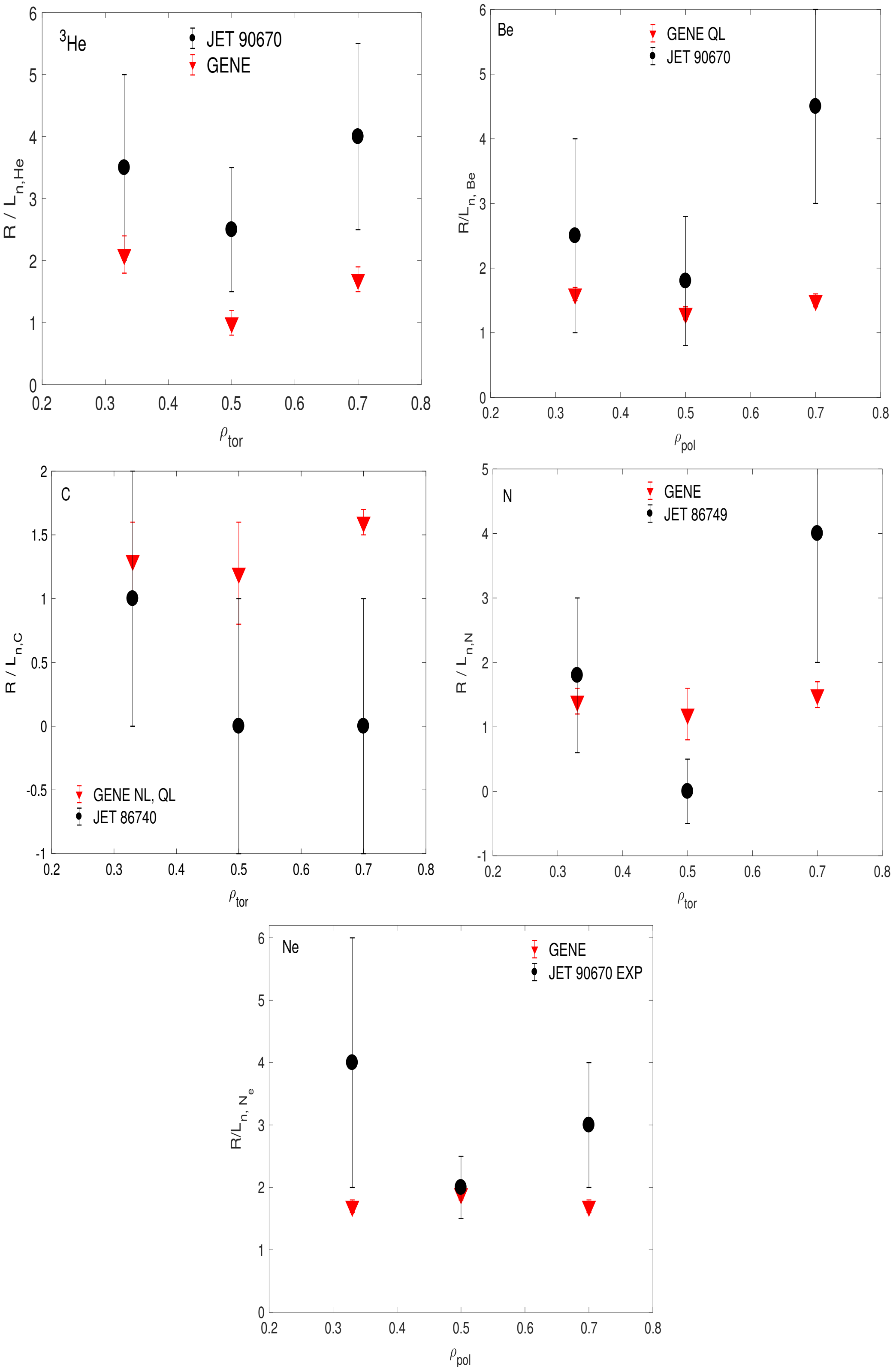

Figure 4.3: *Normalized density peaking at* $\rho_{tor} = 0.33, 0.5, 0.7$ *of* ^3He, Be, C, N, *and* Ne *for JET discharges n. 86740 (3 MW of ICRH + 4 MW of NBI) at t = 10s, n. 86749 (4 MW of ICRH + 4 MW of NBI) at t = 9s and n. 90670 (6 MW of ICRH + 1.7 MW of NBI) at t = 6.2s. The experimental values are indicated with black circles. The best results from the gyrokinetic simulations (quasi-linear and non-linear) are indicated by red triangles.*

References

[1] Mandrekas J., Stacey W. M., Nucl. Fusion 35, 843 (1995).

[2] Pacher G. W., et al., Nucl. Fusion 47, 469 (2007).

[3] Manas P., et al., 16th ITPA Transport and Confinement Topical Group Meeting (ITPA T&C Meeting), Ahmedabad, India (2016).

[4] Angioni C., et al., Plasma Phys. Control. Fusion 51, 124017 (2009).

[5] Manas P. et al, Physics of Plasmas 24, 062511 (2017).

[6] Fable E., Angioni C. and Sauter O., Plasma Phys. Control. Fusion 52, 015007 (2010).

[7] Howard N. T., et al., Nucl. Fusion 52, 063002 (2012).

[8] Nordman H., et al., Plasma Phys. Control. Fusion 53, 105005 (2011)

[9] M. R. Wade et al., Journal of Nuclear Materials 290-293, 773 (2001).

[10] R. Dux et al., Plasma Phys. Control. Fusion 45, 1815 (2003).

[11] Coppi B. and Spight C., Phys. Rev. Lett. 41, 551 (1978).

[12] Weiland J., Jarm´en A.B. and Nordman H., Nucl. Fusion 29, 1810 (1989).

[13] Camenen Y., et al., Phys. Plasmas 16, 012503 (2009).

[14] Casson F. J., et al., Phys. Plasmas 17, 102305 (2010).

[15] Yankov V. V. , JETP Lett. 60, 171 (1994).

[16] Garbet X., et al., Phys. Rev. Lett. 91, 035001 (2003).

[17] Grierson B. A., et al., Phys. Plasmas 22, 055901 (2015).

[18] Van Eester D., et al., Plasma Phys. Control. Fusion 51, 044007 (2009).

[19] J. Hedin, et al., Nuclear Fusion 42, 527 (2002).

[20] T. Hellsten, et al., Nuclear Fusion 44, 892 (2004).

[21] C. Giroud et al., Rev. Sci. Instrum. 79, 10F525 (2008).

[22] M. G. von Hellermann et al., Phys. Scr. 2005 19, (2005).

[23] Fonck R. J., Darrow D. S. and Jaehnig K. P., Phys. Rev. A 29, 3288 (1984).

[24] Kappatou A., Ph.D. thesis: 'Investigations of helium transport in ASDEX Upgrade plasmas with charge exchange recombination spectroscopy', Eindhoven University of Technology Library, ISBN: 978-90-386-3704-4, NUR: 926 (2014).

[25] Hinton F. L. and Hazeltine R. D., Rev. Mod. Phys. 48, 239 (1976).

[26] Angioni C., et al., Nucl. Fusion 52, 114003 (2012).

[27] Angioni C. and Peeters A. G., Phys. Rev. Lett. 96, 095003 (2006).

[28] Belli E. A. and Candy J., Plasma Phys. Control. Fusion 50, 095010 (2008).

[29] Belli E. A. and Candy J., Plasma Phys. Control. Fusion 51, 075018 (2009).

[30] Belli E. A. and Candy J., Plasma Phys. Control. Fusion 54, 015015 (2012).

[31] Jenko F., et al., Phys. Plasmas 7, 1904 (2000).

[32] Görler T., et al., J. Comput. Phys. 230, 7053 (2011).

[33] Brizard A. J., Hahm T. S., Rev. Mod. Phys. 79, 421 (2007).

[34] A.G. Peeters, et al., Computer Physics Communications 180, 2650 (2009).

[35] A.G. Peeters, C. Angioni, D. Strintzi, Phys. Rev. Lett. 98, 265003 (2007).

[36] Jenko F., Dannert T. and Angioni C., Plasma Phys. Control. Fusion 47B, 195 (2005).

[37] Casati A., et al., Nucl. Fusion 49, 085012 (2009).

[38] Angioni C., Nucl. Fusion 51, 023006 (2011).

[39] Miller R. L., et al., Phys. Plasmas 5, 973 (1998).

[40] Manas P., et al., Plasma Phys. Control. Fusion 59, 035002 (2017).

Chapter 5

Effects of nitrogen seeding on core ion thermal transport in JET ILW L-mode plasmas

Paper published in Nucl. Fusion: N. Bonanomi et al., Nucl. Fusion 58, 026028 (2018). †

N. Bonanomi[1,2], P. Mantica[2], J. Citrin[3], C. Giroud[4], E. Lerche[5], C. Sozzi[2], D. Taylor[4],
M. Tsalas[3,4], D. Van Eester[5] and JET contributors*

EUROfusion Consortium, JET, Culham Science Centre, Abingdon, OX14 3DB, UK
1) University of Milano-Bicocca, Milano, Italy
2) CNR- Institute of Plasma Physics "P. Caldirola", Milano, Italy
3)DIFFER - Dutch Institute for Fundamental Energy Research, Eindhoven, The Netherlands
4) Culham Centre for Fusion Energy, Abingdon, OX14 3DB, UK
5)LPP-ERM/KMS, TEC partner, Brussels, Belgium
* See the author list of See the author list of "X. Litaudon et al., 2017 Nucl. Fusion 57, 102001"

Abstract

A set of experiments was carried out in JET ILW (Joint European Torus with ITER-Like Wall) L-mode plasmas in order to study the effects of light impurities on core ion thermal transport. N was puffed into some discharges and its profile was measured by active Charge Exchange diagnostics, while ICRH power was deposited on- and off-axis in $(^3He)-D$ minority scheme in order to have a scan of local heat flux at constant total power with and without N injection. Experimentally, the ion temperature profiles are more peaked for similar heat fluxes when N is injected in the plasma. Gyrokinetic simulations using the GENE code indicate that a stabilization of Ion Temperature Gradient driven turbulent transport due to main ion dilution and to changes in T_e/T_i and s/q is responsible of the enhanced peaking. The quasi-linear models TGLF and QuaLiKiz are tested against the experimental and the gyrokinetic results.

---

† https://doi.org/10.1088/1741-4326/aa9e7c

5.1 Introduction

One of the ways to reduce the heat loss deposition on the ITER (International Thermonuclear Experimental Reactor) divertor [1, 2] is to puff light impurities at the plasma edge. Furthermore, intrinsic light impurities, like Be from the first wall, can enter in ITER plasmas. It is generally found that these impurities have peaked profiles [3, 4], so their impact on the core performances may not be negligible. On one hand, a stabilizing effect on turbulence is predicted by theory [5] and observed experimentally , as discussed below. On the other hand, impurities dilute the main ions thus reducing fusion power. Therefore, it is important to understand what their impact is on the main ion heat transport in the core, and validate existing models, in order to evaluate the trade-off between positive and negative effects and achieve optimal conditions for fusion.

In the last years, the effects of light impurity seeding on the plasma heat transport and energy confinement have been studied on different machines such as FTU [7, 6], TEXTOR-94 [8], ASDEX Upgrade [9], JET [8, 10], DIII-D [8], JT-60U [8] and C-mod [11, 12, 13]. In all these studies, that cover plasmas in Ohmic confinement mode, L-mode and H-mode, an increase of the plasma confinement in presence of light impurities has been observed. In most cases, a stabilization of the Ion Temperature Gradient (ITG) modes has been suggested to explain the improvement in the confinement. In some cases, especially in H mode, the stabilizing effect has been suggested to be more important at the plasma edge and on the plasma pedestal, with negligible effect of light impurities on the stabilization of the plasma core micro-instabilities [9]. In other studies, a direct role of light impurity seeding in the stabilization of micro-instabilities in the plasma core has been observed and studied [6, 7, 8, 9, 11, 12, 13]. At JET, a number of studies in H-modes indicate that N seeding increases the plasma energy confinement time and helps to increase the performances with the ITER-Like wall (ILW) at the levels reached with the old Carbon wall [10, 14, 15]. These observations are linked with the stabilization effects of light impurities in the pedestal region, while no detailed studies of the effects of the light impurity on the core plasma region have been done yet in JET. This paper reports on a specific study of the effects of N injection in the core of JET ILW L-mode plasmas, in which for the first time we determine separately the changes induced by the N injection in the ITG threshold (i.e. the critical ion temperature T_i inverse gradient length for ITG on-set) and in the ITG "stiffness" (i.e. the rate of increase of the ion heat flux with the T_i inverse gradient length). We then compare such results with gyro-kinetic (GK) and quasi-linear (QL) models, thus providing a much more stringent validation test.

The paper is organized as follows. In section 5.2 the experimental set-up is described while in section 5.3 the numerical simulation set-up is presented. In section 5.4 the impact of N on the plasma core heat transport is studied. A discussion on the results and the conclusions are presented in section 5.5.

5.2 Experimental set-up

The discharges studied in this paper were L-mode plasmas made in the JET tokamak (major radius $R_0 = 2.96\,m$, minor radius $a = 1\,m$) with ILW. All plasmas are D plasmas with vacuum toroidal magnetic field $B_T \approx 3.3\,T$, plasma current $I_p \approx 2\,MA$, electron density $n_2 \approx 3.5{\cdot}10^{19}\,m^{-3}$ and safety factor at the flux surface that encloses the 95% of the poloidal flux $q_{95} \approx 5$. The heating power consists of 3-4 MW of ICRH (Ion Cyclotron

Resonance Heating) using a ^3He minority concentration $n_{^3He}/n_e \approx 6\%$, which ensures a dominant ion heating [16], and of 1.7-3 MW of NBI (Neutral Beam Injection), mainly to provide charge exchange measurements of T_i, rotation ω_T and impurity density n_Z profiles. The ICRH power was deposited both on-axis ($R \approx 3.0\ m$) and off-axis ($R \approx 3.45\ m$) in order to obtain low and high values of ion heat flux q_i for the study of q_i versus $R/L_{Ti} = -R_0|\nabla T_i|/T_i$ and its power deposition was evaluated with the PION code [17]. The ICRH power deposition to ions and the T_i profiles for discharges n. 86749 (on-axis) and n. 86756 (off-axis) are shown in figure 5.1. The NBI power and its power deposition radial profile are similar in all the discharges. The NBI heating power on electrons and ions is calculated with the PENCIL code [18].

The measurement of the electron temperature T_e is provided by the ECE (Electron Cyclotron Emission) diagnostic with an error of about 5%, while T_i and ω_T are measured by the active Charge-Exchange (CX) diagnostic with an error for T_i of about 5-10%, depending on the radial position, and for ω_T of about 10% . The error on T_e/T_i is about 9–12%. The electron density n_e is measured by high-resolution Thomson scattering (HRTS) with an uncertainty of about 15%. Local values of $R/L_{Ti}, R/L_{Te}$ and R/L_n were obtained by local linear fits of $ln(T_i), ln(T_e)$ and $ln(n_e)$ radial profiles averaged over a time interval $\Delta t \approx 1\ s$. The fits are done using $r = (R - R_{in})/2$, R and R_{in} being the outer and inner radii of the flux surface on the magnetic axis plane, and averaging other multiple fits using a variable number of data points around the chosen radius (3-9 points). We drop the suffix 0 when indicating these quantities for convenience. The uncertainties on these parameters are then estimated by repeating the same procedure with different space intervals and evaluating the deviation in the set of values so obtained. Errors are typically 10-15% for $R/L_{Te/i}$ and 15-20% for R/L_n. The radial profile of the safety factor q as well as the equilibrium plasma geometry are reconstructed by the EFIT equilibrium code with the MSE (Motional Stark Effect) or the Faraday rotation constraints. Typical errors on the safety factor are about 20%.

The collisional exchange power density between ions and electron is calculated analytically as $p_{ei} = 3n_e m_e/M_i \cdot (T_e - T_i)/\tau_e$, where τ_e is the electron collision time characterizing electron collisions with ions [19]. The radiated power density p_{rad} has been taken into account but is negligible inside $r/a \sim 0.8$. The powers $P_{ICRH}, P_{NBI}, P_{ei}, P_{RAD}$ deposited within a flux surface are obtained integrating the power densities on the plasma volume and the ion heat fluxes are calculated in gyro-Bohm (GB) units as

$$q_{i,gB} = [(P_{ICRH,i} + P_{NBI,i} + P_{ei})/\Sigma] \cdot R^2/(n_e T_e \rho_s^2 c_s) \tag{5.1}$$

where Σ is the flux surface, $c_s = \sqrt{T_e/M_i}$, $\rho_s = c_s M_i/eB_T$ and M_i the main ion mass. Typical error on the heat fluxes is about 20% of the total flux. Turbulent flux threshold and stiffness at a chosen radial location are determined experimentally by quadratic fits on the diagrams of the GB normalized heat flux as a function of R/L_T according to the heat flux parametrization proposed in [20, 21]

$$q_i = q_i^{res} + \chi_s \frac{n_e T_e c_s \rho_s^2}{R^2} \frac{R}{L_{Ti}} \left(\frac{R}{L_{Ti}} - \frac{R}{L_{Ti}}^{crit} \right) \cdot \theta \left(\frac{R}{L_{Ti}} - \frac{R}{L_{Ti}}^{crit} \right) \tag{5.2}$$

where q_i^{res} is the residual flux not carried by the R/L_{Ti} driven instability, $(R/L_{Ti})^{crit}$ is the critical value of R/L_{Ti} above which the turbulent flux is driven by R/L_{Ti}, χ_s is the stiffness coefficient and $\theta(\bullet)$ is the Heaviside function. From the curve of $q_{i,gB}$ versus R/L_{Ti}, we identify $(R/L_{Ti})^{crit}$ as the intercept to zero flux (considering the residual flux to be negligible), whilst χ_s can be inferred from the slope of the curve. Equation 5.2 is a semi-empirical model called critical gradient model (CGM) originally proposed for the study of the electron heat transport. It assumes the existence of a critical temperature gradient length $L_T^{-1} = |\nabla T| / T$ for the turbulent transport and that the main drive of the transport over this critical value is L_T^{-1}. In this work we use the same formula for the ion heat flux, considering ITG modes, driven by L_{Ti}^{-1} over a critical threshold, the main source for the ion turbulent transport. This assumption is confirmed by the linear and non-linear simulations presented in section 4.4 of this work.

In order to study the effect of the presence of light impurities on the core heat transport, N was puffed in discharges n. 86749-86756. The comparison between $(R/L_{Ti})^{crit}$ and χ_s with and without nitrogen is used to observe what kind of impact light impurities have on the core micro-instabilities. The density profiles of $^3He, Be, N$ have been measured by CX, in order to obtain the concentrations and the peaking of the density of the light impurities in the plasma. The data analysis and the simulations are carried out at $\rho_{tor} = \sqrt{(\Phi/\pi B_T)/(\Phi/\pi B_T)_{max}} = 0.33, 0.5$, where Φ is the toroidal magnetic flux. The choice of these two radial positions is due to the changes in the ion temperature peaking observed experimentally and shown in section 4.3 and due to the different peaking of the N density at these radii.

5.3 Numerical simulation set-up

The experimental ion heat fluxes are compared to gyro-kinetic simulations that calculate the turbulent part of the fluxes. Both linear and non-linear gyro-kinetic simulations have been carried out using the GENE (Gyrokinetic Electromagnetic Numerical Experiment) code [22, 23]. GENE solves the gyro-kinetic Vlasov equations coupled with the Maxwell equations within a δf approximation [24] and using the field aligned coordinates $\{x, y, z\}$, where z is the coordinate along the background magnetic field line, x is the radial coordinate and y is the binormal coordinate.

In all the simulations the flux-tube approximation and Miller geometry [25] were used, and collisions, external flow shear and finite-β effects were included. Main ions, electrons and, when indicated, light impurity ions were retained as kinetic species. Typical grid parameters in the non-linear simulations were as follows: perpendicular box sizes $[L_x, L_y] \approx [190, 125]\rho_s$, phase-space grid discretization $[n_x, n_y, n_z, n_{v\parallel}, n_\mu] = [128-256, 24-64, 32, 32-64, 12]$, with $0.25 - 0.5 \leq k_y\rho_s \leq 1.6$, depending on the plasma parameters and on the number of kinetic species considered. The input parameters for the simulations are taken from discharge n. 86740 (without N) averaging over $9.5 < t < 10.5 s$ and from discharge n. 86749 (with N) averaging over $8 < t < 10\ s$. The choice of these time intervals ensured convergence of the q and s profiles to a stable situation and the best CX measurements, as NBI notches (used for background signal subtraction in the CX analysis) are present in these intervals. The main plasma parameters for these discharges are reported in Table 1. In the gyro-kinetic nonlinear simulations just one kinetic light impurity species (N) has been used and $Z_{eff} = 1.0$ has been assumed in simulations of discharge n. 86740 without N, while $Z_{eff} = 1.5$ has been used in the simulations of shot n. 86749 with N. This choice has been made to save computational time and considering that the changes in the plasma are mainly due to N puffing, the other light impurities being present in all the discharges at the same concentrations ($Be \sim 1\%, ^3He \sim 6\%$).

The standalone versions of the quasi-linear models TGLF [26, 27] and QuaLiKiz [28, 29, 30] have also been tested against the experimental results and the non-linear gyrokinetic simulations. The TGLF simulations have been carried out in Miller geometry and the well established 'sat0' saturation rule has been adopted. QuaLiKiz instead features only the $s-\alpha$ geometry. While Miller geometry takes into account the real shape of the flux surfaces though parameters such as triangularity and elongation, the $s-\alpha$ geometry considers simple circular flux surfaces and the Shafranov shift. This can have an impact on the predicted turbulent state, as parameters such as elongation have a stabilizing effect on the micro-instabilities. The same input parameters and settings (finite-β, external flow shear, $k_y\rho_s$ range and n_y, number of kinetic species) used in the GENE gyro-kinetic simulations have been used in the quasi-linear simulations.

#	ρ_{tor}	s	q	R/L_{ne}	R/L_{Te}	R/L_{Ti}	Z_{eff}	T_e/T_i	ν_{eff}	n_N	R/L_N
86740	0.33	0.4	1.5	2.8	7.9	4.2	1.4	0.9	0.08	0%	-
	0.5	0.8	1.9	2.8	7.8	5	1.4	0.86	0.17	0%	-
86749	0.33	0.35	1.35	2.8	8	4.5	1.9	0.9	0.1	1.2%	2.0
	0.5	1.1	1.6	2.9	8.0	6	1.9	0.74	0.2	1.2%	0.5

Table 5.1: *Main plasma parameters of the studied discharges at* $\rho_{tor} = 0.33, 0.5$. *Here* $\nu_{eff} = 0.1{\cdot}Z_{eff}n_e/T_e^2$.

5.4 Light impurity effects on thermal transport

5.4.1 Predict-first simulations

Before showing the experimental results and the related numerical simulations, we present a series of linear and non-linear gyro-kinetic simulations made before the experiment, in a predict-first approach, in order to evaluate the magnitude of the effects to be expected in experimental conditions similar to ours. These simulations have been carried out with the GENE code in flux-tube approximation and using input parameters from the JET discharge n. 73221 at $\rho_{tor} = 0.33$. This discharge had similar settings and plasma parameters as the discharges studied in this work (L-mode, same B_t, I_p, n_e, q_{95}, 1.6 MW of NBI and 3 MW of ICRH on ions using 6% of ^3He), but was done with the old Carbon-wall. In these simulations, kinetic electrons, kinetic deuterium and a third kinetic ion species (N, Ne or Ar) have been used. The geometry parameters have been taken from a CRONOS [31] simulation of the discharge as described in [32]. The results from the simulations are shown in figures 5.2 and 5.3. As can be seen, linear simulations predict a stabilization of ITG modes in presence of light impurities. The level of the stabilization depends, for the same value of Z_{eff}, on the main ion dilution (in this case there is more dilution using N) and on the value of $R/L_{n,Z}$ of the light impurity. An increase in the main ion dilution (and of Z_{eff}) results in an increase of the stabilization effects. An increase in the value of the normalized impurity density gradient results in a stronger stabilizing effect: with $R/L_{n,Z} \approx 0$ there is a reduction of the ion temperature stiffness but no substantial increase of the ITG threshold, while for higher values of $R/L_{n,Z}$ an important increase of the ITG critical threshold is visible. Non-linear simulations confirm what found in the linear simulations. Depending on the level of the main ion dilution and on the peaking of the light impurity species, a stabilization of the ITG turbulent ion heat fluxes is observed.

The simulations predict that, in order to observe a strong effect of the light impurity on the ion thermal transport, Z_{eff} and the main ion dilution are key factors. At the same level of Z_{eff}, the bigger effect between N, Ne and Ar is due to N due to higher main ion dilution. For these reasons, in the experiment carried out at JET and studied in this work, N puffing has been chosen. Furthermore, from the non-linear simulations, a value or $R/L_{n,N} \approx 1.4$ is expected, with the considered plasma parameters, in stationary conditions (zero N flux). With this value of $R/L_{n,N}$, a change in Z_{eff} of at least 1 is expected to be necessary in order to observe a visible effect on the ion thermal transport outside error bars.

5.4.2 Comparison between C-Wall and ITER-Like Wall L-mode plasmas

The validity of the predict-first study of sect. 4.1, based on the parameters of a reference C-wall discharge without N, for planning ILW discharges to study the N effect, relies on the expectation that core plasma transport and local plasma parameters do not depend on the first wall material for L-mode plasmas. This has been indeed verified when L-mode plasmas in ILW with similar experimental settings as in C-wall have become available. When the same settings for B, I_p, q_{95}, n_{e0} , shape, and heating schemes (low NBI power and ICRH in $D -^3 He$ minority scheme) are used, no substantial differences are observed between C-Wall and ILW in the core ion heat turbulent transport. In figure 5.4a, the T_i profiles from discharges n. 78829 (C-Wall with 3.7 MW of NBI and 2.5 MW of on-axis ICRH heating) and n. 86740 (ILW with 3 MW of NBI and 3 MW of on-axis ICRH heating) are shown. In figure 5.4b also a comparison between $q_{i,gB_s}(R/L_{Ti})$ in C-Wall and ILW for discharges studied in the past [see for example [33, 34]], the discharges with no N studied in this paper and other two ILW discharges (n. 90668, 90671) is shown. No substantial differences in the experimental profiles, in the experimental threshold of the ion heat turbulent transport and in the ion stiffness have been observed. In fact, the significant degradation of ILW confinement with respect to C-wall reported e.g. in [35] was found only in H-modes and mainly due to a pedestal reduction, with the core transport substantially unchanged [36].

5.4.3 Experimental observations

In this section, the main differences between discharges with and without N in JET ILW L-modes are presented. The comparison has been made between shot n. 86740, with no N, and shot n. 86749, with $n_N/n_e \approx 1.2\%$, averaging over the same time intervals used for the gyro-kinetic simulations. The measured concentration of N was constant over the chosen time period. For the heat flux scans, also discharges n. 86746, with off-axis ICRH heating and no N, and n. 86756, with off-axis ICRH heating and $n_N/n_e \approx 1.2\%$, have been used. This was close to the maximum level of N that could be puffed into the plasma without causing a disruption. The radial profiles of the temperatures and of the electron density of the two discharges as well as the measured density profile of N (magnified by a factor of 75 to be more visible in the plot) in discharge 86749 are shown in figure 5.5. The level of N reached in the plasma is not predicted by gyro-kinetic simulations to be high enough to have the desired change of at least 1 in Z_{eff} and the density peaking of N changes along the radius, the profile being peaked inside $\rho_{tor} \sim 0.4$ and outside $\rho_{tor} \sim 0.7$ and flat for $0.4 \lesssim \rho_{tor} \lesssim 0.7$ (see also [4]). Considering the gyro-kinetic simulations, no substantial differences outside error bars are then expected. Nevertheless the profiles of T_i and T_e are more peaked in the discharge with N puff and a stabilization of the ion heat turbulent transport can be observed in discharges with N puff with respect to discharges with no N, especially at $\rho_{tor} = 0.5$. This can be seen from the shift of the experimental ion temperature gradient, well outside error bars at $\rho_{tor} = 0.5$, in the ion heat flux scans obtained using on and off-axis ICRH heating at $\rho_{tor} = 0.33, 0.5$ and shown in figure 5.6. No visible effect on the ion stiffness is observed outside error bars.

A change in Z_{eff}, from $Z_{eff} \approx 1.4$ in the discharges without nitrogen to $Z_{eff} \approx 1.9$ in the discharges with nitrogen puff, has been observed. Also, as the electron density has been kept the same and the other light impurities have the same measured concentrations ($\sim 1\%$ of Be and $\sim 6\%$ of ^3He, they have also the same density profiles between the discharges), there is a major dilution of the main ion (D) species in the discharges with nitrogen (from $n_D/n_e \sim 84\%$ to $n_D/n_e \sim 75\%$). As a consequence of the change of Z_{eff}, also the radial profile of the plasma resistivity η_p changes. This leads to a change in the radial profile of the plasma current density and, consequently, to a change in the safety factor q and in the magnetic shear s. The comparisons of the radial profiles of the plasma resistivity and of s/q between shots with and without nitrogen are shown in figure 5.7. Another difference between discharges with and without N puff is the ratio T_e/T_i, as can be seen in figure 5.5. The electron density, the electron density peaking and the edge temperatures do not show substantial changes that could explain the change in the temperature profiles.

5.4.4 Numerical study

In order to investigate the causes of the described changes in the plasma due to the presence of nitrogen, linear and non-linear gyro-kinetic simulations have been carried out using the code GENE as described in section 5.3. At $\rho_{tor} = 0.33$ the radial density profile of N is peaked ($R/L_{n_N} = 2$ has been used in the simulations) and the differences in T_e/T_i and s/q between cases without and with N are small. At $\rho_{tor} = 0.5$ the N radial density profile is flat ($R/L_{n_N} = 0.5$ in the simulations) and the differences in T_e/T_i and s/q are more substantial. The observed changes in $Z_{eff}, n_D, s/q$ and T_e/T_i are all predicted to play a role in the stabilization of the ion heat flux [5, 37, 38].

In figure 5.8 , a study on the effects of the various impurities in the plasma using linear gyro-kinetic simulations and data from discharge n. 86749 at $\rho_{tor} = 0.5$ as input, is shown. The effects of the different impurities in the plasma, using the experimental concentrations and density peaking, on the linear growth rate of the dominant instability is shown on both ion and electron scale modes. From the simulations it is clear that the strongest effect is due to nitrogen and that its effect is stronger with higher impurity density gradients, as expected. Furthermore, a linear scan in R/L_{Ti}, fixing $k_y\rho_s = 0.33$ in the simulation, is shown. These simulations confirm what found in the predict-first study made using the C-Wall discharge.

A study with linear gyro-kinetic simulations on the effect of the changes in the plasma parameters described in section 4.3 has been carried out at $\rho_{tor} = 0.5$ and the results are shown in figure *5.9.* In these simulations the parameters from discharge n. 86740 have been used first (black lines and circles in figure 5.9). In all the simulations, the main instabilities up to $k_y\rho_s \approx 0.7$ are the ITG modes (the real part of the frequency has the same sign of the ion diamagnetic drift), while, at higher values of $k_y\rho_s$, TEM/ETG modes are the dominant ones. Changing the values of s/q and T_e/T_i to the values of discharge n. 86749 leads to a reduction of the ITG growth rate of $\sim 25\%$ at $k_y\rho_s = 0.4$. Adding also 1.2% of N, using $R/L_N = 0.5$, leads to a further reduction of $\sim 12\%$. So, linearly, the stronger stabilizing effect on ITGs are predicted to be related to the changes in T_e/T_i and in s/q in these discharges (figure 5.9a). This stabilization leads to a change in the ITG R/L_{Ti} threshold and is expected to be the main stabilizing mechanism of the ion heat flux. This can also be seen from the nonlinear ion heat flux spectra in $k_y\rho_s$ shown in figure 5.9c. The main contribution to the ion heat flux is coming from $0.2 \leq k_y\rho_s \leq 0.4$, where the ITG modes are dominating. Furthermore, stabilizing effects due to higher Z_{eff} and s on TEM and due to higher $\tau = Z_{eff} \cdot T_e/T_i$ and s/q on ETG modes have been found and can contribute to the reduction of the ion heat flux, but their effect is less important with respect to the stabilization of ITG modes in our case.

The ion heat fluxes from the nonlinear simulations are shown in figure 5.6 and compared with the experimental fluxes. The non-linear simulations were able to reproduce quite well both the electron and the ion heat flux experimental levels, confirming that the changes in the plasma parameters, obtained when N has been puffed into the plasma, lead to an overall stabilizing effect of the turbulent heat transport. At $\rho_{tor} = 0.33$, the changes in s/q and T_e/T_i being small, only the effect of the main ion dilution has a significant role but, as the amount of nitrogen injected in the plasma and the changes induced in Z_{eff} were rather low (higher values causing disruptions), the predicted stabilization is not enough to be visible outside the experimental error bars. At $\rho_{tor} = 0.5$, an increase of the threshold of the turbulent transport as well as a little reduction of the ion stiffness are predicted by the simulations and follow quite well the experimental points. The increase of the threshold in this case is mainly due to the changes of T_e/T_i and s/q, while the reduction of the stiffness level is due to the main ion dilution effect due to the presence of N with rather flat local profile. This can be seen comparing the black full circles and the blue full triangles in figure 5.6b. The blue triangles indicate simulations of discharge n. 86740 where 2% of N with $R/L_N = 0.5$ has been added artificially in order to study the pure effect of N. No big changes in the threshold have been observed in this case, but a clear reduction of the ion stiffness.

As explained in section 5.3, the stand-alone versions of the quasi-linear codes TGLF and QuaLiKiz have been tested against non-linear gyro-kinetic simulations and experiments. The results are shown in figure 5.10 and in figure 5.11. TGLF tends to underestimate the ion stiffness at both radii, while QuaLiKiz reproduces it quite well, although the predicted critical threshold is a little shifted between GENE and QuaLiKiz. Both codes show an overall effect of the changes in $Z_{eff}, n_D, s/q$ and T_e/T_i comparable in magnitude to the experimental observations and with the gyro-kinetic results. When the pure effect of N is considered (using $N = 2\%$ and $R/L_{n,N} = 0.5$), as can be seen in figure 5.10c while GENE and TGLF predict an effect primarily on the ion stiffness, QuaLiKiz predicts an upshift of the threshold but no effects on the stiffness. As QuaLiKiz has been implemented in $s - \alpha$ geometry, we made a comparison also between QuaLiKiz, TGLF and GENE using shifted circular geometry. This comparison is shown figure 5.11b. When circular geometry is used, an important increase in ion stiffness in observed in GENE and TGLF (TGLF still underestimating ion stiffness with respect to GENE as in Miller geometry). Also QuaLiKiz is now significantly below the GENE $s - \alpha$ results.

5.5 Discussion and conclusions

A detailed study of the effect of N seeding on the core ion thermal transport of JET L-mode ILW plasmas has been carried out. A predict-first approach based on gyro-kinetic simulations with parameters from reference shots in C-wall was very useful to guide the experimental choice of the seeding gas and of the level of injection to ensure detectability of the effects. From these simulations a change in Z_{eff} of at least 1 was predicted to impact the experimental ion heat flux enough to be able to observe this impact outside experimental uncertainties. High values of the light impurity density gradient are also expected to increase the stabilizing effects. When executing the experiment, a concentration lower than desired was reached due to high disruptivity. In addition, the N profile at mid radius turned out to be flatter than theoretically predicted (as discussed in [4]). These two unforeseen circumstances led the experiment into a situation where the predicted impurity effect on the ion thermal transport would be inside the experimental uncertainties. Still, a remarkable increase of the ion temperature peaking was observed, well outside uncertainties. Gyro-kinetic simulations using the actual parameters of the discharges with and without N show a stabilization of the ion heat transport when N is puffed into the plasma. This is related to changes in the plasma parameters induced by the N puff, such as main ion dilution, s/q and T_e/T_i, with the changes in s/q and T_e/T_i being the dominant mechanisms leading to the observed ITG critical threshold upshift. This explains why the data show mainly a threshold upshift, rather than a decrease in stiffness as would be expected for dilution in presence of a rather flat impurity profile. The effect of dilution itself, although alone not enough to give an effect on T_i outside uncertainties, is anyway inducing a change of T_i/T_e that produces further ITG stabilization, which together with the q profile change eventually leads to a well observable T_i peaking.

How much the effects that were observed in these experiments will extrapolate to high power scenarios in JET or ITER is difficult to assess. It is however clear that any prediction of a scenario with impurities will have to account in an integrated approach for both the direct effects of main ion dilution and of change in Z_{eff} and the secondary effects due to changes in T_i/T_e or q profile, which can play an important role, as in the experiments described here. It is therefore important to test and improve models in order to have reliable tools for such integrated modelling. This was the main aim of the work presented in this paper. Gyro-kinetic simulations were found to reproduce the experimental observations pretty well, considering experimental uncertainties. We then tested TGLF (sat0) and QuaLiKiz against our experimental observations and also against nonlinear gyro-kinetic simulations in a broader range of N concentrations. TGLF tends to generally underestimate the ion stiffness, but concerning the impurity effects it is able to reproduce quantitatively the effects on both threshold and stiffness observed in gyro-kinetic runs. QuaLiKiz reproduces much better the ion stiffness, but shows critical thresholds slightly shifted respect to GENE. Also, the predicted effects of light impurities on ITGs from QuaLiKiz is mainly a shift of the critical R/L_{Ti} threshold, quantitatively of the right magnitude, but with no effect on stiffness at variance with GENE and TGLF. The effect of geometry has also been found important. When the same geometry $(s-\alpha)$ is used in GENE nonlinear simulations as in QuaLiKiz, the GENE heat flux increases significantly and the shift between their predicted thresholds in R/L_{Ti} is higher. These results call for an improvement of both QL models, particularly on the match of the ion stiffness and threshold already in the case with no N, whilst the effect of N overall is adequately modelled.

Concerning the question if overall the N seeding leads to poorer or better fusion performance, this depends on whether the enhancement of the ion temperature and so of the fusion reaction rate wins over the dilution of the fuel ion density. This depends strongly on the plasma conditions. A factor $\alpha < 1$ that multiplies the D and T densities (supposing for simplicity that $n_D = n_T$ and that the dilution is constant on the plasma profile) can reduce the power from the reactions by $(1-\alpha^2)\%$ (in our case ~16%), but an increase in the ion temperature by ~ 1 keV, as we observe in these experiments, can raise the power more strongly (in our case ~300%). The difference is that the loss due to the main ion dilution is always the same independently of the plasma density, while the gain due to an increase of the ion temperature strongly depends on the plasma temperature. Between 10 and 14 keV, the increase in the fusion reaction rate is still of ~20%/keV, but for higher temperatures the increase drops quickly. Other considerations on the kind of impurity puffed into the plasma (most probably *Ar* for ITER) and on the peaking of the impurity density profile should be taken into account, since linear and non-linear gyrokinetic simulations predict that the ITGs stabilization is stronger with increasing density peaking of the light impurity. In particular, when the impurity density gradient is close to, or lower than, zero, the predicted effect is mainly a reduction of the ion temperature stiffness, while, when the gradient of the light impurity density increases, the dominant effect is an increase of the ITGs critical threshold in R/L_{Ti}.

Acknowledgement

The authors would like to thank Emiliano Fable and Gary Staebler for precious suggestions and discussions on the use of the TGLF model. The authors are grateful to D. R. Mikkelsen for assistance. This research used resources of the National Energy Research Scientific Computing Center, a DOE Office of Science User Facility supported by the Office of Science of the U.S. Department of Energy under Contract No.DE--AC02--05CH11231. A part of this work was carried out using the HELIOS supercomputer system at Computational Simulation Centre of International Fusion Energy Research Centre (IFERC--CSC), Aomori, Japan, under the Broader Approach collaboration between Euratom and Japan, implemented by Fusion for Energy and JAEA. We acknowledge the CINECA award under the ISCRA initiative, for the availability of high performance computing resources and support. This work has been carried out within the framework of the EUROfusion Consortium and has received funding from the Euratom research and training programme 2014–2018 under grant agreement No 633053. The views and opinions expressed herein do not necessarily reflect those of the European Commission.

Figures

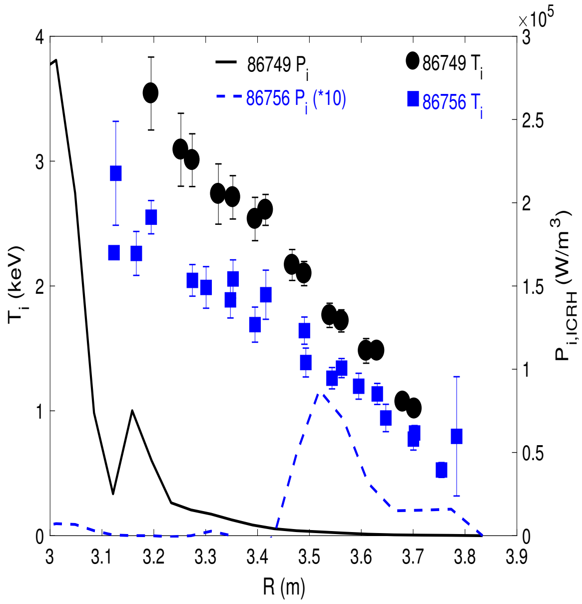

Figure 5.1: *ICRH power deposition and ion temperature of discharge n. 86749 (on-axis ICRH) and n. 86756 (off-axis ICRH).*

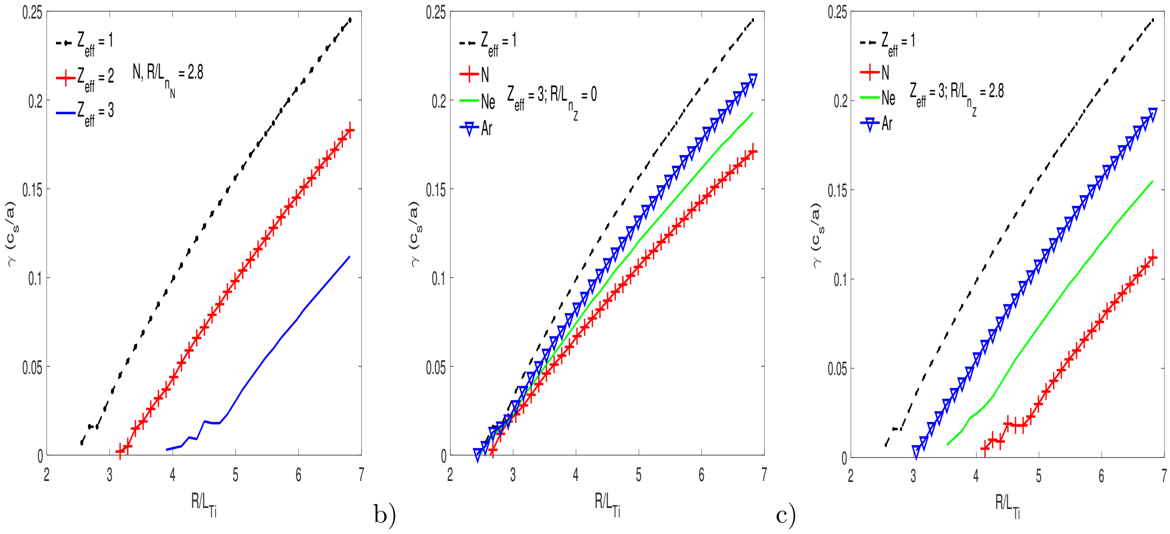

a) b) c)

Figure 5.2: *Normalized linear growth rate γ of the main micro-instability in the simulation as a function of R/L_{Ti} from linear gyro-kinetic simulations at $\rho_{tor} = 0.5$. Effect of N at different concentrations using $R/L_{n,Z} = 2.8$ (a), effects of N, Ne and Ar at the same level of $Z_{eff} = 3$ and using $R/L_{n,Z} = 0$ (b) and effects of N, Ne and Ar at the same level of $Z_{eff} = 3$ and using $R/L_{n,Z} = 3$ (c). Black dotted lines indicate the case with no impurities ($Z_{eff} = 1$).*

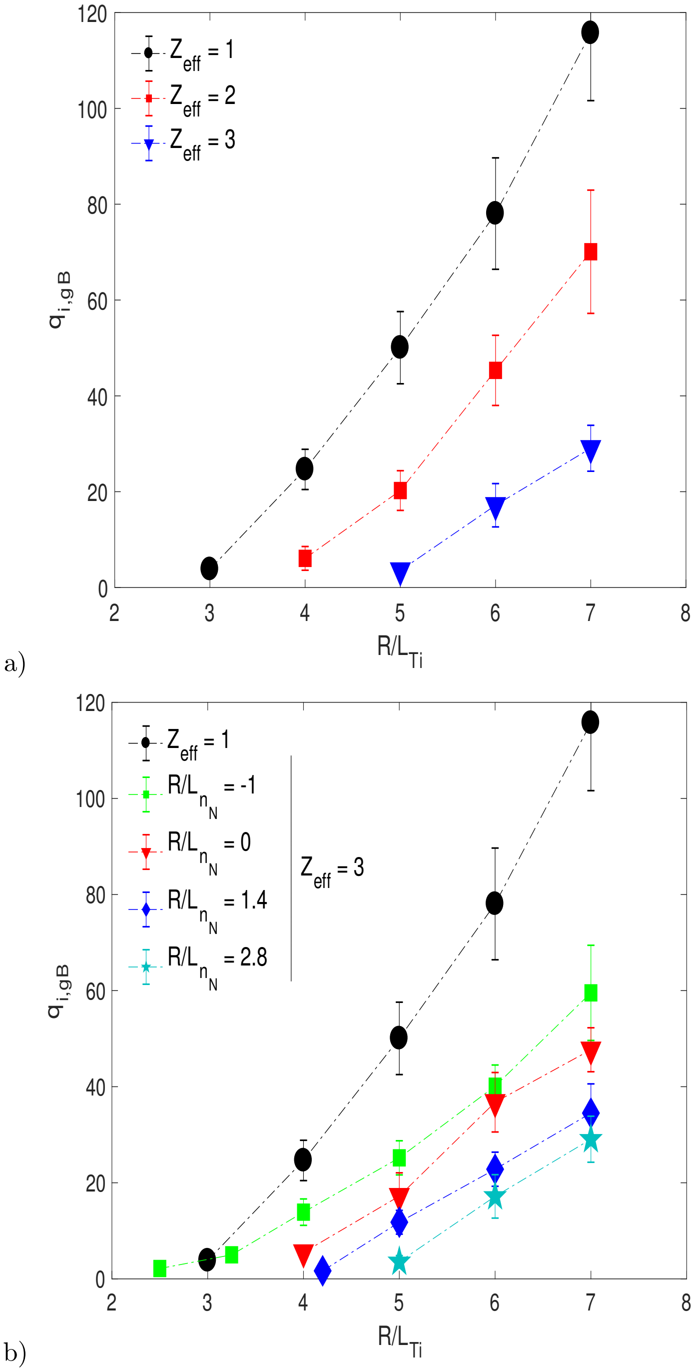

Figure 5.3: *Normalized ion heat flux $q_{i,gB}$ from non-linear gyro-kinetic simulation as a function of R/L_{Ti}. Effects of N at different levels of Z_{eff} and using $R/L_{n,N} = 2.8$ (a) and effects of N at the same level of $Z_{eff} = 3$ but using different values of $R/L_{n,N}$ (b). Black circles indicate the case with no impurities ($Z_{eff} = 1$).*

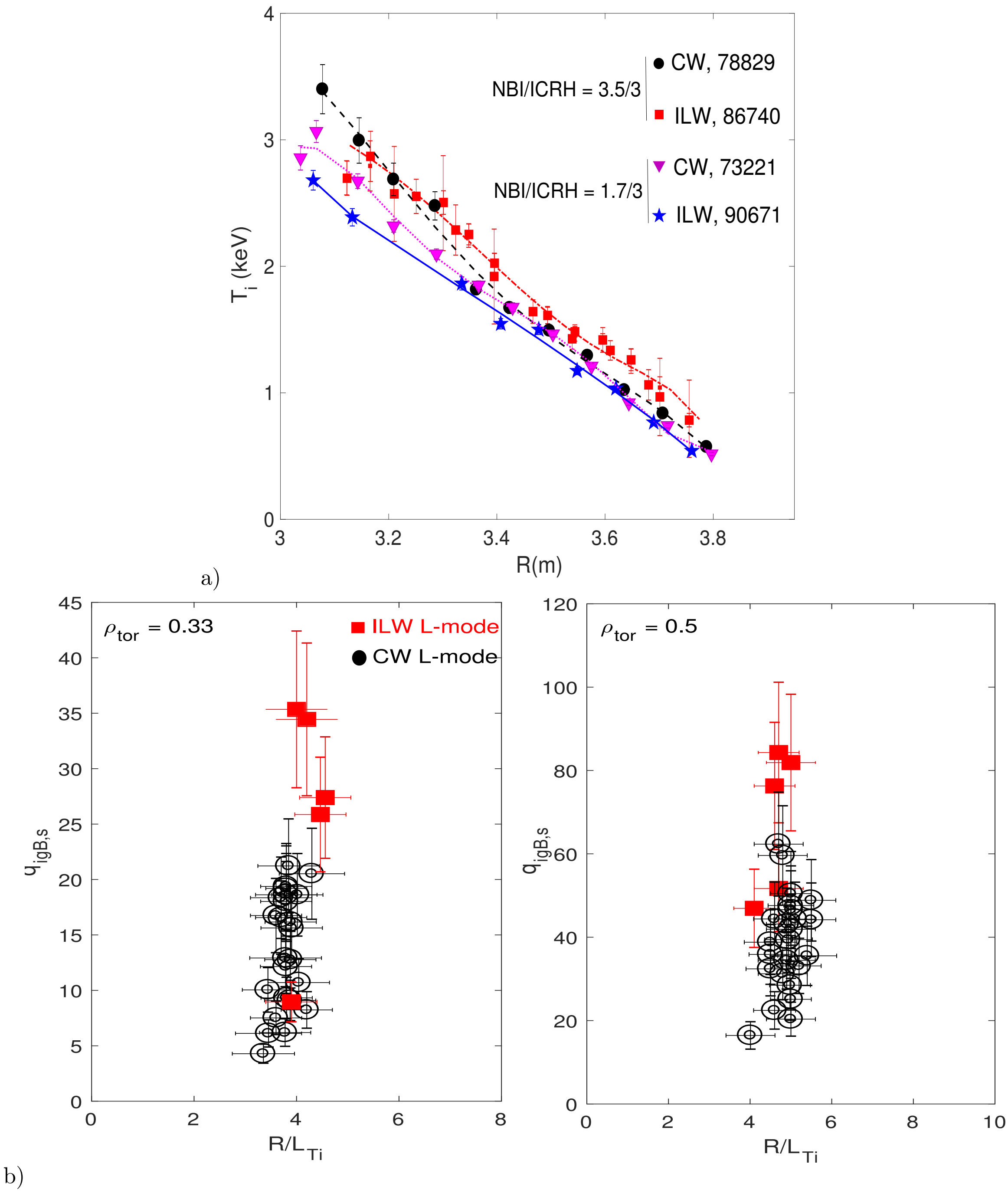

Figure 5.4: *a)Comparison of ion temperature profiles obtained in JET CW and ILW using similar experimental settings (n_e,I_p, q, B_t) and heating scheme. b)Comparison of $q_{i,gB}(R/L_{Ti})$ in JET CW and ILW plasmas.*

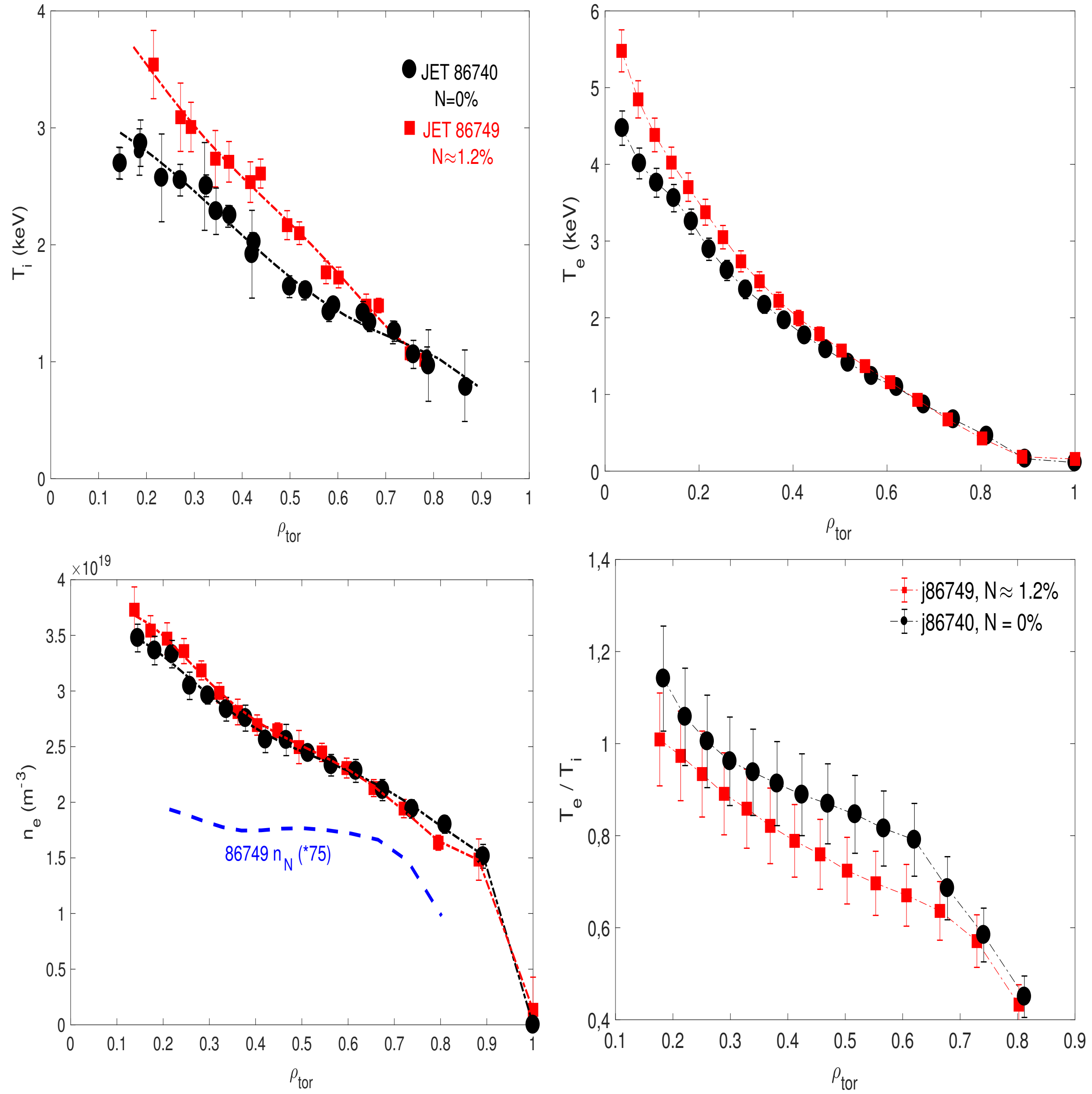

Figure 5.5: *Radial profiles of the ion temperature T_i, electron temperature T_e, electron density n_e and T_e/T_i of JET discharges n. 86740 at t = 10 s (black circles) and n. 86749 at t = 9 s (red squares). Discharge n. 86740 had no N, while discharge n. 86749 had a concentration of nitrogen $n_N/n_N \approx 1.2\%$.*

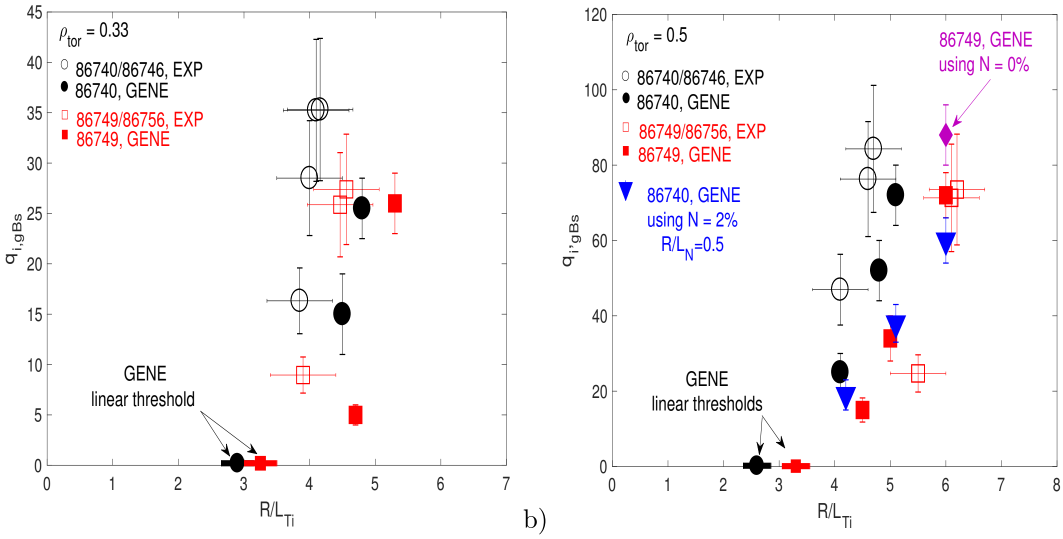

a) b)

Figure 5.6: *$q_{i,gBs}(R/L_{Ti})$ at $\rho_{tor} = 0.33$ (a) and at $\rho_{tor} = 0.5$ (b). The empty black circles represent the experimental results using $n_N/n_e = 0\%$ from discharges n. 86740 (on-axis ICRH) and n. 86746 (off-axis ICRH), while the full black circles represent the results from nonlinear gyro-kinetic simulations. The empty red squares represent the experimental results using $n_N/n_e \approx 1.2\%$ from discharges n. 86749 (on-axis ICRH) and n. 86756 (off-axis ICRH), while the full red squares represent the results from nonlinear gyro-kinetic simulations. In figure (b), the blue triangles in figure 8b represent gyro-kinetic simulations of shot n. 86740 adding $N = 2\%$ and using $R/L_N = 0.5$, while the purple diamond represent a gyro-kinetic simulation of shot n. 86749 but using $N = 0\%$. The gyrokinetic simulations results are discussed in section 4.4.*

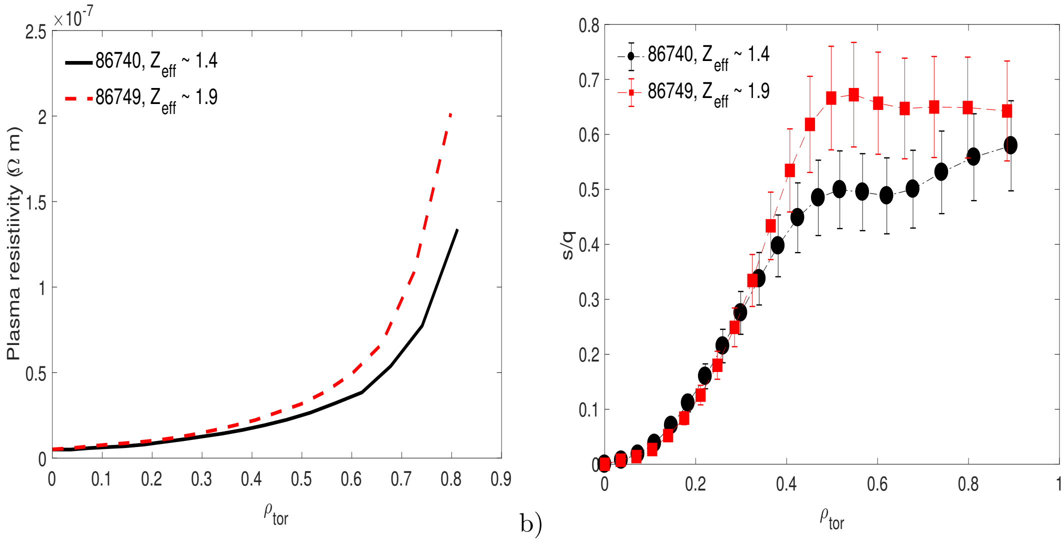

a) b)

Figure 5.7: *Radial profiles of the plasma resistivity (a) and s/q (b) of the JET discharges n. 86740 at $t = 10$ s (black circles) and n. 86749 at $t = 9$ s (red squares). Discharge n. 86740 had $Z_{eff} \approx 1.4$, while discharge n. 86749 had $Z_{eff} \approx 1.9$.*

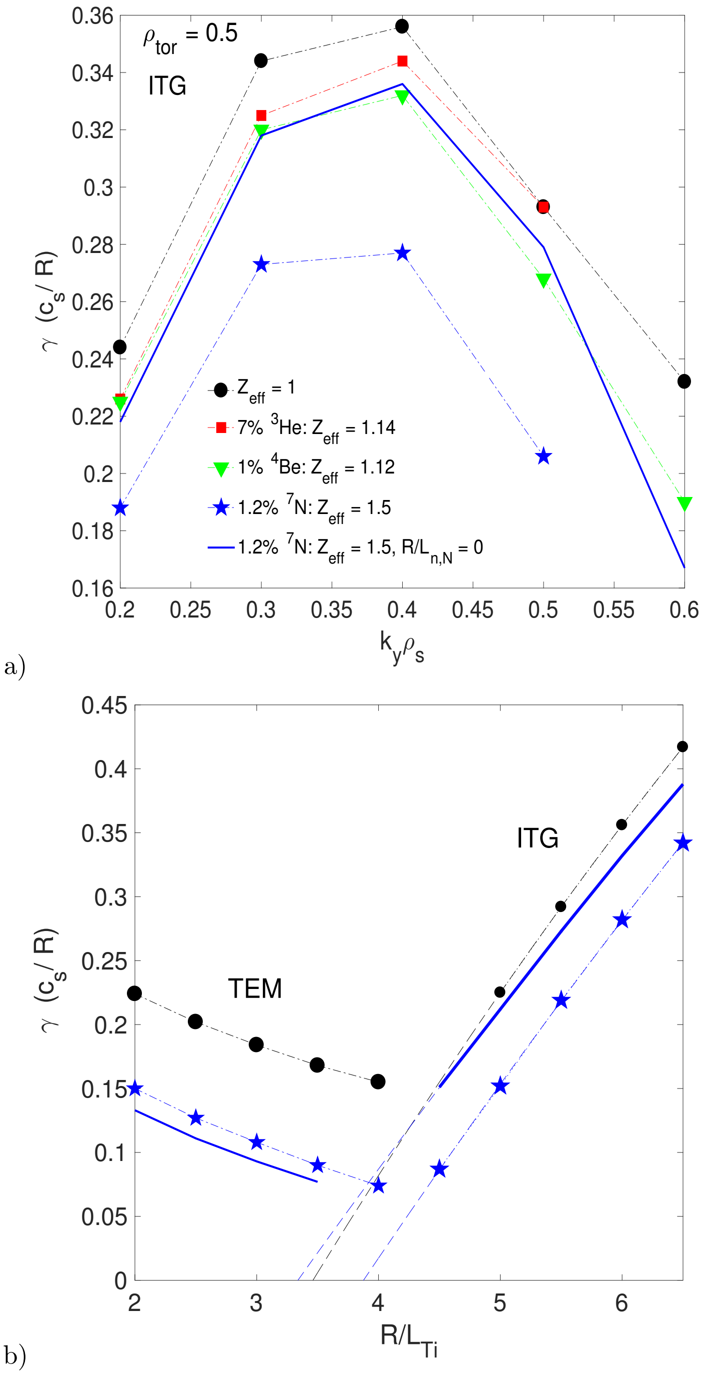

Figure 5.8: *Normalized linear growth rate γ of the main micro-instability from linear gyrokinetic simulations at $\rho_{tor} = 0.5$. a) γ as a function of $k_y\rho_s$: effects on the linear growth rate of ITG of N, ^3He and Be at experimental level using $R/L_{n,Z} = 2.7$. The blue continuos line indicates the case with $N, R/L_{nZ} = 0$. b) γ as a function of R/L_{Ti} ($k_y\rho_s = 0.33$): effects on the linear growth rate of N using $R/L_{n,Z} = 2.7$ (blue pentagrams) and $R/L_{nZ} = 0$ (continuos blue line).*

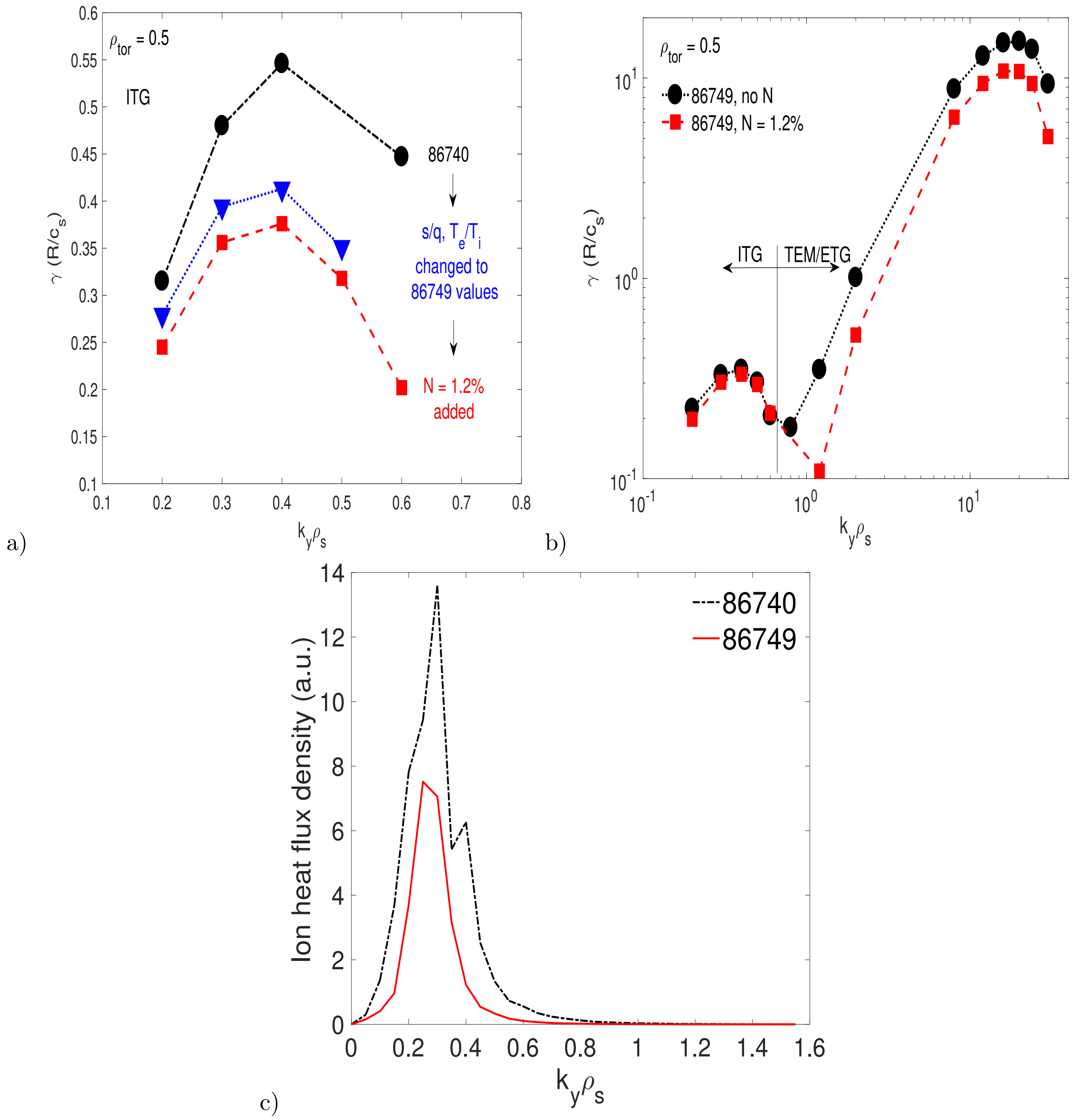

Figure 5.9: *Normalized linear growth rate $\gamma$of the main micro-instability as a function of $k_y\rho_s$ from linear gyro-kinetic simulations at $\rho_{tor} = 0.5$. These results have been obtained using input parameters from shot n. 86740 (black circles), changing the values of T_e/T_i and of s/q to the ones of discharge n. 86749 (blue triangles) and then adding 1.2% of nitrogen (red squares). the results covering both ion and electron range of k_y are shown in figure (b). c) Ion heat flux density as a function of $k_y\rho_s$ for the case $R/L_{Ti} \approx 5$ at $\rho_{tor} = 0.5$.*

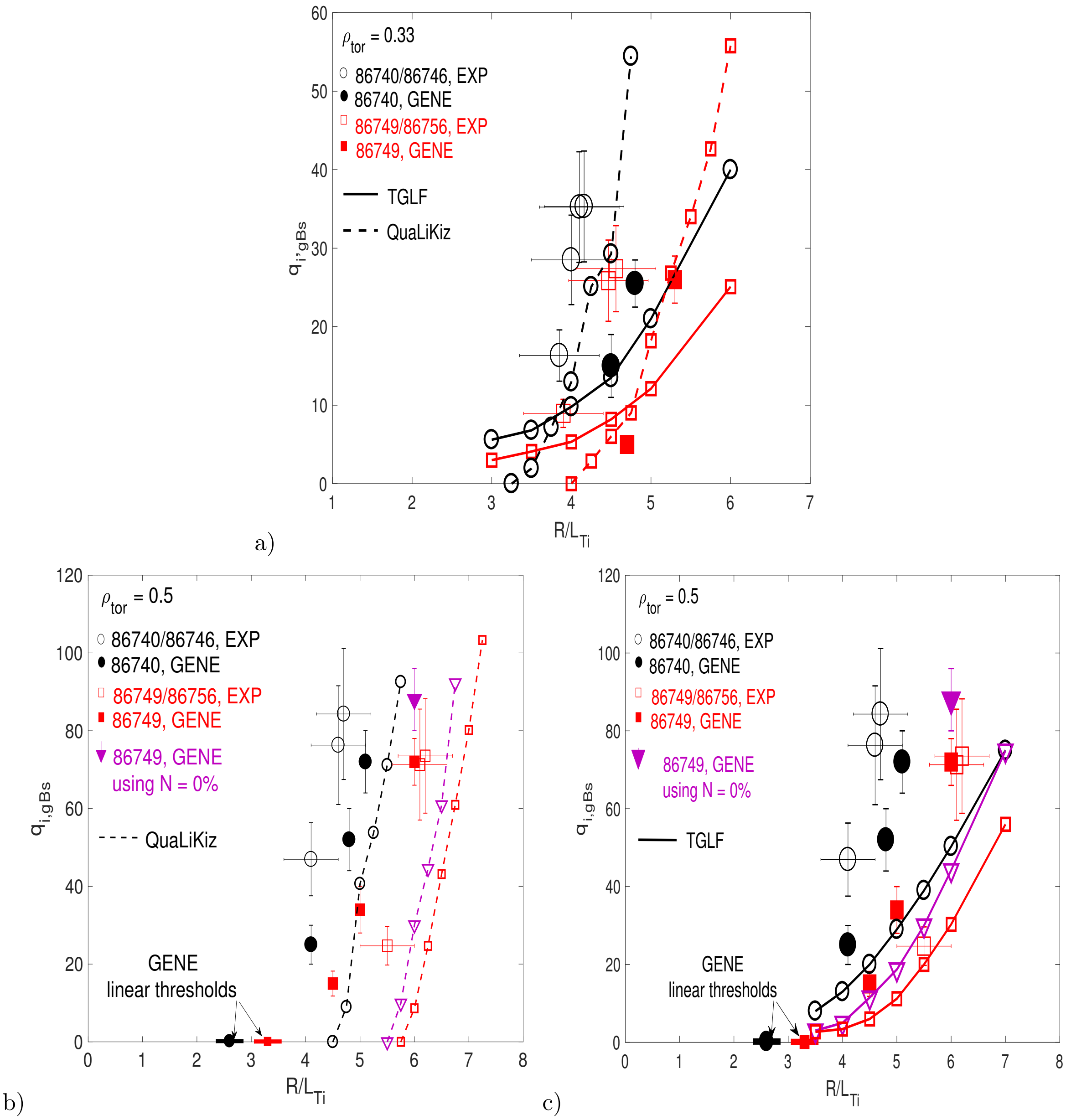

Figure 5.10: *$q_{i,gBs}(R/L_{Ti})$ at $\rho_{tor} = 0.33$ (a) and $\rho_{tor} = 0.5$ (b, c). The black circles indicate the results for discharge n. 86740 ($N = 0\%$) while the red squares indicate the results for discharge n. 86749 ($N = 1.2\%$). The empty symbols represent the experimental results, the full symbols represent the nonlinear gyro-kinetic simulations, the dotted lines represent the QuaLiKiz simulations and the continuous lines represent the TGLF simulations. In figure (b) and (c) the purple triangles represent the simulations of discharge n. 86749 but using $N = 0\%$.*

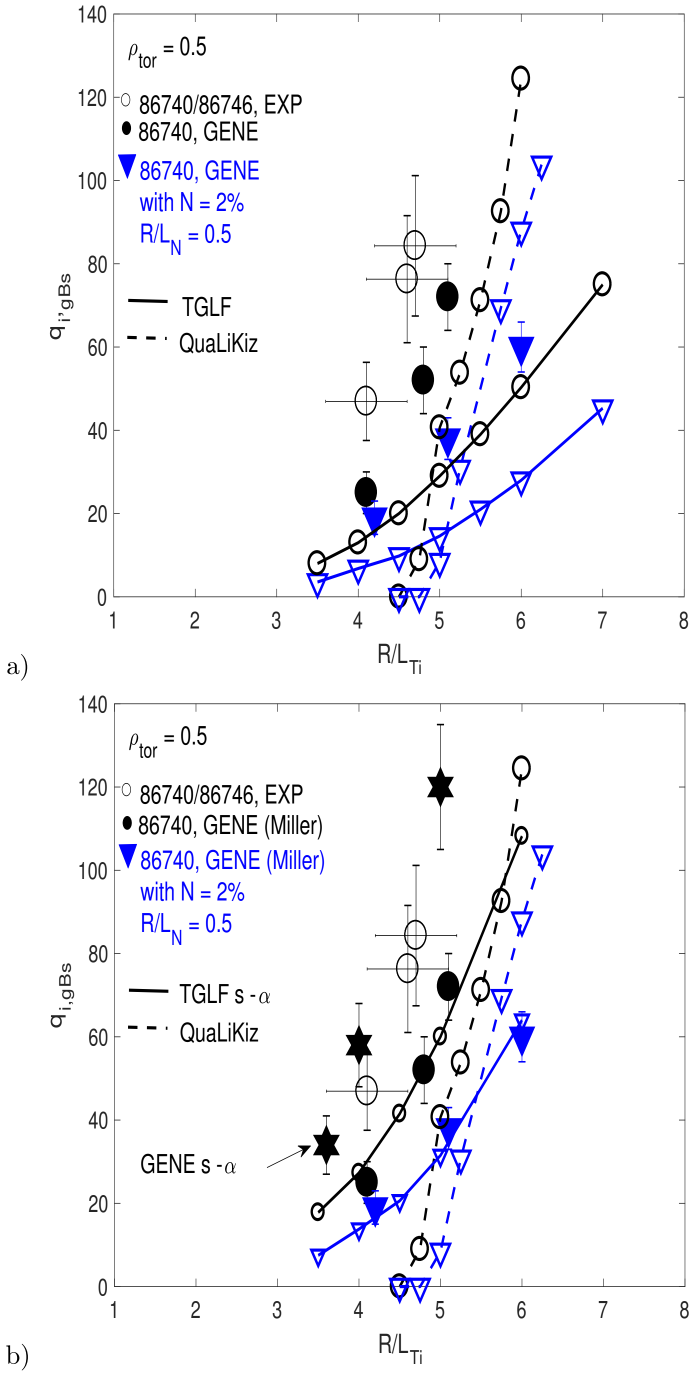

Figure 5.11: $q_{i,gBs}(R/L_{Ti})$ at $\rho_{tor} = 0.5$. *The black circles indicate the results for discharge n. 86740* ($N = 0\%$). *The empty symbols represent the experimental results, the full symbols represent the nonlinear gyro-kinetic simulations, the dotted lines represent the QuaLiKiz simulations and the continuous lines represent the TGLF simulations. The blue triangles represent the simulations of discharge n. 86740 but using* $N = 2\%, R/L_N = 0.5$. *In figure (b) the black hexagons represent GENE simulations for discharge n. 86740 but using* $s - \alpha$ *geometry instead of Miller geometry.*

References

[1] Mandrekas J., Stacey W. M., Nucl. Fusion 35, 843 (1995).

[2] Pacher G. W., et al., Nucl. Fusion 47, 469 (2007).

[3] Manas. P. et al, 42ndEPS conference on plasma physics, Lisbon, Portugal (2015).

[4] N. Bonanomi et al., “Light impurity transport in JET plasmas” (2017), submitted to Nucl. Fusion.

[5] Dominguez R. R. and Rosenbluth M. N., Nucl. Fusion 29, 844 (1989).

[6] M. Romanelli et al., Nucl. Fusion 51, 103008 (2011).

[7] G. Szepesi et al., Nucl. Fusion 53, 033007 (2013).

[8] Ongena J., et al., Phys. Plasmas 8, 2188 (2001).

[9] Tardini G. et al., Plasma Phys. Control. Fusion 55, 015010 (2013).

[10] Giroud C., et al, Plasma. Phys. Control Fusion 57, 035004 (2015).

[11] Porkolab M. et al., Plasma Phys. Control. Fusion 54, 124029 (2012).

[12] Ennever P., et al., Phys. Plasmas 22, 072507 (2015).

[13] Porkolab M., et al., 26th IAEA Fusion Energy Conference, Kyoto, Japan (2016).

[14] Maddison G. P., et al., Nucl. Fusion 54, 073016 (2014)

[15] Jaervin A. D., et al., Nucl. Fusion 56, 046012 (2016)

[16] Van Eester D., et al., Plasma Phys. Control. Fusion 51, 044007 (2009).

[17] Eriksson L. G., Hellsten T. and Willén U., Nucl. Fusion 33, 1037 (1993).

[18] Challis C., et al., Nucl. Fusion 29, 563 (1989).

[19] Wesson J. and Campbell D. J., 'Tokamaks', Oxford University Press, 4th edition (2011).

[20] Cenacchi G. and Taroni A., Rapporto ENEA RT/TIB/88/5 (1998).

[21] F, Imbeaux, F. Ryter. and X. Garbet., Plasma Phys. Control. Fusion 43, 1503 (2001).

[22] Jenko F., et al., Phys. Plasmas 7, 1904 (2000).

[23] Görler T., et al., J. Comput. Phys. 230, 7053 (2011).

[24] Brizard A. J., Hahm T. S., Rev. Mod. Phys. 79, 421 (2007).

[25] Miller R. L., et al., Phys. Plasmas 5, 973 (1998).

[26] Staebler G. M., Kinsey J. E. and Waltz R. E., Phys. Plasmas 12, 102508 (2005)

[27] Staebler G. M., Kinsey J. E. and Waltz R. E., Phys. Plasmas 14, 055909 (2007)

[28] Bourdelle C., et al, Phys. Plasmas 14, 112501 (2007)

[29] Bourdelle C., et al., Plasma Phys. Control. Fusion 58, 014036 (2016)

[30] J. Citrin et al., accepted to Plasma Phys. Control. Fusion (2017), https://doi.org/10.1088/1361-6587/aa8aeb.

[31] Artaud J. F., et al., Nucl. Fusion 50, 043001 (2010).

[32] Citrin J., et al., Nucl. Fusion 54, 023008 (2014).

[33] P. Mantica et al., Phys. Rev. Lett. 107, 135004 (2011).

[34] P. Migliano et al., Plasma Phys. Control. Fusion 55, 055003 (2013).

[35] M. N. A. Beurskens et. al., Nucl. Fusion 54, 043001 (2014).

[36] Hyun-Tae Kim et. al., Plasma Phys. Control. Fusion 57, 065002 (2015).

[37] Guo S. C. and Romanelli F., Phys. Fluids B 5 (2), 520 (1993).

[38] Migliano P., et al., Plasma Phys. Control. Fusion 55, 055003 (2013).

[39] Bonanomi N., et al., Nucl. Fusion 55, (2015).

[40] Peeters A. G., et al., Phys. Plasmas 12, 022505 (2005).

[41] Ryter F., et al., Phys. Rev. Lett. 95, 085001 (2005).

Chapter 6

Turbulent transport stabilization by ICRH minority fast ions in low rotating JET ILW L-mode plasmas

Paper submitted to Nuclear Fusion, 11/2017.

N. Bonanomi[1,2], P. Mantica[2], A. Di Siena[3], E. Delabie[4], C. Giroud[5], T. Johnson[6], E. Lerche[7], S. Menmuir[5], M. Tsalas[8,5], D. Van Eester[7]and JET contributors*

EUROfusion Consortium, JET, Culham Science Centre, Abingdon, OX14 3DB, UK
1) University of Milano-Bicocca, Milano, Italy
2) CNR - Plasma Physics Institute "P. Caldirola", Milano, Italy
3) Max Planck Institute for Plasma Physics, Boltzmannstr. 2, 85748 Garching, Germany
4) Oak Ridge National Laboratory
5) Culham Centre for Fusion Energy, Abingdon, OX14 3DB, UK
6) KTH Royal Institute of Technology, Stockholm, Sweden
7) LPP-ERM/KMS, TEC partner, Brussels, Belgium
8) DIFFER - Dutch Institute for Fundamental Energy Research, Eindhoven, The Netherlands
*See the author list of "X. Litaudon et al., 2017 Nucl. Fusion 57, 102001"

Abstract

The first experimental demonstration that fast ion induced stabilization of turbulent transport takes place irrespective of plasma toroidal rotation has been obtained in JET ILW L-mode plasmas with high power $(^3He) - D$ ICRH. Loss of ion stiffness has been observed at high ICRH power and low NBI power and rotation, with a quantitatively similar effect to previous observations at high NBI power. Gyrokinetic simulations indicate that ion turbulence stabilization induced by the presence of high-energetic ^3He ions is the key mechanism in order to explain the experimental observations. The dependence of the stabilization on the ^3He distribution function has also been studied.

6.1 Introduction

In JET C-Wall L-mode plasmas with high Neutral Beam Injection (NBI) power and with Ion Cyclotron Resonance Heating (ICRH) power in $(^3He) - D$ minority scheme, a strong stabilization of the turbulent ion heat transport has been observed in the inner core region of the plasma ($R \lesssim 3.4m$) [1, 2, 3]. The stabilization is associated with a significant reduction of the ion stiffness (i.e. the rate of increase of the gyro-Bohm normalized ion heat flux in response to an increase in $R/L_{Ti} = -R\nabla T_i/T_i$). Gyrokinetic simulations indicated that the key stabilization mechanism acting on ITGs (Ion Temperature Gradient) was a nonlinear electromagnetic mechanism related to the presence of fast ions (D and ^3He) [4, 5]. The gyrokinetic simulations predict an important reduction of the ITG linear growth rate when considering fast ions and electromagnetic effects, and predict also a nonlinear enhancement of these effects. An important role of electromagnetic stabilization of ITGs in plasma with high β has been found in [6], and a strong nonlinear electromagnetic stabilization of the ion heat transport has been predicted for JET and ASDEX Upgrade H-modes with high plasma β [7, 8]. Recent results [9] indicate that also an electrostatic mechanism, related to fast ions, can play an important role in the stabilization of ITGs in some conditions. This mechanism is related to a wave–fast particle resonant interaction [10, 11] that depends also on the fast ions distribution function. This study predicts also a more important role of fast ^3He with respect to fast D for the stabilization of ITGs in the experimental conditions studied in [2, 4]. Further mechanisms, related to main ion dilution due to the presence of fast ions, leading to a stabilization of ITGs, have been proposed for ASDEX Upgrade plasmas with high NBI heating and low density [12].

Experimentally, all the plasmas where the strong turbulent ion heat transport stabilization by fast ions has been observed so far featured high NBI power. High NBI leads to high toroidal plasma rotation, that can also induce a strong ITG stabilization [13, 14]. It is therefore difficult, when using high NBI power, to separate experimentally the effects of plasma rotation and the effects related to fast ions, and one has to rely on modelling to quantify the impact of the two stabilizing effects, as done in [2, 4, 5]. In ASDEX Upgrade, a study on discharges with 4.5 MW of NBI power and with 0 or 3.5 MW of ICRH power in $(^3He) - D$ minority scheme showed that fast ^3He ions were necessary, in the gyrokinetic simulations, in order to explain the strong reduction of the ion heat flux and the strong increase of the ion temperature peaking observed experimentally [15]. In DIII-D, using co-and counter-NBI, a reduction of the ion heat flux was obtained in absence of plasma rotation [16], but other parameters, such as T_e/T_i (known to have a strong effect on ITGs [17, 18]), were changing between the plasmas. Furthermore, a detailed study of the effects of fast ions is missing for this case. So far, no experimental evidence of a strong stabilization of the turbulent ion heat flux, due to fast ions, has been obtained in absence, or with low, plasma rotation and with no substantial changes in other important parameters such as $s/q, T_e/T_i$. In this work, we present first experimental evidence, in JET ILW (ITER-Like Wall) L-mode plasmas with low plasma rotation, of a strong reduction of the turbulent thermal transport related to an increase of fast ^3He ion energy density, while keeping the other relevant plasma parameters constant. This is a direct experimental evidence that these stabilization mechanisms are effective irrespective of the plasma rotation, which is an important element for the extrapolation of these effects to ITER scenarios. Nonlinear gyrokinetic simulations indicate that stabilization of ITG modes by both electrostatic and electromagnetic effects of fast ^3He ions is the key mechanism to reproduce the experimental heat fluxes. In the cases presented here, unlike in those presented in [4], besides the electromagnetic effects also a significant role of the electrostatic effects related to fast ^3He ions and predicted in [9]is found in the simulations.

The paper is organized as follows: in section 6.2 the experimental set-up is described and in section 6.3 the gyrokinetic simulation set-up is presented. In section 6.4 the experimental results are described, while in section 6.5 the gyrokinetic simulations results are shown and compared to the experiment. The conclusions are reported in section 6.6.

6.2 Experimental set-up and methods

The discharges studied in this paper were made in the JET tokamak (major radius $R_0 = 2.96m$, minor radius $a = 1m$) with ILW and are D plasmas with vacuum toroidal magnetic field $B_T \approx 3.3\,T$, plasma current $I_p \approx 2\,MA$ and safety factor at the flux surface that contains the 95% of the poloidal flux $q_{95} \approx 5$. The heating power consists of 2.6 – 7 MW of ICRH deposited on ions using a ^3He concentration $[^3He] \approx 9\%$, which ensures dominant ion heating [19], and of 1.7 MW of NBI. The ICRH power was deposited on-axis ($R \approx 3.0\,m$) in order to obtain the maximum heating power density and energy density of ^3He fast ions in the centre of the plasma, where the magnetic shear, known to have a strong effect on the stabilization of ITGs by fast ions [2, 4, 9], is minimum. Fixing the NBI heating power to the minimum value for Charge Exchange (CX) measurements and using different levels of ICRH power (and so different levels of fast ^3He energy density), a study of the effects of fast ^3He ions on the plasma thermal transport, while keeping the plasma rotation and the fast D population low, was possible. The ICRH power deposition and the ^3He fast ions density, energy density and distribution function have been evaluated using the SELFO code [20, 21]. Figure 6.1 shows the comparisons of the time evolution of the heating powers (figure 6.1a), of the profiles of the ICRH power deposition on thermal ions and of the fast ^3He energy densities (figure 6.1b), between a discharge with 2.6 MW of ICRH (n. 90671) and a discharge with 7 MW of ICRH (n. 90672). The NBI heating power on electrons and on ions and the fast D pressure in the plasma have been calculated with the PENCIL code [22]. The fast D energy density has been found to be negligible compared to the fast ^3He energy density in discharges with high ICRH power. The ohmic power density has been calculated using $P_{Ohm} = \eta \cdot j^2$, where η is the resistivity of the plasma and j is the plasma current density reconstructed by the EFIT equilibrium code constrained by polarimeter measurements. Also the exchanged power density between ions and electron, p_{ei} [23], has been calculated analytically. The radiated power density p_{rad} has been found to be negligible inside $r/a \sim 0.8$. The powers $P_{OHM}, P_{ICRH}, P_{NBI}, P_{ei}$ and P_{rad} have been obtained integrating on the plasma volume within a flux surface and the ion and electron heat fluxes are expressed in gyro-Bohm units as

$$q_{i,gB_i} = [(P_{ICRH,i} + P_{NBI,i} + P_{ei})/\Sigma] \cdot R_0^2/(n_e T_i \rho_i^2 v_{th,i}) \tag{6.1}$$

$$q_{e,gB_s} = [(P_{ICRH,e} + P_{NBI,e} + P_{OHM} - P_{ei} - P_{rad})/\Sigma] \cdot R_0^2/(n_e T_e \rho_s^2 c_s) \tag{6.2}$$

where Σ is the considered flux surface, $c_s = \sqrt{T_e/M_i}$, $v_{th,i} = \sqrt{T_i/M_i}$, $\rho_i = v_{th,i} M_i/eB_T$ and $\rho_s = c_s M_i/eB_T$. Typical errors on the heat fluxes are $\sim 20\%$. For the measurement of the electron temperature T_e the ECE (Electron Cyclotron Emission) diagnostic has been used, while the ion temperature T_i and the plasma toroidal rotation ω_T have been measured by the CX diagnostic. For the charge exchange measurements, Be and Ne impurities have been used ($\sim 0.1\%$ of Ne has been puffed into the plasma in order to improve the CX measurements). Furthermore, a charge-exchange measurement recently made available at JET, that uses beam modulation for background subtraction and fits all active line features to extract the deuterium charge exchange line [24, 25], has been used and will be indicated as D_α CX . The density profiles of Be, Ne and thermal ^3He have been measured using the CX diagnostic [26]. The electron density n_e has been measured by high-resolution Thomson scattering (HRTS). The radial profile of the safety factor q, of the magnetic shear $s = r/q \cdot dq/dr$ and of the equilibrium plasma geometry have been reconstructed by the EFIT equilibrium code constrained by polarimeter measurements. Local values of $R/L_{Ti} = -R_0 \nabla T_i/T_i, R/L_{Te} = -R_0 \nabla T_e/T_e$ and $R/L_n = -R_0 \nabla n_e/n_e$ are obtained by local linear fits of $ln(T_i), ln(T_e)$ and $ln(n_e)$ radial profiles averaged over a time interval $\Delta t \approx 1\ s$. The fits are done using $r = (R - R_{in})/2$, R and R_{in} being the outer and inner radii of the flux surface on the magnetic axis plane, and averaging other multiple fits using a variable number of data points around the chosen radius (3-9 points). Errors on these quantities are typically $\sim 15\%$.

The data analysis has been carried out at $\rho_{tor} = \sqrt{(\Phi/\pi B_T)/(\Phi/\pi B_T)_{max}} = 0.25$ ($R \approx 3.24\ m$) and $t \approx 6\ s$, Φ being the toroidal magnetic flux. At this radial position and at this time, the changes in $q_{i,gB_i}(R/L_{Ti})$ have been observed to be the largest. Also, no magnetohydrodynamics instabilities (such as sawteeth), that could interfere with the analysis, are present at the chosen time.

6.3 Gyrokinetic simulation set-up

Non-linear gyrokinetic simulations, that calculate the turbulent part of the heat flux, have been carried out using the GENE (Gyrokinetic Electromagnetic Numerical Experiment) [27, 28] code and compared with the experiment. Linear gyrokinetic simulations have also been carried out, in order to study the effects of the changes in the plasma parameters on the linear growth rate of the main micro-instabilities. GENE solves the gyrokinetic Vlasov equations coupled with the Maxwell equations within a δf approximation [29] and using field aligned coordinates $\{x, y, z\}$, where z is the coordinate along the magnetic field line, x is the radial coordinate and y is the binormal coordinate.

In the simulations, that are carried out in the local limit ($1/\rho* \sim 400$), Miller geometry [30] has been used as well as collisions, external flow shear (even if low in our case), finite-β effects (considering both $B_\perp$ and $B_\parallel$ fluctuations), kinetic D ions, kinetic electrons and kinetic ^3He ions. For ^3He, a Maxwellian distribution function has been used in most simulations. However, due to the presence of highly energetic, non thermalized, ^3He particles, the Maxwellian distribution function is not adequate to describe the real distribution function of this species and the results can be affected by this approximation. For this reason, a new version of the GENE code [31, 32] able to use a numerical distribution function for ^3He (calculated using the SELFO code), has been used for few simulations. Typical grid parameters in the non-linear simulations were as follows: perpendicular box sizes $[L_x, L_y] \approx [190, 125]\rho_s$, phase-space grid discretization $[n_x, n_y, n_z, n_{v\parallel}, n_\mu] = [256, 48, 34, 32, 24-48]$ and $0.05 \lesssim k_y\rho_s \lesssim 2.4$. Detailed convergence tests have been carried to choose these settings. The plasma parameters used as input in the simulations have been taken from discharge n. 90672 at $\rho_{tor} = 0.25$ and $t \approx 6\ s$. Some important values, used in the simulation, are: $Z_{eff} = 1.36, q = 1.4, s = 0.46, R/L_{^3He} = R/L_{ne} = 2.6, R/L_{Te} = 8, R/L_{Ti} = 7.2, R/L_{T,^3He} = 15, T_{^3He} = 12T_e, T_i/T_e = 0.8, \beta_{ref} = 8\pi n_e T_e/B_0^2 = 0.00399, \nu* = \nu_{ei}\frac{qR_0}{\epsilon^{1.5} v_{th,e}} 0.06, n_{^3He} = 0.09n_e$, where $\epsilon = r/R_0$ and $v_{th,e} = \sqrt{T_e/m_e}$. When not considering the fast ^3He ions in the simulations, we use $T_{^3He} = T_i$ and $R/L_{T^3He} = R/L_{Ti}$ without changing any other input parameter. In the electrostatic simulations, a value of $\beta_{ref} = 10^{-5}$ is imposed without changing any other input parameter. In the simulation of the low ICRH power case, the same parameters have been used except the reference T_e value (lowered from 3.6 keV to 2.6 keV), considering electromagnetic effects and just thermal ^3He. Also a few electron-scale simulations have been performed, in order to study the impact of fast ions on ETG modes in nonlinear simulations. In these simulations the range $3 \leq k_y\rho_s \leq 96$ has been used and, as the linear growth rate of ETG modes does not depend on the fast ions distribution function (see figure 6.6b), a Maxwellian distribution function has been used for the ^3He.

The effect of other impurities ($\sim 1.2\%\ Be, \sim 0.3\%\ Ne, \sim 0.05\%\ Ni$) has been studied using linear gyrokinetic simulations and found to be negligible compared to the effect of ^3He in our case. Considering that, as shown by the CX measurements, these impurities are present in all the discharges in the same concentrations and with the same density peaking [26], they cannot explain the differences observed between discharges with low and high ICRH power. The difference in Ni concentration is $\sim 0.05\%$, but, as discussed in section 6.5, it has a negligible effect on ITGs as it causes a little main ion dilution. For these reasons, and in order to save computational resources, we decided to not include Be, Ne and Ni impurities in our simulations. For these reasons, and in order to save computational resources, we decided not to include these impurities in our simulations.

The nominal experimental value of the magnetic shear is $s = 0.25$. Using this values, in the electromagnetic simulations with a Maxwellian distribution function for the fast ions, there is the presence of instabilities at $k_y\rho_s \lesssim 0.1$ (KBM/fast particles modes). These modes lead to levels of ion heat flux in the nonlinear simulations not comparable with the experiment, as found also in [5, 8]. For these reason, when using the Maxwellian distribution function for the fast ions, the value of $s = 0.46$ has been chosen, within experimental error bars, in order to avoid the presence of the low-k_y instabilities. When using the numerical distribution function for the fast ions, these modes disappear also at $s = 0.25$ and few simulations have been performed with this value.

6.4 Experimental observations

Although the ^3He concentration of 9% was used to maximize ion heating, in the high ICRH power cases SELFO simulations predict that a substantial part of the ICRH power is still absorbed by electrons due to the high energies achieved by the minority fast ions at such power levels. Both the ion and electron temperature profiles then show a general increase when ICRH power is increased. In addition, inside $\rho_{tor} \approx 0.35$, an important increase of R/L_{Ti} and strong reduction of q_{i,gB_i} are observed in discharges with high ICRH power (figures 6.2a and 6.2b), while the values of R/L_{Te} and of q_{e,gB_s} are not changing (figure 6.5b). In order to study what is causing these changes in $q_{i,gB}(R/L_{Ti})$, a comparison between discharges n. 90668 and n. 90671 (with 1.7 MW of NBI and 2.6 MW of ICRH) and discharges n. 90670 and n. 90672 (with 1.7 MW of NBI and $6-7$ MW of ICRH) has been done at $t = 6\,s$ and at $\rho_{tor} = 0.25$, as already explained in section 6.1. In figure 6.2a the comparison of the T_i radial profiles of discharges n. 90672 and n. 90671 (discharges n. 90668 and n. 90670 show similar behavior) is shown, while the comparison of the experimental $q_{i,gB_i}(R/L_{Ti})$ values is shown in figure 6.2b. The increase in the peaking of T_i, inside $\rho_{tor} \approx 0.35$, and the strong reduction of $q_{i,gB}$ in discharges with high ICRH power are well visible outside error bars. The radial profiles of T_e, n_e, s, q, ω_T for the same discharges are shown in figure 6.3. No substantial differences in these parameters are observed, except for higher values of T_e. Furthermore, $s/q, T_e/T_i, R/L_n, \omega_T, \partial\omega_T/\partial r$, that are known to have an important impact on turbulent thermal transport [13, 14, 17, 18, 33, 34, 35], as well as light impurity density ($n_{^3He}/n_e \approx 9 - 11\%, n_{Be}/n_e \approx 1.2\%, n_{Ne}/n_e \approx 0.3\%$) and light impurity density peaking (also known to have an impact on turbulent thermal transport [36, 37, 38, 39]) are similar, within error bars, over the whole radial profile, between discharges with low and high ICRH heating. Z_{eff} is changing from ~ 1.6, in discharges with low ICRH, to ~ 2, in discharges with high ICRH power. The change in Z_{eff} is mainly due to a medium Z impurity (Ni) coming from the ICRH antenna facilities. A change in the Ni concentration from $\sim 0.02\%$ to $\sim 0.07\%$ is enough to explain the change in Z_{eff}.

The main difference, between the plasmas with high and low ICRH heating power, is the fast ^3He energy density (figure 6.1b) inside $\rho_{tor} \lesssim 0.4$. The ^3He pressure modifies also the total plasma pressure ($p = \sum_s n_s T_s$, the sum being over all the species in the plasma), as can be seen in figure 6.3d, and with the higher T_i and T_e temperatures, increases the plasma $\beta = 8\pi p/B_0^2$ in discharges with high ICRH heating. These changes are expected to lead to a strong stabilization of ITGs and of the turbulent ion thermal transport [4, 6, 7, 8, 9, 15].

6.5 Gyrokinetic simulations

As discussed in section 6.4, the main differences between discharges with low and high ICRH heating power, inside $\rho_{tor} \approx 0.35$, are the increase, at high ICRH power, of the plasma pressure p (and of the local plasma pressure gradient) and of the plasma β, related to a strong increase of the energy density of the fast ^3He ions, and the increase of Z_{eff}, related to the presence of Ni coming from the ICRH antenna facilities. The analysis with gyrokinetic simulations, carried out as described in section 6.3, focuses on these aspects.

6.5.1 Linear gyrokinetic simulations

Using linear gyrokinetic simulations, the effects of the change of 0.05% of the Ni density, and consequent change in Z_{eff}, of the change in $\alpha_{MHD} = -q^2 R(d\beta/dr)$ (that can induce a stabilization of the ITG modes [40]), of finite-β effects and of the presence of fast ^3He on the linear growth rate of the most unstable mode in the plasma (ITG) have been studied.

The effects due to a change of 0.05% in the Ni concentration have been found negligible (reduction of γ_{ITG} of $\sim 4\%$) compared to the effects related to ^3He, the Ni concentration being too low and the main ion dilution minimal. Also the effects related to the changes in α_{MHD} have been found to be minimal in our case. For these reasons, the value of α_{MHD} has been fixed, in all the simulations, equal to the one obtained considering the fast ^3He, while Ni has not been considered in the simulations.

Effects of fast ions on ITG modes

Figure 6.4a shows the normalized linear growth rates of ITG modes, which are the dominant modes up to $k_y = 1$, obtained from simulations with/without the electromagnetic effects and the fast ^3He ions. In the same figure, also the results obtained using the numerical distribution function for ^3He are shown. At $0.2 \leq k_y\rho_s \leq 0.4$, where the major part of the ion heat flux is carried in the non-linear simulations, a little stabilization, or a little destabilization, depending on k_y, of the ITG growth rate is obtained when considering electromagnetic (finite-β) effects but not the fast ^3He ions. When adding the fast ^3He ions, a strong stabilization of γ is visible. The stabilization is due to electrostatic (reduction by $\sim$ 25% of γ) and electromagnetic (further reduction of γ by $\sim$ 15%) effects, with a total reduction of the linear growth rate by $\sim$ 40%. When considering the numerical distribution function ('SELFO') for ^3He, this reduction is lower with respect to the one obtained considering a Maxwellian distribution function, but still strong ($\sim$ 25%). Using $s = 0.25$, the same relative ITG growth rate reduction as for the case $s = 0.46$ is obtained, but the values of γ are lower with respect to the ones obtained using $s = 0.46$ (figure 6.4b). Furthermore, using $s = 0.25$, electromagnetic instabilities (KBM/fast particle modes) appear at $k_y \lesssim 0.1$, causing a strong enhancement of the heat fluxes in the nonlinear simulations, not comparable with the experiment. Interestingly, when considering the numerical distribution function for ^3He, these modes disappear and the nonlinear simulations give results comparable with the experiment.

Effects of fast ions on high-k instabilities

In figure 6.6a, the effects of fast ions and e.m. mechanisms on the linear growth rate of the Electron Temperature Gradient modes (ETGs) are shown. The presence of fast ^3He ions induces a strong increase (+50%) of the ETG linear growth rate, in opposition to what happens for ITG modes. The increase of the ETG linear growth rate is related only to the presence of the fast ^3He ions and does not depend on electromagnetic effects or on the distribution function of ^3He. The effect of fast ions can be quantified, at least its linear effect, considering the change in $\tau = Z_{eff}T_e/T_i$ they induce. In our case $\tau = 1.48$ with no fast ions while τ=1.06 with fast ions. This parameter strongly affects the linear growth rate of ETG modes [35].

6.5.2 Nonlinear gyrokinetic simulations

The results from the non-linear gyrokinetic simulations and their comparison with the experiment are shown in figure 6.5a (for ions) and in figure 6.5b (for electrons). The results from the electron-scale non-linear simulations for ETG modes are shown in figure 6.6b.

Effects of fast ions on ion thermal transport

When the fast ^3He ions are not considered, the experimental ion heat flux is strongly over predicted by the simulations, with $q_i^{sim} \sim 4q_i^{exp}$, in both the electrostatic and in the electromagnetic simulations. In our case, electromagnetic effects without fast ions have no strong effects in the simulation. A reduction of $\sim$ 40% of the ion heat flux is predicted when fast ions are considered in the simulation without taking into account the electromagnetic effects. This reduction is caused by pure electrostatic effects and can be explained by mechanisms related to a wave–fast particles resonant interaction, as suggested in [9]. Considering also the electromagnetic effects in the simulations with fast ions, a strong stabilization of q_i (-60%) is obtained. This reduction of q_i permits to reach the experimental level of the ion heat flux. In total, a q_i reduction of $\sim$ 75% is predicted when considering fast ions and electromagnetic effects and using a Maxwellian distribution function for fast ions. Using a numerical distribution function for the ^3He ('SELFO' in the figures), there is still a total strong reduction of the ion heat flux with respect to the case without fast ions (−55%), but q_i is now overestimated with respect to the experiment (+75%). Using a numerical distribution function for the ^3He, as observed in the previous section, avoids the presence of low-k_y electromagnetic modes and allows to compare the results from nonlinear simulations and the experimental fluxes also for the nominal value of the magnetic shear, $s = 0.25$. In this case, the experimental q_i is well reproduced within error bars.

Non-linear simulations have been performed also for the low ICRH case (green stars in the figures). In this case both q_e and q_i are well reproduced within error bars. Comparing the results for the low ICRH case and for the high ICRH case, it appears that the nonlinear simulations predict a reduction of the ion stiffness when fast ions and electromagnetic effects are considered. This is in agreement with previous studies [4, 7, 8] and with past experimental observations [2]. These results clearly show that both fast ^3He ions and electromagnetic effects are necessary in order to reproduce the experimental level of the ion heat flux. Their effects lead to a strong stabilization of ITG modes, both linear and non-linear, and is independent of the plasma rotation. The mechanisms that participate in the ITG stabilization are both electrostatic and electromagnetic, the last being determinant to reproduce the experimental fluxes.

Effect of fast ions on electron thermal transport

The effect of fast ^3He on the electron heat flux is similar to the one observed for the ion heat flux. When the fast ^3He ions are not considered, the experimental electron heat flux is strongly over predicted by the simulations, with $q_e^{sim} \sim 2.5 q_i^{exp}$, while a strong reduction of q_e is predicted when fast ions and electromagnetic effects are considered in the simulation. This is related to the strong suppression of ITG modes that causes also the strong reduction of q_i.

When the ion heat flux is matched in the simulations, the experimental electron heat flux is under-predicted ($-(30-50)\%$). The lack of electron heat flux in the low-k electromagnetic simulations with fast ^3He could be due to the fact that high-k modes are more important in presence of fast ions, as suggested by the linear gyrokinetic simulations (figure 6.6a). Fast ions strongly affects our electron-scale nonlinear simulations (figure 6.6b). In these simulations, with $s = 0.25$, the amount of q_e due to ETG modes is $\sim 5\%$ of the experimental value when not considering fast ions and $\sim 10\%$ of the experimental value when the fast ions are considered (+100%). If $s = 0.46$ is used, the electron heat flux carried by ETG modes in the simulation increase to the $\sim 30\%$ of the experimental value. These indications suggest that fast ions must be considered, at least in certain experimental conditions, for a proper study of both low-k and high-k instabilities.

6.6 Conclusions

Experimental evidence of a strong stabilization of thermal transport when using high ICRH power in $(^3He)-D$ minority scheme in JET ILW L-mode plasmas with low plasma rotation and low fast D ion pressure has been obtained. The only substantial changes in the plasmas are related to the enhancement of the fast ^3He ions density energy, inside $\rho_{tor} \approx 0.35$, when high ICRH power ($\sim 7\ MW$) is applied. Linear and non-linear gyrokinetic simulations predict that the key mechanisms able to explain the experimental observations are related to this enhancement of fast ^3He ion pressure. Both electrostatic and electromagnetic effects are acting to stabilize the ITG modes, leading to a reduction of the ion stiffness. The main electrostatic mechanism can be related to a resonant wave-fast particles interaction [10, 11], as suggested in reference [9], and contribute significantly in the reduction of the linear growth rate of ITG. The electromagnetic stabilization acts on the linear growth rate of ITGs, but is strongly enhanced through nonlinear effects and is fundamental to reproduce the experimental results. These results demonstrate that such stabilization mechanisms are at work irrespective of the plasma rotation, which implies that they can contribute to thermal transport reduction also in low rotating ITER plasmas. Furthermore, a strong dependence of these effects on the distribution function of the fast particles has been observed, underlying the importance of considering a realistic distribution function for fast particles when modelling them. These results strongly support the role of fast particles in the stabilization of the thermal transport in the plasma core in some experimental conditions. Regarding the effect of fast ions on high-k instabilities, a strong destabilization of ETG modes by fast ions, that leads to a reduction of $\tau = Z_{eff}T_e/T_i$, is predicted. Considering just single ion and single electron scale simulations, up to $\sim 30\%$ of the electron heat flux is predicted to be caused by ETG modes. As suggested in ref. [41, 42, 43], when ITG modes are stabilized or close to marginal stability, ETG modes can become very important for the heat fluxes of both ions and electrons. The presence of fast ions induces a strong stabilization of ITG modes while at the same time it strongly destabilizes ETG modes. This double effect can lead to a situation where ETG modes play a major role for the heat fluxes. For this reason, considering the effects of fast ions can be essential for the study of both ion and electron-scale instabilities.

Acknowledgement

The authors are grateful to D. R. Mikkelsen for assistance and to Jonathan Citrin and Tobias Goerler for precious suggestions. This research used resources of the National Energy Research Scientific Computing Center, a DOE Office of Science User Facility supported by the Office of Science of the U.S. Department of Energy under Contract No.DE--AC02--05CH11231. Part of the simulations presented in this work were performed at the HYDRA HPC system at the Max Planck Computing and Data Facility (MPCDF), Germany. We acknowledge the CINECA award under the ISCRA initiative, for the availability of high performance computing resources and support. This work has been carried out within the framework of the EUROfusion Consortium and has received funding from the Euratom research and training programme 2014–2018 under grant agreement No 633053. The views and opinions expressed herein do not necessarily reflect those of the European Commission.

Figures

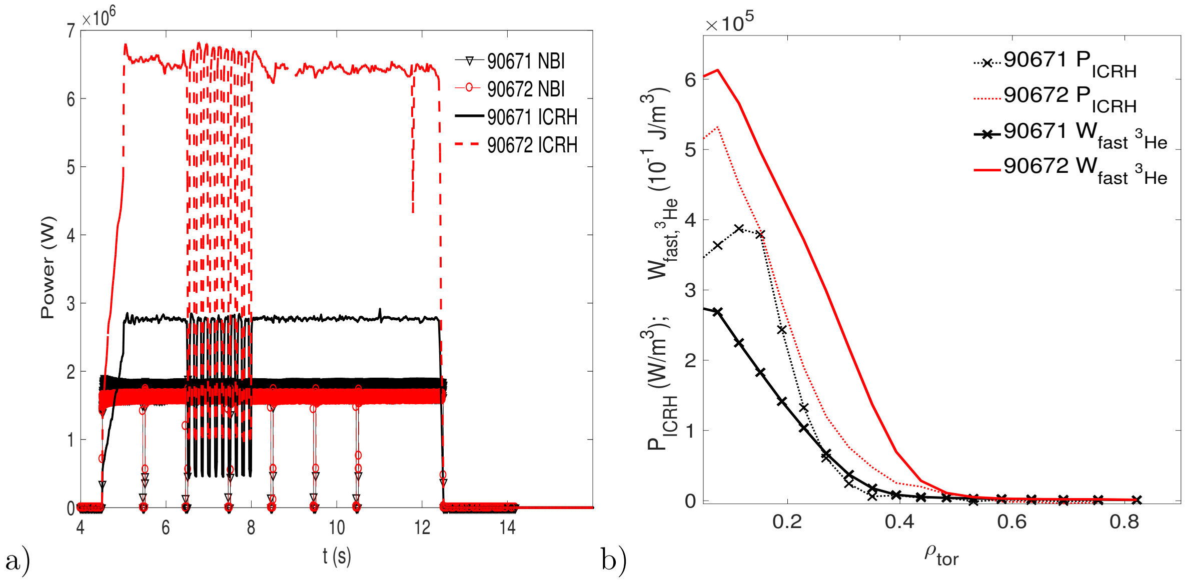

Figure 6.1: *Comparison between discharges n. 90671 and n. 90672: a) NBI and ICRH heating vs. time; b)ICRH power density to ions (dotted lines) and fast* ^3He *energy density calculated using the SELFO code.*

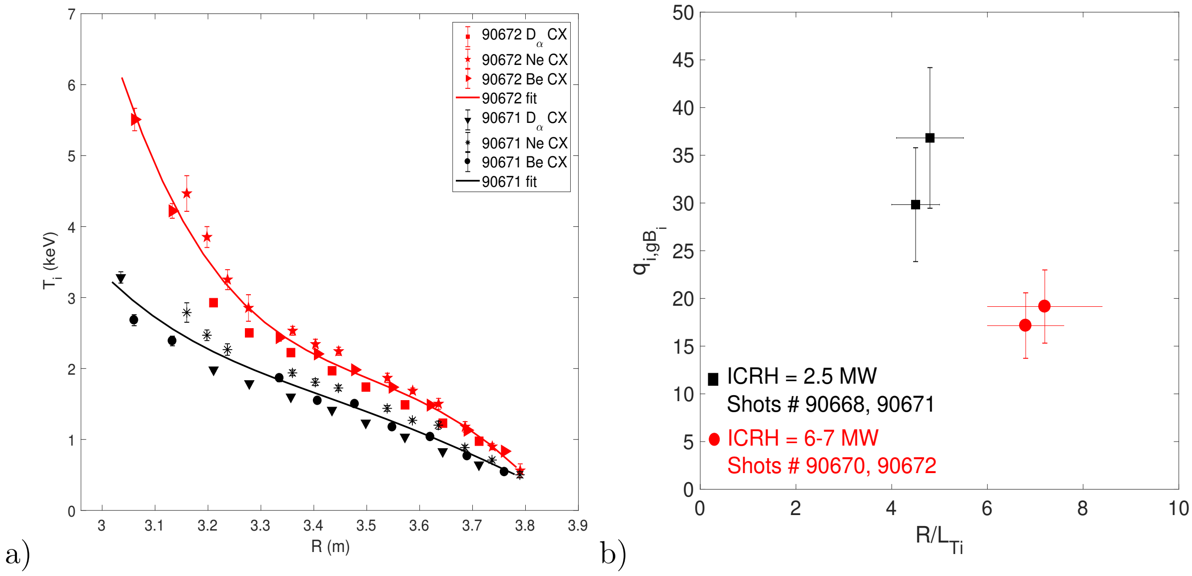

Figure 6.2: *a) Comparison between the* T_i *profile of discharges n. 90671 (black squares) and n. 90672 (red circles). b)* $q_{i,gB}(R/L_{Ti})$ *at* $\rho_{tor} = 0.25$ *of discharges with low ICRH power (~ 2.6 MW, discharges n. 90668 and n. 90671) and of discharges with high ICRH power (~ 6-7 MW, discharges n. 90670 and n. 90672).*

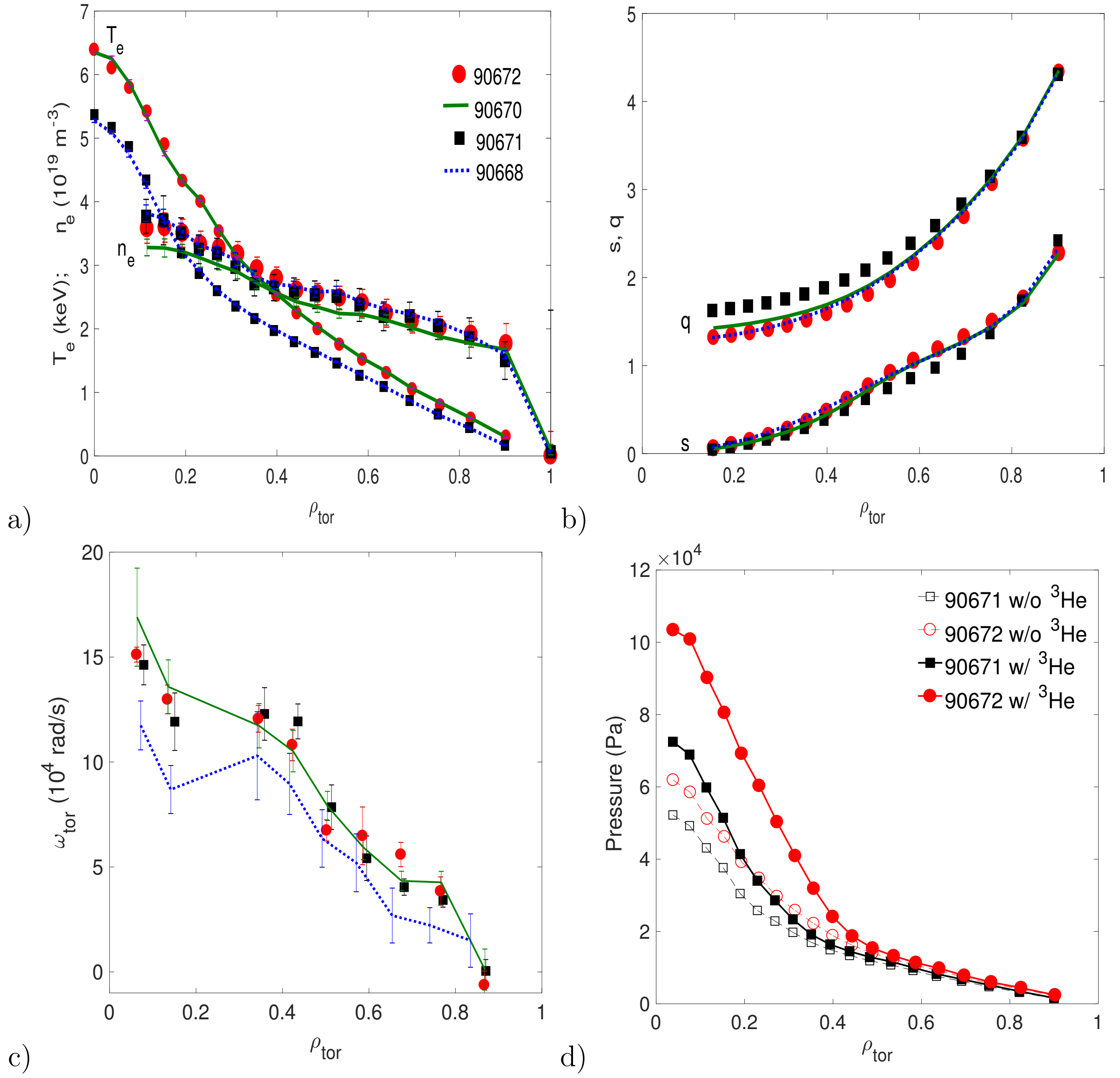

Figure 6.3: *Comparison of radial profiles of* T_e, n_e *(a), safety factor qand magnetic shear s (b) and plasma rotation (c) of discharges n. 90668 (dotted blue lines), n. 90670 (continuos green lines), n. 90671 (black squares) and n. 90672 (red circles). d) Plasma pressure without (open symbols) and with (full symbols)* ^3He *pressure for discharges n. 90671 (black squares) and n. 90672 (red circles).*

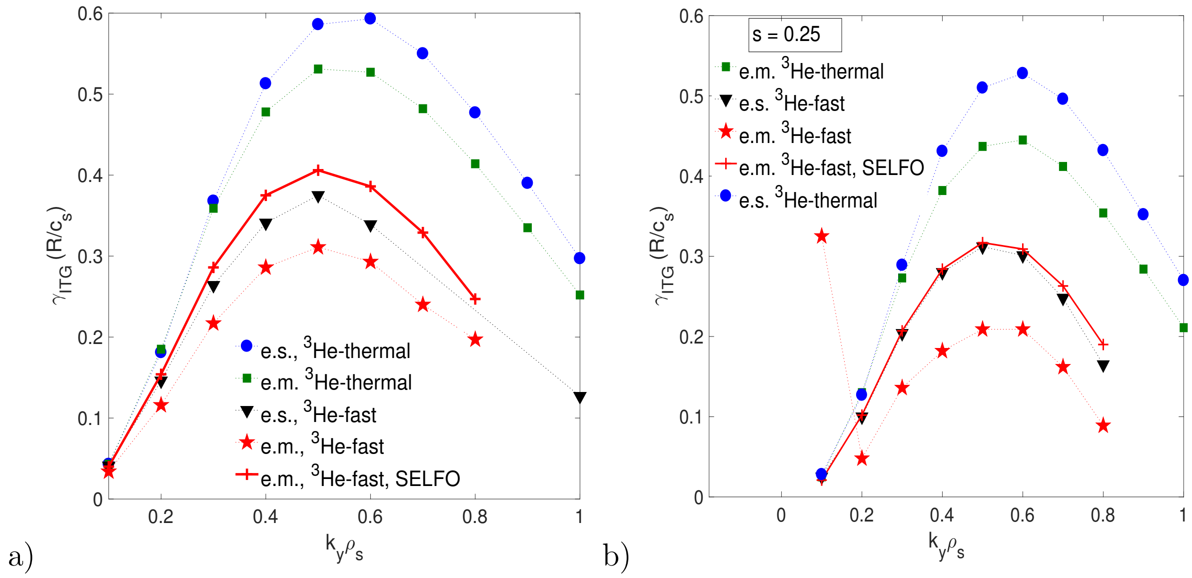

Figure 6.4: *Linear growth rate of the most unstable mode $\gamma(R/c_s)$ as a function of $k_y\rho_s$. ITG growth rate using $s = 0.46$ (a) and $s = 0.25$ (b).*

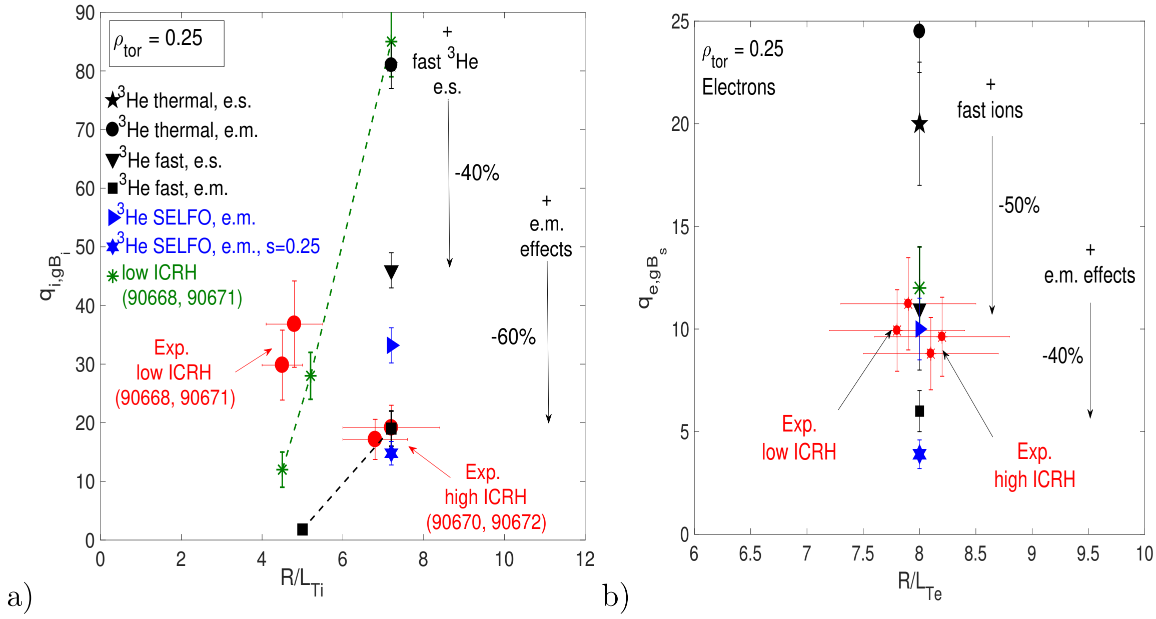

Figure 6.5: *a)$q_{i,gB_i}(R/L_{Ti})$. b)$q_{e,gB_s}(R/L_{Te})$. Comparison between non-linear gyrokinetic simulations and experiment.*

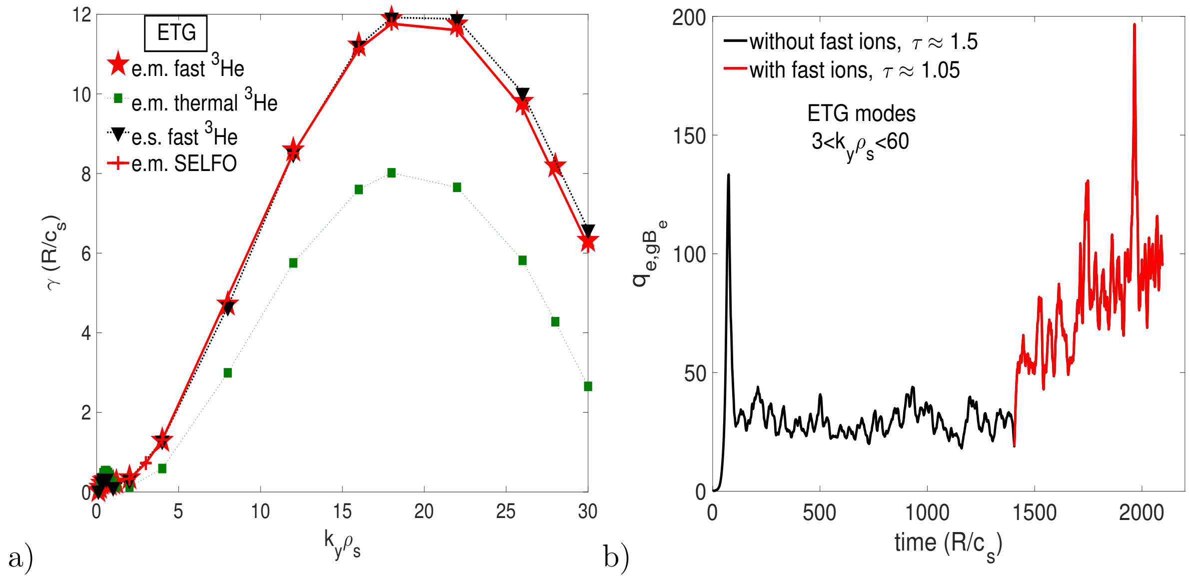

Figure 6.6: *a)Linear growth rate of ETG $\gamma(R/c_s)$ as a function of $k_y\rho_s$. b)q_{e,gB_e} as a function of the simulation time (using $s = 0.25$).*

References

[1] P. Mantica et al., Phys. Rev. Lett. 102, 175002 (2009).

[2] P. Mantica et al., Phys. Rev. Lett. 107, 135004 (2011).

[3] P. Mantica et al., Plasma Phys. Control. Fusion 53 124033 (2011).

[4] J. Citrin et al., Phys. Rev. Lett. 111, 155001 (2013).

[5] J. Citrin et al., Nucl. Fusion 54, 023008 (2014).

[6] C. F. Maggi et al., Nucl. Fusion 50, 025023 (2010).

[7] J. Citrin et al., Plasma Phys. Control. Fusion 57, 014032 (2015).

[8] H. Doerk et al., Phys. Plasmas 22, 042503 (2015).

[9] A. Di Siena et al., “Fast-ion stabilization of tokamak plasma turbulence”, 2017. Submitted to Phys. Rev. Lett..

[10] C. Angioni and A. G. Peeters, Phys. Plasmas 15, 052307 (2008).

[11] T. Dannert et al., Phys. Plasmas 15, 062508 (2008).

[12] G. Tardini et al., Nucl. Fusion 47, 280 (2007).

[13] R. E. Waltz, G. D. Kerbel and J. Milovich, Phys. Plasmas 1, 2229 (1994).

[14] R. E. Waltz et al., Phys. Plasmas 2, 2408 (1995).

[15] F. N. De Oliveira et al., EPS 2017, (http://ocs.ciemat.es/EPS2017PAP/pdf/P2.176.pdf).

[16] T. Luce et al., submitted for publication to Nucl. Fusion.

[17] S. C. Guo and F. Romanelli, Phys. Fluids B 5 (2), 520 (1993).

[18] P. Migliano et al., Plasma Phys. Control. Fusion 55, 055003 (2013).

[19] D. Van Eester et al., Plasma Phys. Control. Fusion 51, 044007 (2009).

[20] J. Hedin et al., Nuclear Fusion 42, 527 (2002).

[21] T. Hellsten et al., Nuclear Fusion 44, 892 (2004).

[22] C. Challis et al., Nucl. Fusion 29, 563 (1989).

[23] J. Wesson and D. J. Campbell, 'Tokamaks', Oxford University Press, 4^{th} edition (2011).

[24] B. A. Grierson et al., Rev. Sci. Instr. 83, 10D529 (2012).

[25] E. Delabie et al., Plasma Phys. Control. Fusion 52, 125008 (2010).

[26] N. Bonanomi et al., “Light impurity transport in JET plasmas” (2017), submitted to Nucl. Fusion.

[27] F. Jenko et al., Phys. Plasmas 7, 1904 (2000).

[28] T. Görler et al., J. Comput. Phys. 230, 7053 (2011).

[29] A. J. Brizard and T. S. Hahm, Rev. Mod. Phys. 79, 421 (2007).

[30] R. L. Miller et al., Phys. Plasmas 5, 973 (1998).

[31] A. Di Siena et al., EPS 2017, Belfast, UK.

[32] A. Di Siena et al., “Non-Maxwellian fast particle effects in gyrokinetic GENE simulations”, 2017, to be submitted to Physics of Plasmas.

[33] Peeters A. G. et al., Phys. Plasmas 12, 022505 (2005)

[34] N. Bonanomi et al., Nucl. Fusion 55, 113016 (2015).

[35] F. Jenko et al., Phys. Plasmas 8, 4096 (2001).

[36] R. R. Dominguez and M. N. Rosenbluth, Nucl. Fusion 29, 844 (1989).

[37] N. Bonanomi et al., “Effects of nitrogen seeding on core ion thermal transport in JET ILW L-mode plasmas”, 2017, submitted to Nuclear Fusion.

[38] M. Porkolab et al., Plasma Phys. Control. Fusion 54, 124029 (2012).

[39] P. Ennever et al., Phys. Plasmas 22, 072507 (2015).

[40] C. Bourdelle et al., Nucl. Fusion 45, 110 (2005).

[41] T. Görler and F. Jenko, Phys. Rev. Lett. 100, (2008)

[42] S. Maeyama and Y. Idomura, Phys. Rev. Lett. 114, 255002 (2015).

[43] N. T. Howard et al., Phys. Plasmas 21, (2014).

Part III

Electron heat transport

Introduction

As discussed in section 3.2, full understanding of turbulent electron heat transport has not yet been reached, in view of a possible significant role of electron scale instabilities and multi-scale interactions, which are topics only recently addressed due to their high computational requirements. Electron heat transport has a heavier impact on the performance of ITER and future reactors with respect to present day machines, since the former will have dominant electron heating, so that fuel ions will not be able to achieve temperatures higher than the electron temperature, unlike in present devices where the highest fusion performance has always been reached with ions much hotter than electrons. Therefore, in future reactors electron heat transport may severely limit the core ion temperature, which calls for a deeper physics understanding in order to optimize fusion performance. It has been established that turbulent electron heat transport can be driven by ion-scale (low-k) instabilities such as ITG (Ion Temperature Gradient) modes and TEM (Trapped Electron Modes) and by electron-scale (high-k) instabilities such as ETG (Electron Temperature Gradient) modes. TEM and ETG modes are both triggered above a critical value of $R/L_{Te} = -R\nabla T_e/T_e$ (where R is the plasma major radius for normalization), which is radially dependent. The level of the turbulent transport increases above the local critical values of R/L_{Te}, with a rate that determines the stiffness of the temperature profile against an increase of heating power. The critical thresholds are predicted to depend on plasma parameters, and especially on $R/L_n, s$, collisionality and the fraction of trapped electrons for TEMs (see ref. [5] of chapter 7 and chapter 7) and on $\tau = Z_{eff}{\cdot}T_e/T_i$ and s/q in the case of ETGs (see ref. [30] of chapter 7 and chapter 9). Electron heat transport in several tokamaks, including AUG, DIII-D and JET, has been historically ascribed to ITG/TEM (see for example ref. [4-6] of chapter 9), since a good match between experimental and TEM critical R/L_{Te} from linear gyrokinetic (GK) simulations was found and the low-k contribution to the heat flux was expected to dominate over the high-k contribution. However, at the time of those experiments, no comparison between electron heat fluxes from experiment and from non-linear GK simulations was available. Experiments done in AUG observed the stabilizing effect of collisionality on the electron heat transport expected to be related to a stabilization of TEMs (see ref. [7] of chapter 7) and other studies observed a stabilizing effect of the magnetic shear on the electron heat transport. Studies performed on tokamak DIII-D indicated that stiffness increases with radius, while a higher electron stiffness in presence of NBI heating was observed in studies in ASDEX-Upgrade, JET and DIII-D (see ref. [9-11] of chapter 7), which is still lacking a physical explanation. More recently, in JET (see chapter 8), in C-MOD (see ref. [9] of chapter 9) and, in some experimental conditions, in DIII-D (see ref. [10] of chapter 9), it was found that neither the q_e values nor the electron stiffness were matched by low-k non-linear GK simulations, i.e. considering just ITG modes and TEM. A possible explanation that has been found is the lack of ETG modes and multi-scale interactions in the simulations, as suggested in ref. [9] of chapter 9. ETG modes have been found to be linearly unstable in many experimental conditions, but their nonlinear physics has been found to depend on many factors and also to strongly depend on the ion-scale instabilities. In ref. [9,15,16] of chapter 9, a strong correlation between ion and electron-scale instabilities has been found. Ion-scale structures (such as zonal flows, ITG/TEM eddies) strongly stabilize the ETG modes, while ETG structures are suggested to be able to damp the saturation of ion-scale instabilities, with a consequent enhancement of their contribution to the turbulent fluxes. On the fluctuation side, experimental measurements of high-k instabilities have been reported in different machines (see ref. [11-14] of chapter 9), with a dependence on radius and heating scheme. Also a correlation between the increase of q_e and the increase of high-k density fluctuations has been reported (see ref. [11,14] of chapter 9). All these experimental and theoretical observations point to an important role of high-k instabilities in some experimental conditions, especially when ion-scale instabilities are strongly suppressed (like inside a transport barrier) or are close to marginal stability, as will be the case in ITER.

In this chapter we focus our attention on two aspects of electron heat transport in JET core plasmas:

- The dependence of the critical threshold on plasma parameters, and especially on s and on τ;
- The role of multi-scale interactions and electron-scale instabilities in the thermal transport in the plasma core.

The study reports results from dedicated experiments in JET L-mode plasmas and gyrokinetic simulations including a first multi-scale simulation for a JET plasma. In chapter 7 the work on the study of the correlation between electron heat transport and $s$is shown, as well as the first indications of a role of ETG modes. In chapter 8 a study on the effect of τ and ETG modes in two specific cases analyzed in chapter 7 is reported. In chapter 9 the study of ETG modes using a wide database of JET L-mode C-Wall plasmas and the results from the multi-scale nonlinear simulation are reported.

Chapter 7

Trapped electron mode driven electron heat transport in JET: experimental investigation and gyrokinetic theory validation.

Paper published in Nuclear Fusion: N. Bonanomi et al., Nucl. Fusion 55, 113016 (2015)[†].

N. Bonanomi[1,2], P. Mantica[1], G. Szepesi[1,6], N. Hawkes[6], E. Lerche[3], P. Migliano[4], A. Peeters[4], C. Sozzi[1], M. Tsalas[5,6], D. Van Eester[3] and JET Contributors*

EUROfusion Consortium, JET, Culham Science Centre, Abingdon, OX14 3DB, UK
1)Istituto di Fisica del Plasma CNR, Milano, Italy
2)Università degli Studi di Milano-Bicocca, Milano, Italy
3)LPP-ERM/KMS, TEC partner, Brussels, Belgium
4)University of Bayreuth, Germany
5)FOM Institute DIFFER, TEC partner, Nieuwegein, The Netherlands
6)Culham Centre for Fusion Energy, Abingdon, OX14 3DB, UK
*See the Appendix of F. Romanelli et al., Proceedings of the 25th IAEA Fusion Energy Conference 2014, Saint Petersburg, Russia

Abstract

The main purpose of this work is to study the dependence of Trapped Electron Modes (TEM) threshold and of electron stiffness on the most relevant plasma parameters. Dedicated transport experiments based on heat flux scans and T_e modulation have been performed in JET in TEM dominated plasmas with pure ICRH electron heating and a numerical study using gyrokinetic simulations has been performed with the code GKW. Using multilinear regressions on the experimental data, the stabilizing effect of magnetic shear predicted by theory for our plasma parameters is confirmed while no significant effect of safety factor was found. Good quantitative agreement is found between the TEM

[†] doi:10.1088/0029-5515/55/11/113016

thresholds found in the experiments and calculated with linear GKW simulations. Non-linear simulations have given further confirmation of the threshold values and allowed comparison with the values of stiffness found experimentally. Perturbative studies using RF power modulation indicate the existence of an inward convective term for the electron heat flux. Adding NBI power, Ion Temperature Gradient (ITG) modes become dominant and a reduction of $|\nabla T_e| / T_e$ with respect pure ICRH, TEM dominant discharges has been experimentally observed, in spite of increased total electron power. Possible explanations are discussed.

7.1 Introduction

Recent findings on JET that ion heat transport can be considerably reduced in the core by electromagnetic effects related to high thermal and supra-thermal pressure gradients [1,2] have opened positive perspectives of reaching improved confinement regimes at high β. However, before extrapolating to ITER from present machines with dominant NBI ion heating, it is essential to complete the understanding of electron heat transport, which in ITER electron heating dominated plasmas may limit the benefits of improved ion confinement.

This paper is part of a long-lasting effort to characterize electron heat transport driven by Trapped Electron Modes (TEM) by means of dedicated experiments and theoretical modeling. Theory indicates that there is a critical value of the normalized inverse temperature gradient length $R/L_{Te} = R|\nabla T_e|/T_e$ (with R the tokamak major radius) above which TEM become unstable [3,4], so electron heat transport features a threshold $(R/L_{Te})_{crit}$, or κ_c, above which the electron heat flux increases strongly with R/L_{Te}. This property leads to stiffness of T_e profiles with respect to changes in heating profiles. The level of stiffness χ_s characterizes how strongly T_e profiles are tied to the threshold.

Numerical studies of TEM linear growth rate and threshold have been performed using linear gyrokinetic simulations with the code GS2 and the code KINEZERO, on the role of plasma parameters such as $s, R/L_n$ and effective collisionality $\nu_{eff} \approx 0.1 \cdot Z_{eff} \cdot n_e \cdot R/T_e^2$ on electron heat transport due to TEM. These simulations predict a stabilizing effect of the magnetic shear [5] and a dependence of the effect of collisionality on other plasma parameters, in particular on R/L_n [6]. In all the plasmas studied in this paper, the values of the density gradient and of the collisionality are such that a stabilizing effect of collisionality is expected. Experiments done in tokamak ASDEX-Upgrade confirmed the stabilizing effect of collisionality on TEM in our range of parameters [7], but no experimental evidence of the roles of magnetic shear and of density gradient has been obtained yet. The correlation between TEM threshold and the ratio of electron to ion temperature T_e/T_i has been investigated analytically and with linear gyrokinetic simulations with the code KINEZERO [7]. These studies predict different effects of T_e/T_i on TEM threshold depending on the value of R/L_n: for low values of R/L_n ($R/L_n \lesssim 1.3$) they predict a stabilizing effect of T_e/T_i, while a destabilizing effect of the same parameter is predicted with higher values of R/L_n. Studies on electron stiffness have been done on different machines. Studies performed on tokamak DIII-D indicate that stiffness increases with radius. A higher electron stiffness in presence of NBI heating was also observed in other studies in ASDEX-Upgrade, JET and DIII-D [9, 10, 11].

The aim of this paper is to study the dependence of turbulent electron heat transport due to TEMs on plasma parameters in JET plasmas with dominant RF electron heating obtained by ICRH in Mode Conversion and to compare the experimental observations with theory-based models, with also a comparison to previous studies. In particular, experimentally we identify separately the values of threshold and stiffness, which allows a more stringent comparison with theoretical predictions. Lastly, initial results of an investigation of the effect of the presence of significant ion heating (NBI) on TEM are presented.

The paper is organized as follows: in section 7.2 we present the experimental set up; in section 7.3 the main experimental observations in plasmas with dominant electron heating are presented; in section 7.4 the modeling effort is described and its results are compared with the experimental observations of section 7.3; in section 7.5 the effects of the presence of NBI heating are discussed; summary and conclusions are presented in section 7.6.

7.2 Experimental set up and methods

The discharges studied in this paper were made in the JET tokamak ($R = 2.96$ m $a \approx 1$ m) and are all L-mode $(^3He) - D$ plasmas with $B_T \approx 3.45$ T, $n_{e,0} \approx (2\text{–}3) \cdot 10^{19}$ m^{-3} and $I_p \approx 1.8 - 3$ MA. The session dedicated to TEM study is composed of seven discharges (described in Table 7.1) with ICRH (Ion Cyclotron Resonance Heating) of about $2.5 - 3$ MW deposited directly on electrons via Mode Conversion (MC) using a ^3He concentration $[^3He] \approx 20\%$, which ensures a dominant electron heating with about 70% of the ICRH power deposited on electrons [12].

	78830	**78834**	**78835**	**78836**	**78839**	**78840**	**78842**
B **(T)**	3.45	3.45	3.45	3.45	3.45	3.45	3.45
I_p **(MA)**	1.8 - 3 RU	1.8 OS	1.8 OS	1.8 OS	3 - 1.8 RD	3 -1.8 RD	1.8 OS
$ICRH$ **(MW)**	2.5	3	2.5	3	3	2.5	3
ν_{ICRH} **(MHz)**	32 On-axis	32 On-axis	37 Off-axis	37 Off-axis	32 Off-axis	37 On-axis	37 On-axis
NBI **(MW)**	0	0	0	6.8	0	0	6.8
$T_{e,0}$ **(keV)**	4	4	3	5	4	4	5
$T_{i,0}$ **(keV)**	2.5	2.5	2	5	2.5	2.5	5
$n_{e,0}$ **(m^{-3})**	3	3	3	3	3	3	3
Z_{eff}	2.2	2.2	2.2	2.2	2.2	2.2	2.2

Table 7.1: *Main parameters of the TEM session discharges. RU = Ramp-up, RD = Ramp-down, OS = Overshoot*

The RF power was square wave modulated with a 70/30 duty-cycle, a modulation amplitude of about 70% and a frequency of 20 Hz in order to use perturbative techniques to calculate TEM stiffness and threshold [13, 14]. The RF power deposition in MC scheme is not easily and reliably calculated by RF codes, and is therefore calculated by fitting the profiles of modulation amplitudes and phases of different harmonics using adjustable profiles of heat diffusivity, convection and RF heat deposition using the ASTRA transport code (Automated System for TRansport Analysis [15]). Fitting the highest harmonics, which are less influenced by transport and depend mostly on the power deposition, it is estimated that the uncertainty on such reconstruction of RF deposition is in the order of ±10%. ICRH power was deposited both on-axis ($R \approx 3.0$ m) and off-axis ($R \approx 3.4$ m) in order to obtain low and high values of heat flux q_e for the study of the electron heat flux scan versus $R/L_{Te} = R\left|\nabla T_e\right|/T_e$. In two of the analyzed discharges , NBI (Neutral Beam Injection) heating of about 6.8 MW was also used in order to study the effect of the presence of significant ion heating , i.e. of ITG modes, on TEM. NBI heating also introduces a high rotation of the plasma and the presence of a fast ion population. The NBI heating power on electrons and ions is calculated with the PENCIL code with an uncertainly of about ±100 kW. The ohmic power density is calculated using $P_{Ohm} = \eta \cdot j^2$, where η is the resistivity of the plasma and j is the plasma current density reconstructed by the EFIT equilibrium code with the MSE (Motional Stark Effect) constraints. The error on the estimated ohmic power is about 5%. The electron heat flux is calculated in gyro-Bohm units as $q_e = [(P_{e,Ohm} + P_{e,ICRH} + P_{e,NBI} - P_{e,rad} - P_{ei})/S] \cdot (R/T_e) \cdot (R/\rho_s^2 c_s)$, where S is the considered flux surface, $P_{e,rad}$ is the radiated power (negligible within $r/R \approx 0.8$), $c_s = \sqrt{T_e/m_i}$ and $\rho_s = c_s m_i/eB$. Typical error on electron heat flux is about $15 - 20\%$ of the total flux. The measurement of the electron temperature T_e is provided by the ECE (Electron Cyclotron Emission) diagnostic with an error on the measurements of about 5% while the ion temperature T_i and plasma rotation ω_t are measured by the Charge Exchange (CX) diagnostic with an error of about 5% for the ion temperature and of about 8% for the plasma rotation. The charge exchange diagnostic needs NBI heating; for the measurements of the ion temperature in discharges without NBI heating, blips of NBI heating of 1.5 MW and $\Delta t = 0.15$ s are used. The error on T_e/T_i is about $7 - 10\%$. The electron density n_e is measured by high-resolution Thomson scattering (HRTS) with an uncertainty of about 10%. Radial profiles of the ICRH power density on electrons $P_{e,ICRH}$ and of T_e, T_i, n_e, q, s of discharges n. 78834 (on-axis ICRH, no NBI), n. 78839 (off-axis ICRH, no NBI) and 78842 (on-axis ICRH, 7 MW NBI) are shown in Figure 7.1 and in Figure 7.2. The time waveforms of heating power of discharges n. 78834 and n. 78842 are shown in Figure 7.3 (note the ICRH modulation phase between $t = 5.5$ s and $t = 10$ s). The radial profiles of heating power of discharge n. 78834 are reported in Figure 7.4.

Values of $R/L_{Ti}, R/L_{Te}$ and R/L_n were obtained by linear best fit of $ln(T_i), ln(T_e)$ and $ln(n_e)$ data after having time averaged the measurements over a time interval in which the plasma conditions are stationary (usually$\Delta t \approx \pm 0.25$ s). The uncertainties on these parameters are then estimated by repeating the same procedure with different time and space intervals and evaluating the deviation in the set of values so obtained. Error bars are typically $\Delta(R/L_{Ti}) \approx \pm 0.3$–$0.6, \Delta(R/L_{Te}) \approx \pm 0.25 - 0.5$ and $\Delta(R/L_n) \approx \pm 0.3 - 0.6$. The spatial derivatives in these parameters are taken with respect to the flux surface label $r = (R_{out} - R_{in})/2$, where R_{out} and R_{in} are the outer and inner boundaries of the flux surface on the magnetic axis plane.

By using different time waveforms of the plasma current (I_p ramp-up, ramp-down and overshoot with $1.8 \lesssim I_p \lesssim 3$ MA, Figure 7.5), independent variations of the safety factor q and of the magnetic shear $\hat{s}$ (Figure 7.6) needed for the study of the correlation between these parameters and the TEM threshold were obtained. The safety factor q profiles are reconstructed by MSE with an error of about 20%. The error on the values of the magnetic shear $\hat{s}$ is estimated to be $\Delta s \approx \pm 0.08$. TEM threshold and electron stiffness at a chosen radial location are determined experimentally by quadratic fits on the diagrams of the normalized electron heat flux q_e as a function of R/L_{Te} on data points with $q, s, \nu_{eff}, R/L_n, T_e/T_i$ constant and using the formula (1) given below [16, 17]. Small values of q_e (nearest to threshold) necessary for the fits are obtained near the core ($\rho_{tor} < 0.4$) with off-axis heating while for the study far off-axis ($\rho_{tor} \approx 0.5$) data points from previously existing discharges with ICRH directed on ions are used.

The experimental set-up for these discharges is identical to that used for the TEM session except that the ICRH power is directed on ions, for which the power deposition is evaluated with the PION code.

The data analysis is carried out at 3 radial positions, corresponding to normalized radius $\rho_{tor} = \sqrt{(\Phi/\pi B_T)/\left(\Phi/\pi B_T\right)_{max}} = 0.33, 0.4, 0.5$, where Φ is the toroidal magnetic flux and B_T is the toroidal magnetic field.

7.3 TEM studies in dominant ICRH heating plasmas

In this section the experimental data analysis of the discharges with dominant electron heating (~3 MW of ICRH on electrons via MC) is presented. The main instability that is expected to determine the turbulent electron heat transport in these discharges is TEM and a study of TEM threshold, also including its dependence on some plasma parameters, and of the electron stiffness is carried out. For this purpose a direct analysis of the electron heat flux using a semi-empirical model (Critical Gradient Model), a perturbative study using the modulation of the electron temperature and a study using multilinear regressions are used.

The electron heat flux is predicted by theory to follow a gyro-Bohm scaling and to become turbulent above a threshold value of $\left|\nabla T_e\right|/T_e$, so that q_e can be written as [16, 17]

$$q_e = q_e^{res} + q^{1.5}\chi_s \frac{n_e T_e^2 \rho_s}{eBR^2}\frac{R}{L_{Te}}\left(\frac{R}{L_{Te}} - \kappa_c\right)\cdot\theta\left(\frac{R}{L_{Te}} - \kappa_c\right) \tag{7.1}$$

where q_e^{res} is the residual flux not carried by TEMs (neglected in our case for the discharges with dominant electron heating), κ_c is the critical R/L_{Te}value, χ_s is the stiffness coefficient and $\theta(\bullet)$ is the Heaviside function. Equation (7.1) is a semi-empirical model called critical gradient model (CGM). Evaluating the values of q_e from the volume integral of the calculated sources at different radii and times, we can build the curve of the gyro-Bohm normalized flux $q_e^{GB}/q^{1.5}$ versus R/L_{Te} (where $q_e^{GB} = q_e/(n_e T_e^2 \rho_s/eBR^2)$), which allows to identify κ_c as the intercept to zero flux, whilst χ_s can be inferred from the slope of the curve. In this section only the results obtained from discharges with dominant electron heating in which TEM are dominant are shown. The results obtained from the heat flux scan are shown in Figure 7.7, where points with the same color and marks correspond to experimental data with same values of $s, q, R/L_n, T_e/T_i, \nu_{eff}$ (reported in Table 7.2). For each set of points the threshold and stiffness values have been evaluated with equation (7.1). The values of stiffness and threshold are different at different radii and for different parameters. The stiffness is found to be higher at outer radius: the mean value of stiffness at $\rho_{tor} = 0.3$ is $\chi_s^{0.3} \approx 1.5$, at $\rho_{tor} = 0.4$ is $\chi_s^{0.4} \approx 3.2$ and at $\rho_{tor} = 0.5$ is $\chi_s^{0.5} \approx 3.2$.

The values of TEM threshold and stiffness are also calculated from the modulation data using the transport code ASTRA to simulate the profiles of time averaged T_e, amplitudes and phases with equation (7.1) as transport model and adjusting χ_s and κ_c to best fit the data. Using information from upper harmonics also the RF power deposition profile is reconstructed.The values found with this method are comparable with those obtained with the heat flux study and are shown in Figure 7.8 and in Figure 7.9 together with the fits obtained for T_e and $1st$ harmonic A, φ. The comparison with the values found with the heat flux scan is shown in Figure 7.10. Furthermore, the perturbative study confirms the growth of the stiffness with radius. In order to reproduce the profiles of the electron temperature with ASTRA simulations, a heat pinch $U \sim 3$ m/s is needed because of the

ρ_{tor}	# fit	R/L_n	q	$\hat{s}$	T_e/T_i	ν_{eff}	κ_c	χ_s
$\rho_{tor} = 0.33$	(1)	1.7	1.3	0.3	1.4	0.2	~ 6	~ 1.8
	(2)	2.3	1.3	0.6	1.3	0.2	~ 7	~ 1.3
$\rho_{tor} = 0.4$	(1)	2.5	1.6	0.7	1.3	0.4	~ 6.3	~ 2.5
	(2)	2.6	1.5	0.8	1.3	0.4	~ 6	~ 3.8
	(3)	3.2	1.2	0.7	1.4	0.3	~ 7.1	~ 3.3
$\rho_{tor} = 0.5$	(1)	2.5	1.6	0.7	1.3	0.4	~ 6.8	~ 3.0
	(2)	2.7	2.3	0.9	1.3	0.4	~ 7.3	~ 3.9
	(3)	3.1	1.4	1	1.3	0.6	~ 7.8	~ 3.4
	(4)	2.6	2	1.2	1.2	0.6	~ 8.3	~ 2.5

Table 7.2: *Mean values of $s, q, R/L_n, T_e/T_i, \nu_{eff}$ of the data points used for the fits shown in Figure 7.7 and corresponding threshold values.*

high stiffness in the core indicated by the modulation profiles. An electron heat pinch was also observed in DIII-D, FTU, ASDEX-Upgrade and Tore Supra discharges [18, 19, 20, 21].

Since the subset of points with identical parameters plotted in Figure 7.7 is significantly smaller than the total set of points, in order to best estimate the correlations between TEM threshold and plasma parameters from the heat flux scan data, a multilinear regression method with the whole data set is used. In order to use values of κ_c instead of actual R/L_{Te} in the regressions, for each experimental measurement at a given radius and time, formula (1) is used with $q^{res} = 0$ and the mean values of stiffness found experimentally to extrapolate to the threshold from the experimental value of R/L_{Te}. The multilinear regressions express κ_c in the form $\kappa_c = \sum_j C_j X_j$, where C_j are the estimated regression coefficients and the vectors of regression variables X_j represent the considered plasma parameters. All values of κ_c used in the regressions are divided by the factor $(0.357\sqrt{\epsilon} + 0.271)/\sqrt{\epsilon}$, where $\epsilon = r/R$ and which takes into account the radius at which the thresholds are measured and allows regressions mixing data from different radii. This coefficient is the same used in [5].

In the present work, all the regressions are performed with a robust fit algorithm (Tukey algorithm), which uses iteratively re-weighted least squares with the bi-square weighting function, and are performed with MATLAB[*]. To test the validity of the regression models, a Student's t-test is used. The t-statistic is useful for making inferences about the regression coefficients and it tests the hypothesis that a coefficient is equal to zero – meaning the corresponding term is not significant – versus the alternate hypothesis that the coefficient is different from zero. A high value of tStat ($>> 1$), that corresponds to a low p-value, indicates that the corresponding parameter is important in the model. Here we decided to take only parameters with $p - value < 0.05$, which indicates that the parameters is statistical significant in the model at 95%. To test and compare different models, the p-value of the models, the F-statistic and the R^2_{adj} of the models are used. The F-statistic indicates the statistical significance of a whole model and it is useful to compare 'complete' models with reduced models. The higher the value of the F-statistic is, the higher is the significance of the model. The R^2_{adj} value indicate the amount of the variability in the response data that the model can explain: a value of 1 indicates that the model can explain all the response dataset while a value of 0 indicates that the model

---

[*] http://www.mathworks.it/

can not explain any point of the dataset. All the statistical test function used for this study are incorporated in the MATLAB script used for the regressions ('fitlm').

The plots of κ_c as a function of the various plasma parameters considered in the regressions are shown in Figure 7.11. In these plots the mean value (blue dashed line), the standard deviations from the mean value (green dashed lines) and the experimental error on the mean value (red continuos lines) of the parameters are shown.

As it appears from these plots, there is a clear positive correlation between the threshold and the magnetic shear, a less evident positive correlation between threshold and collisionality and no correlation is evident with the safety factor. Regarding $T_e/T_i, R/L_n$ and ν_{eff}, it appears that their experimental range does not allow a clear study of the effect of these two parameters on electron heat transport.

The covariance matrix for the considered parameters is shown in Table 7.3 and was calculated with MATLAB using all the experimental values at $\rho_{tor} = 0.4, 0.5$.

	κ_c	R/L_n	q	$\hat{s}$	ν_{eff}	T_e/T_i
κ_c	1	0.4	0.3	0.7	0.5	- 0.2
R/L_n	-	1	- 0.4	0.5	-0.1	0.2
q	-	-	1	0.04	0.5	- 0.2
$\hat{s}$	-	-	-	1	0.6	- 0.2
ν_{eff}	-	-	-	-	1	- 0.3
T_e/T_i	-	-	-	-	-	1

Table 7.3: *Covariance matrix between the plasma parameters for the data at* $\rho_{tor} = 0.4, 0.5$.

The strongest correlations with κ_c that appear from the covariance matrix are again those with $\hat{s}$ and ν_{eff}. Also, correlations between $\hat{s}$ and $\nu_{eff}, R/L_n$ are observed that could distort the regressions. To establish which parameters are the most influent on the threshold a number of regressions with different sets of parameters has been performed. A first multilinear regression was made using the complete set of parameters of Table 7.3.

	Estimate	SE	tStat	p-Value	MODEL:
$Intercept$	1.4	0.8	1.3	0.2	$R^2_{adj} = 0.54$
R/L_n	0.8	0.2	4.0	1e-04	$p - Value = 5e - 24$
q	0.7	0.2	4.0	9e-05	$F_{stat} = 36.4$
s	1.7	0.4	4.0	1e-04	
T_e/T_i	- 0.1	0.2	- 0.7	0.5	
$log(1 + 20\nu_{eff})$	0.5	0.3	1.6	0.1	

The low values of tStat and the high values of p-Value of T_e/T_i and collisionality indicate that these two parameters can be removed from the model. Omitting them a new model is obtained:

	Estimate	SE	tStat	p-Value	MODEL:
$Intercept$	1.8	0.6	3.3	1e-03	$R^2_{adj} = 0.54$
R/L_n	0.6	0.2	3.4	8e-04	$p - Value = 1e - 25$
q	0.9	0.2	5.4	3e-07	$F_{stat} = 60.6$
s	2.3	0.3	7.9	7e-13	

The new model has the same R^2 and a higher F_{stat} than the complete one: this indicate that this model is more significant. All the coefficients of this model seem solid looking at their tStat and p-Value, but there are correlations between R/L_n and $\hat{s}$ and between R/L_n and q as indicated by the covariance matrix (Table 7.3). To establish how much these correlations influence the results, regressions with only two parameters are made:

	Estimate	SE	tStat	p-Value	MODEL:
$Intercept$	0.8	0.7	1.2	0.2	$R^2_{adj} = 0.36$
R/L_n	1.4	0.2	8.4	2e-14	$p - Value = 2e - 15$
q	1.3	0.2	7.1	4e-11	$F_{stat} = 42.8$

	Estimate	SE	tStat	p-Value	MODEL:
$Intercept$	3.5	0.3	11.0	5e-21	$R^2_{adj} = 0.51$
q	0.6	0.1	4.1	7e-05	$p - Value = 1e - 24$
s	2.9	0.2	11.8	3e-23	$F_{stat} = 80.7$

	Estimate	SE	tStat	p-Value	MODEL:
$Intercept$	4.3	0.4	11.4	2e-13	$R^2_{adj} = 0.46$
R/L_n	0.1	0.2	0.6	0.6	$p - Value = 1e - 21$
s	2.9	0.3	9.5	4e-17	$F_{stat} = 64.6$

The coefficient of R/L_n is strongly influenced by the set of parameters used in the regression while it appears that the coefficient of the magnetic shear is the most reliable and the most stable among the various regressions. From the regressions it appears also that there is a weak correlation between the threshold and the safety factor. Lastly, a regression using only magnetic shear is presented.

	Estimate	SE	tStat	p-Value	MODEL:
$Intercept$	4.4	0.2	20.3	8e-45	$R^2_{adj} = 0.46$
s	2.9	0.3	11.3	7e-22	$p - Value = 7e - 22$, $F_{stat} = 128$

It appears from these regressions that the most significant parameter is $\hat{s}$, which has the most stable coefficient and that alone can explain almost 50% of the variation of the threshold. As appears from Table 7.3, there is a correlation between $\hat{s}$ and other parameters. This can have a great influence on the results of the regressions. In order to isolate the correlation between the magnetic shear and the threshold in a more accurate way, a sub dataset is created, in which the only relevant variation is that of $\hat{s}$. A dataset was found with 46 experimental points and with $1.23 \leq T_e/T_i \leq 1.31$; $0.33 \leq \nu_{eff} \leq 0.55$; $2.1 R/L_n \leq 3.2$; _$1.2 \leq q \leq 2.7$; $0.21 \leq \hat{s} \leq 1.2$. There are again relevant variations of the safety factor and of the magnetic shear, while the other parameters can be considered fixed. The covariance matrix for this sub dataset is reported in Table 7.4.

	κ_c	q	$\hat{s}$
κ_c	1	0.2	0.7
q	-	1	- 0.1
$\hat{s}$	-	-	1

Table 7.4: *Covariance matrix between the plasma parameters for the sub dataset at* $\rho_{tor} = 0.4, 0.5$.

Two regressions has been made using this sub dataset: a regression made taking into account $\hat{s}$ and q and a regression with only the magnetic shear.

	Estimate	SE	tStat	p-Value	MODEL:
Intercept	5.2	0.4	12.3	5e-21	$R^2_{adj} = 0.51$
q	0.3	0.1	1.9	0.06	$p - Value = 4e - 06$
s	2.0	0.3	5.9	2e-06	$F_{stat} = 19$

	Estimate	SE	tStat	p-Value	MODEL:
Intercept	5.7	0.3	18.4	6e-19	$R^2_{adj} = 0.49$
s	2.0	0.3	5.9	2e-06	$p - Value = 2e - 06$; $F_{stat} = 34$

These regressions confirm the positive correlation between the threshold and $\hat{s}$ that appears in Figure 7.11, in all the regressions presented and from the covariance matrices (Table 7.3 and Table 7.4). Moreover, they show again that there is not a strong correlation between the threshold and the safety factor.

Another proof of the positive correlation between the magnetic shear and κ_c and of the low effect of safety factor is visible also in Figure 7.77 for the points at $\rho_{tor} \approx 0.5$. Looking at Table 7.2, and using the results from regressions, the correlation between the change of threshold (6.8 -> 8.4) and the change of the magnetic shear (0.7 -> 1.2) is clear. We tried to calculate the correlation between threshold and magnetic shear for the points at $\rho_{tor} = 0.5$ in Table 7.2 using multilinear regressions. It appears from regressions that the only important parameters is $\hat{s}$.

	Estimate	SE	tStat	p-Value	MODEL:
Intercept	4.7	0.3	17.6	3e-03	$R^2_{adj} = 0.98$
s	3.1	0.3	11.3	8e-03	$p - Value = 8e - 03$; $F_{stat} = 128$

To conclude, a clear positive correlation between TEM threshold and magnetic shear was observed from the data analysis: the magnetic shear has a stabilizing effect on ∇T_e instabilities. Also, from our analysis it appear that the safety factor doesn't afflict in a strong way this kind of instabilities for our range of parameters.

7.4 Modelling and comparison with experiments

The analysis presented in the previous section provides an overview of the TEM instability characteristics, concerning the typical threshold values, the level of electron stiffness and a proof of the stabilizing effect of the magnetic shear on TEM. We want now to compare these experimental results with gyrokinetic simulations in order to establish if the theory can predict the observed values of the TEM threshold, the linear dependences of TEM threshold on the considered plasma parameters and the experimental electron heat flux levels. For this aim a set of linear and nonlinear simulations with the gyrokinetic code GKW [25, 26] were carried out on supercomputers HECTOR[†] and HELIOS[‡].

With the results obtained with the linear simulations an indicative formula to predict TEMs thresholds was found. In this section the values of thresholds predicted by this

---

[†] http://www.hector.ac.uk/

[‡] http://www.iferc.org/

formula are compared both with the experimental values and with the values predicted by a previous formula presented by A. G. Peeters in [5]:

$$\kappa_c^{[5]} \approx \frac{0.357\sqrt{\epsilon}+0.271}{\sqrt{\epsilon}}\left(4.90-1.21\frac{R}{L_n}+2.68\hat{s}+log(1+20\nu_{eff})\right) \tag{7.2}$$

This formula was derived from linear simulations with the code GS2, using plasma parameters from discharges of ASDEX-Upgrade and circular geometry and was not meant to give an universal scaling but rather to highlight the main dependences of TEM threshold on plasma parameters in the range of the AUG discharges considered.

Nonlinear simulations allow to estimate the electron heat flux and are used to try to reproduce the experimental levels of the flux and the experimental level of electron stiffness.

7.4.1 Linear simulations

In a linear simulation, GKW finds the fastest growing eigenmode in the plasma excited by a perturbation of a prescribed length scale. This length scale is defined by a bi-normal (perpendicular to both the magnetic field line and the flux surface normal vector) Fourier mode wavenumber k_θ that is provided as input to the code. The main output of the code used in this analysis is the linear growth rate of the eigenmode, and from its other characteristics, such as real frequency or parallel structure, the main driving mechanism of the instability can be determined (ITG, TEM etc.).

All linear simulations have been performed with kinetic electrons, collisions, Miller geometry, electro-static perturbations only ($\beta = 0$) and $k_\theta \rho_i = 0.4$. The plasma parameters used as inputs in the simulations are typical values of the TEM session discharges at $\rho_{tor} = 0.5$. The reference set is given by electron and ion density $n_e = n_i = 1.97 \cdot 10^{19}$ m^{-3}, electron temperature $T_e = 1.45$ keV, ion temperature $T_i = 1.15$ keV, normalized inverse gradient lengths of the density and ion temperature profile are $R/L_n = 3.4, R/L_{Ti} = 4$, safety factor $q = 2.01$, magnetic shear $\hat{s} = 0.99$, inverse aspect ratio $\epsilon = r/R = 0.19$, and effective charge $Z_{eff} = 2.16$. Starting from the reference case, the values of the growth rate as a function of R/L_{Te} are calculated in the range $0 \leq R/L_{Te} \leq 16$, with different values of $s, R/L_n, \nu_{eff}, T_e/T_i$ to study the correlations between these parameters and TEM growth rate. In this kind of simulations, just the main instability growth rate is calculated. The real part of the frequency allow to determine which kind of instability is observed: in this case the transition between ITG to TEM dominant instability is located in the region where the growth rate starts to increase significantly with R/L_{Te}(this region is indicated with a line in Figure 7.12). The values of the threshold are then obtained by performing a parabolic fit on the points of the curve of γ versus R/L_{Te} where TEM are dominant (real part of the frequency $\omega_{k_\theta} < 0$) and then by an extrapolation to $\gamma = 0$.

Figure 7.12 shows results obtained for the scans in $\hat{s}, R/L_n, \nu_{eff}$ and T_e/T_i. The linear simulations indicate a stabilizing effect of the magnetic shear $\hat{s}$ and of the collisionality while a destabilizing effect of R/L_n on TEM is predicted, especially for higher values of R/L_n ($R/L_n > 3$). The effect of T_e/T_i, while significant in the ITG regime, is very weak in the TEM regime.

An indicative formula for the TEM threshold is obtained using the results from linear simulations:

$$\kappa_c^{GKW} \approx \frac{0.357\sqrt{\epsilon}+0.271}{\sqrt{\epsilon}}\left(-1.2-0.11\frac{R}{L_n}+2.5\hat{s}+2.5log(1+20\nu_{eff})\right). \tag{7.3}$$

The comparisons with the experimental thresholds and with the ones obtained with formula (4) are shown in Figure 7.13. First of all, the trend of the thresholds obtained with the formula based on GKW linear simulations is in good agreement with the experimental ones. The simulations predict the stabilizing effect of the magnetic shear, also found experimentally, and the weak effect of R/L_n (weaker than that found in [5] for their range of parameters). The stabilizing effect of collisionality predicted by the simulations is stronger than that found experimentally. The correlation between ν_{eff} and $\hat{s}$ found in the experimental data could hide a stronger experimental correlation between κ_c and ν_{eff}. The values of the thresholds predicted by linear simulations are in good quantitative agreement with the experimental ones.

7.4.2 Nonlinear simulations

Non-linear gyrokinetic simulations allow to calculate the electron heat flux values and so to do a direct comparison with the experimental electron temperature stiffness. In a non-linear run the simulation domain and spatial resolution in the perpendicular plane is determined by a set of coupled bi-normal and radial Fourier-modes. Input to the code are the range and number of bi-normal modes and number of radial modes. The coupling between these modes provides a numerical scheme which is equivalent to the ballooning approximation commonly applied in other gyrokinetic codes, such as GS2.

In all simulations the value of the maximum binormal mode is fixed to $(k_\theta \rho_i)_{max} = 1.6$, collisions are considered, Miller geometry is used and all simulations have $\beta = 0.0008$ (to stabilize some long wavelength instabilities, like the electrostatic shear-Alfven waves, allowing a much larger stable time step). The plasma parameters used as inputs are taken at $\rho_{tor} = 0.5$ from the pulse n.78834 and averaged in the time interval $6.855 \leq t \leq 7.155$ s. The main input parameters are electron and ion density $n_e = n_i = 1.94 \cdot 10^{19}$ m^{-3}, electron temperature $T_e = 1.35$ keV, ion temperature $T_i = 1.11$ keV, normalized inverse gradient lengths of the density and ion temperature profile $R/L_n = 2.63, R/L_{Ti} = 3$, safety factor $q = 2.08$, magnetic shear $\hat{s} = 1.14$, inverse aspect ratio $\epsilon = r/R = 0.19$, and effective charge $Z_{eff} = 2.16$. The values of the heat flux at $\rho_{tor} = 0.5$ are calculated for $R/L_{Te} = 8.5, 9.1, 9.5, 10.1, 10.5$. All simulations were carried out considering 43 values of binormal modes k_θ and 167 values of radial modes k_Ψ. An estimate of threshold and stiffness is obtained performing a parabolic fit on the curve $q_{e,gB}/q^{3/2}$ versus R/L_{Te} following the formula (1). The obtained results are shown in Figure 7.14. Considering the uncertainties on the measurements of the plasma parameters used as input for the simulations and the uncertainty on the theoretical determination of the threshold values, the experimental threshold and the theoretical threshold are in good agreement. The validation of threshold models is important because for the experimental conditions in which electrons are close to marginality (which is the case in highly performing scenarios in present large machines and ITER due to low gyro-Bohm normalized heat flux) we can have a reliable prediction of plasma profiles from linear TEM theory, as stiffness considerations close to marginality do not matter. The flux levels and the related stiffness are lower than the experimental ones, but a rigorous study changing the input parameters in the experimental error bar range and considering high-k ETG modes, which may contribute to the transport, is needed to achieve an accurate comparison between simulations and experiments. This study is not included in this preliminary analysis due to limited computational resources, but will be presented in a future paper.

7.5 TEM studies in plasmas with dominant NBI heating

The results presented in section 7.3 and 7.4 concern plasmas with dominant electron heating leading to dominant TEM instability, where the main source of heating is 3MW of ICRH directed on electrons via MC. This section focuses on the analysis of electron heat transport in presence of significant NBI power in order to strengthen the ITG component. It was observed that the presence of substantial NBI heating causes a significant change in the ion heat transport, with a strong reduction of the ion stiffness [1, 2]. In order to establish which effect the presence of NBI heating has on the electron channel, two discharges with 3 MW of ICRH power directed on electrons and 6.8 MW of NBI power were carried out in the JET TEM session. In these discharges lower values of R/L_{Te} were found, compared with discharges without NBI heating for same values of normalized heat flux $q_{e,gB}$, as shown in Figure 7.15. The main differences in plasma parameters between these discharges and those with dominant electron heating are different values of $T_e/T_i(1.2-1.6$ in the ICRH case, $0.8-1$ in the ICRH+NBI case), different rotation of the plasma and different values of $R/L_{Ti}(3-5$ in the ICRH case, $5-7$ in the ICRH+NBI case). The effect of T_e/T_i on TEM, as indicated by linear simulations with GKW, are not expected to be the cause of the observed decrease in R/L_{Te}. High values of R/L_{Ti} could have some effects on the electron heat transport, if a significant fraction of electron heat flux is driven by ITG modes. However we know from [1, 2] that in this kind of shots with NBI and ICRH, strong ion de-stiffening is observed (ascribed to electromagnetic stabilization of ITG by fast ions pressure gradient), which leads to a significant decrease of flux driven by ITGs (both ion and electron flux). Therefore this mechanism does not appear a plausible candidate to explain observations, especially at inner radii where the magnetic effects on ITG are stronger.

A second effect that could be correlated to high value of R/L_{Ti} could concern the electron stiffness. The perturbative study, shown in Figure 7.16, indicates indeed higher values of stiffness with NBI heating. An increase of electron stiffness in presence of NBI heating has also been previously reported [9, 10, 11]. However, the effects of the presence of NBI heating on ITG and the results from linear simulations with GKW, shown in Figure 7.17, indicate that the higher electron stiffness are not correlated with the higher values of R/L_{Ti}. Higher values of R/L_{Ti}, as indicated in Figure 7.17, seem to stabilize the TEM for lower values of $k_\theta \rho_i$, which are known to be responsible of most of the heat flux due to TEM.

A third possibility is that, due to lower values of T_e/T_i, ETG modes could be more unstable [30] and increase the electron heat transport. This effect could be investigate with dedicate gyrokinetic simulations that take into account the electron scale instabilities.

We would like to underline the opposite behavior observed in the ion and electron channels when NBI heating is added to pure ICRH plasma. This is shown in Figure 7.18. For ions, as reported in [1, 2], a significant reduction in stiffness is observed. Unfortunately, this is not observed in the electron channel, for which at the contrary an increase in stiffness and a threshold reduction are observed. Since ITER will be dominated by electron heating, i.e. $T_i \leqslant T_e$, it is important to continue the effort to understand the mechanisms that govern electron transport in mixed ITG+TEM regime, since such high electron stiffness (if it would be extrapolated to ITER) may partly cancel the benefit of ion de-stiffening. On the positive side, we note that a beneficial point is in any case that the TEM electron threshold is significantly higher than the ITG ion threshold, therefore allowing some increase in R/L_{Ti} due to de-stiffening even in presence of high electron stiffness.

7.6 Conclusions

Experiments have been carried out in JET L-mode plasmas with dominant ICRH electron heating to explore the q and $\hat{s}$ dependence of TEMs using I_p ramp-up, ramp-down and overshoots in order to obtain non correlated variations of the safety factor and magnetic shear. Scans of electron heat flux and T_e modulation have been used to determine electron threshold and stiffness. The experimental results have been found in good agreement with theoretical predictions, in particular a first experimental confirmation of the stabilizing effect of the magnetic shear $\hat{s}$ on TEMs has been obtained. Also no experimental evidence of strong dependences of the TEM threshold on safety factor has been found. The effects of $R/L_n, T_e/T_i$ and ν_{eff}, given the low variations of these parameters, were not isolated in a satisfactory manner. Furthermore, an increase of the experimental electron stiffness with radius was observed. To be noted, a convective component of the electron heat flux was required in the simulations to achieve good reproduction of the data.

With the experimental parameters as input, a large number of linear gyrokinetic simulations and also a limited number of non-linear simulations were carried out using GKW. The simulations have confirmed the stabilizing effect of magnetic shear and collisionality and predict a weak destabilizing effect of R/L_n. The study of the effect of T_e/T_i suggests that this parameter does not significantly affect either the values of the threshold or the growth rate of the TEM. An indicative formula for the prediction of the TEM threshold was obtained from the results of the linear simulations. This is found to slightly underestimate the experimental observations. Nonlinear simulations with GKW has allowed a comparison with the experimental stiffness. In general, linear and nonlinear gyrokinetic simulations with GKW are in agreement with the experimental values of the TEM threshold and also with the observed dependences of the threshold on plasma parameters.

When significant ion heating (NBI heating) is added, leading to a transition from dominant TEM to mixed ITG-TEM with dominant ITG, a higher electron stiffness and lower values of R/L_{Te} with same levels of $q_{e,gB}$ are observed. These effects could be due to the presence of other modes like ETG (Electron Temperature Gradient modes) due to lower values of T_e/T_i. The full theoretical understanding, via nonlinear simulations, of electron heat transport in these mixed ITG-TEM conditions goes beyond the scope of the present paper, but it deserves further work both experimentally and theoretically given its importance to achieve reliable predictions for ITER, which is electron heating dominated.

Acknowledgement

The authors would like to thank Jonathan Citrin for precious advice and stimulating discussions.

A part of this work was carried out using the HELIOS supercomputer system at Computational Simulation Centre of International Fusion Energy Research Centre (IFERC-CSC), Aomori, Japan, under the Broader Approach collaboration between Euratom and Japan, implemented by Fusion for Energy and JAEA. The linear gyrokinetic simulations were performed on Hector supercomputer (UK Research Councils).

This work has been carried out within the framework of the EUROfusion Consortium and has received funding from the Euratom research and training programme 2014-2018 under grant agreement No 633053. The views and opinions expressed herein do not necessarily reflect those of the European Commission.

Figures

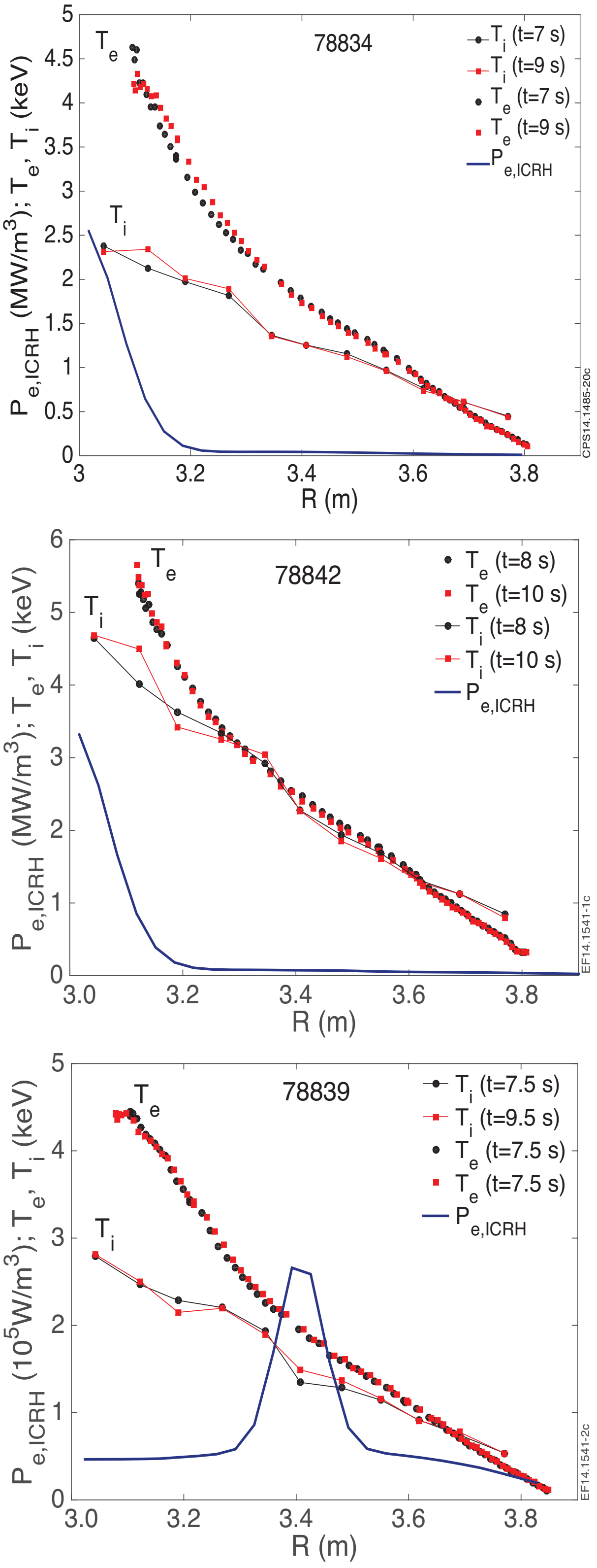

Figure 7.1: *Radial profiles of electron and ion temperatures and of P_{ICRH} deposition of discharges n. 78834 (ICRH on-axis, no NBI), n. 78842 (ICRH on-axis, 7 MW NBI) and n. 78839 (ICRH off-axis, no NBI) at two different times.*

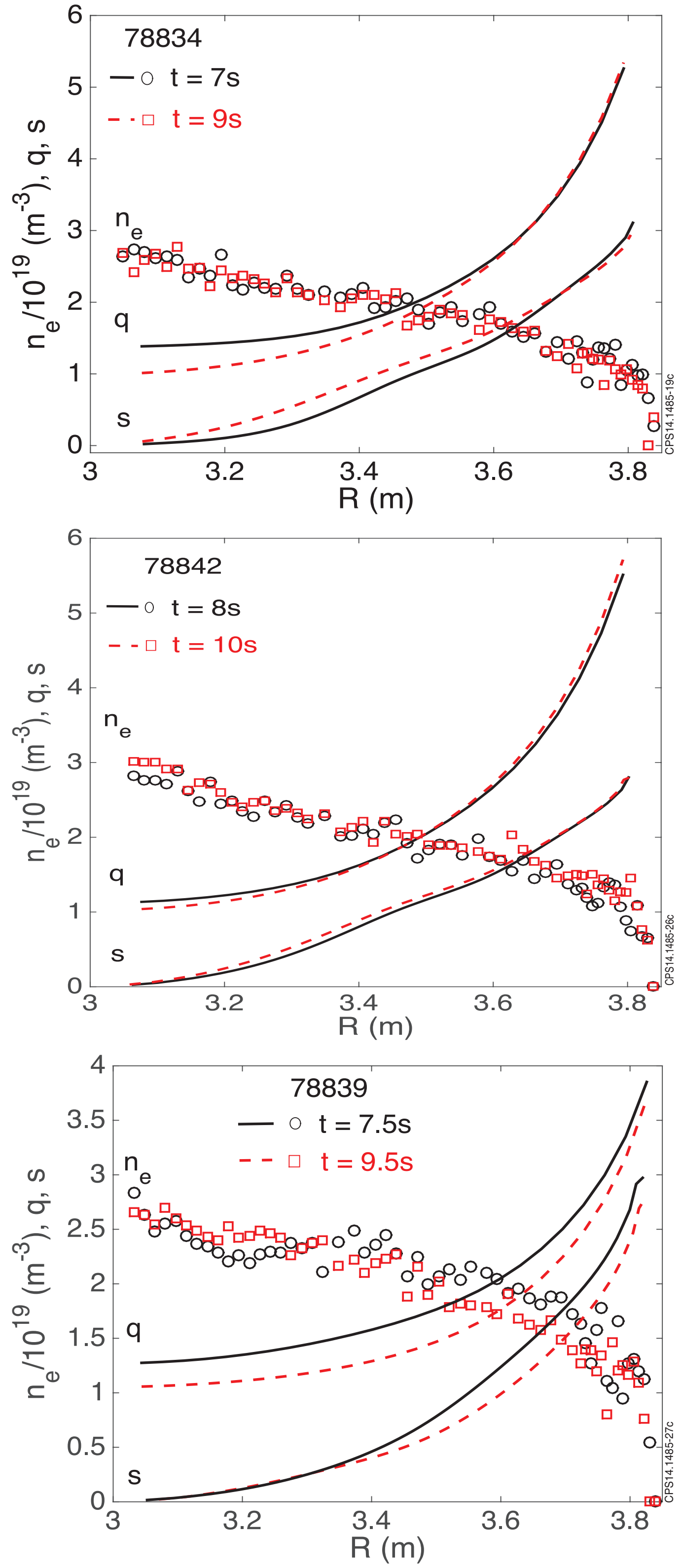

Figure 7.2: *Radial profiles of electron density, safety factor and magnetic shear of discharges n. 78834 (ICRH on-axis, no NBI), n. 78842 (ICRH on-axis, 7 MW NBI) and n. 78839 (ICRH off-axis, no NBI) at two different times.*

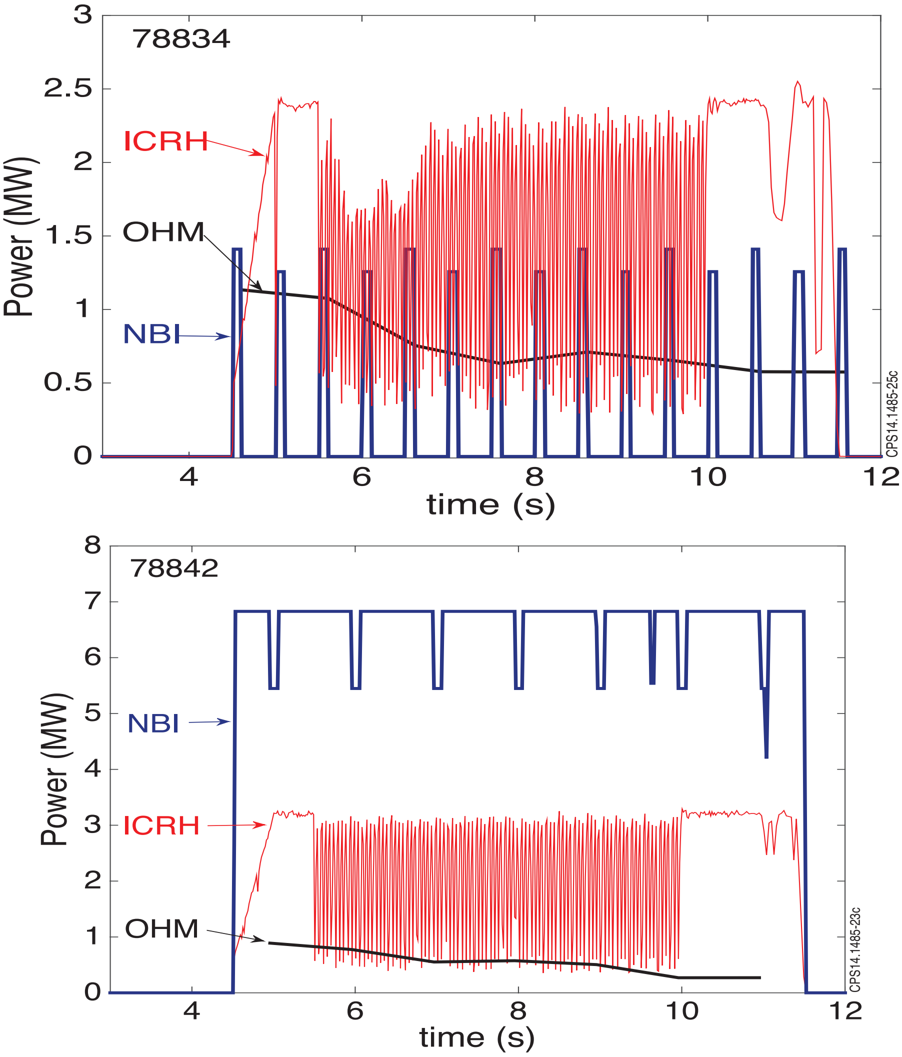

Figure 7.3: *Time waveforms of heating powers of discharges n. 78834 (ICRH on-axis, no NBI) and n. 78842 (ICRH on-axis, 7 MW NBI).*

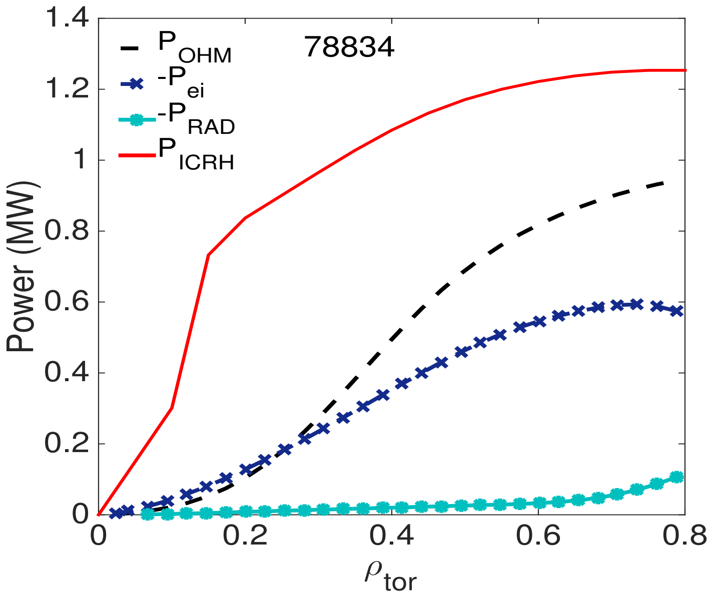

Figure 7.4: *Radial profiles of NBI heating (P_{NBI}), ohmic heating (P_{OHM}), ICRH heating (P_{ICRH}), radiated power (P_{RAD}) and heat exchange power due to ion-electron collisions ($P_{e,i}$) of the discharge n. 78834.*

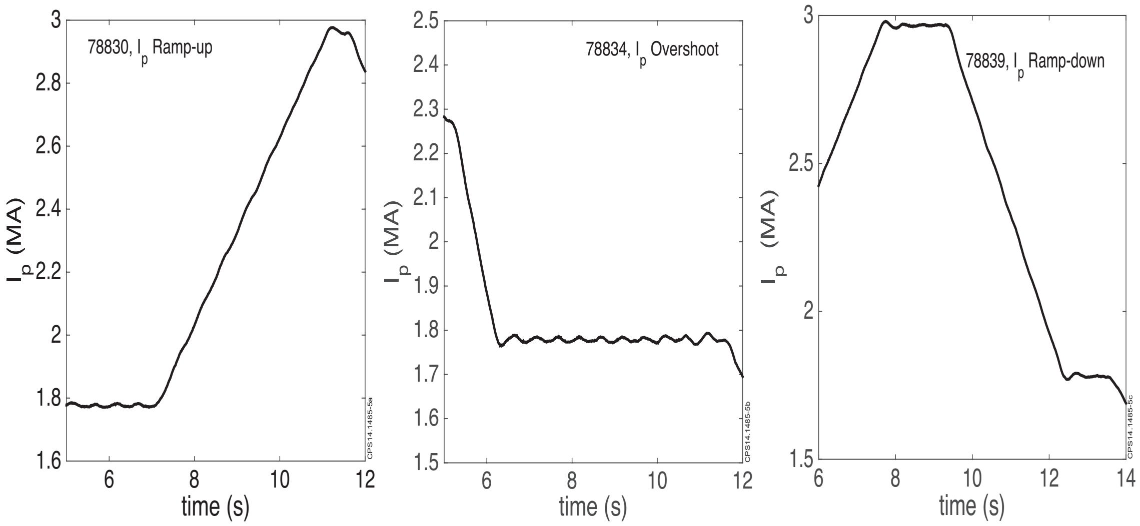

Figure 7.5: *Time waveforms of plasma current of discharges n. 78830 (I_p ramp-up), n. 78834 (I_p overshoot) and n. 78839 (I_p ramp-down).*

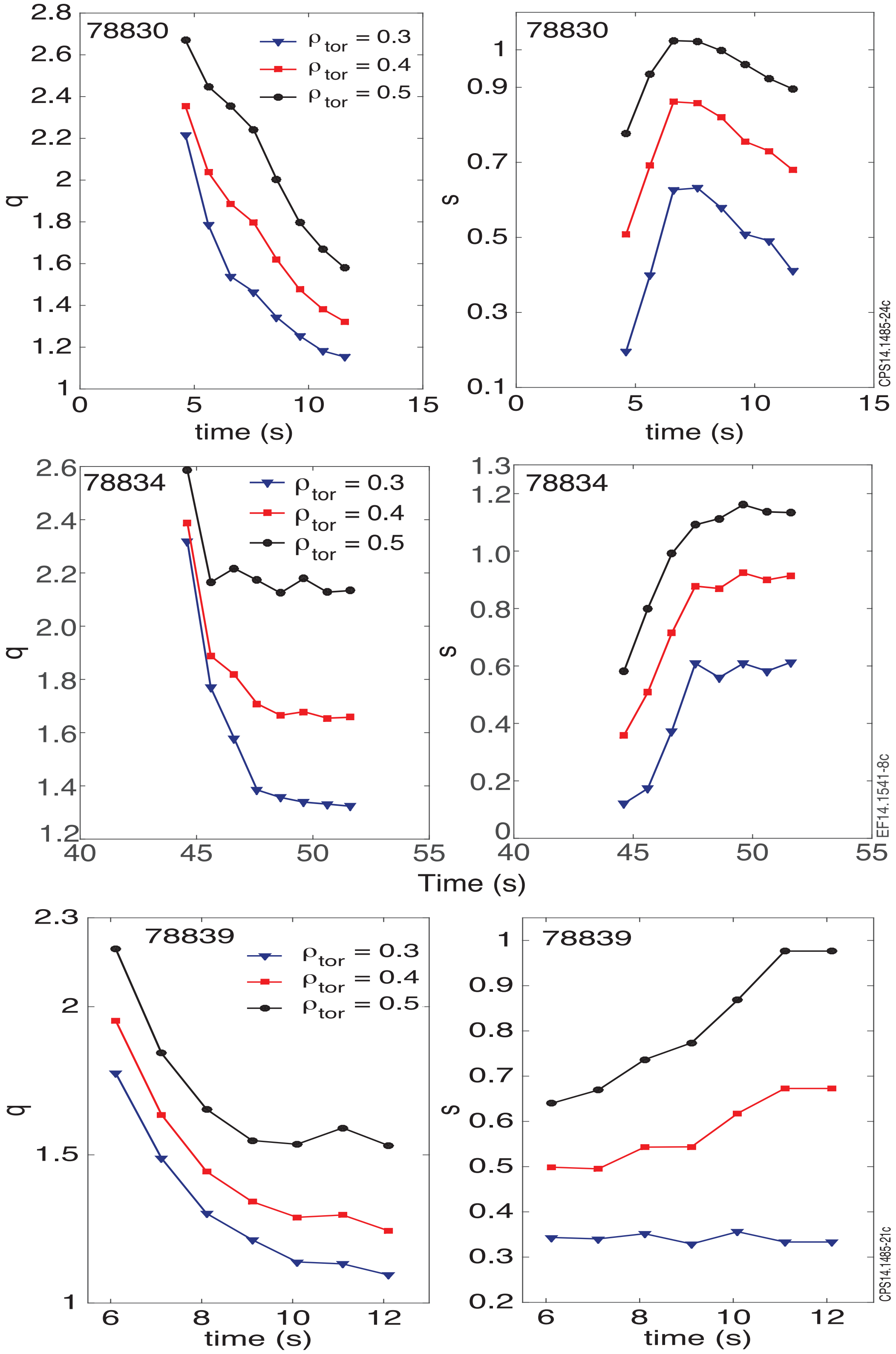

Figure 7.6: *Time evolution of safety factor and magnetic shear of discharges n. 78830 (I_p ramp-up), n. 78834 (I_p overshoot) and n. 78839 (I_p ramp-down) at* $\rho_{tor} = 0.33, 0.4, 0.5$.

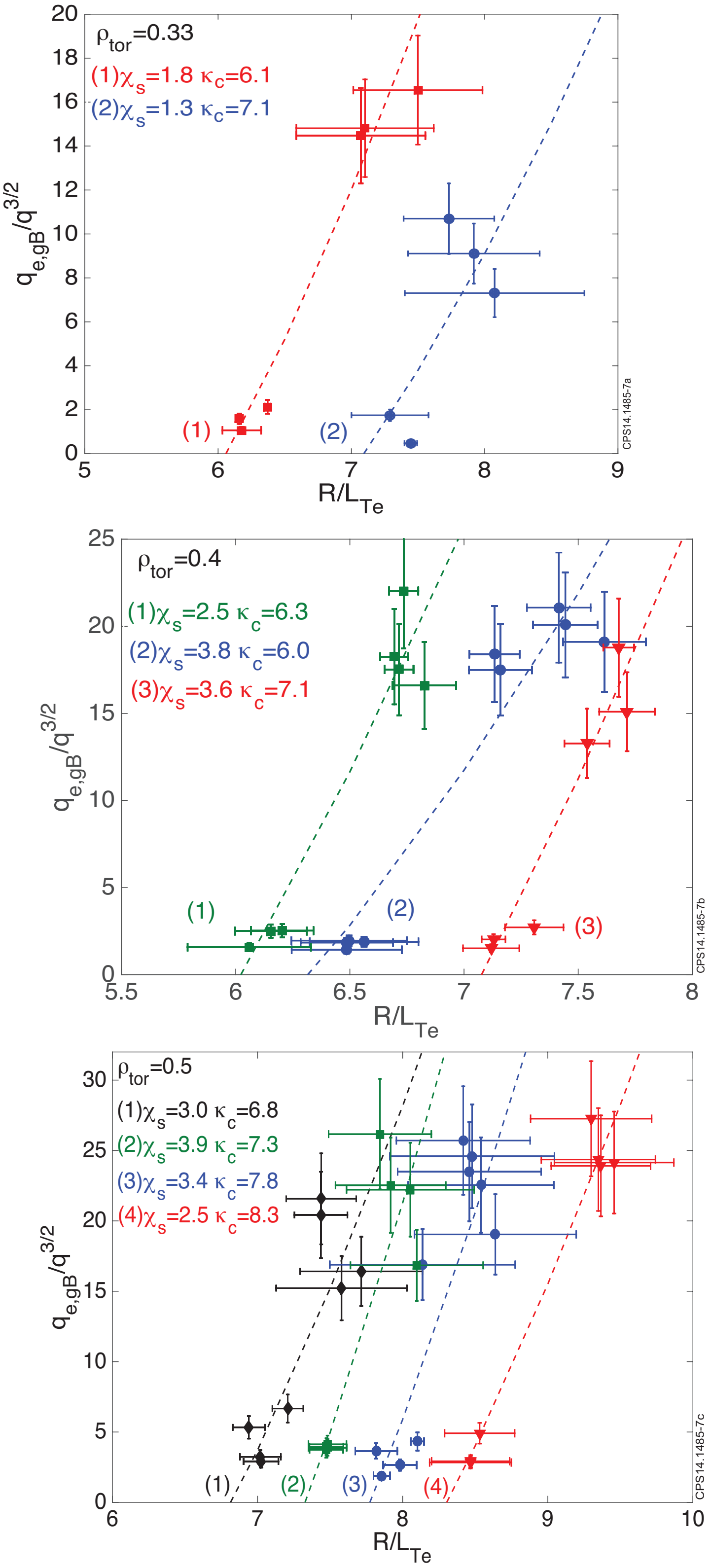

Figure 7.7: *Normalized electron heat flux as a function of* R/L_{Te}*at* $\rho_{tor} = 0.3, 0.4, 0.5$*. At each radius points with same colors and marks correspond to experimental points with same values of* $R/L_n, s, q, T_e/T_i, \nu_{eff}$*. For each set of points the corresponding value of* χ_s *is indicated. The threshold is the intercept at zero flux as indicate in the figures.*

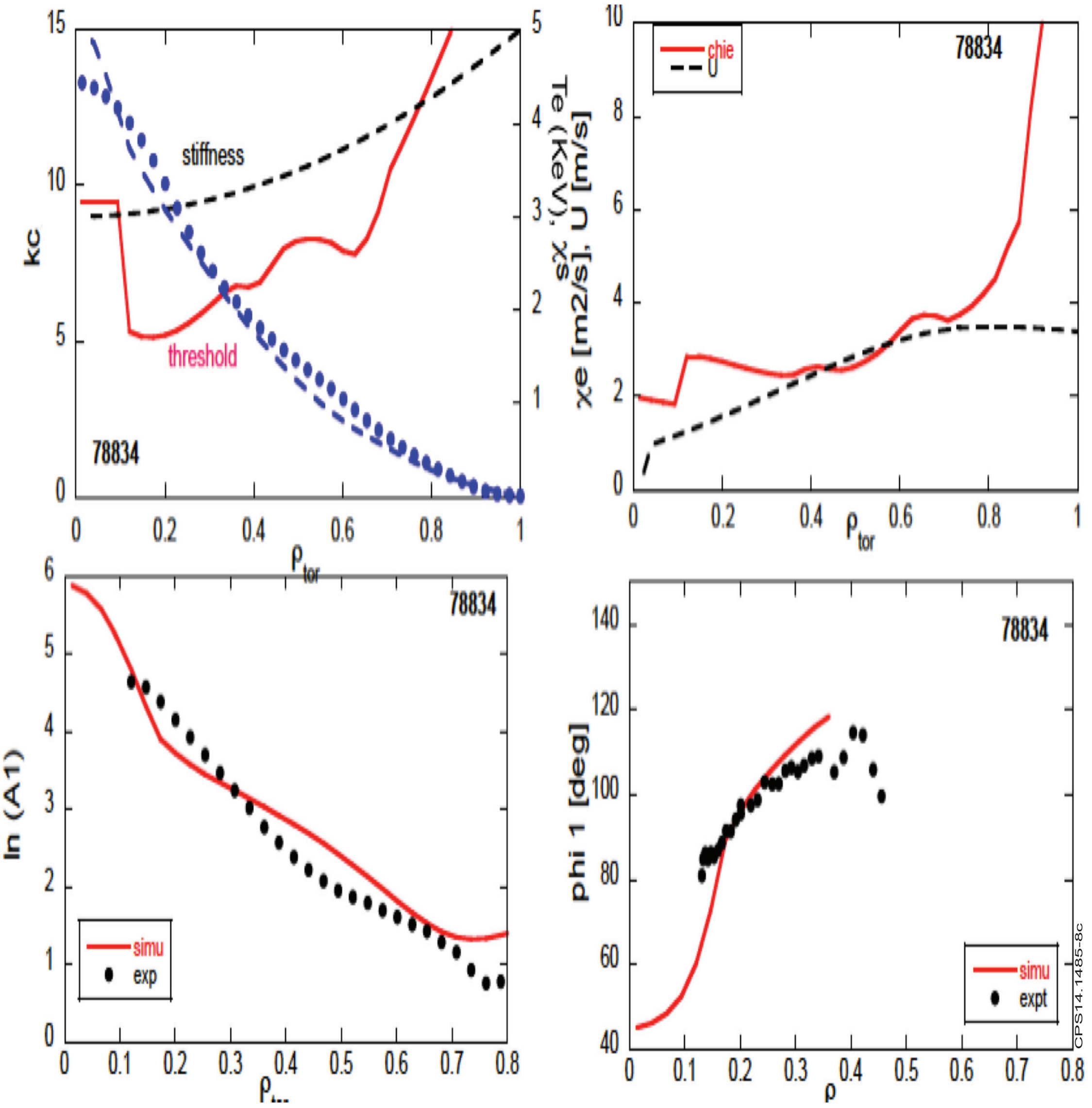

Figure 7.8: *ASTRA simulations of the* T_e *modulation for shot n. 78834 (ICRH on-axis). a)Profiles of* T_e *(blue points are the experimental values while blue dashed line is the profile obtained from the transport simulation),* χ_s *(black dashed line) and* κ_c *(red line). b)Profiles of* χ_e *(red line) and of the heat pinch* U *(black dashed line). c) Profiles of* $ln(A)$ *of* 1*st harmonic (black points are the experimental values while red lines are the profile obtained from the transport simulations). d) Profiles of* ϕ *of* 1*st harmonic (black points are the experimental values while red lines are the profile obtained from the transport simulations).*

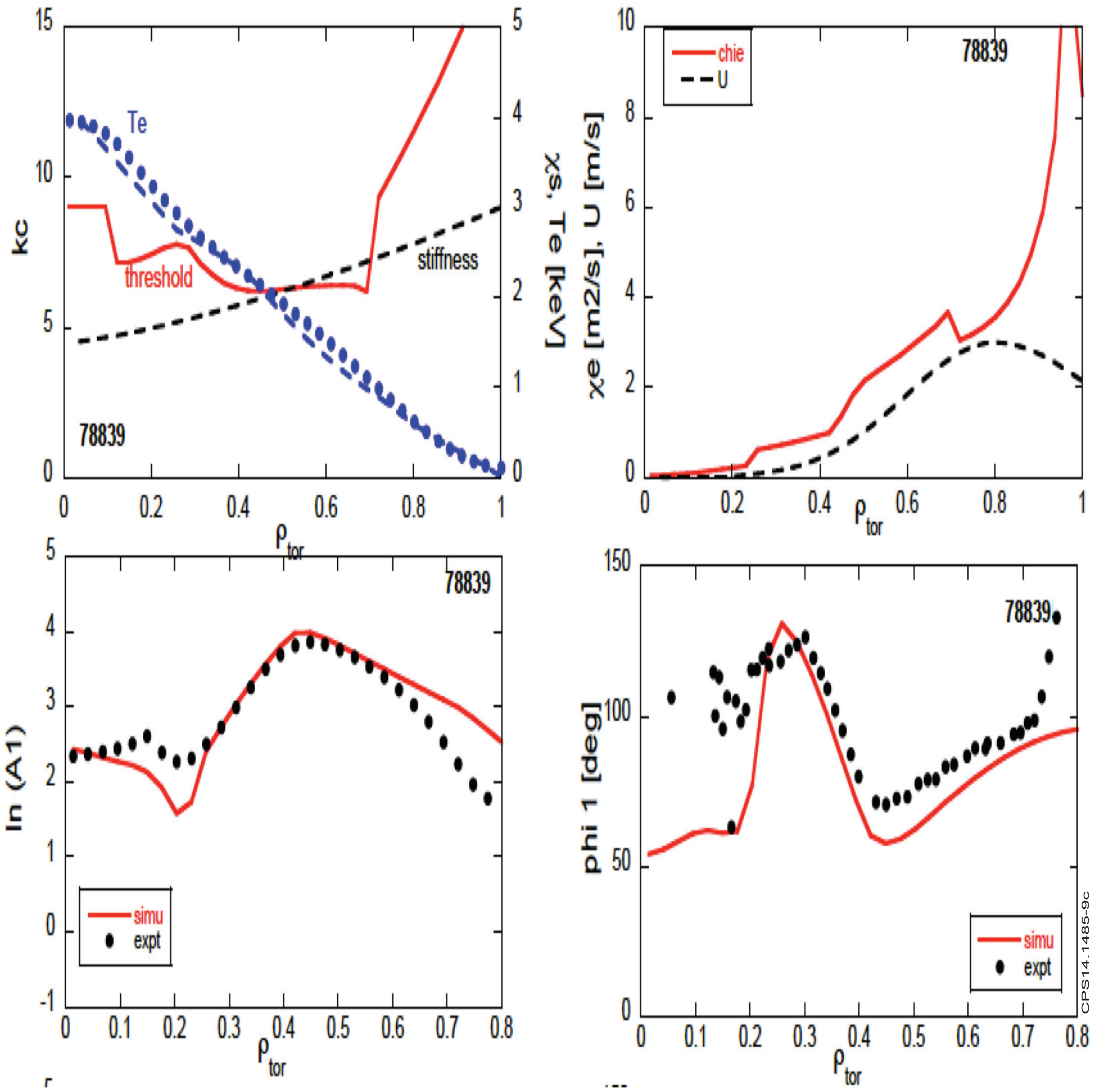

Figure 7.9: *ASTRA simulations of the* T_e *modulation for shot n. 78839 (ICRH off-axis). a)Profiles of* T_e *(blue points are the experimental values while blue dashed line is the profile obtained from the transport simulation),* χ_s *(black dashed line) and* κ_c *(red line). b)Profiles of* χ_e *(red line) and of the heat pinch* U *(black dashed line). c) Profiles of* $ln(A)$ *of* 1*st harmonic (black points are the experimental values while red lines are the profile obtained from the transport simulations). d) Profiles of* ϕ *of* 1*st harmonic (black points are the experimental values while red lines are the profile obtained from the transport simulations).*

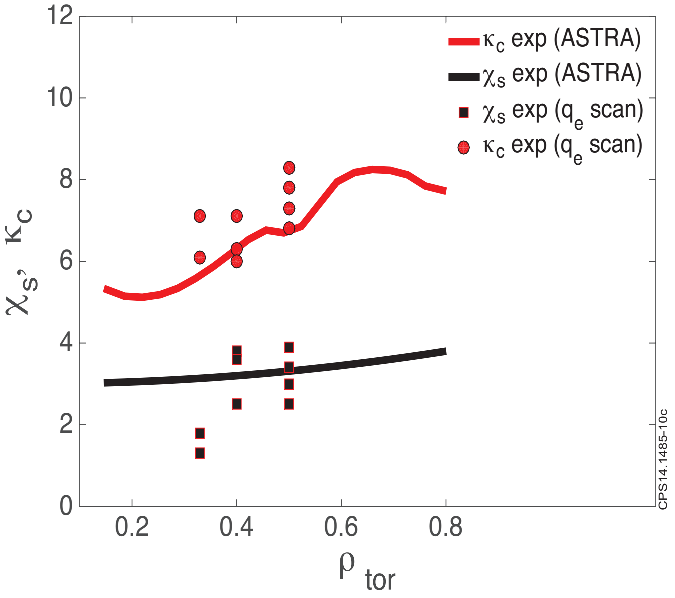

Figure 7.10: *Comparison between the values of stiffness and thresholds found with the heat flux scan and with the perturbative study.*

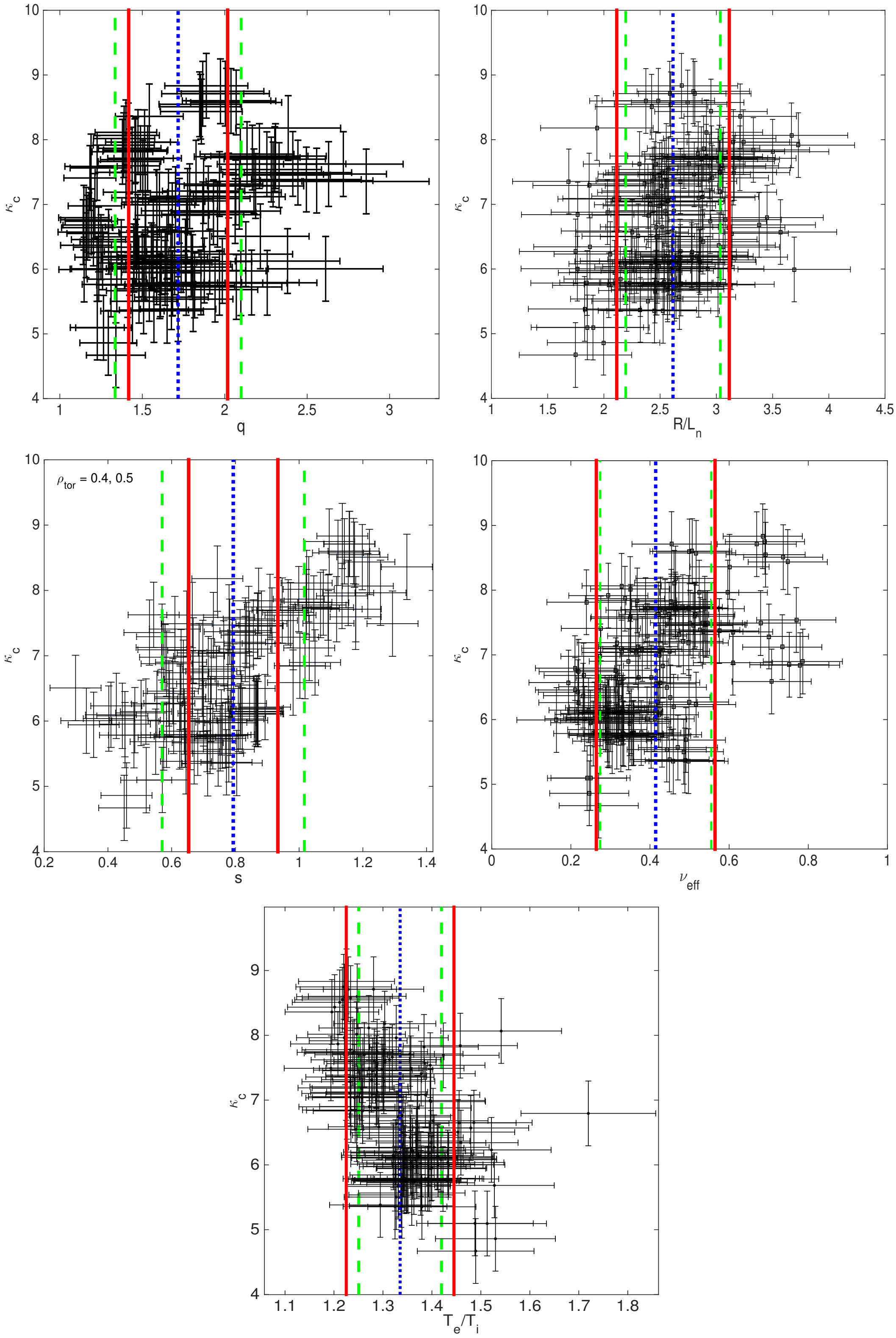

Figure 7.11: *κ_c as a function of the various plasma parameters considered in Table 7.3. The mean value (blue dashed line), the standard deviations from the mean value (green dashed lines) and the experimental error on the mean value (red continuos lines) of the parameters are shown.*

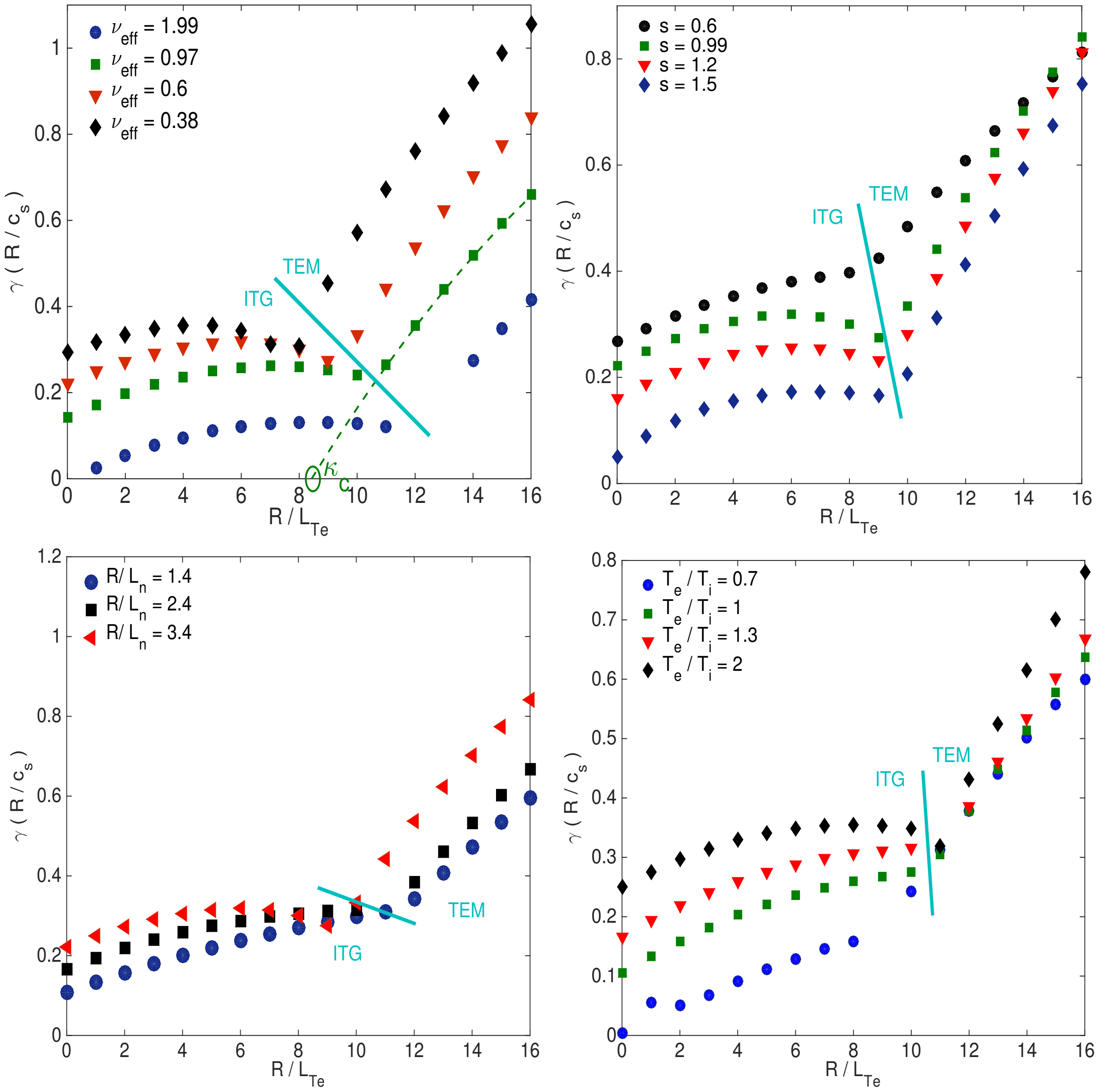

Figure 7.12: *Normalized linear growth rates as a function of R/L_{Te} obtained with linear gyrokinetic simulations with GKW. Continuos lines indicate the transition between ITG dominant instability region and TEM dominant instability region. The values of thresholds are obtained with quadratic fits on the points where the most unstable modes are the TEM as shown in the first figure.*

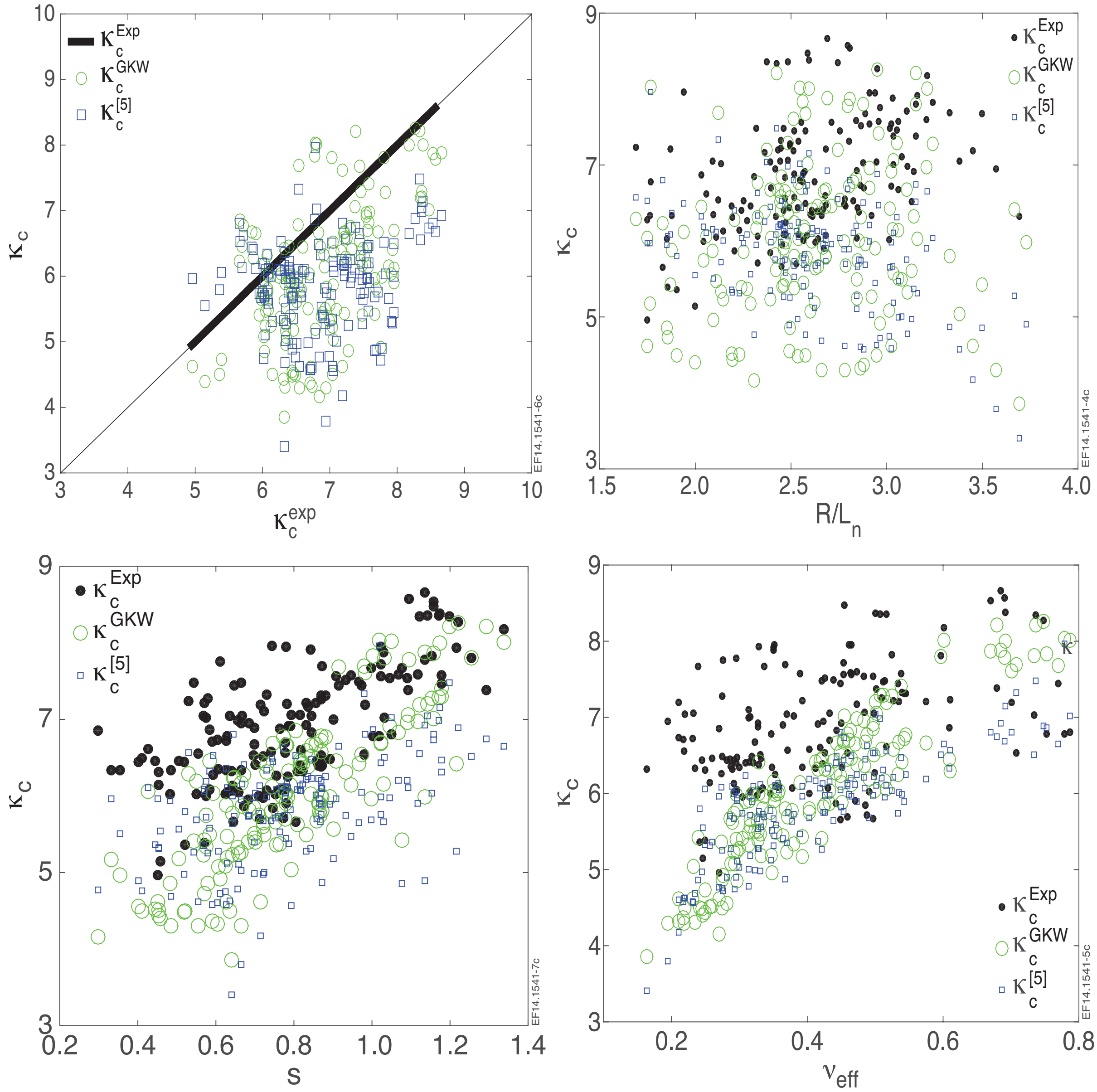

Figure 7.13: *Experimental values of* κ_c*(black circles), values of* κ_c^{GKW} *(green circles) obtained with (5) using experimental values of* $R/L_n, s, \nu_{eff}$ *and values of* $\kappa_c^{[5]}$ *(blue squares) obtained with (4) using experimental values of* $R/L_n, s, \nu_{eff}$ *as a function of* $\kappa_c^{exp}, R/L_n, s$ *and* ν_{eff}*.*

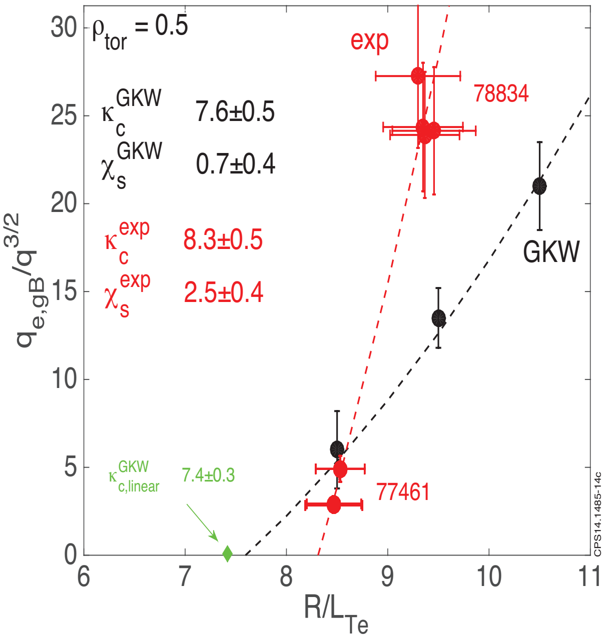

Figure 7.14: *Electron heat fluxes obtained with nonlinear gyrokinetic simulations with GKW. Red squares indicate the experimental data, black circles indicate the fluxes obtained from non-linear gyrokinetic simulations and the green diamond indicates the thresholds obtained from linear gyrokinetic simulations with GKW.*

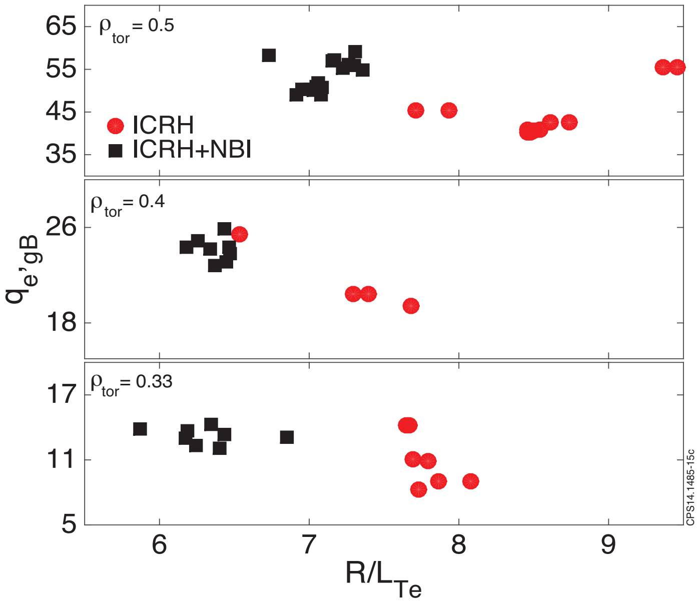

Figure 7.15: *Experimental values of R/L_{Te} at same value of $q_{e,gB}$ at $\rho_{tor} = 0.3, 0.4, 0.5$. Red circles are data points from discharges without NBI heating while black squares are data points from discharges with NBI heating.*

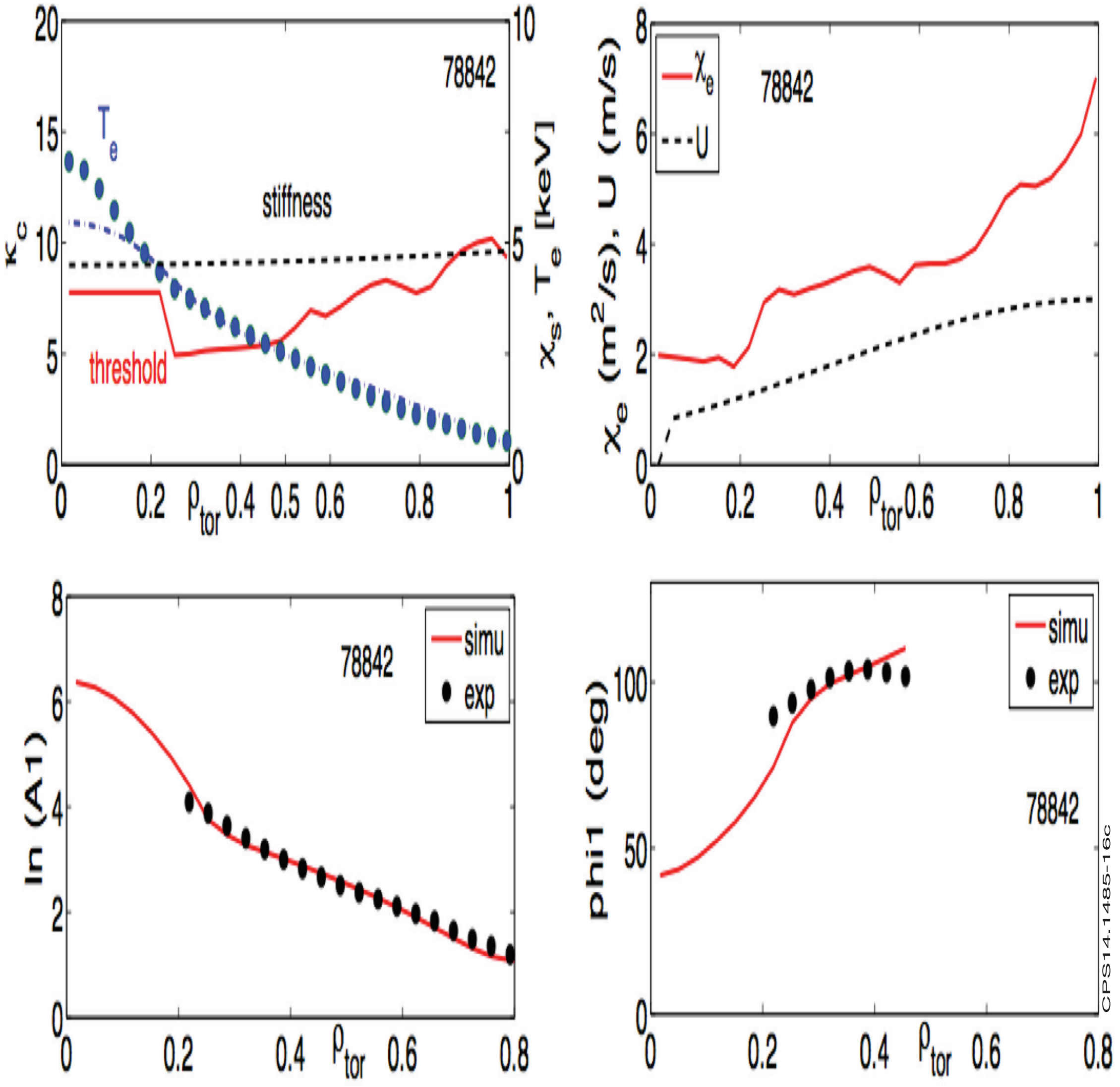

Figure 7.16: *ASTRA simulations of the T_e modulation for shot n. 78842 (ICRH on-axis, NBI=7 MW). a)Profiles of T_e (blue points are the experimental values while blue dashed line is the profile obtained from the transport simulation), χ_s (black dashed line) and κ_c (red line). b)Profiles of χ_e (red line) and of the heat pinch U (black dashed line). c) Profiles of $ln(A)$ of $1st$ harmonic (black points are the experimental values while red lines are the profile obtained from the transport simulations). d) Profiles of ϕ of $1st$ harmonic (black points are the experimental values while red lines are the profile obtained from the transport simulations).*

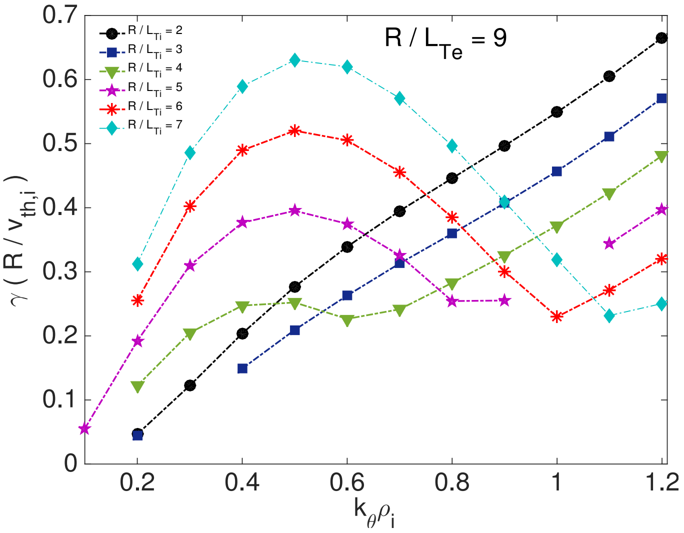

Figure 7.17: *Linear growth rates vs $k_\theta \rho_i$ for different values of R/L_{Ti} obtained from linear simulations with GKW.*

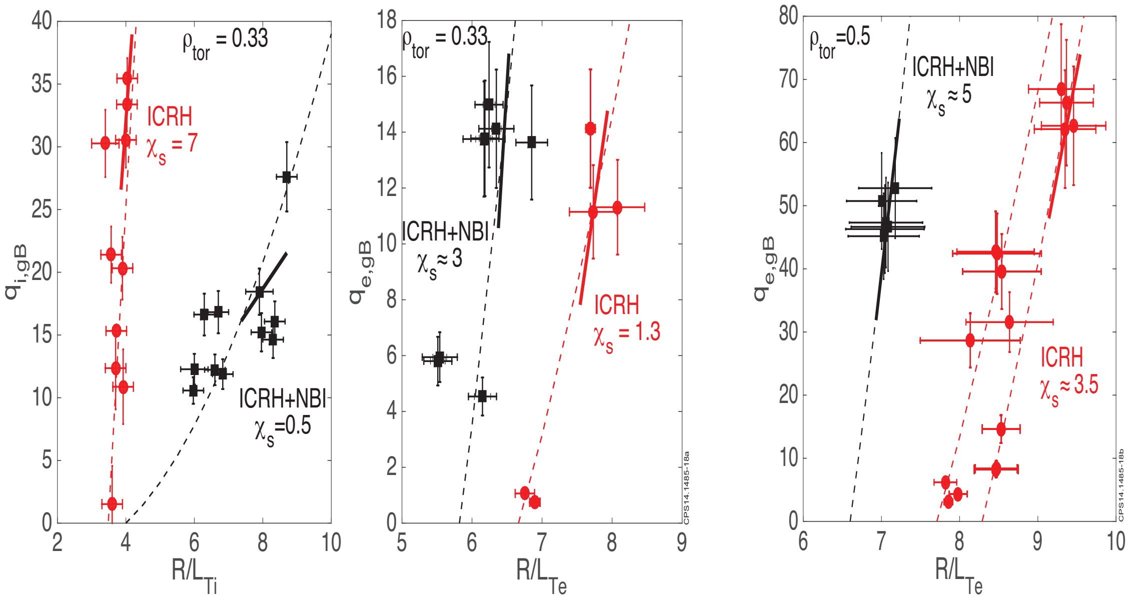

Figure 7.18: *$Q_{i,gB} vs R/L_{Ti}$ at $\rho_{tor} = 0.33$ from [1] and $Q_{e,gB} v R/L_{te}$ at $\rho_{tor} = 0.33, 05$ for similar plasmas without NBI heating (red circles) and with NBI heating (black squares). Dotted lines indicate the quadratic fits used for the identification of threshold and stiffness while continuos segments indicate the fits obtained from the modulation. While for ions the addition of NBI heating leads to an increase of R/L_{Ti} due to a significant reduction of ion stiffness, for electrons the addition of NBI has the opposite effect, decreasing R/L_{Te} due to both a threshold reduction and an increase in stiffness.*

References

[1] P. Mantica et al., Physical Review Letters 107, 135004 (2011).

[2] J. Citrin, Nuclear Fusion 54, 023008 (2014).

[3] J. Weiland, “Collective modes in inhomogeneous plasmas”, IOP Publishing Ltd, 2000.

[4] W. Horton, Reviews of Modern Physics 71, 735 (1999).

[5] A. G. Peeters et al., Physics of Plasmas 12, 022505 (2005).

[6] M. Romanelli, G. Regnoli, C. Bourdelle, Physics of Plasmas 14, 082305 (2007).

[7] F. Ryter et al., Physical Review Letters 95, 085001 (2005).

[8] A. Casati, Physics of Plasmas 15, 042310 (2008).

[9] J. C. DeBoo et al., Physics of Plasmas 19, 082518 (2012).

[10] X. Garbet et al., Plasma Physics and Controlled Fusion 46, B557 (2004).

[11] P. Mantica, F. Ryter, EFDA_PR(06)07 (2007).

[12] D. Van Eester et al., Plasma Physics and Controlled Fusion 51, 044007 (2009).

[13] P. Mantica, F. Ryter, C. R. Physique 7, (2006).

[14] N. J. Lopes Cardozo, Plasma Physics and Controlled Fusion 37, 799 (1995).

[15] G. V. Pereverzev, P. N. Yushmanov, Max-Planck-Institute fur Plasmaphysik, (2002).

[16] G. Cenacchi and A. Taroni, Rapporto ENEA RT/TIB (88)5 (1998).

[17] F. Imbeaux, F. Ryter and X. Garbet, Plasma Physics and Controlled Fusion 43, 1503 (2001).

[18] P. Mantica et al., Plasma Physics and Controlled Fusion 48, 385 (2006).

[19] P. Mantica et al., Physical Review Letters 95, 185002 (2005).

[20] X. L. Zou et al., 35th EPS Conference on Plasma Physics , Hersonissos, Greece (2008).

[21] S. D. Song et al., Nuclear Fusion 52, 033006 (2012).

[22] M. B. Isichenko et al., Physics of Plasmas 3, 1916 (1996).

[23] X. Garbet et al., Physical Review Letters 91, 035001-1 (2003).

[24] C. Angioni et al., Plasma Physics and Controlled Fusion 51, 124017 (2009).

[25] A.G. Peeters et al., Computer Physics Communications, 180, 2650, (2009).

[26] A.G. Peeters, D. Strintzi, Phys. Plasmas 11, 3748, (2004).

[27] F. Ryter et al., Nuclear Fusion 51, 113016 (2011).

[28] S. C. Guo, F. Romanelli, Physics of Fluid B 5, 520 (1993).

[29] P. Mantica et al., Phys. Rev. Lett. 107, 124033 (2011).

[30] F. Jenko, W. Dorland, G. W. Hammett, Physics of Plasmas 9, 4096 (2001).

Chapter 8

Impact of electron scale modes on electron heat transport in the JET tokamak

Proc. 42nd EPS Conference on Plasma Physics, Lisbon, 2015, ECA Vol. 39E P2.122[†].

N. Bonanomi[1,2], J. Citrin[3,4], P.Mantica[1] and JET contributors*

EUROfusion Consortium, JET, Culham Science Centre, Abingdon, OX14 3DB, UK
1) Istituto di Fisica del Plasma “P.Caldirola”, Consiglio Nazionale delle Ricerche, Milano, Italy
2) Università di Milano-Bicocca, Milano, Italy
3) CEA-Cadarache, St. Paul Lez Durance, France
4) FOM Institute DIFFER, P.O. box 6336, 5600 HH Eindhoven, The Netherlands
*See the Appendix of F. Romanelli et al., Proceedings of the 25th IAEA Fusion Energy Conference 2014, Saint Petersburg, Russia

In dedicated electron heat transport experiments in JET L-mode plasmas [1], lower values of R/L_{Te} are observed, at the same level of gyro-Bohm normalized electron heat flux, in the presence of significant NBI (Neutral Beam Injection) power with respect to discharges with pure ICRH (Ion Cyclotron Resonance Heating) applied in mode conversion (MC) scheme yielding dominant electron heating. The discharges studied in this paper were made with C-wall and with $B_0 \sim 3.45\,T, T_{e,0} \sim 5\,keV, T_{i,0} \sim 2.5\text{–}5\,keV, n_{e,0} \sim (2\text{–}3)10^{19}\,m^{-3}$and $Ip \sim (1.8\text{–}3)\,MA$ with I_p overshoot, ramp-up and ramp-down. As seen in Fig. 8.1, the R/L_{Te} decrease is due to both a decrease in inverse critical gradient length and an increase in stiffness. This is in contrast with the strong reduction of ion stiffness observed in presence of NBI (Fig. 8.1a, [2]), which was interpreted as due to non-linear electromagnetic stabilization of ITG modes by fast ion pressure gradient [3].

The main differences in NBI heated plasmas with respect to pure ICRH-MC plasmas are lower values of T_e/T_i, higher values of R/L_{Ti}, the presence of additional fast ions and higher toroidal rotation. Due to the stabilization effects of fast ions on ITG, the effects of higher R/L_{Ti} are not expected to be significant. Possible effects of T_e/T_i, on TEM modes thresholds have been analyzed with linear gyrokinetic simulations and the results suggest that it cannot explain the experimental observation [1]. However, one possible effect of

---

[†] http://ocs.ciemat.es/EPS2015PAP/pdf/P2.122.pdf

lower values of T_e/T_i is an increase of the electron heat flux carried by ETG modes, for which a stabilizing effect of $\tau = Z_{eff}T_e/T_i$ is expected [4]. In this work we investigate the presence of ETG modes in these JET discharges and their effects on the electron heat flux using linear and nonlinear gyrokinetic simulations with the gyro- kinetic code GENE in the local limit [5]. To study properly the impact of ETG modes on transport, multi-scale gyrokinetic simulations including both electron and ions scales are necessary: ion scale zonal flows can provide a mechanism for ETG streamer saturation; ETG modes can affect the ion scales through nonlinear coupling mechanisms, increasing the level of heat transport carried by TEM/ITG modes [6,7,8,9]. However, such simulations demand exceeding computational resources (10^6–10^7 CPUh per run) and could not be afforded for this work. Instead, we carried out separate scale simulations. In all simulations, Miller geometry, collisions, kinetic electrons and experimental input parameters varying within their error range were used. In all ion-scale simulations, a carbon impurity was included, at a level consistent with the experimental values of Z_{eff}. Fast ions and electromagnetic effects were retained in the NBI case. In the ETG simulations, we used adiabatic ions and included the measured external flow shear. This leads to ETG streamer saturation. We assume here that the external flow shear leads to a similar ETG saturation level as the ion scale zonal flows would have done in a multi-scale simulation. However, validating this assumption is out of the scope of this work. Extensive convergence tests were made for both linear and non-linear cases. Linear gyrokinetic simulations were carried out to establish the effect of τ on ETG linear threshold within the experimental parameters range. The results obtained at $\rho_{tor} = 0.5$ are shown in Fig. 8.2.

The linear threshold of ETG modes decreases for lower values of τ, i. e. for lower values of T_e/T_i. The values found are below the experimental values of R/L_{Te}, indicating that ETG modes are unstable for the experimental set of parameters in both ICRH and ICRH+NBI cases. Regarding non-linear simulations, we used the parameters of JET discharge n. 78834 for the pure ICRH heating case and of JET discharge n. 78842 for the ICRH+NBI heating case. In the TEM/ITG nonlinear runs, we used a box size of $[L_x, L_y] \approx [100, 125]\rho_i$, with a numerical resolution of $[128, 24, 48, 48, 12]$ points in $[x, y, z, v_\parallel, \mu]$ and $0.05 \leq k_y\rho_i \leq 1.2$. In the ETG case, we used a box size of $[L_x, L_y] \approx [195, 125]\rho_e$, with a numerical resolution of $[256, 24, 48, 48, 12]$ points in $[x, y, z, v_\parallel, \mu]$ and $0.05 \leq k_y\rho_e \leq 1.2$. $x, y, z, v_\parallel, \mu$ indicate respectively the radial direction, the binormal direction, the parallel direction, parallel velocity and magnetic moments. k_y is the binormal mode number and $\rho_{i/e}$ is the ion/electron Larmor radius. We made a scan in R/L_{Te} of the electron heat flux in order to compare the levels of the heat flux and of the electron stiffness with the experimental values. The results obtained at $\rho_{tor} = 0.5$ for the electron heat flux are shown in Fig. 8.3. In Fig. 8.4 the results obtained at $\rho_{tor} = 0.5$ for ions are compared with the experimental values. All the fluxes are normalized to gyro-Bohm units using $q_{e/i,gB} = q_{e/i}/(T_e n_e \rho_s^{*2} c_s)$, where $c_s = \sqrt{T_e/m_i}$ and $\rho_s^* = c_s m_i/eB_0R$.

The experimental normalized ion heat flux remains unchanged in the two cases despite the differences in R/L_{Ti} and this is reproduced quite well in the simulations using fast ions and electromagnetic effects, confirming what found in previous works [3]. The fact that the ion heat flux is reproduced is an indication of the consistency of our simulations. Regarding the electron heat flux, the simulations indicate that a considerable amount of flux is independent of R/L_{Te} and is carried by non-diagonal terms such as R/L_n TEM modes and especially ITG modes (~25% of the experimental flux in the ICRH case and ~40% of the experimental flux in the NBI case). The flux carried by ion scale modes is in both cases too low to reproduce the experimental flux: in both cases we can reproduce the ~50% of the experimental flux with TEM-ITG modes. The scan in R/L_{Te} allows also a comparison with the experimental slope of the flux and also in this case the TEM/ITG contribution to the flux cannot alone reproduce the experimental slope. In the NBI case, the experimental values of R/L_{Te} are also very close to the nonlinear threshold of ∇T_e TEM modes: this could indicate that another kind of instability, such as ETG, is carrying the remaining part of the flux. In both cases ETG modes are unstable: as mentioned, the amount of ETG flux calculated is just indicative as multi-scale scale simulations would be needed, but in both cases we can't reproduce the experimental values and especially the experimental slope of the electron heat flux without retaining the ETG flux. This suggests that ETG modes could play an important role for electron heat flux for our experimental range of parameters and can help to explain the higher electron stiffness and the lower threshold values found experimentally in the NBI case. Also, a small reduction of the TEM modes threshold due to lower collisionality in the NBI case can contribute to explain the experimental observations.

Conclusions This work provides a comparison between experiments and gyrokinetic simulations for JET L-mode discharges with and without substantial ion heating provided by NBI. It indicates that a significant amount of electron heat flux (~25%) can be carried by non-diagonal terms such as ITG modes. Using ion scale modes alone it is difficult to reproduce the experimental slope and the experimental electron heat flux, reaching only the ~50% of the experimental values. Electron scale modes can help to reproduce the experimental fluxes in both ICRH and ICRH+NBI cases. Furthermore, being more unstable in presence of substantial ion heating due to lower values of T_e/T_i, ETG modes can help to explain why, in presence of NBI heating, we observe lower values of R/L_{Te}: the electron heat flux carried by ions scale modes does not increase significantly in the NBI case, but in this case there is almost the same amount of electron heat flux carried by ETG modes at lower values of R/L_{Te}. It is important to underline again that these results are only indicative. Complete scale simulations should be done in order to properly consider the nonlinear interactions between different scales modes.

Acknowledgements The authors would like to thank Tobias Görler, Daniel Told and Frank Jenko for precious advice on GENE simulations. The authors are also grateful to D. R. Mikkelsen for assistance. This research used resources of the National Energy Research Scientific Computing Center, a DOE Office of Science User Facility supported by the Office of Science of the U.S. Department of Energy under Contract No. DE-AC02-05CH11231. A part of this work was carried out using the HELIOS supercomputer system at Computational Simulation Centre of International Fusion Energy Research Centre (IFERC-CSC), Aomori, Japan, under the Broader Approach collaboration between Euratom and Japan, implemented by Fusion for Energy and JAEA. This work has been carried out within the framework of the EUROfusion Consortium and has received funding from the Euratom research and training programme 2014-2018 under grant agreement No 633053. The views and opinions expressed herein do not necessarily reflect those of the European Commission.

Figures

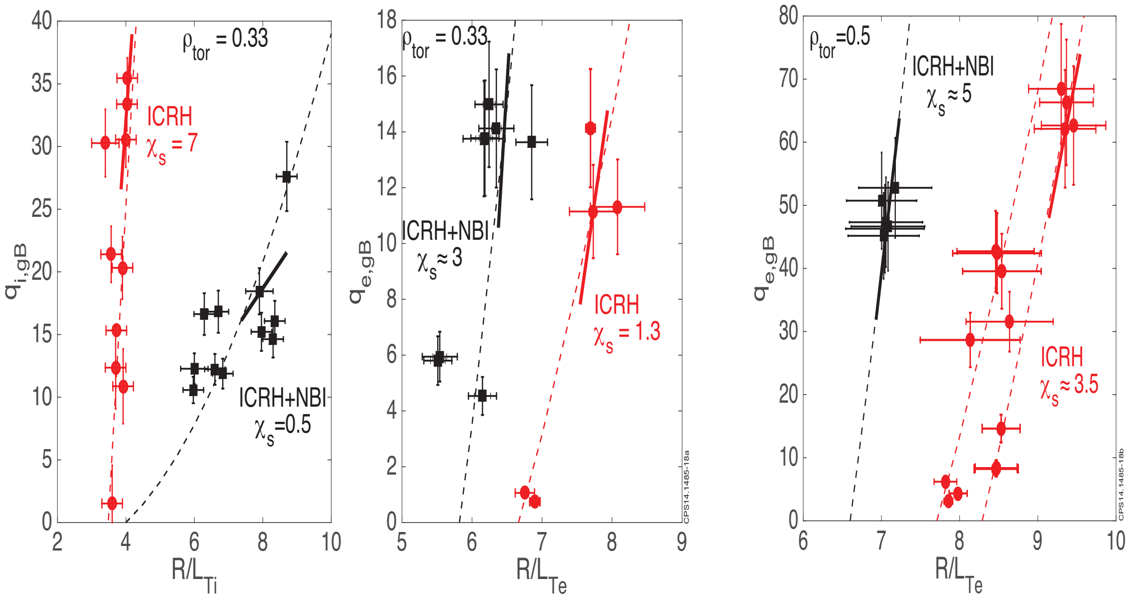

Figure 8.1: *Effect of the presence of NBI heating on ions in L-mode JET discharges at* $\rho_{tor} = 0.33$ *(left panel, reproduced from [2]) and on electrons at* $\rho_{tor} = 0.33$ *(centre panel) and* $\rho_{tor} = 0.5$ *(right panel, [1]).*

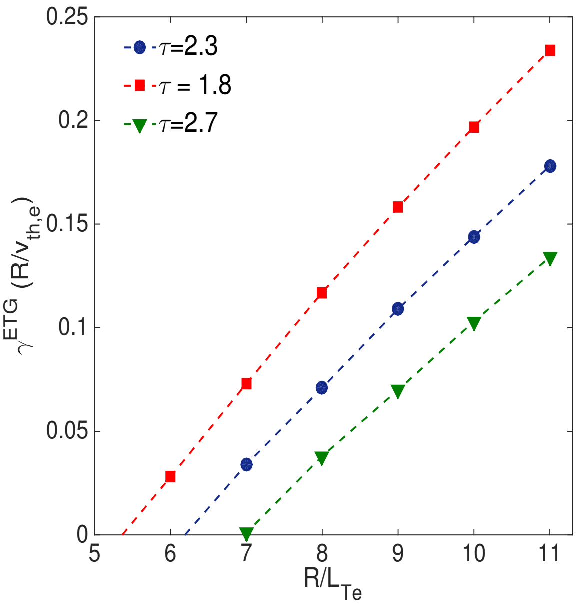

Figure 8.2: *ETG linear growth rates vs* R/L_{Te} *for different values of* $\tau = Z_{eff}T_e/T_i$.

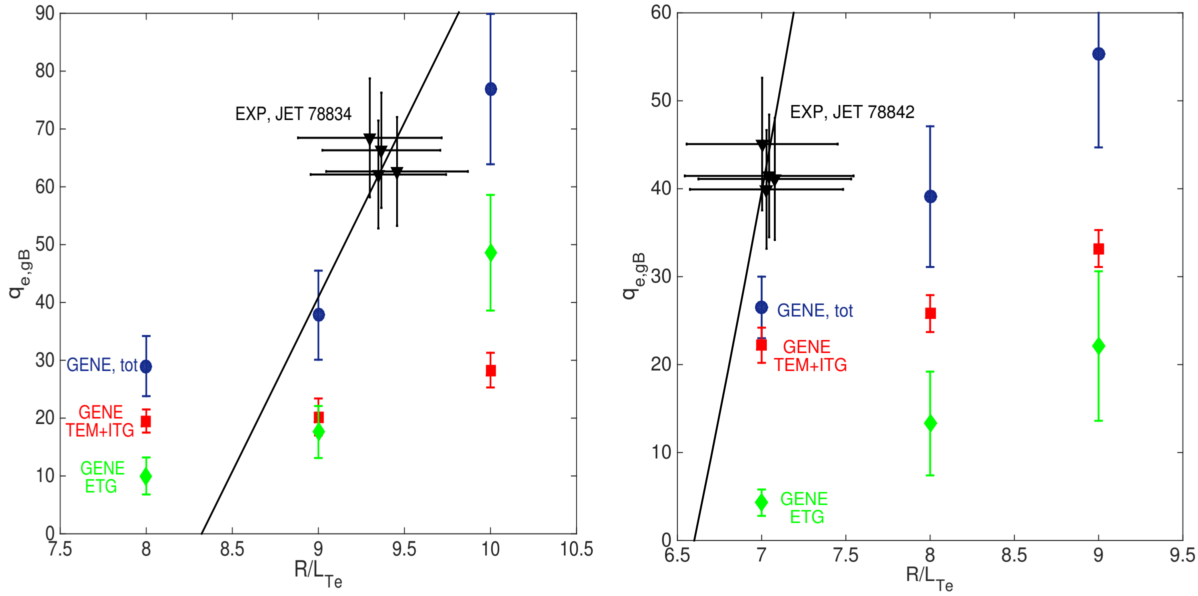

Figure 8.3: *Normalized electron heat flux vs R/L_{Te}. Experimental flux (black triangles), GENE TEM/ITG flux (red squares), GENE ETG flux (green diamonds) and GENE TEM/ITG+ETG flux (blue circles) for discharges with pure ICRH heating (left) and for discharges with ICRH+NBI heating (right). The black lines indicate the experimental slope (stiffness) of the electron heat flux.*

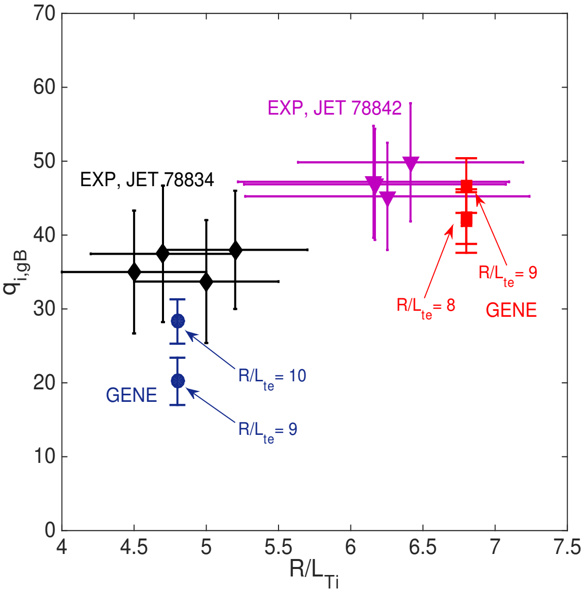

Figure 8.4: *Normalized ion heat flux vs R/L_{Ti}. Experimental flux of the ICRH case (black diamonds) and of the ICRH+NBI case (purple triangles); GENE TEM/ITG flux for the ICRH case (blue circles) and GENE TEM/ITG flux for the ICRH+NBI case (red squares).*

References

[1] N. Bonanomi et al., Nucl. Fusion 55, (2015).

[2] P. Mantica et al., Phys. Rev.Lett. 107, 135004 (2011).

[3] J. Citrin et al., Phys. Rev.Lett. 111, 155001 (2013).

[4] F. Jenko et al., Phys. Plasmas 8, 4096 (2001).

[5] F. Jenko et al., Phys. Plasmas 7, 1904 (2000).

[6] N. T. Howard et al., Phys. Plasmas 21, 112510 (2014).

[7] T. Gorler and F. Jenko, Phys. Rev.Lett. 100, 185002 (2008).

[8] R. E. Waltz et al., Phys. Plasmas 14, 056116 (2007).

Chapter 9

Impact of electron scale turbulence and multi-scale interactions in the JET tokamak

Paper submitted to Physical Review Letters, 01/2018.

N. Bonanomi[1,2], P. Mantica[2], J. Citrin[3], T. Goerler[4], B. Teaca[5] and JET contributors*

EUROfusion Consortium, JET, Culham Science Centre, Abingdon, OX14 3DB, UK
1)Università di Milano-Bicocca, Milano, Italy
2)CNR - Istituto di Fisica del Plasma "P. Caldirola", Milano, Italy
3)DIFFER - Dutch Institute for Fundamental Energy Research, 5600 HH, Eindhoven, The Netherlands
4)Max Planck Institute for Plasma Physics, Boltzmannstr. 2, 85748 Garching, Germany
5)Applied Mathematics Research Centre, Coventry University, Coventry CV1 5FB, United Kingdom
* See the author list of "X. Litaudon et al., Nucl. Fusion 57, 102001, (2017)"

Abstract

Experimental observations in JET tokamak plasmas and gyro-kinetic simulations point to an important role, for electron heat transport, of electron scale instabilities and of their interaction with ion scale instabilities. Since these effects are maximized for strong electron heating and ion-scale modes close to marginal stability, these findings are of high relevance for ITER plasmas, featuring both conditions. Gyro-kinetic and quasi-linear transport models accounting for multi-scale effects are assessed against JET experimental results.

9.1 *Introduction*

Understanding turbulent electron heat transport is of fundamental importance for future magnetic fusion reactors such as ITER. Both the main heating systems and, in a Deuterium-Tritium plasma, the fusion born α-particle heating will deliver power mainly to the electron channel, whilst ions will be mainly heated by electrons via collisional coupling. Therefore, the core temperature and fusion performance will strongly depend on electron heat transport, which is dominated by turbulent processes. Historically, ion-scale micro-instabilities, i.e. ITGs (Ion Temperature Gradient) modes [1] and TEM (Trapped Electron Modes) [2], have been deemed to carry most of the electron heat flux, q_e [3, 4, 5], with electron-scale ETG (Electron Temperature Gradient) modes [6] playing a minor role due to their small wavelength. However, a quantitative comparison with non-linear gyrokinetic (GK) simulations of the experimental q_e and its slope vs $R/L_{Te} = R\left|\nabla Te\right|/Te$ (R being the plasma major radius and T_e the electron temperature) - which determines the stiffness of the T_e profiles against a flux increase - was attempted only very recently. This pointed out that in some cases ion-scale low-k modes are not able to account for the measured electron heat transport [7, 8, 9]. Both theoretical [6, 8, 10, 11, 12] and experimental [13, 14, 15] studies extending to the high-k range have then shown that, in some experimental conditions, ETGs can carry a significant fraction of the turbulent heat flux and electron and ion scales can have strong interactions. The importance of sub-ion instabilities and of the interactions between different scales has also been investigated and observed in other magnetized plasma phenomena, such as in magnetic reconnection [16, 17] and solar wind [18]. In fusion plasmas, it was found in computationally demanding multi-scale GK simulations that a large impact of ETGs takes place when ion-scale instabilities are close to marginal stability and high electron heating is present [8, 11]. This will be the case in the ITER baseline scenario, motivating the present study on JET, the largest existing tokamak. We focus on JET L-mode plasmas with high electron heating, on which we performed dedicated transport experiments, comparing results with GK simulations. The target of the work is to quantify the role of electron-scale instabilities in electron heat transport in these low power plasmas, more amenable than high performance scenarios to detailed transport physics studies. A precise experimental quantification of electron heat transport properties such as critical gradient for ETG onset and stiffness level on JET is an essential piece of information to validate both GK models and the most recent TGLF (SAT1) [19, 20, 21] quasi-linear model, to support their application to high power scenario predictions in present and future devices. A first experimental evidence of the role of ETG modes in JET plasmas will be reported as well as strong confirmations from gyrokinetic simulations, including a first multi-scale simulation of a JET discharge.

9.2 *Experimental observations*

A variety of experimental observations pointing to a significant role of ETG modes in determining q_e has been gathered in a set of JET C-wall dedicated electron heat transport experiments in L-mode plasmas with toroidal magnetic field $B_T \sim 3.35T$, plasma current $I_p \sim 2\,MA$, safety factor at the magnetic surface enclosing the 95% of the poloidal magnetic flux $q_{95} \sim 5$, electron density in the plasma center $n_{e,0} \sim 2$–$3.5{\cdot}10^{19}m^{-3}$ and different levels of Neutral Beam Injection (NBI) and Ion Cyclotron Resonance Heating (ICRH). In these experiments, mid-radius q_e scans at constant total power were carried out by using on- vs off-axis ICRH power in ${}^3He - D$ plasmas with $n_{{}^3He}/n_e \sim 18\%$ to achieve mode conversion and pure electron heating, as discussed in detail in Ref. [11]. These q_e scans allow to determine the R/L_{Te} threshold for the onset of turbulent electron heat transport and the electron stiffness [3, 4]. In addition, T_e modulation was also carried out, to complement the information [22, 23]. The first striking observation (Fig. 9.1a) is a remarkable correlation at the analyzed radius $\rho_{tor} = \sqrt{(\Phi/\pi B_T)/(\Phi/\pi B_T)_{max}} = 0.5$ (where Φ is the toroidal magnetic flux) between R/L_{Te} and the parameter $\tau = Z_{\text{eff}} \cdot T_e/T_i$ (T_i being the ion temperature and Z_{eff} the effective plasma charge), which is a key term in the ETG threshold [24]. The τ dependence dominates over dependences on other parameters that also vary in the dataset, including the power level. The stabilizing effect of τ for electron heat transport can be seen in more detail in Fig. 9.1b, showing the gyro-Bohm normalized electron heat flux $q_{e,gB} = q_e/(n_e T_e c_s \rho_s^2)$, where $c_s = \sqrt{T_e/M_i}$ and $\rho_s = M_i c_s/eB$, M_i being the ion mass, as a function of R/L_{Te} and for different τ values. Here a clear increase of the electron threshold (i.e. the intercept at $q_{e,gB} = 0$) is seen for increasing τ, dominating over the scatter due to having included all points in the database, regardless of variations in other parameters (except B_T and I_p which are always the same). A consistent sound observation is that adding NBI power to an ICRH electron heated plasma induces a flattening of the T_e profile and an increase of the electron stiffness, as reported in Ref. [7, 25]. Last, using a critical gradient formula [26] and the electron stiffness measured experimentally for few cases using q_e scans and T_e modulation, the R/L_{Te} thresholds have been calculated for these discharges. These thresholds are compared, as a function of τ, in Fig. 9.1c, with the theoretical values using analytical formulae proposed in Ref. [2] for TEM and in Ref. [24] for ETGs. We see that experimental thresholds lie close to the ETG threshold and have a similar trend with τ up to $\tau \sim 4$, whilst TEM thresholds have an opposite trend with τ.

The experimental observations presented above are suggestive of a dominant role of ETG in electron heat transport in our dataset, but the quantitative evaluation of the relative impact of ITG, TEM and ETG modes on q_e requires comparing the experimental plot of $q_{e,gB}(R/L_{Te})$ (at constant other parameters) with non-linear gyro-kinetic simulations.

Gyro-kinetic simulation setup: For detailed non-linear simulations, carried out using the GENE code [6] in the radially local limit, input data from JET discharge n. 78834 (with 2.5 MW of ICRH power directed to electrons and with 1.7 MW of NBI power) at $t = 7\ s$ and $\rho_{tor} = 0.53$ have been used. Non-linear single-scale (on both ion and electron scales) and a first JET non-linear multi-scale simulation have been performed. A scan in $R/L_{Te} = 8.5, 10, 11$ has been done in the simulations. Other important parameters are $s = 0.98, q = 2.1, R/L_n = 2.1, R/L_{Ti} = 3.6, T_i/T_e = 0.8, Z_{eff} = 1.82$, where s is the magnetic shear. The simulations are electrostatic and feature Miller geometry, collisions, kinetic D ions and electrons and perpendicular flow shear rate. In order to cover both ion and electron scales, toroidal mode numbers up to electron-scale have been coupled in the multi-scale simulation, using $0.1 \lesssim k_y \rho_s \lesssim 48$. In the single ion and electron-scale simulations $0.1 \lesssim k_y \rho_s \lesssim 1.6$ and $3 \lesssim k_y \rho_s \lesssim 48$ have been used respectively. Perpendicular box sizes were $[L_x, L_y] \approx [64, 64]\rho_s$ in the ion-scale and multi-scale simulations and $[L_x, L_y] \approx [4, 4]\rho_s$ in the electron-scale simulations ($\rho_s = c_s/\Omega_i$, $c_s = (T_e/m_i)^{0.5}$ and $\Omega_i = eB_0/m_i$, m_i being the D mass and B_0 being the background magnetic field). The number of grid points used in the multi-scale simulation were $[n_x, n_y, n_z, n_v, n_\mu] = [1280, 448, 36, 32, 12]$ (GENE field-aligned coordinates: x=radial direction, y=binormal direction, z=parallel direction (to B_0), v=parallel velocity, μ= magnetic moments). In the single-scale simulations $[n_x, n_y, n_z, n_v, n_\mu] = [256, 48, 36, 32, 12]$. In the electron-scale simulations, the saturation of q_e has been achieved by artificially increasing the level of the perpendicular flow shear until heat flux convergence was reached, due to ETG streamer shearing leading to a reduction of box-scale effects. This technique has been assumed to be a proxy for ion-scale structures saturating the ETG streamers. The total predicted $q_{e,gB}$ from single-scale simulations has then been calculated with a simple sum of the fluxes from ion-scale and electron-scale simulations.

9.3 *Gyro-kinetic simulation results*

A first assessment of linear stability using GENE for plasmas at different values of τ is shown in Fig. 9.2. In the simulations, C has been used as an impurity species in the plasma in order to reproduce the experimental levels of Z_{eff}. In general, ITGs tend to be the dominant low-k mode for $k_y \lesssim 0.7$. For higher k_y values TEM/ETG dominate. In many cases, ETGs have been found unstable also for high τ values, but a region with almost zero growth rate is present between the low and the high-k regions. For lower τ values, ITGs are in general more stable (in many cases due to an increase in T_i/T_e [28]), while TEM and ETG growth rates never decrease going from ion to electron scales. Considering that ETGs are expected to play a significant role when ion-scale instabilities are not highly unstable [8, 10, 11], the results from the linear simulations go in the right direction to predict a stronger role of ETGs for lower τ values in these JET discharges.
Regarding non-linear simulations, the time evolution of $q_{e,gB}, q_{i,gB}$ from the multi-scale simulation is shown in Fig. 9.3, while the comparison between non-linear simulations and experiment is shown in Fig. 9.5a. In both ion-scale and multi-scale simulations the $q_{i,gB}$ was matched within error-bars and no substantial differences in $q_{i,gB}$ have been observed when multi-scale interactions and high-k instabilities have been considered. The $q_{e,gB}$ predicted by ion-scale simulations is not enough to reproduce the experimental data. This was first pointed out in Ref. [7], but without any study of the electron-scale contribution, which is addressed in detail in this Letter. As shown in Fig. 9.5a, adding the $q_{e,gB}$ from the electron-scale simulations it is possible to reproduce both the $q_{e,gB}$ level and the electron stiffness. When multi-scale interactions are considered, no big differences in $q_{e,gB}$ with respect to the single ion-scale simulations have been observed for $R/L_{Te} = 8.5$, while a strong increase of $q_{e,gB}$ has been observed with respect to the ion-scale simulations for $R/L_{Te} = 10$ (+50%) and $R/L_{Te} = 11$ (+80%). These increments are due to an increase of the high-k instabilities as can be seen from the $\phi - T_{\parallel}$ (electrostatic potential-parallel temperature fluctuations) cross-phases and from the appearance of the typical ETG streamer structures when R/L_{Te} is increased (Fig. 9.4). A strong reduction of the fluxes and of the stiffness is observed with respect to the sum of the single-scale simulations, indicating that the saturation of ETGs due to ion-scale turbulent structures is a key factor and must be considered, as reported also in [8, 11, 10]. Similar to previous works [29, 30], studying the net free energy received by a mode from the interaction with all other modes, i.e. $\mathcal{T}(k_x, k_y, z)$, we can gauge the role of a k_y mode on the overall flux of free energy across the $k_\perp(z)$ ($\equiv |\mathbf{k}_\perp(z)|$) scales. In Fig. 9.4e, the plot of the flux of free energy across the $k_\perp$ scales, for each value of z, is shown for the case $R/L_{Te} = 10$. As can be seen, the overall flux is directed from large to small scales (direct cascade, positive flux values) with the main contribution from modes that coincide with the ITG ($0.2 < k_y\rho_s < 0.4$) and ETG ($5 < k_y\rho_s < 10$) peaks for $q_{e,gB}$. When looking at the same quantity, but computed only for ETG k_y modes (Fig. 9.4f), we note that a flux from small to large scales (inverse cascade, negative flux values), that is z dependent, is visible. This indicates that, while the overall scale flux is indicative of energy cascading down to smaller scales, ETG modes can influence the ITG like scales through an inverse energy cascade, impacting the self-organization of structures (streamers) and the saturation level of $q_{e,gB}$. These gyro-kinetic results indicate that ETGs and multi-scale interactions can be important contributors to electron heat transport in these JET L-mode plasmas. The fact that quantitatively the $q_{e,gB}$ values of the multi-scale simulation are still lower than the experimental ones should not be seen as a failure of the multi-scale simulation, but

rather as an indication that more ITG stabilizing mechanisms have to be introduced in the simulation, such as the presence of light impurities in the plasma ($C,^3He$ in this case) [31, 32]. These have not been included for sake of numerical resources. As indicated in Ref. [8, 10, 11], when ITG modes are close to threshold, a strong increment of both electron and ion heat flux can be observed. In our case, lower values of R/L_{Ti}, outside error bars, would be needed in the present multi-scale simulation. However, adding impurities would lead to further stabilization of ITG modes whilst keeping the experimental R/L_{Ti} [31, 32]. This could lead to an enhancement of both electron and ion heat fluxes related to the presence of ETGs, with better agreement with experiment. This is left to future work.

9.4 *Quasi-linear simulations*

A study using the quasi-linear model TGLF has been done using the same input parameters and settings as in the GENE multi-scale simulation and the new TGLF saturation rule (sat 1) [21]. In figure 5b the comparison between TGLF and the multi-scale simulation is shown. TGLF predicts a strong impact of ion-scale ZF on ETGs, as can be seen by the large variation of $q_{e,gB}$ with R/L_{Ti}, with large ETG fluxes when ions are close to marginality. When the $q_{i,gB}$ is matched between TGLF and the multi-scale simulation, the predictions for $q_{e,gB}$ are in good agreement (red triangles). Furthermore, a strong increase of $q_{e,gB}$ due to ETGs is predicted by TGLF for higher values of R/L_{Te}, reaching the experimental level of $q_{e,gB}$ and also of the electron stiffness. We note that also the comparison with the ion-scale simulation is quite good. Both GENE and TGLF indicate that ion-scale instabilities alone are not explaining the experimental $q_{e,gB}$, and inclusion of electron-scales is essential.

9.5 *Discussion*

Experimental results in JET L-mode plasmas and their modelling with gyro-kinetic simulations point to an important role of high-k instabilities and multi-scale interactions for electron heat transport. These findings represents a first proof of the role of ETGs in JET plasmas. Quasi-linear simulations are in good agreement, when the ion heat flux is matched, with the multi-scale GK simulation, indicating that these tools are useful for an at least qualitative prediction for ITER. Both the decrease of tau and the ITG stabilization due to increased rotation and non-linear e.m. stabilization [33], leading to enhanced ETG modes, may be the cause for the reduced value to which T_e peaking is seen clamped in JET high NBI power performant scenarios. In JET, due to lower collisional coupling and to the presence of ion heating, this deterioration of electron heat transport is less penalizing for fusion performance than it could be in ITER. Indeed simple linear GK simulations of the ITER baseline plasma with the parameters predicted in [27] yield a ratio of high to low k growth rates comparable to what observed in these JET plasmas (Fig. 9.2), suggesting a similarly non-negligible role of ETGs. Therefore, these findings call for the need of properly accounting for high-k instabilities and multi-scale interactions in future ITER simulations and also of foreseeing ITER turbulence diagnostics covering reliably both low and high k ranges.

Acknowledgements

The authors would like to thank B. Baiocchi, G. Szepesi, E. Fable and G. Staebler for their help with the TGLF simulations and N. T. Howard for precious discussions. The authors are grateful to D. R. Mikkelsen for assistance. This research used resources of the NERSC center, a DOE Office of Science User Facility supported by the Office of Science of the U.S. Department of Energy under Contract No. DE--AC02--05CH11231. A part of this work was carried out using the HELIOS supercomputer system at IFERC-CSC, Aomori, Japan, under the Broader Approach collaboration between Euratom and Japan, implemented by Fusion for Energy and JAEA. We acknowledge the CINECA award under the ISCRA initiative, for the availability of high performance computing resources and support. B. Teaca is partially supported by EPSRC grant No. EP/P02064X/1. This work has been carried out within the framework of the EUROfusion Consortium and has received funding from the Euratom research and training programme 2014–2018 under grant agreement No. 633053. The views and opinions expressed herein do not necessarily reflect those of the European Commission.

Figures

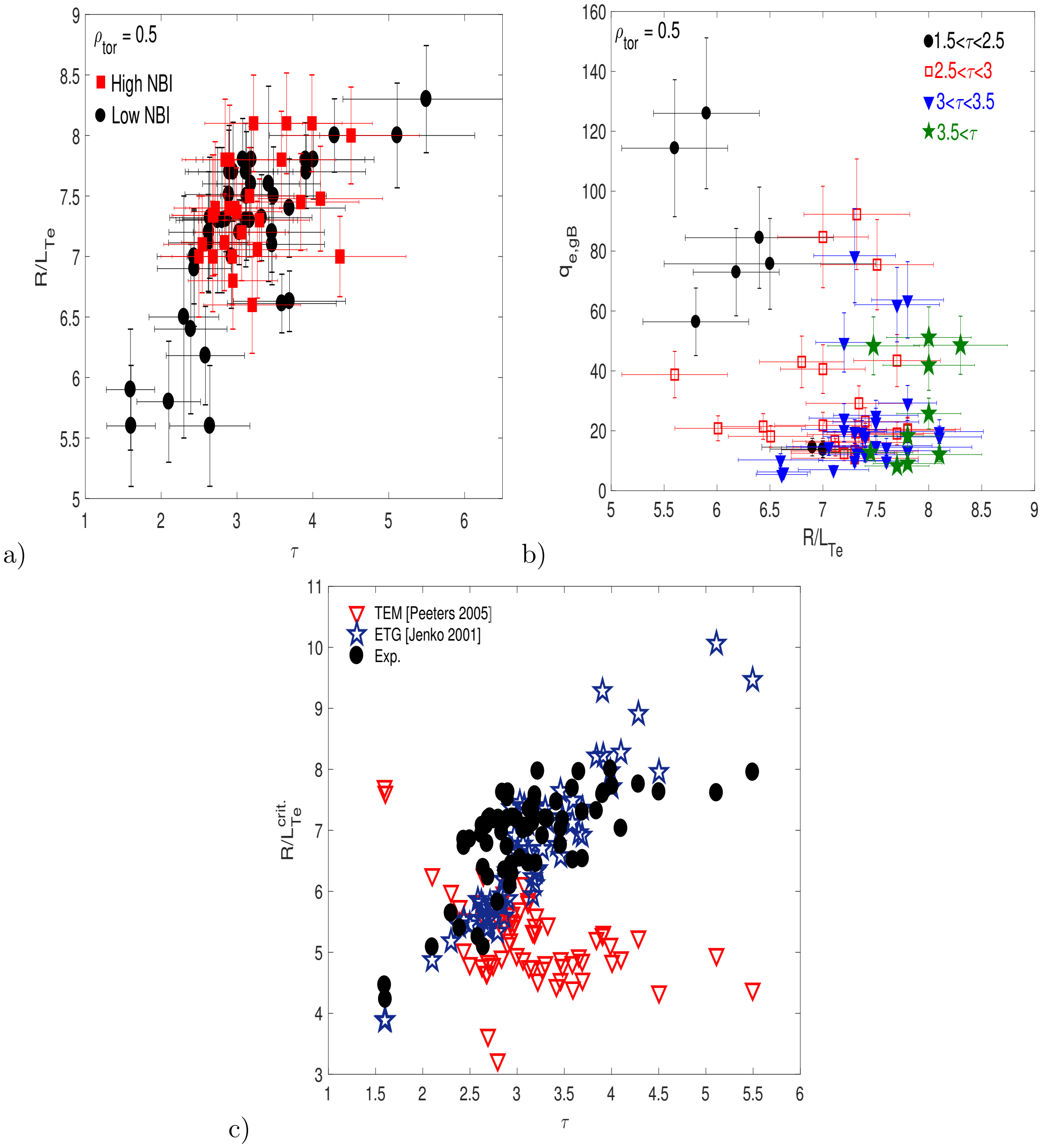

a) b)

c)

Figure 9.1: *a)*$R/L_{Te}(\tau)$ *with high (red) and low (black) NBI at* $\rho_{tor} = 0.5$*. b)*$q_{e,gB}(R/L_{Te})$ *at* $\rho_{tor} = 0.5$*. Different colors indicate different ranges of* $\tau = Z_{eff}T_e/T_i$*. c)Experimental, TEM [2] and ETG [24]* R/L_{Te} *threshold as a function of* τ*.*

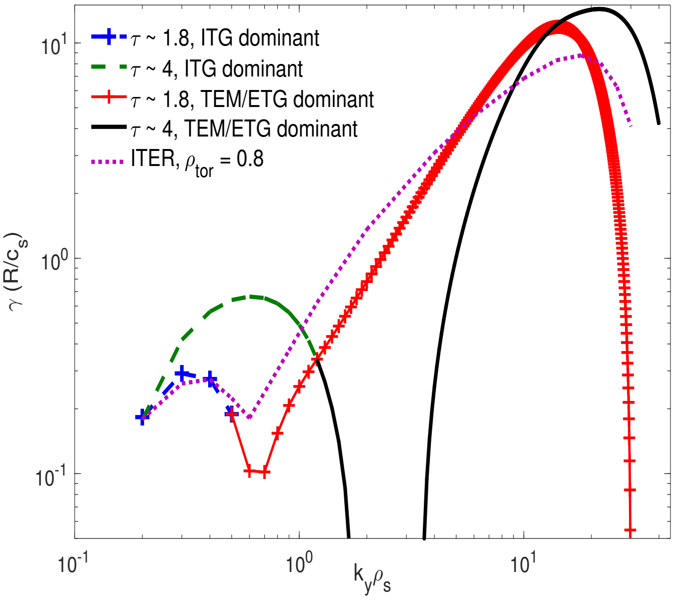

Figure 9.2: *Normalized linear growth rate of the main instability from GENE linear simulations at* $\rho_{tor} = 0.5$ *for* $\tau = 1.8$ *(black) and* $\tau = 4.0$ *(red). A simulation using ITER parameters from Ref. [27] at* $\rho_{tor} = 0.8$ *is also shown, indicating that the linear growth rate of ion and electron-scale instabilities is similar to what found in JET.*

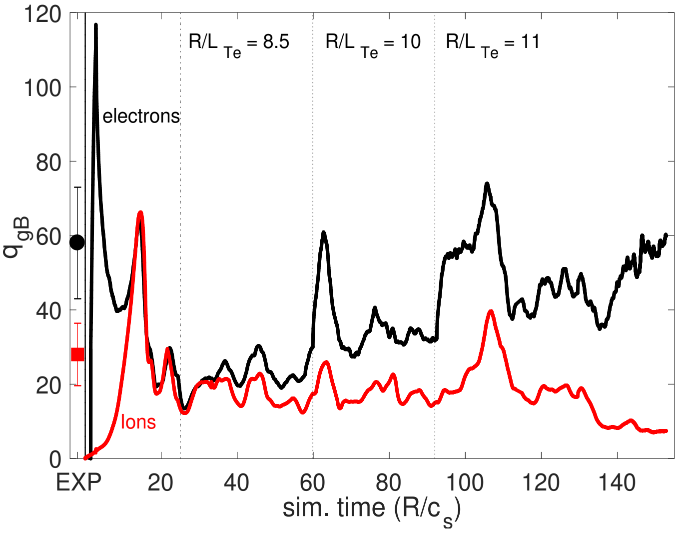

Figure 9.3: *Multi-scale time evolution of* $q_{i,gB}$ *(red) and* $q_{e,gB}$ *(black). The three phases of the simulation with* $R/L_{Te} = 8.5, 10, 11$ *are indicated. The experimental* q_i *and* q_e *are shown on the left (EXP). The simulation required ~20.000.000 CPU-hours.*

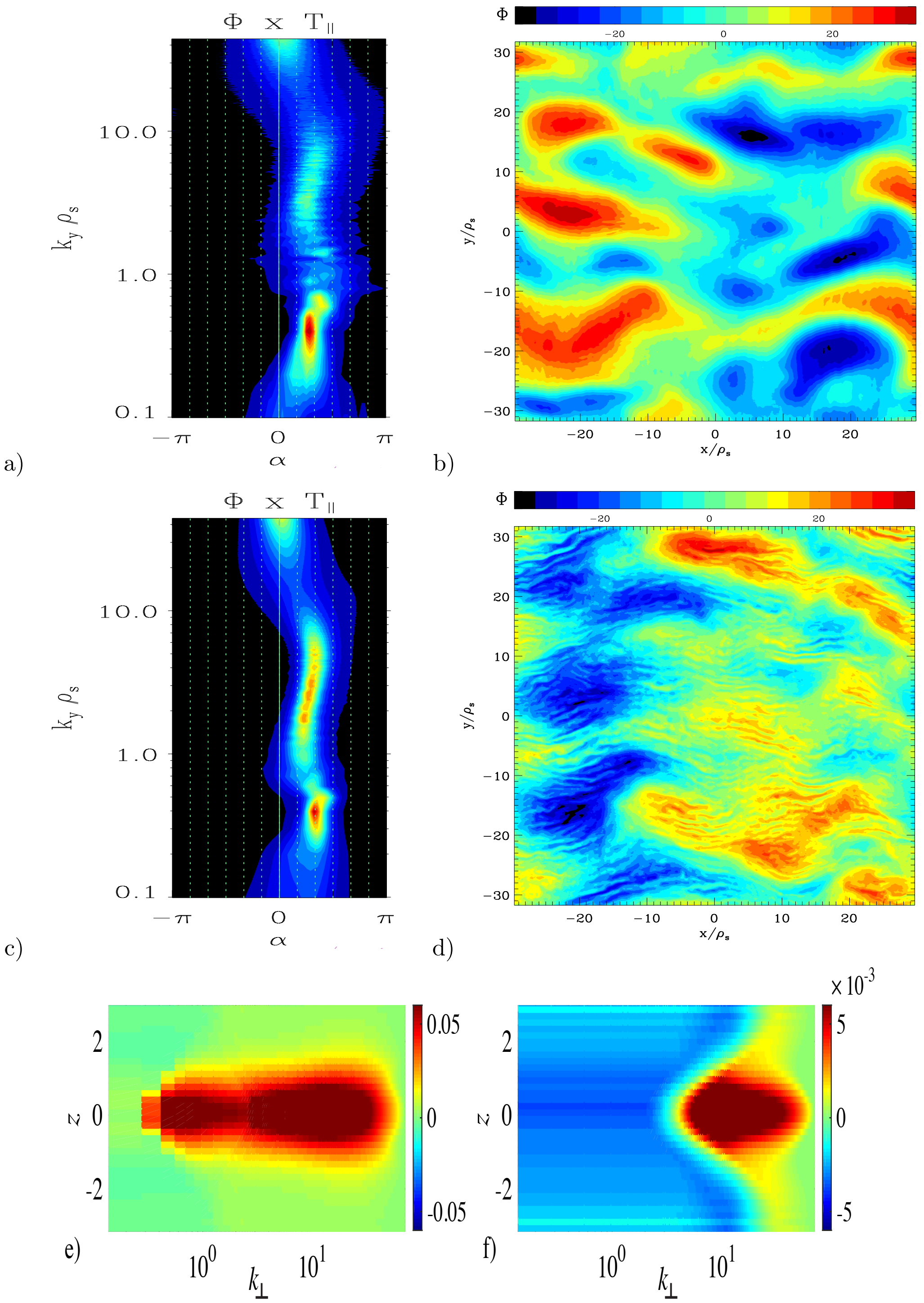

Figure 9.4: *Cross phases between* Φ *and* $T_{e,\|}$ *against phase angle* α *and* k_y *for* $R/L_{Te} = 8.5$ *(a) and* $R/L_{Te} = 11$*(c). Snapshot of* $\Phi(x/\rho_s, y/\rho_s)$ *for* $R/L_{Te} = 8.5$ *(b) and* $R/L_{Te} = 11$ *(d). e)Free energy flux across perpendicular scales* $k_\perp$ *for each* z $(\Pi(k_\perp, z) = \int_{k_\perp}^{\infty} \mathcal{T}(k'_\perp, z) dk'_\perp$*, normalized to* $\epsilon = \frac{1}{2} \int |\mathcal{T}(k_x, k_y, z)| \, dk_x dk_y dz)$ *for* $R/L_{Te} = 10$ *and (f) the contribution to* $\Pi(k_\perp, z)$ *from modes in the ETG range.*

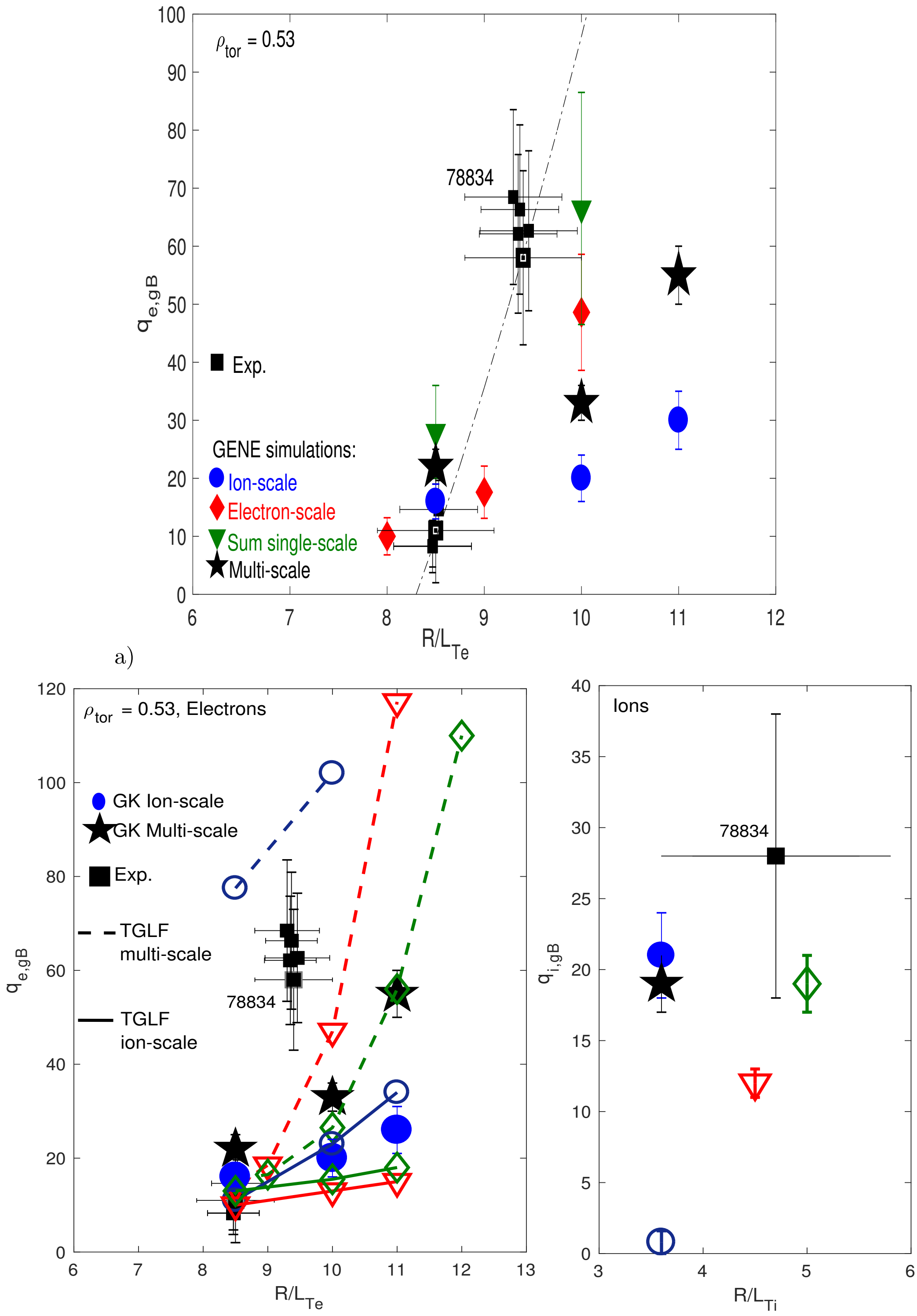

a)

b)

Figure 9.5: *a)* $q_{e,gB}(R/L_{Te})$. *Comparison between experiment, gyro-kinetic single-scale simulations and gyro-kinetic multi-scale simulations (scans in* R/L_{Te} *at different values of* R/L_{Ti} *with TGLF) b)* $q_{e,gB}(R/L_{Te})$ *and* $q_{i,gBs}(R/L_{Ti})$. *Comparison between experiment, gyro-kinetic multi-scale simulations and TGLF-sat1 simulations.*

References

[1] Romanelli F., Phys. Fluids B 1, 1018 (1989)

[2] Peeters A. G. et al., Phys. Plasmas 12, 022505 (2005)

[3] F. Ryter et al., Plasma Phys. Control Fusion 48, B453 (2006)

[4] P. Mantica et al., Fusion Science and Technology 53, 1152 (2008)

[5] J. C. Deboo et al., Phys. Plasmas 19, 082518 (2012)

[6] F. Jenko, et al., Phys. Plasmas 7, 1904 (2000)

[7] N. Bonanomi et al., Nucl. Fusion 55, 113016 (2015)

[8] N. T. Howard et al., Physics of Plasmas 21, 112510 (2014)

[9] Smith S. P. et al., Nucl. Fusion 55, 083011(2015)

[10] T. Görler and F. Jenko, Phys. Rev. Lett. 100, 185002 (2008)

[11] S. Maeyama and Y. Idomura, Phys. Rev. Lett. 114, 255002 (2015)

[12] N. T. Howard et al., Nucl. Fusion 56, 014004 (2016)

[13] T. L. Rhodes et al., Physics of Plasmas 14, 056117 (2007)

[14] W. Horton et al., Nucl. Fusion 45, 976 (2005)

[15] A. D. Gurchenko and E. Z. Gusakov, Plasma Phys. Control. Fusion 52, 124035 (2010)

[16] J. L. Burch et al. , Science Vol. 352, Issue 6290, aaf2939, 2016.

[17] M.O.Leubner, Z.Voros, Multi-scale Dynamical Processes in Space and Astrophysical Plasmas, Astrophysics and Space Science Proceedings Vol.33, Springer-Verlag Berlin Heidelberg, 2012.

[18] C. H. K. Chen et al., Phys. Rev. Lett. 110, 225002 (2013).

[19] G. M. Staebler et al., Phys. Plasmas 12, (2005)

[20] G. M. Staebler et al., Phys. Plasmas 14, (2007)

[21] G. M. Staebler et al., Phys. Plasmas 23, (2016)

[22] Mantica P. and Ryter F., C. R. Phys. 7, 634 (2006)

[23] Lopes N.J., Plasma Phys. Control. Fusion 37, 799 (1995)

[24] F. Jenko, et al., Phys. Plasmas 8, 4096 (2001)

[25] X. Garbet et al., Plasma Phys. Control. Fusion 46, B557 (2006)

[26] Imbeaux F., Ryter F. and Garbet X., Plasma Phys. Control. Fusion 43, 1503 (2001)

[27] B. Baiocchi et al., 2016 Joint Varenna–Lausanne International Workshop on the Theory of Fusion Plasmas, Varenna, Italy (Invited talk) and final report of ITER contract IO/CT/4300001087.

[28] S.C. Guo and F. Romanelli, Phys. Fluids B 5 (2), 520 (1993).

[29] Navarro A. B., Teaca B. and Jenko F., Phys Plasmas 23, 042301 (2016).

[30] Teaca B. et al., New J. Phys. 19, 045001 (2017).

[31] N. Bonanomi et al., Nucl. Fusion 58, 026028 (2018)

[32] Ennever P., et al., Phys. Plasmas 22, 072507 (2015).

[33] J. Citrin et al., Phys. Rev. Lett. 111, 155001 (2013).

Part IV

Effects of the isotope mass

Chapter 10

Effects of the isotope mass of the main ion species on thermal transport in JET L-mode plasmas

10.1 Introduction

In dedicated experiments in different machines it has been observed that the plasma thermal energy confinement time (τ_E) varies significantly with the mass of the plasma hydrogen isotope of the main ion species, in particular it increases with increasing isotope mass [1, 2, 3]. Effects of the isotope mass have been observed both at the plasma edge and in the plasma core [1]. In experiments performed in TFTR (Tokamak Fusion Test Reactor) and in JET, a strong ion heat transport reduction was obtained when changing the main ion species in the plasma from pure Deuterium (D) to a mixture of Deuterium–Tritium (DT) [1, 2]. Furthermore, an increase of τ_E and an increase of the ion temperature have been observed in TFTR $D-T$ plasmas with T NBI beam with respect to $D-T$ plasmas with D NBI beams [2]. This is of particular interest as many studies in nowadays tokamaks have been carried out using H or D isotopes, while in a future thermonuclear reactor a $D-T$ mixture will be used. It is therefore important to understand why and how the plasma confinement time varies with the isotope mass and how the isotope mass affects the plasma turbulence. The described experimental observations are in contrast to collisional and turbulent theory, that predict a decrease of the transport with lower isotope mass. The turbulent flux is expected to follow the Gyro-Bohm scaling and the step size of collisional transport and the turbulent structures are both expected to increase with the plasma gyro-radius, i. e. the flux is expected to scale with $m_i^{0.5}$. In the following we will name “isotope effect” any deviation from such mass dependence. Several physical mechanisms have been proposed as explanations of the experimentally observed ’isotope effect’, including effects on zonal flows [4, 5], differences of the plasma edge [6] or of the scrape off-layer density [1], differences in the ion-electron exchanged power [7], different impact of the external flow shear [8, 9] and different nonlinear electromagnetic effects [9].

In this chapter we will show the results of the analysis of experimental data obtained in JET ILW L-mode H plasmas and their comparison with L-mode D plasmas, with similar experimental settings and heating schemes, obtained in JET C-Wall and ILW. The analysis and modelling are still ongoing. What is new in our approach with respect to previous studies is that we measure and compare not just temperature profiles and power-balance diffusivities, but ion and electron threshold and stiffness level in H and

D plasmas with similar experimental parameters, so providing additional physical insight into the reasons for the observed differences.

10.2 Experimental set-up and methods

In order to compare H and D plasmas, the same settings and heating schemes have been used for both isotopes. We analyze a dataset of L-mode plasmas, from JET with C-Wall (only D plasmas) and ILW (both H and D plasmas), with vacuum toroidal magnetic field $B_T = 3.1 - 3.3\,T$, plasma current $I_p \approx 2\,MA$, electron density on the magnetic axis $n_{e,0} \sim 2.5 - 4{\cdot}10^{19}\,m^{-3}$ and safety factor at the flux surface that contains the 95% of the poloidal flux $q_{95} \approx 5$. The RF heating power consists of 2.5 – 7 MW of ICRH (Ion Cyclotron Resonance Heating) deposited on ions using as minority concentration $[^3He] \approx 6/2\%$ for D/H plasmas, or on electrons using $[^3He] \approx 18/6\%$ in D/H plasmas [10]. In addition to RF heating, 1.5 - 8 MW of NBI (Neutral Beam Injection) have been applied using H-ion beams in H plasmas and D-ion beams in D plasmas. The ICRH power was deposited both on-axis ($R \approx 3.0\,m$) and off-axis ($3.2 < R < 3.6\,m$) in order to obtain a scan of the ion and electron heat fluxes as a function of R/L_{Ti} and R/L_{Te}. An evaluation of the effects of different plasma rotation, different fast ion population and fast ions species (D, H and ^3He fast ions), different values of T_e/T_i, s, q, Z_{eff} was possible within the dataset. The ICRH power deposition and the ^3He fast ions density and energy density have been evaluated using the PION code [11] or, for few selected cases, the SELFO code [12, 13]. Using the SELFO code, it was also possible to calculate the distribution function of fast ^3He ions. The NBI heating power on electrons and on ions and the fast D pressure in the plasma have been calculated with the PENCIL code [14]. The ohmic power density has been calculated as $P_{Ohm} = \eta \cdot j^2$, where η is the resistivity of the plasma and j is the plasma current density reconstructed by the EFIT equilibrium code constrained by polarimeter measurements. Also the exchanged power density between ions and electron, p_{ei}, has been calculated analytically. The radiated power density p_{rad} has been estimated from bolometric measurements. The powers $P_{OHM}, P_{ICRH}, P_{NBI}, P_{ei}$ and P_{rad} have been obtained integrating over the plasma volume and the ion and electron heat fluxes are expressed in gyro-Bohm units as

$$q_{i,gB_i} = [(P_{ICRH,i} + P_{NBI,i} + P_{ei})/\Sigma] \cdot R_0^2/(n_e T_i \rho_i^2 v_{th,i}) \qquad (10.1)$$

$$q_{e,gB_s} = [(P_{ICRH,e} + P_{NBI,e} + P_{OHM} - P_{ei} - P_{rad})/\Sigma] \cdot R_0^2/(n_e T_e \rho_s^2 c_s) \qquad (10.2)$$

where Σ is the considered flux surface, $c_s = \sqrt{T_e/M_i}$, $v_{th,i} = \sqrt{T_i/M_i}$, $\rho_i = v_{th,i} M_i/eB_T$ and $\rho_s = c_s M_i/eB_T$, M_i being the ion mass ($H\,or\,D$). Typical errors on the heat fluxes are $\sim 20\%$. For the measurement of the electron temperature T_e the ECE (Electron Cyclotron Emission) diagnostic has been used, while the ion temperature T_i and the plasma toroidal rotation ω_T have been measured by the active Charge Exchange (CX) diagnostic. The electron density n_e has been measured by high-resolution Thomson scattering (HRTS). The radial profile of the safety factor q, of the magnetic shear $s = r/q \cdot dq/dr$ and of the equilibrium plasma geometry have been reconstructed by the EFIT equilibrium code with Faraday rotation or Motional Stark Effect constraints, depending on the availability. Local values of $R/L_{Ti} = -R_0 \nabla T_i/T_i, R/L_{Te} = -R_0 \nabla T_e/T_e$ and $R/L_n = -R_0 \nabla n_e/n_e$ are obtained by local linear fits of $ln(T_i), ln(T_e)$ and $ln(n_e)$ radial profiles. The fits are done using $r = (R - R_{in})/2$, R and R_{in} being the outer and inner radii of the flux surface on the magnetic axis plane, and averaging other multiple fits using a variable number of data points around the chosen radius (3-9 points). Errors on these quantities are typically $\sim$ 15%. The data analysis has been carried out at $\rho_{tor} = 0.33$ and $\rho_{tor} = 0.5$, where$\rho_{tor} = \sqrt{(\Phi/\pi B_T)/(\Phi/\pi B_T)_{max}}$, Φ being the toroidal magnetic flux.

10.3 Experimental results

10.3.1 Ion heat transport

In the following two different heating schemes will be analyzed: the 'low power' one, corresponding to ~1.5 MW of NBI power plus ~3 MW of ICRH power, and the 'high power' one, corresponding to ~8MW of NBI plus ~3 MW of ICRH or to ~1.5 MW of NBI and ~7 MW of ICRH. In the low power case a high ion stiffness has been observed on the whole temperature profile, while in the high power case a region with a strong reduction of the ion turbulent transport has been observed in the inner central core region of the plasma, due to non-linear e.m. stabilization by fast and thermal pressure, as discussed in chapter 6.

For the same amount of heating power, the core ion temperature is lower over the whole radial profile in H plasmas with respect to D plasmas (see figure 10.1). This difference starts outside $R \approx 3.8\, m$. The behavior of the core ion heat transport does not show substantial differences between H and D plasmas in our low power cases (figure 10.2) and it seems consistent with the gyro-Bohm scaling. This is difficult to proof outside the experimental uncertainties in the studied plasmas as the variation of T_i, the high ion stiffness and the uncertainties on R/L_{Ti} mask possible deviations form the scaling. In any case, no substantial differences in the R/L_{Ti} critical threshold or in the ion stiffness are visible between H and D plasmas in the low power case.

In the high power case, a difference between D and H plasmas has been observed inside $\rho_{tor} \lesssim 0.4$. As can be seen in figure 10.2a, while in D plasmas a strong reduction of the ion stiffness is visible (red points and squares), in H plasmas this effect is lower (red pentagons). The question is then whether the nonlinear electromagnetic stabilization due to fast ions is less effective in H plasmas, as suggested in [9], or whether more simply there is a different fast ions pressure in H plasmas with respect to D plasmas, or also whether the fast H ions are less effective in the electrostatic ITG mode stabilization, which is an additional stabilizing effect beyond dilution recently studied in ref. [15] (see also chapter 6).

The first hypothesis has been studied in reference [9], where it was found that nonlinear electromagnetic stabilization and external flow shear are less effective in stabilizing the ITG modes with lower plasma main ion mass. Regarding the third hypothesis, it appears that there is a dependence of the electrostatic effects related to the fast ions on the fast ion energy [15], which depends on the fast ion velocity and so on T_{fast} and m_{fast}. So at the same temperature, the effect of fast ions can be different for different fast ion species. In general, it is expected that lower temperatures are needed to obtain the same ITG electrostatic stabilization with lower fast ions mass. In our fast ions temperature range, without considering the possible differences in the fast ions densities, the electrostatic stabilization of ITG modes due to H fast ions is expected to be more effective with respect to the electrostatic stabilization due to fast D. In our case, the electromagnetic effect is expected to be the dominant one, especially for NBI fast particles in our range of temperatures [16], and the differences between the electrostatic effect of fast H and D ions should not be the determinant one in the discharges with high NBI power but low ICRH power. More studies are needed to confirm and quantify this. Regarding the second hypothesis, a comparison between the fast ion density, temperature and total pressure radial profiles in D and H plasmas is shown in figure 10.3. The fast ion pressure is lower in H plasmas both with high ICRH and with high NBI power. In the high ICRH case this is due to the fact the the ion heating in $H-({}^3He)$ plasmas is obtained using a ${}^3He$ concentration $\sim 2\%$, while in $D-({}^3He)$ plasmas it is obtained using ${}^3He \sim 6-9\%$. The fast ${}^3He$ density is then lower in H plasmas, while the fast ${}^3He$ temperature is comparable between H and D plasmas. In the high NBI power case, both the fast ion density and temperature are lower in H plasmas. These differences can be understood considering different factors. The typical voltage used to accelerate the neutral beams injected in the plasma was lower for H beams ($\sim 70\,kV$) with respect to the ones used to accelerate the D beams ($\sim 100\,kV$), leading to an average energy of the D beams that is almost twice the one of the H beams. The injection rate of H beams was almost twice the one of D beams, but the slowing down time for H beams was only 1/3 of the one of D beams. These two factors explain why the number of fast H ions is $\sim 40\%$ less than the number of fast D ions. Another factor that contributes to the differences between D and H fast ions is the different energy composition of the beams. In D plasmas a larger fraction ($\sim 55\%$) of the beam was injected in the plasma at full energy, leading to a more on-axis power deposition, while in H plasmas the full energy beams where just $\sim 30\%$ of the total injected beams, leading to a more off-axis power deposition. The differences in fast ion pressure between H and D plasmas can indeed cause differences in the fast ion stabilization of ITG modes and contribute to the observed positive scaling of confinement with isotope mass.

10.3.2 Electron heat transport

The electron temperatures in H plasmas are lower over the whole radial profile, for the same amount of heating power, with respect to the ones in D plasmas (figure 10.4). Looking at the electron temperatures and densities (figures 10.5 and 10.6) it appears that T_e is flat/hollow while n_e peaks inside $\rho_{tor} \approx 0.35$ in the discharges with dominant ICRH ion heating and especially in the discharges with high NBI power. This is an indication of a possible accumulation of heavy impurities in the plasma core. In the same plasma conditions, an accumulation of heavy impurities in JET L-mode D plasmas is difficult to observe. More investigations are needed on the particle transport in these plasmas to understand if the differences observed between H and D plasmas are linked to differences in the particle transport. Furthermore, in all the H plasmas, a high radiated power in the outer region of the plasma ($\rho_{tor} \gtrsim 0.8$) is present, with values 3-4 times higher with respect to the ones in D plasmas (figure 10.7). These observations suggest that there are differences, between H and D plasmas, in the impurity content. More study is needed to understand the reasons of these differences.

Finally, from the values of $q_{e,gB}(R/L_{T_e})$, plotted in figure 10.8, no differences in electron heat transport between D and H plasmas is evident. At $\rho_{tor} = 0.5$, the values of R/L_{Te} are in general higher in H plasmas. Looking at the plot in figure 10.9 of $R/L_{Te}(\tau)$, where $\tau = Z_{eff}T_e/T_i$ is an important factor for ETG modes [17], the strong dependence of R/L_{Te} on τ, observed in D plasmas and indicative of a possible role of ETG modes (see chapter 9), is not visible.

10.4 Gyrokinetic simulations

In this section, some initial results on the study of the effect of fast ions in different isotope plasmas and of the impact of the different fast ion pressure in H and D plasmas gyrokinetic simulations are shown. For the study of the effect of fast ions in different isotope plasmas, the input parameters and settings used for the gyrokinetic analysis presented in chapter 6 have been used considering H, D and T as main ion species. As a reminder, the plasma parameters used as input in the simulations have been taken from discharge n. 90672 at $\rho_{tor} = 0.25$ and $t \approx 6\ s$. Some important values, used in the simulation, are: $Z_{eff} = 1.36, q = 1.4, s = 0.46, R/L_{^3He} = R/L_{ne} = 2.6, R/L_{Te} = 8, R/L_{Ti} = 7.2, R/L_{T,^3He} = 15, T_{^3He} = 12T_e, T_i/T_e = 0.8, \beta_{ref} = 8\pi n_e T_e/B_0^2 = 0.00399, \nu* = \nu_{ei}\frac{qR_0}{\epsilon^{1.5}v_{th,e}}0.06, n_{^3He} = 0.09n_e$, where $\epsilon = r/R_0$ and $v_{th,e} = \sqrt{T_e/m_e}$. When not considering the fast ^3He ions in the simulations, we use $T_{^3He} = T_i$ and $R/L_{T^3He} = R/L_{Ti}$ without changing any other input parameter. In these simulations we then fix the fast ions (^3He) pressure while changing the main ions (H, D, T). The results from the linear gyrokinetic simulations are shown in figure 10.10.

The linear growth rate fulfills the expected scaling $\sim (T_{ions}/m_{ions})^{0.5}/R$ with the isotope mass, with the peaks of the growth rate at $\sim k_y\rho_i = 0.5$, ρ_i being the Larmor radius of the different isotope considered. This corresponds to $k_y\rho_s \approx 0.45$ for T, $k_y\rho_s \approx 0.55$ for D and $k_y\rho_s \approx 0.7$ for H. The stabilization of ITG modes, when considering fast ions and electromagnetic effects, is the same for all the isotopes (-40% of the linear growth rate) in the $k_y\rho_s$ range around the peak of the nonlinear flux. In the ETG range, the enhancement of the linear growth rate is the same for the three isotopes ($+50\%$), with no differences in the wavenumber of the peak of the linear growth rate, $k_y\rho_s \approx 20$ for all the isotopes.

Regarding the nonlinear simulations, some preliminary results are shown in figure 10.11. The differences in the scaling of the heat flux, when considering electromagnetic effects, observed in ref. [9], has not been observed. We obtain $q_H = 61 \pm 5\ kWm^{-2}$ for hydrogen, $q_D = 88 \pm 6\ kWm^{-2}$ for deuterium and $q_T = 97 \pm 12\ kWm^{-2}$ for tritium, with $q_T \approx \sqrt{1.5}q_D \approx \sqrt{2}q_H$. No substantial deviations from the expected scaling has been observed, the fluxes from the nonlinear simulations following the gyro-Bohm scaling. More detailed studies need to be done, studying for example the effects of rotation or the impact of fast ions with respect to the cases without fast ions in the simulations.

For the study of the effects of the changes in the fast ion pressure between D and H plasmas, discharges n. 73224 (D, C-Wall) and n. 91710 (H, ILW) have been considered. In the linear simulations the input parameters from discharge n. 73224 at t = 6 s have been used, changing the fast ion pressure as indicated in table 10.1. Kinetic ^3He and fast D ions have been considered in the simulations as well as electromagnetic effects $(\delta B_{\parallel}, \delta B_{\perp})$. Some important values, used in the simulation, are: $Z_{eff} \approx 1.3, 1.36, q = 1.736, s = 0.523, R/L_{ne} = 1.24, R/L_{Te} = 6.6, R/L_{Ti} = 10.6, T_i/T_e = 1.0, \beta_{ref} = 8\pi n_e T_e/B_0^2 = 0.0033, \nu* = \nu_{ei}\frac{qR_0}{\epsilon^{1.5}v_{th,e}} \approx 0.08$.

The ITG linear growth rate is reduced by $\sim 47\%$ at the position of the peak with the fast ion pressure of discharge 73224, while just by $\sim 18\%$ when the fast ions of discharge 91710 are considered (see figure 10.12). This result suggests that the differences in the fast ions pressure between D and H plasma have a strong impact on the stabilization of ITG modes.

	fast D				fast ^3He			
	n	T/T_e	R/L_n	R/L_T	n/n_e	T/T_e	R/L_n	R/L_T
73224	6%	9.8	14	3.1	7%	7	1.49	22
91710	4%	7	8	1.3	2%	12	1.24	22

Table 10.1: *Parameters for fast deuterium and fast ^3He used as input in the gyrokinetic simulations.*

10.5 Conclusions

Differences have been observed between H and D plasmas with the same operational settings (heating power, geometry, I_p, B, q, n_e). Both T_e and T_i are lower in H plasmas, the difference starting at the plasma edge. In low power plasmas, the ion heat flux in the plasma core does not deviate from the gyro-Bohm scaling law outside error bars, but, as the strong influence of T_i dominates over the mass one in the gyro-Bohm normalization, it is difficult to make a certain conclusion from our data. A difference in the ion heat flux has been observed at higher power, in the situation where a strong stabilization of ITG modes by fast ions is expected. In this case, the stabilization of the ion heat transport is less strong in H plasmas with respect to D plasmas. A possible explanation of this difference has been found in the difference of the fast ion pressure in H and D plasmas, in H plasmas being $\sim 1/2$ of the one in D plasmas when high NBI or ICRH heating is applied. This is mainly due for NBI fast ions to the lower beam injection energies and shorter beam slowing down time in H plasmas and for the ICRH fast ions to the lower ^3H e concentration needed for the ICRH minority scheme heating in H. The electron heat transport shows in general higher values of R/L_{Te} in H plasmas. Also, the strong correlation between R/L_{Te} and τ observed in D plasmas has not been observed in H plasmas. Further studies are needed in order to explain the observed differences. Another difference between H and D plasmas is the accumulation of heavy impurities in the plasma core observed in H plasmas with dominant ICRH ion heating and not observed in similar conditions in D plasmas. No accumulation has been observed using dominant electron ICRH heating. Further investigations are needed on possible differences of the particle transport in D and H plasmas.

Figures

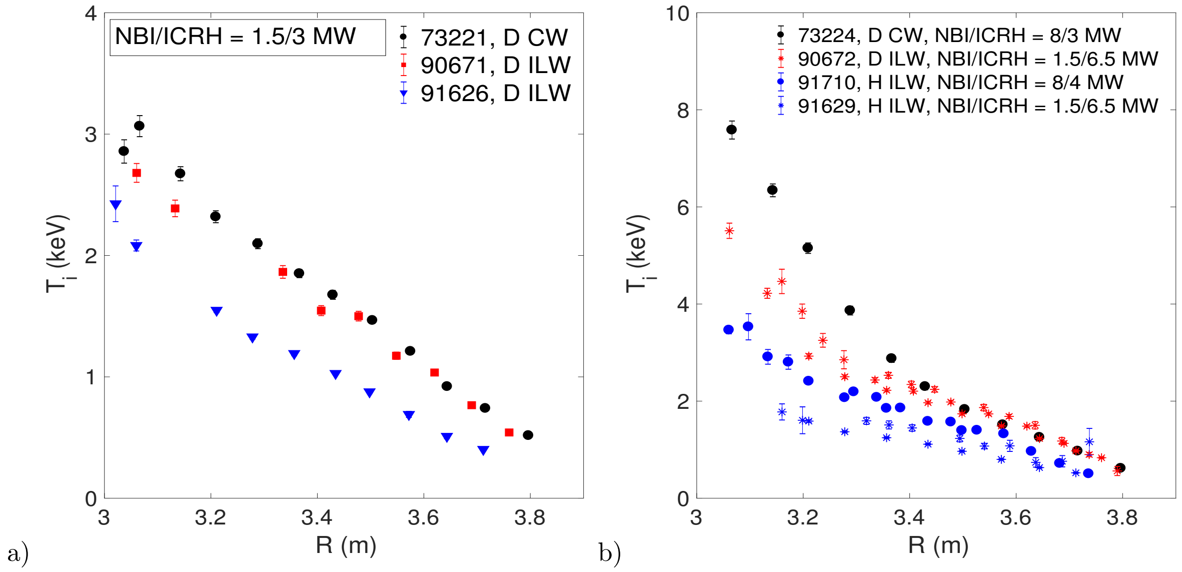

Figure 10.1: *Comparison of radial T_i profiles in JET C-Wall and ILW D plasmas and in JET ILW H plasmas with low heating power (a) and high heating power (b).*

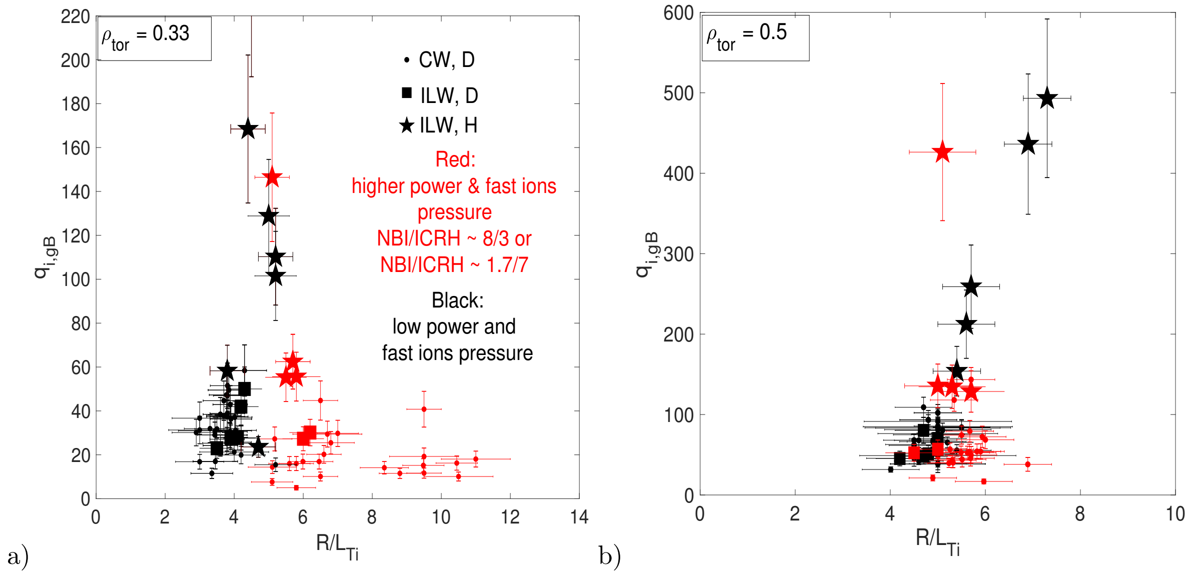

Figure 10.2: *Comparison of $q_{i,gB}(R/L_{Ti})$ in JET C-Wall and ILW D plasmas and in JET ILW H plasmas at $\rho_{toe} = 0.33$ (a) and at $\rho_{tor} = 0.5$ (b).*

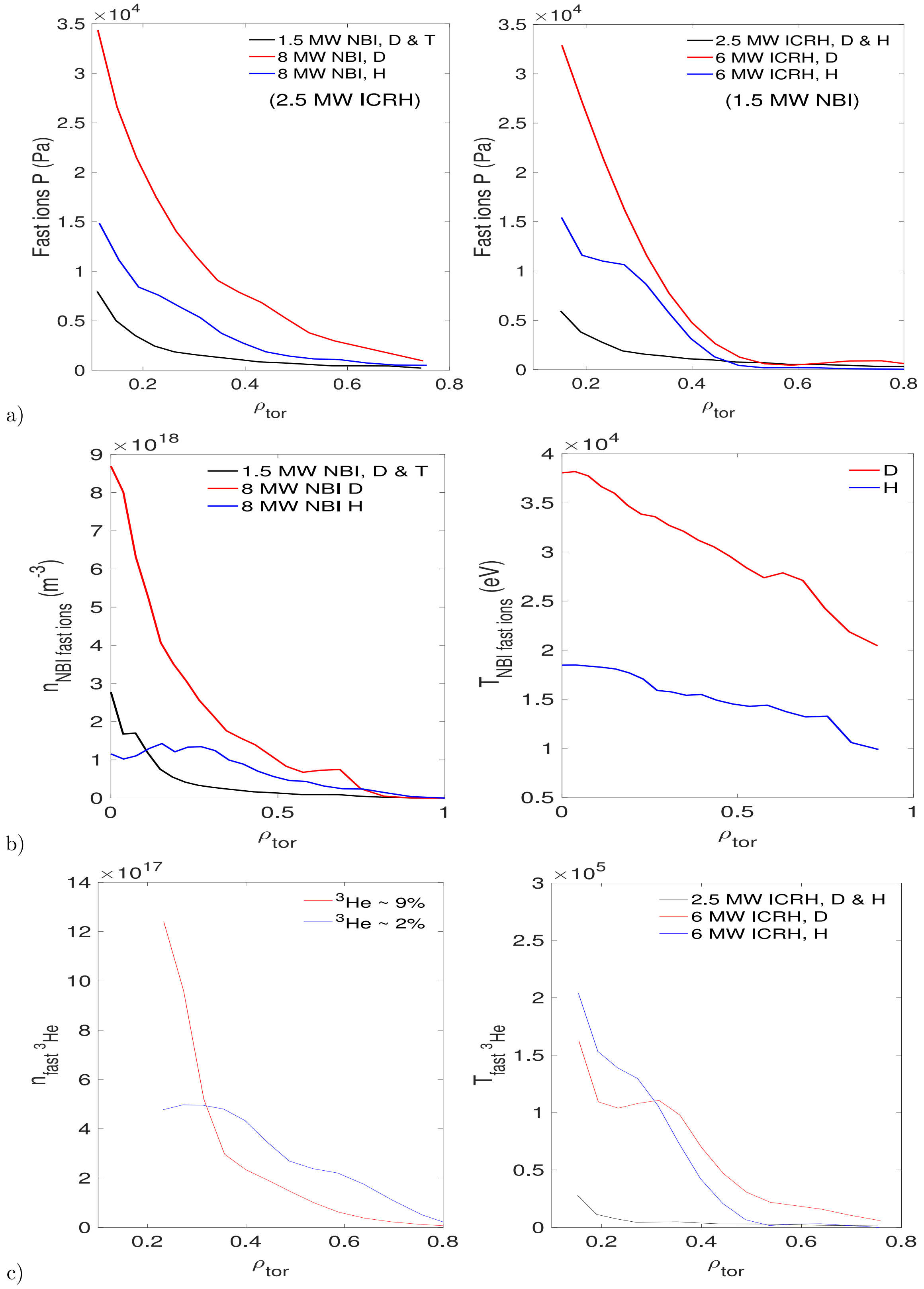

Figure 10.3: *Comparison of radial profiles of fast ions pressure (a), fast ions density and fast ions temperatures (c) in D plasmas and H plasmas with different heating power.*

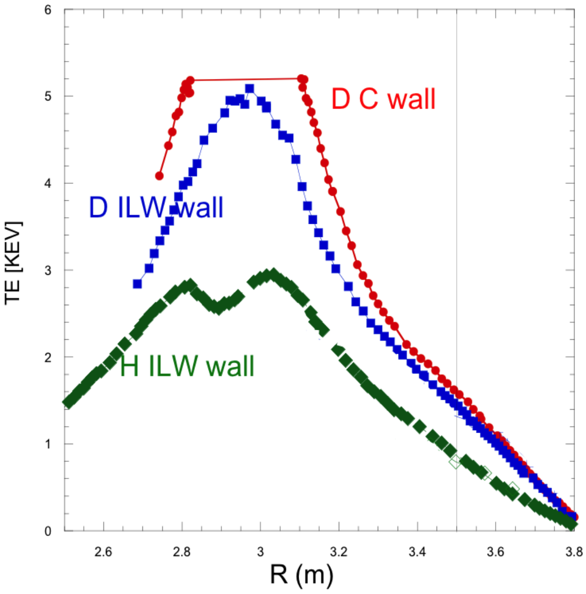

Figure 10.4: *Comparison of radial T_e profiles in JET C-Wall and ILW D plasmas and in JET ILW H plasmas.*

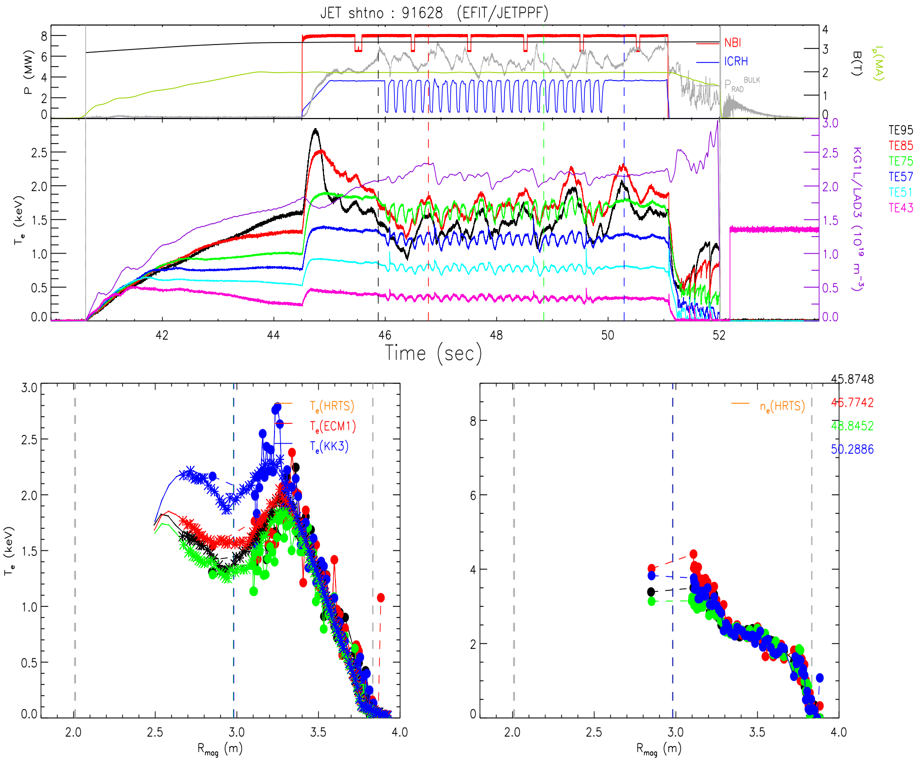

JET profiles (nbonan), Mon Oct 23 10:00:34 2017

Figure 10.5: *Time evolution of NBI and ICRH heating and radial profiles of T_e and n_e of the JET ILW H discharge n. 91628. Different colors of the radial profiles correspond to different times.*

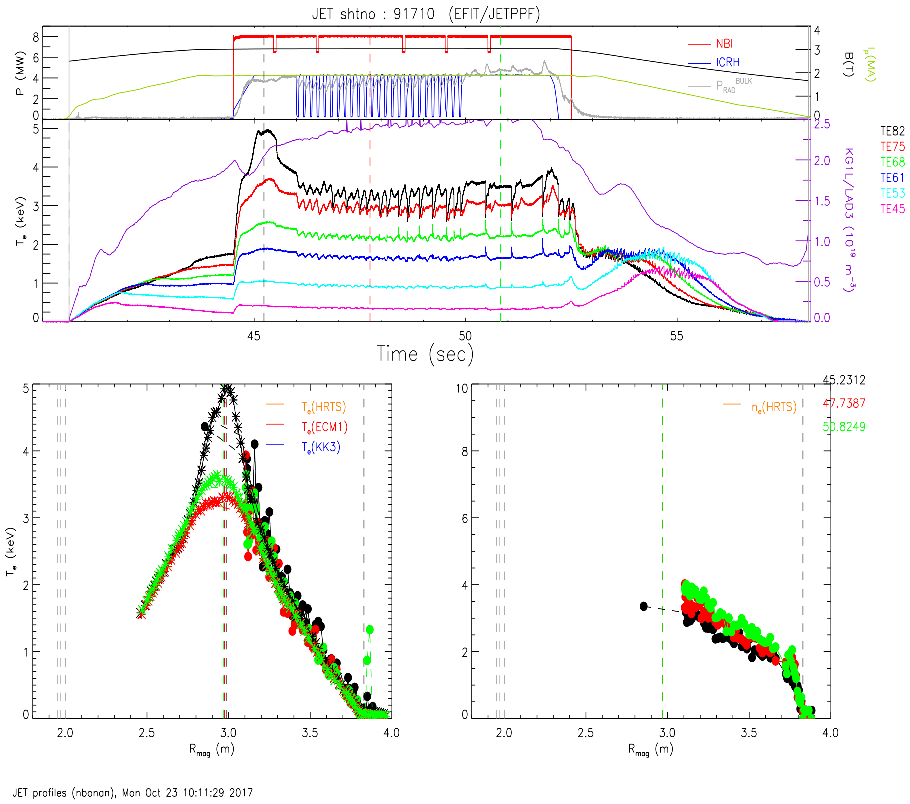

Figure 10.6: *Time evolution of NBI and ICRH heating and radial profiles of T_e and n_e of the JET ILW H discharge n. 91710. Different colors of the radial profiles correspond to different times.*

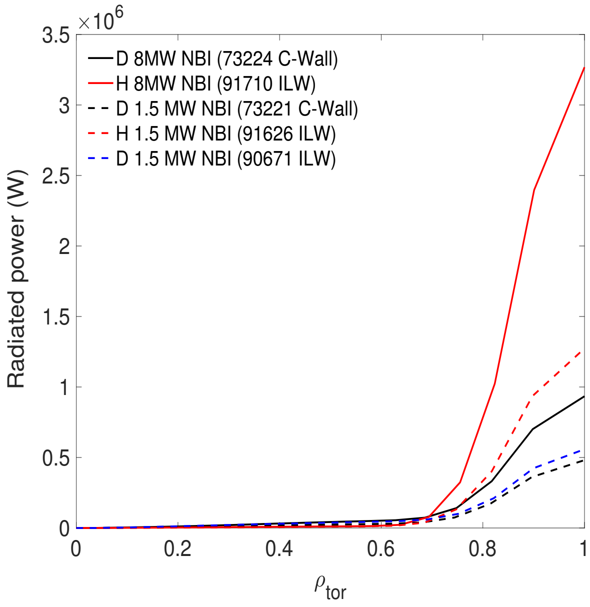

Figure 10.7: *Comparison of the radial profiles of the radiated power in JET C-Wall and ILW D plasmas and in JET ILW H plasmas with high (8 MW) and low (1.5 MW) NBI power.*

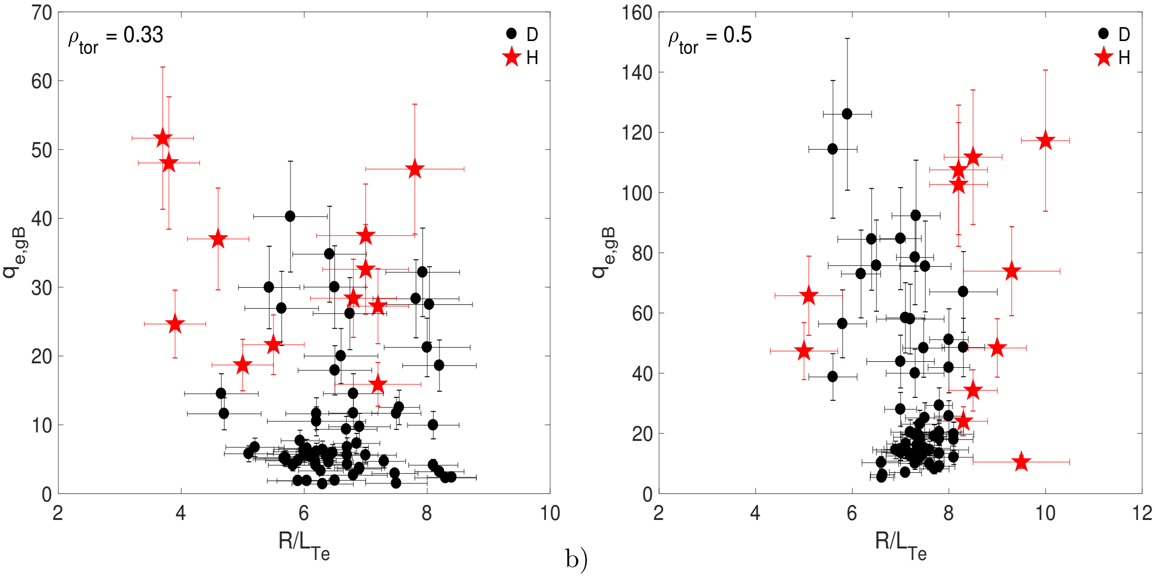

a) b)

Figure 10.8: *Comparison of* $q_{e,gB}(R/L_{Te})$ *in JET C-Wall and ILW D plasmas and in JET ILW H plasmas at* $\rho_{toe} = 0.33$ *(a) and at* $\rho_{tor} = 0.5$ *(b).*

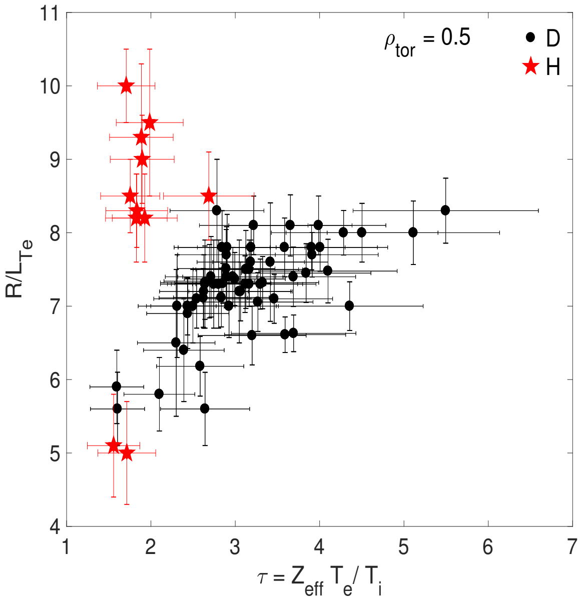

Figure 10.9: *Comparison of* $R/L_{Te}(\tau = Z_{eff}T_e/T_i)$ *in JET D andH plasmas at* $\rho_{tor} = 0.5$.

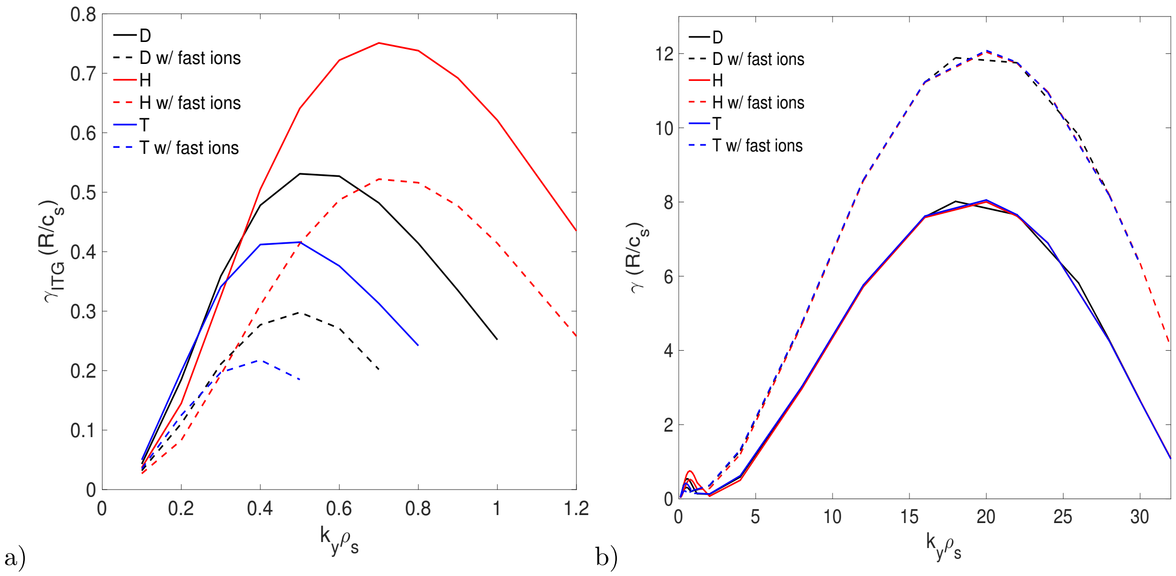

Figure 10.10: *Linear growth rate of the ITG instability (a) and ETG instability (b) from linear gyrokinetic simulations using H, D and T as main ion species in the simulation.*

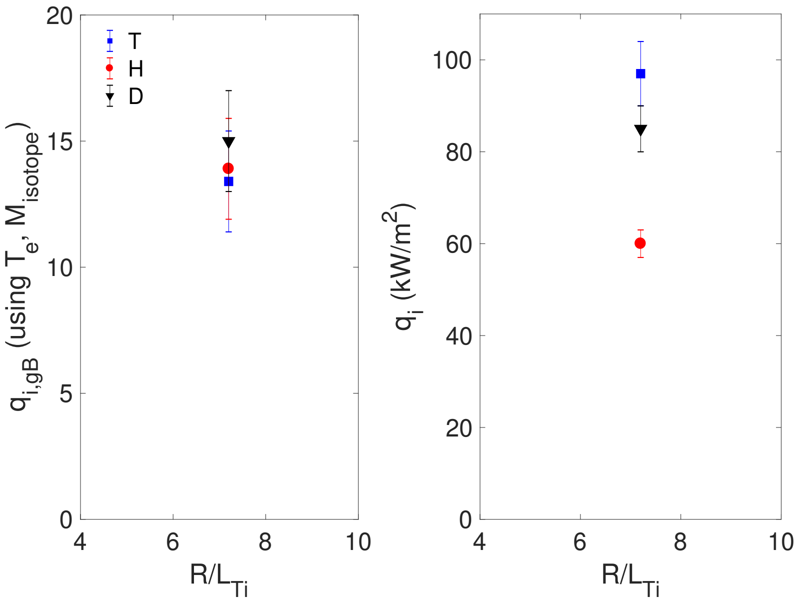

Figure 10.11: *Nonlinear GENE simulations using parameters from discharge 90672 at $\rho_{tor} = 0.25$. In the simulations three main ion species have been considered: H, D and T. The heat fluxes from simulations respect the gyro-Bohm scaling. No simulations without fast ions, in order to study the relative effect of fast ions with different isotope, have been carried out yet.*

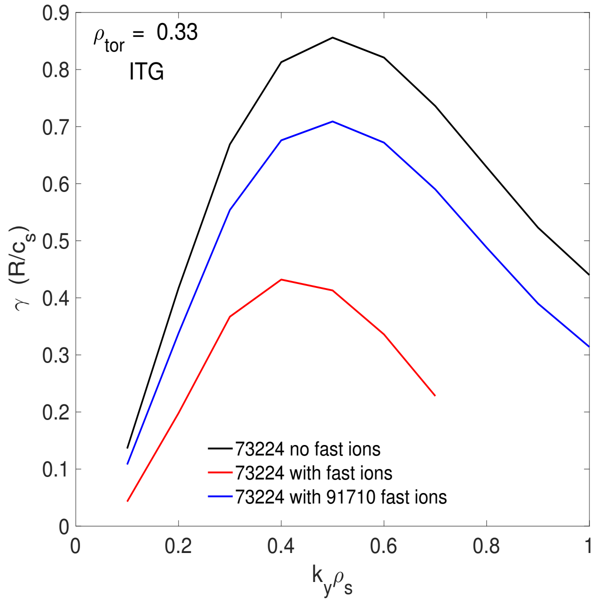

Figure 10.12: *Linear growth rate of the ITG instability using different fast ion pressure.*

References

[1] M. Bessenrodt-Weberpals et al., Nucl. Fusion 33, 1205 (1993).

[2] S. D. Scott et al., Plasma Phys. 2, 2299 (1995).

[3] C. Gormenzano et al., Phys. Rev. Letter 80, 5544 (1998).

[4] T. S. Hahm et al., Nucl. Fusion 53, 072002 (2013).

[5] Y. Xu et al., Phys. Rev. Lett. 110, 265005 (2013).

[6] G. Saibene et al., Nucl. Fusion 39, 1133 (1999).

[7] P. A. Schneider et al., Nucl. Fusion 57, 066003 (2017).

[8] X. Garbet and R. E. Waltz, Phys. Plasmas 3, 1898 (1996).

[9] J. Garcia et al., Nucl. Fusion 57, 014007 (2017).

[10] D. Van Eester et al., Plasma Phys. Control. Fusion 51, 044007 (2009).

[11] L. G. Eriksson, T. Hellsten and U. Willén, Nucl. Fusion 33, 1037 (1993).

[12] J. Hedin et al., Nuclear Fusion 42, 527 (2002).

[13] T. Hellsten et al., Nuclear Fusion 44, 892 (2004).

[14] C. Challis et al., Nucl. Fusion 29, 563 (1989).

[15] A. Di Siena et al., “Fast-ion stabilization of tokamak plasma turbulence”, 2017. Submitted to Phys. Rev. Lett..

[16] J. Citrin et al., Nucl. Fusion 54, 023008 (2014).

[17] F. Jenko et al., Phys. Plasmas 8, 4096 (2001).

Part V

Conclusions and future work

Chapter 11

Conclusions and future work

Different fundamental aspects of thermal turbulent transport have been studied in JET L-mode plasmas through both experimental analysis and gyrokinetic simulations. An interpretation of the experimental results has been reached with the help of gyrokinetic simulations, and some physical effects have been evidenced in JET plasmas that are relevant for future ITER scenarios. Some important indications on the validity of the available numerical models of turbulent transport have been also obtained, as well as suggestions for possible improvements. In the following a review of the main results obtained and some perspectives on possible future developments of the work are provided.

Light impurity particle transport:

The radial density profiles of $^3He, Be, C, N$ and Ne, all measured by active charge-exchange diagnostic in JET ITER-like wall L-mode plasmas, have been shown and studied. While ^3He, Be and Ne density profiles are peaked over the whole plasma core region, the profiles of C and N show a flat/hollow region inside $0.3 \lesssim \rho_{tor} \lesssim 0.7$. Our neoclassical, quasi-linear and nonlinear gyrokinetic simulations could not reproduce the observed behavior, the simulations predicting similar peaking of the density profiles for all the light impurities studied and peaked profiles at all the studied radii. Regarding ^3He, a possible role of the Plume effect on the measured peaking will have to be estimated. An ongoing analysis shows that the Plume effect in the JET shots considered may contribute to up to $\sim 30\%$ of the measured ^3He density, but with less influence on the peaking. On the simulation side, considering fast particles and making wider scans of parameters such as $q, s, R/L_{ne}$ could help to reproduce the experimental observations.

Effects of puffed light impurities on the core thermal transport:

A detailed study of the effect of N seeding on the core ion thermal transport of JET L-mode ILW plasmas has been carried out. The following aspects emerged:

- From nonlinear gyrokinetic simulations it appears that not only the main ion dilution is a key factor for the stabilization of ITG modes and ion thermal transport, but also the density peaking of the light impurity is important. While main ion dilution induces a reduction of the ion stiffness, higher light impurity density peaking induces a higher upshift of the ITG critical threshold in R/L_{Ti}. Hollow or flat light impurity density peaking can also induce a decrease of the ITG critical threshold. The stabilizing effect of the normalized light impurity density peaking ($R/L_{n,Z}$) could be related to the fact that, for a fixed value of the electron density peaking, a higher value of $R/L_{n,Z}$ means a lower value of $R/L_{n,i}$, the main ion density peaking, leading to a lower destabilization of ITG modes, mainly driven by the main ions.

- Changes in plasma parameters induced by the presence of the light impurity also affect core transport. In our experiment, puffing N induced changes in Z_{eff} and in main ion dilution that, in addition to directly stabilizing the ITG modes, induced changes in T_e/T_i and, through a change in the plasma resistivity, in q and s. The changes in s/q and T_e/T_i turned out to be the dominant mechanisms leading to the ITG critical threshold upshift observed in the experiment.

- Our nonlinear gyrokinetic simulations were able to reproduce well the experiment and were fundamental in explaining the observed changes in the plasmas. The predict-first study with linear and nonlinear gyrokinetic simulation turned out to be a precious guide in the experimental choice of the seeding gas and of the level of injection to ensure detectability of the effects;

- TGLF tends to generally underestimate the ion stiffness, as already observed for JET discharges. Concerning the effects of the light impurity, it is able to reproduce quantitatively the effects on both threshold and stiffness observed in gyrokinetic runs.

- QuaLiKiz reproduces well the ion stiffness, but shows critical thresholds slightly shifted respect to gyrokinetic simulations. It predicts mainly a shift of the ITG critical R/L_{Ti} threshold in presence of light impurities, quantitatively of the right magnitude, but no effect on the ion stiffness at variance with GENE and TGLF. The effect of geometry has also been found important.

It is clear that being able to predict how the impurities propagate in the plasma and to reproduce their density profile is essential to correctly predict how the turbulences will change due to their presence. An improvement of both QL models is necessary, particularly on the match of the ion stiffness and threshold already in the case with no N. An overall conclusion on the benefits of the presence of light impurities in a reactor plasma are difficult to draw. The fusion power strongly depends on both T_i and n_i. A reduction of n_i for D and T can be justified if the rate of the fusion reaction increases substantially with a little increase of T_i. In ITER, temperatures $\gtrsim 10\,keV$ are expected toward the plasma center. With these temperatures, a strong increase in T_i is needed in order to obtain a substantial increase in the fusion reaction rate, with the consequence that loosing ion density to obtain the needed increment of temperature is not worth it. The picture is different if the light impurity introduced in the plasma is light enough to not dilute much the ion density and at the same time can be accelerated by Radio Frequency to produce fast ions that strongly stabilize the thermal transport, as discussed in the next paragraph.

Effects of fast ions on core thermal transport:

The analysis of JET ILW L-mode plasmas with low NBI power (~1.5 MW) and high ICRH power (up to ~7 MW) in $(^3He)-D$ minority scheme allowed to obtain the following results:

- Experimental evidence of strong stabilization of thermal transport in presence of high fast ion pressure in low rotation plasmas has been obtained. These results represent the first experimental demonstration that fast ion stabilization is independent of rotation.

- Gyrokinetic simulations were able to explain the experimental observations when fast ^3He ions and electromagnetic effects were considered, indicating that the effects related to the presence of the fast ions are the key mechanisms. Two main mechanisms are responsible of the ITG stabilization: an electrostatic mechanism related to a resonant wave-fast particle interaction and an electromagnetic effect enhanced by the fast ion pressure that leads to higher values of the plasma β. These results confirm what found in past studies and also represent a first observation of a strong electrostatic stabilization of ITG modes due to fast ions and not related to main ion dilution.

- It was also found that the fast ion distribution function influences the quantitative prediction of the stabilization.

- Fast ions also reduce the value of $\tau = Z_{eff} \cdot T_e/T_i$, due to their high temperatures, and strongly destabilize the ETG modes. It is then important to consider the effect of fast ions for a consistent study of ETG modes and electron heat transport.

While the electrostatic mechanism has been recently explained, the nonlinear electromagnetic mechanism is still under investigation. The electromagnetic mechanism is related to the plasma pressure and pressure gradient. The presence of fast ions, especially in the analyzed L-mode low- β plasmas, enhances this effect thanks to the high fast ion pressure. A possible explanation of the electromagnetic stabilization in terms of non-linear correlation of triplets of wave numbers has been recently proposed in a work of M. J. Pueschel et al. presented at the 19th ITPA-Transport and Confinement Topical Group Meeting (Espoo, September 19, 2017). Better physical understanding is needed in order to be able to introduce this effect in a quasi-linear model such as TGLF or QuaLiKiz. Further work is also needed to understand what will be the role of fast ions in ITER. The fast α particles, created by the fusion reactions, are not expected to play any role in the electrostatic stabilizing mechanism of ITGs mentioned above, due to their high energies, but we need to evaluate what will be their role for the electromagnetic stabilization. Furthermore, the use of ICRH heating with a minority species could be useful to increase ITER core temperatures via fast ion stabilization. In this way, something similar to an internal transport barrier could be reproduced without the need of flat or reversed q profiles. More experiments and modelling on possible ITER scenarios with RF fast particle stabilization in the plasma core should be done.

Role of multi-scale interactions and electron-scale instabilities in core thermal transport. Dependence of the critical threshold on plasma parameters, and especially on s and on τ:

Regarding the electron heat transport, our analysis lead to the following results:

- A first direct experimental observation of the stabilizing effect of the magnetic shear on the electron heat transport has been obtained in JET. Increasing s leads to an upshift of the turbulent electron heat flux critical threshold in R/L_{Te}.

- An increase of the electron stiffness and a decrease of the threshold in R/L_{Te} have been observed when NBI heating is used with respect to plasmas where only RF electron heating is used. One parameter that is changing is T_e/T_i, which has been found to have a negligible effect on TEM, but to be important for ETG modes through the $\tau = Z_{eff} \cdot T_e/T_i$ parameter. Analyzing a wider database of JET L-modes, a strong correlation between the electron turbulent transport critical threshold and τ has been found. This correlation indicates that ETG modes can indeed be important for the electron heat transport.

- Nonlinear gyrokinetic simulations predict that the ion-scale instabilities (TEM/ITG) are unable, at least in the considered cases, to reproduce the experimental electron heat flux and especially the electron stiffness. The response of the electron heat flux to a change in R/L_{Te} predicted by our simulations is much lower than the one observed experimentally.

- Our nonlinear gyrokinetic multi-scale simulation predicts a strong role of ETG modes for the electron heat flux. The level of the electron heat flux and of the electron stiffness predicted by the multi-scale simulation is much higher with respect to the one predicted by ion-scale simulations and is in better agreement with the experiment. It also appears from the simulation that multi-scale interactions are fundamental for the turbulent dynamics in the plasma. While ion-scale structures, such as zonal flows, have a strong impact on the ETG structures, leading to a stabilization of ETG modes, it has also been found that an inverse energy cascade is present from ETG scales to ITG scales. This means that the ETG structures can impact the turbulent dynamics on ion-scale.

- There is a mismatch, at the same value of R/L_{Ti}, between the ion heat flux predicted by TGLF and by our gyrokinetic simulations. This is related to the already observed underestimation of the ion stiffness in TGLF and, in the studied case, also to an overestimation of the ITG critical threshold in R/L_{Ti}. When the ion heat flux is matched between the gyrokinetic simulations and TGLF, the predicted electron heat flux is in good agreement between the two, with TGLF predicting a strong increase of the electron stiffness due to ETG modes, but at values of R/L_{Te} higher with respect to the experimental one.

The previous results confirmed the expected stabilizing effect of s and τ on the electron heat transport. These results point to an important role of ETG modes in the electron heat transport in some conditions. This is true in particular when the ion-scale instabilities are not strongly unstable and high values of R/L_{Te} are reached. From the results obtained in this thesis and in other studies (see Refs. of chapter 9), it also appears that high-k instabilities and multi-scale interactions are not important only for electron heat flux, but can influence the ion heat flux and the particle transport. If it is true that particle and ion heat fluxes are not directly caused by high-k fluctuations due to the quasi-adiabatic response of ions at these scales, it is also true that high-k instabilities have an impact on ion-scale structures. For example, one mechanism proposed is a damping of ion-scale zonal flows in presence of strong ETG instabilities. This can lead to changes in the ion and electron heat fluxes carried by low-k instabilities but also to modifications of the particle transport. For example modifications of the thermo-diffusive term for the particle transport can be induced by a strong change in the low-k micro-instabilities. Since all these effects may be important in plasma conditions similar to those of the ITER baseline scenario, this study calls for the need of accounting for high-k instabilities and multi-scale interactions in future ITER simulations. A way to take into account the multi-scale interactions is needed also in quasi-linear models. A first attempt in this direction has already been started with TGLF, but some improvements and a similar work with QuaLiKiz are needed. Further multi-scale simulations of JET plasmas, considering all the possible ITG stabilizing mechanisms, such as fast ions, that can also destabilize the ETG modes, electromagnetic effects and impurities should be done, as well as simulations of more ITER-relevant discharges, such as hybrid or H-mode plasmas. Experimentally, measurements of the plasma density and/or temperature fluctuations can help to understand the role of ETG modes, as indicated by the density fluctuation spectra from the multi-scale simulation. A change in the slope at ion-scale wavelength or a formation of a second peak at shorter wavelength could reveal the presence of high-k instabilities in the plasmas. Tokamaks such as DIII-D or TCV have the diagnostics required to do such study.

The isotope effect:

From the analysis of JET C-wall and ITER-like wall L-mode H and D plasmas with similar heating power, geometry, I_p, B, q, s and n_e it appears that:

- Both T_e and T_i are lower in H plasmas, the difference starting at the plasma edge.
- In low power plasmas, with low fast ion pressure, the ion heat flux in the plasma core does not deviate from the gyro-Bohm scaling law outside error bars, but, as the strong influence of T_i dominates over the mass one in the gyro-Bohm normalization, it is difficult to make a certain conclusion on the mass dependence from our data.
- A difference in the ion heat flux has been observed at higher power, in the situation where a strong stabilization of ITG modes by fast ions is expected. In this case, the stabilization of the ion heat transport is less strong in H plasmas with respect to D plasmas. A possible explanation of this difference has been found in the difference of the fast ion pressure in H and D plasmas, in H plasmas being $\sim 1/2$ of the one in D plasmas. This is mainly due for NBI fast ions to the lower beam injection energies and shorter beam slowing down time in H plasmas and for the ICRH fast ions to the lower ^3He concentration needed for the ICRH minority scheme heating in H.
- The electron heat transport shows in general higher values of R/L_{Te} in H plasmas. Also, the strong correlation between R/L_{Te} and τ observed in D plasmas has not

been observed in H plasmas, which is consistent with reduced importance of ETG modes.

- Another difference between H and D plasmas is the accumulation of heavy impurities in the plasma core observed in H plasmas with dominant ICRH ion heating and not observed in similar conditions in D plasmas. No accumulation has been observed using dominant electron ICRH heating. Further investigations are needed on possible differences of the particle transport in D and H plasmas.

The different effect of fast ions between H and D plasmas, related to experimental settings, can participate in explaining the differences in the plasma core transport in particular situations (i.e. when the role of fast ions is important). However, the deviation of the transport level from the expected scaling has been observed in a wide range of experimental settings, including Ohmic confinement plasmas, where there are no fast ions. As already pointed out, some differences come from the plasma edge, influencing the global plasma confinement. Other differences in the plasma related to the different ion mass are the energy exchange between ions and electrons ($\propto m_i$) and the plasma effective collisionality ($\propto m_i^{-0.5}$). These two factors have been proposed in different works in order to explain the isotope effect. The changes in the exchanged power lead to higher values of T_i/T_e in H Ohmic plasmas and to higher values of R/L_{Ti}, that can explain the higher transport observed in H compared to D Ohmic plasmas. The differences in the effective collisionality can affect the electron instabilities such as TEM, leading to more TEM stabilization in D plasmas. In addition, since the linear growth rate scales as $m_i^{0.5}$, for a given rotation profile the $E \times B$ stabilization is going to be less strong in H plasmas. To summarize, an exact gyro-Bohm scaling with isotope mass is expected for ITG driven instabilities. If, however, when changing main ion species there are changes in parameters that can affect the ITG modes in a way that these are more destabilized with lower isotope mass, or that can lead to a dominance of electron instabilities such as TEM and ETG modes, these can explain the deterioration of the ion confinement with lower isotope mass without a breaking in the ITG gyro-Bohm scaling.

A new experimental campaign is starting at JET, with H, D and T plasmas. This will be a unique occasion to further investigate the role of the isotope mass on the turbulent transport in the plasma core. More studies using gyrokinetic simulation are also needed, to understand if and to what extent the change of the main ion mass will affect in ITER stabilization mechanisms like rotation and electromagnetic effects.

List of publications, conference proceedings and international meeting presentations

See also my ORCID page: https://orcid.org/0000-0003-4344-3330.

Papers published or submitted to journals:

- N. Bonanomi, P. Mantica, G. Szepesi, N. Hawkes, E. Lerche, P. Migliano, A. G. Peeters, C. Sozzi, M. Tsalas, D. Van Eester, "Trapped electron mode driven electron heat transport in JET: experimental investigation and gyrokinetic theory validation", Nucl. Fusion 55, 113016 (2015). https://doi.org/10.1088/0029-5515/55/11/113016.
- N. Bonanomi, P. Mantica, C. Giroud, C. Angioni, P. Manas, S. Menmuir, "Light impurity transport in JET ILW L-mode plasmas", Nucl. Fusion 58, 036009 (2018). https://doi.org/10.1088/1741-4326/aaa4d3.
- N. Bonanomi, P. Mantica, J. Citrin, C. Giroud, E. Lerche, C. Sozzi, D. Taylor, M. Tsalas, D. Van Eester, "Effects of nitrogen seeding on core ion thermal transport in JET ILW L-mode plasmas", Nucl. Fusion 58 026028, (2018). https://doi.org/10.1088/1741-4326/aa9e7c.
- N. Bonanomi, P. Mantica, A. Di Siena, E. Delabie, C. Giroud, T. Johnson, E. Lerche, S. Menmuir, M. Tsalas, D. Van Eester, "Turbulent transport stabilization by ICRH minority fast ions in low rotating JET ILW L-mode plasmas", submitted to Nucl. Fusion, 11/2017.
- N. Bonanomi, P. Mantica, J. Citrin, T. Goerler, B. Teaca, "Impact of electron scale turbulence and multi-scale interactions in the JET tokamak", submitted to Phys. Rev. Lett., 01/2018.
- J. Citrin, C. Bourdelle, F. J. Casson, C. Angioni, N. Bonanomi, Y. Camenen, X. Garbet, L. Garzotti, T. Gorler, O. Gurcan, F. Koechl, F. Imbeaux, O. Linder, K. van de Plassche, P. Strand, G. Szepesi, "Tractable flux-driven temperature, density, and rotation profile evolution with the quasilinear gyrokinetic transport model QuaLiKiz", Plasma Phys. Control. Fusion 59, 124005 (2017). https://doi.org/10.1088/1361-6587/aa8aeb.
- X. Litaudon et al., "Overview of the JET results in support to ITER", Nucl. Fusion 57, 102001 (2017). https://doi.org/10.1088/1741-4326/aa5e28.

Conference proceedings:

- N. Bonanomi et al., Poster: “Impact of electron scale modes on electron heat transport in the JET tokamak”, Proc. 42nd EPS Conference on Plasma Physics, Lisbon, Portugal, June 2015. Europhysics Conference Abstracts, vol. 39E.
- N. Bonanomi et al., Poster: “Light impurities in JET plasmas: transport mechanisms and effects on thermal transport”, 43rd EPS Conference on Plasma Physics, Leuven, Belgium, July 2016. Europhysics Conference Abstracts, vol. 40A.
- N. Bonanomi et al., Poster: “Electron Heat Transport in JET from Ion to Electron scales: Experimental Investigation and Gyrokinetic Simulations”, Proc. 26th Fusion Energy Conference, Kyoto, Japan, 2016. CN-234, EX/P6-14, IAEA, Vienna.
- N. Bonanomi et al., Poster: “Impact of electron scale modes on electron heat transport in the JET tokamak”, 44th EPS Conference on Plasma Physics, Belfast, UK, June 2017, Europhysics Conference Abstracts, Vol. 41F.

Meeting presentations:

- N. Bonanomi et al., Poster & Oral: “Role of small scale turbulence and multi-scale interactions in electron heat transport in JET”, 21st joint EU – US TTF Meeting, Leysin, Switzerland, 5-8/09/2016.
- N. Bonanomi et al., Poster: ”Light impurity transport in JET plasmas”, 21st joint EU – US TTF Meeting, Leysin, Switzerland, 5-8/09/2016.
- N. Bonanomi et al., Oral: “Analysis and gyrokinetic modelling of light impurities in JET L-mode plasmas with ILW”, 16th ITPA Transport and Confinement Topical Group Meeting, IPR, Ahmedabad, India: 16-18 March 2016.
- N. Bonanomi et al., Oral: “Role of ETGs and multi-scale interactions in JET plasmas”, 17th ITPA Transport and Confinement Topical Group Meeting, Naka Fusion Institute, Japan: 24-26 October 2016.
- N. Bonanomi et al., Oral: “Update on light impurity transport studies on JET”, 18th ITPA Transport and Confinement Topical Group Meeting, PPPL, Princeton, US, 1-3 May 2017.
- N. Bonanomi et al., Oral: “Ion destiffening due to high ICHR power with low NBI at JET”, 19th ITPA Transport and Confinement Topical Group Meeting, Espoo, Finland, 18-21 September 2017.

JET Task Force Meeting presentations:

- N. Bonanomi et al., “Trapped electron mode driven heat transport in JET”, CCFE, Culham, UK. 03/02/2015.
- N. Bonanomi et al., “Impact of electron scale modes on electron heat transport in the JET tokamak”, CCFE, Culham, UK. 26/03/2015.

- N. Bonanomi et al., “Light impurities in JET plasmas: transport mechanisms and effects on thermal transport”, CCFE, Culham, UK. 21/06/2016.
- N. Bonanomi et al., “Role of small-scale turbulence and multi-scale interactions in electron heat transport in JET”, CCFE, Culham, UK. 23/09/2016.
- N. Bonanomi et al., “Isotope effect in JET L-mode plasmas”, CCFE, Culham, UK. 04/04/2017.
- N. Bonanomi et al., “Light impurities in JET plasmas: transport mechanisms and effects on thermal transport.”, CCFE, Culham, UK. 31/05/2017.
- N. Bonanomi et al., “Role of small-scale turbulence and multi-scale interactions in electron heat transport in JET”, CCFE, Culham, UK. 06/06/2017.
- N. Bonanomi et al., “Impact of electron scale turbulence and multi-scale interactions in the JET tokamak”, CCFE, Culham, UK. 10/10/2017.
- N. Bonanomi et al., “Ion and electron heat transport in JET L-mode plasmas”, CCFE, Culham, UK. 30/11/2017.

I'd like to thank Dr. Paola Mantica for all the help and for all the time she spent following my work in the last three years. I'd like to thank her also for the trust and the freedom she gave me. I'm also grateful to Prof. Giuseppe Gorini of University of Milano-Bicocca and to the CNR-Plasma Physics Institute 'P. Caldirola' for the resources they gave me for this thesis. I'd like to thank Dr. Gabor Szepesi, Dr. Jonathan Citrin, Dr. Tobias Goerler, Dr. Michele Romanelli, Dr. Clarisse Bourdelle and Dr. Clemente Angioni for very precious suggestions, help and great disponilility in following me during my visits in their research centers. During my PhD I met some very nice people and I spent some very nice moments with them. In particular I'd like to thank Dario, Luigi, Michele, James, Cristian, Alessandro, Jonathan and Clarisse for the nights spent in Aix-en-Provence, Lisbon, Oxford, Leuven, Munich, and Belfast. I'd like to thank my friends and Tanya for all the moments they spent with me. They really helped me to relax and enjoy also during the more 'tough' periods. Last, but not least, I'd like to thank my parents and all my family for all the support they gave me during these years.

I'd like to dedicate this thesis to my nona Antonietta (Crista!).